RÉPUBLIQUE FRANÇAISE
Liberté Égalité Fraternité

Université de Toulouse

Doctorat de l'Université de Toulouse

Propriétés moléculaires de haute précision par la théorie de coupled-cluster relativiste d'ordre élevé

Thèse présentée et soutenue, le 5 décembre 2025 par

Gabriele FABBRO

École doctorale
SDM - SCIENCES DE LA MATIERE - Toulouse

Spécialité
Physico-Chimie Théorique

Unité de recherche
LCPQ - Laboratoire de Chimie et Physique Quantiques

Thèse dirigée par
Trond SAUE

Composition du jury
Mme Pina ROMANIELLO, Présidente, CNRS Occitanie Ouest
M. Robert BERGER, Rapporteur, Philipps-Universität Marburg
Mme Stella STOPKOWICZ, Rapporteure, Universität des Saarlandes
M. Andre Severo PEREIRA GOMES, Examinateur, CNRS Hauts-de-France
M. Trond SAUE, Directeur de thèse, CNRS Occitanie Ouest

Highly Accurate Molecular Properties using High-Order Relativistic Coupled Cluster Theory

Gabriele Fabbro

Submitted in total fulfillment of the requirements of the degree of

Doctor of Philosophy

Université de Toulouse

5 December 2025

Alla mia famiglia,
che mi è sempre stata accanto e ha sempre creduto in me.

Abstract

Heavy atoms present formidable theoretical challenges, arising from the interplay of relativistic motion of inner electrons, quantum electrodynamics (QED) effects, and strong electron correlation. The HAMP-vQED (Highly Accurate Molecular Properties using variational Quantum Electrodynamics) project tackles these challenges by providing a unified computational framework that simultaneously incorporates relativistic, QED, and correlation effects, enabling highly accurate predictions of molecular properties. Among these effects, this thesis focuses on the accurate treatment of electron correlation. To achieve this, the Coupled-Cluster (CC) method has been adopted as the primary computational approach, due to its high accuracy and systematic improvability. However, extending CC methods to higher excitation levels, such as triple, quadruple, or beyond, makes the derivation of the corresponding working equations extremely complex and prone to errors. These challenges can be effectively addressed through the development of automated equation generators, such as the `tenpi` toolchain, developed within the HAMP-vQED project. The primary goal of this thesis has therefore been the implementation of analytical first derivatives of the CC energy at arbitrary excitation levels using the `tenpi` toolchain. To do that, following the Lagrangian formalism, we derived and implemented the Λ-equations and the corresponding one-body density matrices for high-level order of theory. This enabled the calculation of molecular properties at the CCSDT and CCSDTQ levels within the `DIRAC` program package. The molecular property that we have primarily investigated in this thesis is the electric field gradient (EFG) evaluated at the nuclear positions. For nuclei possessing a nuclear quadrupole moment (NQM), the latter couples to the EFG, and their interaction is quantified by the nuclear quadrupole coupling constant (NQCC). Accurate values of NQM can be extracted from experimentally determined NQCCs combined with high-level quantum-chemical calculations of the EFG. For heavy atoms, the EFG is highly sensitive to both electron correlation and relativistic effects, making it a particularly appealing property in the context of this thesis. In addition to these electronic-structure contributions, the accurate prediction of molecular properties also requires the inclusion of rovibrational corrections, which arise from the fact that molecules rotate and vibrate around their equilibrium geometry. Within this thesis, these contributions have been derived and implemented for diatomic molecules in order to enhance the agreement between theory and experiment. Beyond its connection to the nuclear quadrupole moment, the EFG also encodes chemically relevant information, particularly regarding the nature of chemical bonding. This aspect is emphasized in the Dailey-Townes model, which assumes that the dominant contribution to the EFG at the self-consistent field (SCF) level arises from valence p orbitals. However, this model neglects the role of partially occupied d and f shells, relativistic effects, and polarization contributions. Part of this thesis has been

devoted to critically assessing and refining this model in order to provide a more complete and accurate description of the chemical factors influencing the EFG.

Résumé

Les atomes lourds présentent des défis théoriques considérables, résultant de l'interaction entre le mouvement relativiste des électrons internes, les effets de l'électrodynamique quantique (QED) et la forte corrélation électronique. Le projet HAMP-vQED (Highly Accurate Molecular Properties using variational Quantum Electrodynamics) relève ces défis en fournissant un cadre de calcul unifié qui intègre simultanément les effets relativistes, de QED et de corrélation, permettant des prédictions très précises des propriétés moléculaires. Parmi ces effets, cette thèse se concentre sur le traitement précis de la corrélation électronique. Pour cela, la méthode Coupled-Cluster (CC) a été adoptée comme approche principale en raison de sa grande précision et de sa possibilité d'amélioration systématique. Cependant, l'extension des méthodes CC à des niveaux d'excitation plus élevés, tels que triple, quadruple ou plus, rend la dérivation des équations de travail correspondantes extrêmement complexe et sujette à erreurs. Ces défis peuvent être efficacement relevés grâce au développement de générateurs automatiques d'équations, tels que la chaîne d'outils `tenpi`, développée dans le cadre du projet HAMP-vQED. L'objectif principal de cette thèse a donc été la mise en œuvre des dérivées analytiques du premier ordre de l'énergie CC à des niveaux d'excitation arbitraires, en s'appuyant sur la chaîne `tenpi`. Pour ce faire, en suivant le formalisme lagrangien, nous avons dérivé et implémenté les équations Λ ainsi que les matrices de densité à un corps pour des niveaux élevés de théorie. Cela a permis le calcul de propriétés moléculaires aux niveaux CCSDT et CCSDTQ au sein du programme `DIRAC`. La propriété moléculaire que nous avons principalement étudiée dans cette thèse est le gradient de champ électrique (EFG) évalué aux positions nucléaires. Pour les noyaux possédant un moment quadrupolaire nucléaire (NQM), celui-ci s'accouple à l'EFG, et leur interaction est quantifiée par la constante de couplage quadrupolaire nucléaire (NQCC). Des valeurs précises de NQM peuvent être extraites à partir de NQCCs déterminées expérimentalement combinées à des calculs quantiques de haute précision du gradient de champ électrique. Pour les atomes lourds, l'EFG est très sensible à la fois à la corrélation électronique et aux effets relativistes, ce qui en fait une propriété particulièrement intéressante dans le contexte de cette thèse. En plus de ces contributions provenant de la structure électronique, la prédiction précise des propriétés moléculaires nécessite également l'inclusion de corrections rovibrationnelles, qui résultent du fait que les molécules tournent et vibrent autour de leur géométrie d'équilibre. Dans cette thèse, ces contributions ont été dérivées et mises en œuvre pour des molécules diatomiques afin d'améliorer la concordance entre théorie et expérience. Au-delà de son lien avec le moment quadrupolaire nucléaire, l'EFG encode également des informations chimiquement pertinentes, en particulier sur la nature des liaisons chimiques. Cet aspect est mis en évidence dans le modèle de Dailey-Townes, qui suppose que la contribution dominante à l'EFG au niveau du champ auto-cohérent (SCF) provient des orbitales de

valence p. Cependant, ce modèle néglige le rôle des orbitales d et f partiellement occupées, les effets relativistes et les contributions de polarisation. Une partie de cette thèse a été consacrée à l'évaluation critique et à l'affinement de ce modèle afin de fournir une description plus complète et précise des facteurs chimiques influençant l'EFG.

Preface

This Ph.D. thesis has been submitted as part of the requirements for earning a Ph.D. degree in theoretical chemistry at the Université de Toulouse - Paul Sabatier. The research presented in this thesis was conducted from November 2022 to November 2025 at the Laboratoire de Chimie et Physique Quantiques under the supervision of Trond Saue. My initial exposure to this area of research came during my Master's internship from March to June 2022, where I worked on a project closely related to the one discussed in this thesis. The research output of this project, which greatly influenced the work presented here, is listed below in chronological order of publication.

1. Gabriele Fabbro, Johann Pototschnig, and Trond Saue, "Beyond the Dailey–Townes Model: Chemical Information from the Electric Field Gradient," *The Journal of Physical Chemistry A*, vol. 129, pp. 1006–1025, 2025. DOI: 10.1021/acs.jpca.4c06884.
   In this project, I performed all the calculations, carried out the data analysis, and wrote the first draft of the manuscript.

2. Gabriele Fabbro, Jan Brandejs, and Trond Saue, "Highly Accurate Expectation Values Using High-Order Relativistic Coupled Cluster Theory," *The Journal of Physical Chemistry A*, vol. 129, pp. 7360–7372, 2025. DOI: 10.1021/acs.jpca.5c02844.
   In this project, I derived the equations for the Λ *amplitudes and the density matrices at arbitrary coupled-cluster (CC) level, formulated them within the tenpi framework, and implemented the CCSDT and CCSDTQ expectation values in the DIRAC program. I also developed and implemented the ro-vibrational corrections, carried out all the calculations and the data analysis, and wrote the manuscript.*

3. Gabriele Fabbro, Jan Brandejs, and Trond Saue, "The nuclear electric quadrupole moment of ^{87}Sr from highly accurate molecular relativistic calculations", Submitted to *The Journal of Physical Chemistry*, arXiv:2602.00855.
   In this project, I proposed the idea, performed all the calculations, carried out the data analysis, and wrote the manuscript.

Funding. This thesis was funded by the European Research Council (ERC) under the European Union's Horizon 2020 research and innovation program (grant agreement ID:101019907).

Acknowledgements

"I wish there was a way to know you're in the good old days, before you've actually left them."
— Andy "Nard Dog" Bernard (The Office)

First and foremost, I would like to express my deepest gratitude to my PhD supervisor, Trond Saue, for believing in me, pushing me to give my best, and always being open to dialogue. I have learned invaluable lessons from you. I also thank my research group, the HAMP-vQED team, for sharing these three years and nice moments together, and the DIRAC family for always making me feel welcome and at ease in Odense.

Stare lontano dal mio paese e dagli amici non è mai semplice, e adattarsi a una nuova città, a un nuovo ambiente e a nuove persone può essere ancora più difficile quando si è introversi. Eppure, qui a Tolosa, tutto questo è diventato sorprendentemente più leggero grazie alle persone meravigliose che ho avuto la fortuna di incontrare e che hanno trasformato un'esperienza incerta in qualcosa di speciale. Per questo desidero ringraziare di cuore le mie biologhe preferite: Marika, Jessica, Michela e Teresa, che mi hanno accolto con naturalezza, mi hanno fatto sentire parte del loro mondo e hanno saputo regalarmi momenti di divertimento, serenità e felicità. Senza di loro, questi anni non sarebbero stati gli stessi, e non avrei imparato a fare tutti questi risotti!

Anche se mi sono trasferito in un altro paese, i miei amici di lunga data sono sempre stati presenti, e ogni volta che torno in Italia e li rivedo, sembra che nulla sia cambiato. In particolare, voglio ringraziare Lorenzo, Francesca, Costanza, Daniele e "gli amici del C11" per la loro amicizia duratura.

Ringrazio Lucia per la presenza costante, la pazienza e il sostegno dimostrati nel corso del dottorato. Anche se le nostre strade si sono poi separate, ciò che abbiamo condiviso in questi anni resta, e resterà, una parte preziosa di questo percorso.

Voglio ringraziare di cuore mia cugina Elisa, che in questi tre anni è stata al mio fianco, ascoltandomi in lunghe videochiamate e dandomi consigli su moltissime, troppe cose. Sono davvero fortunato ad avere una persona speciale come te nella mia vita.

Un immenso grazie va a tutta la mia famiglia che mi ha sempre sostenuto, compreso e capito. Grazie Michele per tutte le centinaia di volte che hai fatto il tragitto Pordenone-Treviso per accompagnarmi in aeroporto e, più in generale, per essere sempre stato presente in tutte le tappe più importanti della mia vita. Grazie mamma per farmi sentire a casa ogni volta, come se il tempo non passasse. Grazie per farmi ogni volta il mio piatto

preferito quando torno, le lasagne (stereotipo da italiano, però è vero!). Grazie per aver creduto in me anche nei momenti in cui io stesso avevo perso fiducia.

Introduction

"So this is a very exciting day for me, because today, we're going to start quantum mechanics and that's all we'll do till the end of the term. Now I've got bad news and good news. The bad news is that it's a subject that's kind of hard to follow intuitively, and the good news is that nobody can follow it intuitively. Richard Feynman, one of the big figures in physics, used to say, 'No one understands quantum mechanics.' So in some sense, the pressure is off for you guys, because I don't get it and you don't get it and Feynman doesn't get it. The point is, here is my goal. Right now, I'm the only one who doesn't understand quantum mechanics. In about seven days, all of you will be unable to understand quantum mechanics. Then you can go back and spread your ignorance everywhere else. That's the only legacy a teacher can want. All right, so that's the spirit in which we are doing this. I want you to think about this as a real adventure. Try to think beyond the exams and grades and everything. It's one of the biggest discoveries in physics, in science, and it's marvelous how people even figured out this is what's going on."
— Professor Ramamurti Shankar

By the mid-1920s, physicists had developed a fundamentally new framework for describing atoms: quantum mechanics, which treats electrons as wave-like entities rather than classical particles. This theory revolutionized chemistry by providing a rigorous explanation for atomic energy levels, electron configurations, and the nature of chemical bonding. Within this framework, quantum chemistry emerged as a discipline devoted to solving the electronic structure problem with increasing precision. One of its central goals is to achieve the highest possible accuracy in the theoretical prediction of energies and molecular properties. This ambition is driven both by the need to support and interpret experimental findings, and by the ability to provide reliable data in cases where experiments are challenging, costly, or infeasible.

For systems containing heavy elements (typically for elements with atomic number $Z \geq 40$), however, non-relativistic quantum mechanics becomes fundamentally inadequate. In such atoms, inner-shell electrons move at velocities approaching a significant fraction of the speed of light, and their correct description requires the incorporation of relativistic effects [1]. If one seeks quantitative agreement with experiment in these systems, especially for spectroscopic properties, bond lengths, or energetics, relativistic corrections are not optional—they are essential. Relativistic quantum chemistry, based on the Dirac equation for electrons [2, 3], provides the appropriate theoretical framework to account for these phenomena. Relativistic contributions, both scalar and spin–orbit in nature, have a profound influence on the chemical behavior of heavy-element compounds, shaping their structure, bonding, reactivity, and spectroscopic signatures [4–11].

A second essential pillar of high-accuracy quantum chemistry is the proper treatment of electron correlation. In many-electron systems, electrons repel each other and tend to avoid one another. The Hartree–Fock (HF) method incorporates only a mean-field approximation of this repulsion [12, 13], neglecting the instantaneous interactions that lower the total energy when electrons avoid each other. The missing contribution is known as the *correlation energy* [14]. Electron correlation is usually classified into two types. Dynamic correlation refers to the short-range, instantaneous adjustments of the electron motions that are absent in the HF picture and are essential for an accurate description of the total energy. Static (or nondynamic) correlation, on the other hand, arises when a single Slater determinant is insufficient to represent the qualitative electronic structure, such as in bond dissociation or near-degeneracy situations. In this thesis, we will primarily focus on the accurate description of dynamic correlation. To recover the correlation effects, post-HF methods are employed. Among these, coupled-cluster (CC) theory has emerged as the standard for achieving chemical accuracy in small to medium-sized systems [15]. CC theory builds upon the HF reference wavefunction by introducing an exponential cluster operator that systematically includes electron correlation through excited determinants. Truncating the expansion at the level of single and double excitations (CCSD), or including higher-order terms such as triples (CCSDT) and quadruples (CCSDTQ), allows for a hierarchical increase in the level of electron correlation and typically leads to improved accuracy. While CC theory is conceptually powerful, implementing high-order CC is notoriously difficult. The CC equations for CCSDT or CCSDTQ consist of hundreds of tensorial terms, each corresponding to diagrams or algebraic contributions. Deriving these terms by hand – either algebraically or by drawing Goldstone diagrams – is extremely tedious and error-prone. A lot of work has been done for the construction of general-order CC equations generators [16–27]. Recently, Brandejs and co-workers introduced the Tensor Programming Interface (`tenpi`) [28], an open-source framework that

systematically generates CC equations of arbitrary excitation rank. `tenpi` uses diagrammatic and symbolic algebra to produce optimized code for given tensor backends (GPU libraries, MPI, etc.). This approach has brought two-component relativistic CCSDT and CCSDTQ into reach in the relativistic `DIRAC` program package [29]. It is worth noting that relativistic and correlation effects are strongly coupled and interact in a non-additive manner [30–32]. Therefore, to achieve truly high-accuracy results for heavy-element systems, it is essential to be able to perform *correlated relativistic calculations*, in which both electron correlation and relativistic effects are treated simultaneously.

One might ask whether the Dirac equation is enough to fully describe atomic structure, or if additional effects must be considered. A pivotal insight, first demonstrated by Lamb and Retherford in their landmark experiment [33], revealed that the hydrogenic $2s_{1/2}$ and $2p_{1/2}$ states are not degenerate, contrary to the predictions of the Dirac equation. This energy difference, known as the Lamb shift, cannot be explained within the framework of relativistic quantum mechanics alone. Its proper understanding requires the more comprehensive theory of Quantum Electrodynamics (QED) [34], which accounts for the interaction between the electron and the fluctuating quantum vacuum as well as the quantized electromagnetic field. These radiative corrections lift the degeneracy, producing a small but experimentally measurable energy splitting and thereby demonstrating the necessity to extend beyond the Dirac formalism for high-precision atomic calculations. Among the radiative corrections introduced by QED, two main effects stand out: *vacuum polarization* and *self-energy*. Vacuum polarization modifies the short-range behavior of the Coulomb potential through the virtual creation of electron–positron pairs, effectively altering the perceived *charge*. Self-energy arises from the electron's interaction with its own quantized electromagnetic field, resulting in shifts to its *mass* and energy levels. These corrections become increasingly significant for heavy atoms [35]. From a chemical perspective, QED effects are indeed observable. For instance, studies on gold have shown that QED corrections to ionization potentials and electron affinities are comparable in magnitude to high-order electron correlation effects [36]. QED contributions typically reduce relativistic effects by about 1% [37]. In molecular systems, subtle QED effects can also be detected; for example, the persistent discrepancy between calculated and experimental bond lengths in AuCN [38–40] has been attributed to missing QED contributions, a hypothesis recently supported by state-of-the-art relativistic QED calculations [41].

Much of chemistry is fundamentally grounded in light elements such as carbon, hydrogen, oxygen, nitrogen, and a few others. This may lead one to question whether the inclusion of elaborate corrections is truly necessary for such seemingly simple systems. However, even for light atoms, achieving high accuracy requires the systematic incorporation of several effects—relativistic corrections, QED, high-order electron correlation,

and nuclear motion contributions. This necessity has been clearly demonstrated in recent high-precision studies, such as the work by Usov and co-workers on the ground-state potential energy curve and dipole moment of CO, where relativistic, QED, adiabatic, and nonadiabatic effects are all accounted for at a high level of theory [42]. As recently emphasized in a mini-review by Saue, *chemistry needs more physics* [43].

Beyond total energies, we ultimately care about molecular properties, such as spectroscopic constants, polarizabilities, hyperfine couplings, and so forth, that bridge theory and experiment [44]. A primary reason is that computed properties can be directly compared to measurements, providing stringent tests of theory and predictive chemical insights. For fully variational wave functions, the Hellmann–Feynman theorem [45, 46] guarantees that first-order derivatives of the energy with respect to external perturbations can be obtained directly from the wave function, without requiring derivatives of the wave function itself. However, properties in coupled-cluster theory are nontrivial to compute. Unlike variational methods, the CC energy is not a variational minimum in the wavefunction parameters, so the Hellmann–Feynman theorem does not hold in the straightforward way. A simple approach to computing coupled-cluster energy derivatives is to employ numerical techniques such as finite-difference methods. However, numerical derivatives are typically less accurate than their analytic counterparts, especially when high precision is required. Also, they are computationally demanding, as multiple independent energy evaluations are needed for each derivative component. Moreover, extending finite-difference techniques to the calculation of more complex response properties, such as time-dependent or magnetic observables, presents additional challenges. Therefore, for the computation of the CC analytical derivatives we employ the Lagrangian formalism [47, 48]. The upshot is that analytic energy derivatives (properties) can then be obtained as derivatives of the Lagrangian, effectively solving a perturbed-independent set of linear equations for the multipliers.

The primary objective of this thesis has been the formulation and implementation of analytic first derivatives of the energy at arbitrary excitation levels within coupled-cluster theory, utilizing the `tenpi` toolchain.

One of the central properties investigated in this thesis is the electric field gradient (EFG) tensor at the nuclear positions. The EFG is defined as the negative of the second spatial derivative of the electrostatic potential at the position of the nucleus, or equivalently, the gradient of the local electric field. It quantifies how sharply the electric field varies in the vicinity of a nucleus due to the surrounding electronic and nuclear charge distributions. Nuclei with nuclear quantum spin number $I > 1/2$ may posses a nuclear electric quadrupole moment (NQM), which describes the intrinsic asphericity (deviation from spherical symmetry) of the nuclear charge distribution. Physically, the quadrupole

moment reflects how the charge is distributed along different spatial axes within the nucleus—typically associated with an oblate or prolate shape, as showed in Figure 1.

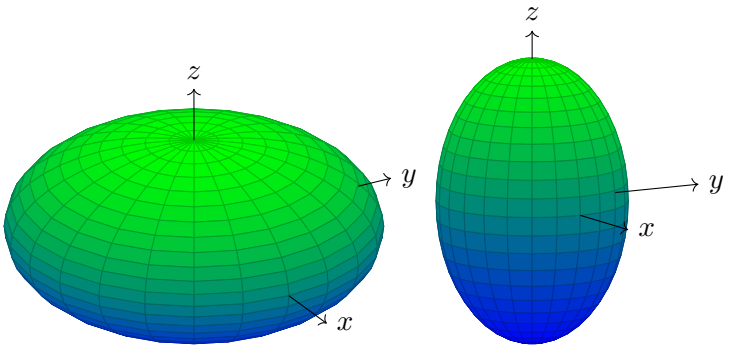

FIGURE 1: Illustration of the nuclear quadrupole moment (NQM) shapes: the first surface shows an oblate symmetry, corresponding to a flattening of the charge distribution along the z-axis, while the second surface shows a prolate symmetry, corresponding to an elongation along the z-axis.

The direct determination of the nuclear electric quadrupole moment Q, however, is challenging [49]. It can nonetheless be inferred by exploiting the nuclear quadrupole interaction (NQI), which arises from the interaction between the nuclear electric quadrupole moment and the EFG generated by the surrounding particles at the considered nucleus (electrons and possibly other nuclei). This interaction induces shifts and splittings of the nuclear energy levels, which can be experimentally observed using techniques such as Nuclear Quadrupole Resonance (NQR) [50], Mössbauer spectroscopy [51], and perturbed angular correlation spectroscopy [52], among others. A comprehensive overview of these methods is provided by Stone [53]. From experimental measurements, the coupling can be extracted in the form of the *nuclear quadrupole coupling constant* (NQCC):

$$\text{NQCC [MHz]} = 234.9647 \times Q(X)\,\text{[b]} \times q(X)\,[E_\text{h}/a_0^2], \tag{1}$$

where $q(X)$ is the EFG at nucleus X. The direct determination of Q using Eq. (1) is commonly referred to as the *direct method* [54]. This approach, however, is highly sensitive to small inaccuracies in the calculated EFG, particularly when the EFG is close to zero, as even minor errors in electron correlation contributions can lead to large relative deviations [55]. An alternative is the *indirect method*, which estimates Q by performing a fit over multiple molecules: variations in the experimental NQCCs are compared with the corresponding changes in calculated EFGs. This procedure mitigates systematic errors and is generally more robust against small inaccuracies in the EFG of any single molecule [56, 57]. Thus, since the NQCC is determined experimentally, our efforts to obtain an accurate value of Q rely entirely on a precise determination of the EFG using quantum-mechanical methods. However, its accurate determination is far to be simple. The EFG is extremely sensitive to the electronic charge distribution in the immediate vicinity of

the nucleus, as it proportional to $\langle r^{-3} \rangle$. This makes it especially susceptible to relativistic effects [5, 58, 59]. At the same time, spherically symmetric shells do not contribute to the EFG; according to Unsöld's theorem [60], fully occupied shells behave effectively as spherically symmetric and thus also yield no contribution. Consequently, the EFG is highly sensitive to the valence electronic structure, and therefore to electron correlation effects. We thus conclude that the EFG is sensitive to both relativistic effects and electron correlation effects, making it a particularly appealing quantity in the context of this thesis. This is precisely where our implementation of analytic derivatives at the high-order CC level, discussed previously, comes into play.

Beside the *physical* information, Q, the EFG also encodes *chemical* information. The EFG at a nucleus is intimately connected to the distribution of electrons around that atom, providing valuable insights into its chemical environment. Understanding how electron density, especially in the valence shell, shapes the EFG can help interpret experimental data in terms of chemical bonding and electronic structure. A classic and influential framework to rationalize this connection was proposed by Dailey and Townes [61]. They suggested that, in molecules, the EFG at a nucleus is primarily determined by the partially occupied valence p-orbitals of that atom. For instance, in halogen compounds, the dominant contribution to the EFG arises from the asymmetric occupancy of the p orbitals. Thus, in principle, EFG measurements can be interpreted as probes of the valence p-electron distributions. However, this raises questions about its applicability to systems that not only possess partially occupied p shells, but also d and/or f shells, as is the case in heavy metals, and about the implications of relativistic effects within this model.

Both types of information will be addressed in the applications section of this thesis.

Layout of the Thesis

The thesis is organized into two main *parts*:

- **Part I: Theory**

Chapter 1 This chapter introduces the principles of relativistic quantum mechanics and relativistic quantum chemistry.

Chapter 2 This chapter presents the fundamental aspects of the Coupled Cluster method, which serves as the primary wavefunction model employed throughout this thesis. Emphasis is placed on diagrammatic techniques.

Chapter 3 This chapter discusses the general framework for computing molecular properties, with particular emphasis on non-variational wavefunctions such as those arising in Coupled Cluster theory.

Chapter 4 This chapter introduces the nuclear quadrupole interaction and the Dailey–Townes model for determining the electric field gradient (EFG).

- **Part II: Applications**

Chapter 5 This chapter examines the validity of the Dailey–Townes model in the presence of relativistic effects, contributions from orbitals beyond the p-shell, and core polarization phenomena.

Chapter 6 This chapter details the derivation and implementation of analytic expectation values at arbitrary excitation levels using the `tenpi` toolchain. Applications include the accurate determination of $Q(^{7}\mathrm{Li})$ and $Q(^{27}\mathrm{Al})$ by computing CCSDT and CCSDTQ corrections using the `DIRAC` program package.

Chapter 7 This chapter applies the molecular approach to determine $Q(^{87}\mathrm{Sr})$ using three different treatments of electron correlation: CCSD(T), CCSD-T, and CCSD$\tilde{\mathrm{T}}$. The latter is a composite scheme enabled by a newly implemented multi-node parallel framework, which allows the efficient inclusion of high-order correlation effects in large active spaces.

Chapter 8 The final chapter summarizes the main conclusions and outlines perspectives for future research.

Contents

Abstract ii

Résumé iv

Preface vi

Acknowledgements vii

Introduction ix

Layout of the Thesis xv

I Theory 1

1 Relativistic Quantum Chemistry 2
- 1.1 Relativistic effects in chemistry . . . 3
- 1.2 Special relativity . . . 6
  - 1.2.1 Relativistic dynamics . . . 9
- 1.3 Relativistic theory of an electron . . . 13
  - 1.3.1 From Schrödinger to Klein-Gordon: adapting to relativity . . . 14
  - 1.3.2 Solving the relativistic puzzle: the Dirac equation . . . 17
    - 1.3.2.1 Time-independent Dirac equation . . . 21
    - 1.3.2.2 Negative-energy solutions . . . 22
- 1.4 Relativistic molecular calculations . . . 25
  - 1.4.1 Two-electron interaction . . . 26
  - 1.4.2 Relativistic basis set requirements . . . 28
  - 1.4.3 Relativistic Hartree-Fock theory . . . 31
  - 1.4.4 Relativistic density functional theory . . . 35
  - 1.4.5 Two-component methodologies . . . 37

2 Coupled Cluster Theory 41
- 2.1 The electron correlation problem . . . 42
  - 2.1.1 Size-extensivity and size-consistency . . . 45
  - 2.1.2 Towards size-extensive wave functions: the Coupled Cluster ansatz 46
- 2.2 Second-quantization background . . . 48

2.3 Formal Coupled Cluster method . . . 52
2.3.1 Coupled Cluster equations . . . 54
2.4 The diagrammatic approach . . . 60
2.4.1 Diagrammatic rules . . . 61
2.5 Intermediates . . . 72
2.6 High-order excitations . . . 73
2.6.1 tenpi: Tensor Programming Interface . . . 75

3 Molecular Properties **79**
3.1 Time-independent molecular properties . . . 80
3.1.1 Analytical vs numerical derivatives . . . 81
3.1.2 Variational perturbation theory . . . 83
3.2 Molecular properties using the CC wave-functions . . . 85
3.2.1 Λ-equations from the direct differentiation of the energy . . . 86
3.2.2 Λ-equations from the Lagrangian framework . . . 92
3.2.3 A diagrammatic perspective on the Λ−equations . . . 95
3.2.4 Expectation values . . . 98
3.2.4.1 Comments on the size-extensivity . . . 99
3.2.5 One-body CC response density matrix . . . 100

4 Nuclear Electric Quadrupole Interaction **104**
4.1 Electrostatic interaction energy . . . 105
4.2 Nuclear electric quadrupole moment interaction . . . 107
4.3 Dailey–Townes model . . . 112
4.3.1 Projection analysis . . . 113
4.3.2 Decomposition of the EFG in terms of reference orbitals . . . 114

II Applications **119**

5 Beyond the Dailey-Townes Model: Chemical information from the Electric Field Gradient **120**
5.1 Introduction . . . 122
5.2 Computational Details . . . 124
5.3 Results . . . 124
5.3.1 Chlorine compounds . . . 124
5.3.2 Uranyl . . . 133
5.4 Conclusions . . . 141

6 Highly Accurate Expectation Values Using High-Order Relativistic Coupled Cluster Theory **143**
6.1 Introduction . . . 145
6.2 Implementation . . . 148
6.2.1 Generation of the Λ−equations and density matrices . . . 148
6.3 Computational Details . . . 151
6.3.1 Basis set and Active space . . . 152
6.3.2 Determination of nuclear electric quadrupole moments Q . . . 156
6.4 Results & Discussion . . . 156

6.4.1 Correctness: dipole moment of LiH . . . 156
6.4.2 Nuclear Electric Quadrupole Moments of ^{7}Li . . . 157
6.4.3 Nuclear Quadrupole Moment of ^{27}Al from molecular data . . . 161
6.5 Conclusions . . . 166

7 The nuclear electric quadrupole moment of ^{87}Sr from highly accurate molecular relativistic calculations 170
7.1 Introduction . . . 172
7.2 Computational Details . . . 174
7.2.1 CCSD(T) & CCSD-T . . . 175
7.2.2 CCSD$\tilde{\text{T}}$ . . . 177
7.2.3 Massively parallel tensor operations . . . 178
7.3 Results and Discussion . . . 179
7.3.1 Bonding analysis . . . 179
7.3.2 Basis set and active space choice . . . 179
7.3.3 Electric field gradient analysis . . . 181
7.3.4 Quadrupole moment analysis . . . 183
7.3.5 Error estimation . . . 185
7.4 Conclusions . . . 187

8 Summary, Conclusions and Perspectives 189

A Complements to Chapter 1 193
A.1 Electromagnetic Potentials . . . 193

B Complements to Chapter 2 197
B.1 Normal-ordered Hamiltonian . . . 197
B.2 Proof of the BCH Expansion for the similarity-transformed Operator . . . 200
B.3 Why similarity transformations preserve the spectrum . . . 200

C Complements to Chapter 3 202
C.1 Second-order molecular properties . . . 202
C.1.1 Response equations . . . 205

D Complements to Chapter 4 207
D.1 Derivatives of the electrostatic potential . . . 207
D.2 Sternheimer shielding . . . 209
D.3 Time reversal symmetry and Kramers partners . . . 214

E Complements to Chapter 5 219
E.1 Localization and core orbitals . . . 219
E.1.1 Basic theory . . . 220
E.1.2 Will the Pipek–Mezey algorithm modify core orbitals ? . . . 222

F Complements to Chapter 6 223
F.1 Rovibrationally-averaged properties . . . 223

G Résumé en Français **230**

Bibliography **254**

Part I

Theory

Chapter 1

Relativistic Quantum Chemistry

> *"Henceforth space by itself, and time by itself, are doomed to fade away into mere shadows, and only a kind of union of the two will preserve an independent reality."*
>
> — *Hermann Minkowski [62]*

The aim of this chapter is to provide the reader with a comprehensive understanding of why and how relativistic effects are incorporated into quantum chemistry. In this chapter, we explore the intersection of quantum mechanics and the theory of special relativity as applied to chemical systems. Relativistic effects become increasingly significant when dealing with heavy elements, where electrons move at speeds that approach the speed of light. Such conditions necessitate corrections to non-relativistic quantum chemistry models in order to accurately predict electronic structure, bonding, and reactivity.

In writing this chapter, I have relied on some of the most authoritative texts in the field, notably the book by Dyall and Faegri [63], as well as the comprehensive book by Reiher and Wolf [64].

1.1 Relativistic effects in chemistry

In relativistic quantum mechanics, deviations from Newtonian mechanics become important when particles approach speeds comparable to the speed of light, $c = 299\,792\,458\,\mathrm{m/s} \approx 137.036(E_\mathrm{h}/a_0\hbar)$ [65]. A useful diagnostic for estimating the importance of relativistic effects is the Lorentz factor, defined as

$$\gamma = \frac{1}{\sqrt{1 - v^2/c^2}}\,, \tag{1.1}$$

which quantifies the increase in relativistic mass $m = \gamma m_e$ for a particle of rest mass m_e and velocity v. In atoms, particularly those with high atomic number Z, inner-shell electrons such as the $1s$ electron can achieve substantial fractions of the speed of light. In atomic units, the average velocity of a $1s$ electron is approximately $v_{1s} \approx Z$, so the ratio Z/c provides a direct estimate of the relativistic regime. For instance, for a hydrogen-like gold ion Au^{78+}, one finds $Z/c \approx 0.58$, corresponding to a relativistic mass increase of nearly 25% and a contraction of the $1s$ orbital by about 18%. Relativistic effects influence the electron's effective mass, which, in turn, affects the Bohr radius as $a_0 \propto m^{-1}$. An increase in effective mass due to relativistic motion thus leads to a contraction of the electron's orbital radius (*direct* effect). This contraction is most pronounced for s and p orbitals, conversely, d and f orbitals, experience relativistic expansion due to enhanced screening by the contracted inner shells (*indirect* effect). These *scalar* relativistic effects manifest in observable physical and chemical phenomena. One of the most exemplary consequences of relativistic effects in chemistry is the characteristic yellow color of elemental gold [4, 5]. Without scalar relativistic effects, the energy gap between the filled $5d^{10}$ band and the half-filled $6s^1$ conduction band would be too large to absorb visible light; only ultraviolet photons would have sufficient energy to bridge the gap. As a result, non-relativistic gold would appear silvery, much like silver itself. Scalar relativistic effects lower the energy of the 6s orbital and raise that of the 5d orbitals, reducing the gap between them, as illustrated in Fig.(1.1). This contraction–expansion interplay shifts the onset of interband transitions into the blue region of the visible spectrum. The consequence is selective absorption of blue light, making reflected light appear yellow, giving gold its distinctive color. Relativistic orbital contraction can also profoundly alter chemical bonding. In the gas-phase complex $Ag(H_2O)^+$, bonding is dominated by classical electrostatic interactions between the positive ion and the dipole moment of water. In

contrast, $Au(H_2O)^+$ exhibits significant covalent character due to relativistic stabilization of the gold $6s$ orbital, which enhances charge transfer and bonding interactions [6]. The contrasting properties of gold and mercury also underscore the chemical significance of scalar relativistic effects. Mercury exhibits a low melting point of $-38.83°C$, which is a relativistic phenomenon. Scalar relativistic effects lead to the full occupation and stabilization of the $6s$ orbital, resulting in weak metal-metal bonding in the bulk phase and consequently a liquid state at room temperature [7]. A striking technological implication of relativistic effects is found in the standard electrochemical potential of the lead-acid battery. The overall redox reaction is:

$$Pb(s) + PbO_2(s) + 2H_2SO_4(aq) \rightarrow 2PbSO_4(s) + 2H_2O(l)\,,$$

Non-relativistic quantum chemical calculations yield a cell potential of only $+0.39\,V$, while inclusion of scalar relativistic effects raises the predicted value to $+2.13\,V$, in excellent agreement with the experimental value of $+2.11\,V$ [8]. This result illustrates that cars effectively start because of scalar relativistic corrections.

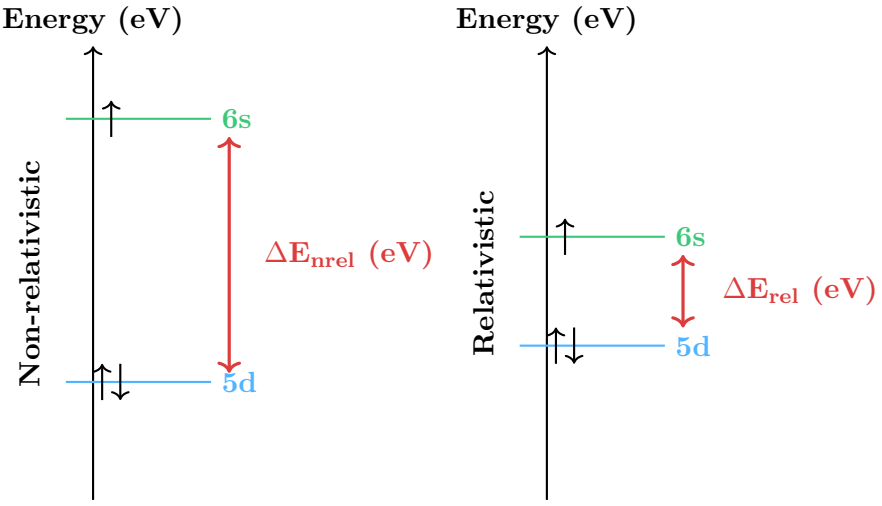

FIGURE 1.1: Comparison of the energy levels of gold's 6s and 5d orbitals without (left) and with (right) relativistic effects. The relativistic contraction of the 6s orbital and expansion of the 5d orbital significantly reduce the energy gap. All energies are given in electronvolts (eV).

Another important relativistic effect is the *spin–orbit (SO) interaction*, usually expressed as

$$\hat{H}_{\mathrm{SO}} = \frac{1}{2m^2c^2}\,\mathbf{s}\cdot\big[\,\nabla V(\mathbf{r})\times\mathbf{p}\,\big], \tag{1.2}$$

where $\mathbf{s}$ is the spin operator representing the intrinsic angular momentum of the electron, $\mathbf{p}$ is the momentum operator, and $V(\mathbf{r})$ is the electrostatic potential experienced by the electron. The prefactor $1/(2m^2c^2)$ arises from relativistic corrections in the Dirac equation. In the case of a central Coulomb potential $V(r) = -Z/r$, where Z is the nuclear charge and $r = |\mathbf{r}|$ is the distance from the nucleus, this expression simplifies to the usual form

$$\hat{H}_{\mathrm{SO}} = \frac{Z}{2m^2c^2r^3}\,\mathbf{s}\cdot\mathbf{l}, \tag{1.3}$$

where $\mathbf{l} = \mathbf{r} \times \mathbf{p}$ is the orbital angular momentum operator. Here, the spin couples directly to the orbital motion of the electron, leading to energy splittings that are particularly significant in heavy atoms due to the strong nuclear potential. It is crucial to stress that this term does not represent an intrinsic coupling of an electron's spin with its own orbital angular momentum. In fact, an isolated free electron *does not* exhibit any spin–orbit interaction. The effect originates only when the electron moves in the electric field of an external charge distribution (e.g., a nucleus). From the viewpoint of the electron's rest frame, the external electric field $\boldsymbol{\mathcal{E}}$ is partly transformed into a magnetic field due to the relative motion between the electron and the source of the field. This effective field interacts with the magnetic moment associated with the electron's spin. The resulting interaction is what we call spin–orbit interaction. A further subtlety arises because the electron's motion is accelerated, not uniform. A sequence of Lorentz boosts is therefore involved, and their composition generates an additional rotation of the spin axis—the *Thomas precession*. This effect reduces the magnitude of the spin–orbit interaction by a factor of two. The spin–orbit (SO) operator describes the interaction between the electron's spin and the magnetic field generated by its orbital motion. As a result, the Hamiltonian no longer commutes with $\boldsymbol{\ell}$ and $\mathbf{s}$ separately, but only with their sum, the total angular momentum $\mathbf{j} = \boldsymbol{\ell} + \mathbf{s}$. This coupling intertwines the spin and spatial degrees of freedom, preventing a separate classification of spin and orbital symmetries. Consequently, atomic states can no longer be labeled solely by the quantum numbers ℓ, m_ℓ, s, and m_s; instead, the proper quantum numbers are the total angular momentum $\mathbf{j}$ and its projection m_j.

Among the various chemical effects arising from spin-orbit coupling (SOC), one notable phenomenon is the *heavy-atom shift*. This term describes the changes observed in nuclear magnetic resonance (NMR) chemical shifts of nuclei located in proximity to heavy atoms. The underlying cause of these shifts is predominantly the spin-orbit coupling introduced

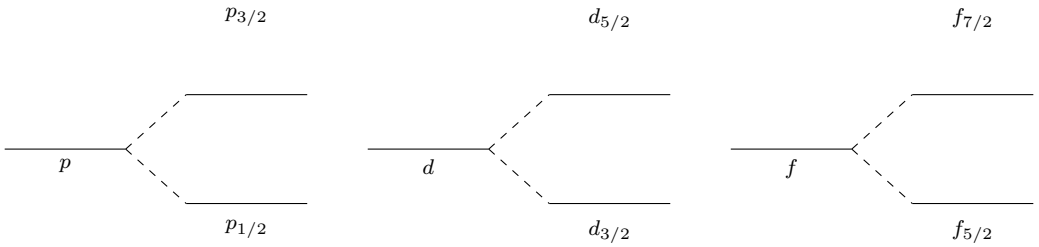

FIGURE 1.2: Schematic illustration of spin–orbit splitting of atomic orbitals due to spin-orbit coupling. Pure ℓ orbitals (left) split into $j = \ell \pm \frac{1}{2}$ components (right), lifting the degeneracy in total angular momentum.

by the presence of the heavy atom within the molecular framework [9, 10]. Another example is provided by the U_2 chemical bond. Gagliardi and co-workers performed non-relativistic CASSCF calculations (with spin–orbit coupling included a posteriori) on the uranium dimer (U_2), revealing that its ground state possesses a formal quintuple bond [11]. Fourteen years later, Knecht and co-workers revisited the bonding in U_2 using multi-configurational CASSCF calculations with the same active space, but crucially included variational spin-orbit coupling [66]. Their results showed that the true ground state of U_2 is a quadruple bond. When SOC is included variationally, it introduces strong mixing between states of different spin, leading to a redistribution of electrons among the bonding and antibonding orbitals. This mixing effectively reduces the number of net bonding interactions, resulting in a lower bond order.

These are just some of the most well-known relativistic effects in chemistry. I strongly recommend the review by Pyykkö [1] for further insights.

1.2 Special relativity

Newtonian mechanics, established by Newton in his groundbreaking work *Philosophiæ Naturalis Principia Mathematica* [67], revolutionized the understanding of physical laws. Building upon the earlier insights of Galileo Galilei and Johannes Kepler [68–71], Newton unified terrestrial and celestial mechanics under a single set of mathematical laws, providing a comprehensive description of motion and force. Newton's laws is based on the existence of absolute space and time, which provide the backdrop for *inertial reference frames*—frames in which a free particle experiences no acceleration. All inertial frames are equivalent in the sense that the fundamental laws of mechanics take the same form in any such frame. The Galilean transformations describe how coordinates and velocities

transform between two inertial frames in relative motion, ensuring the invariance of Newton's laws under such transformations. For two inertial frames S and S', with S' moving at velocity v relative to S, they are given by [72]:

$$\mathbf{r}' = \mathbf{r} - \mathbf{v}t, \tag{1.4}$$

$$t' = t, \tag{1.5}$$

Newton's laws are invariant under such transformations, preserving their form in all inertial systems. However, the Galilean transformations encountered significant issues when applied to the Maxwell's equations, the equations that govern the electromagnetism.

In the late 19$^{\text{th}}$ century, Maxwell formulated a set of equations that describe the behavior of electric and magnetic fields [73–75]. Although originally published in their integral form, they are here reported in the differential form, which is more suitable for the purposes of this thesis:

$$\nabla \cdot \boldsymbol{\mathcal{E}} = \frac{\rho}{\varepsilon_0} \tag{1.6}$$

$$\nabla \cdot \mathbf{B} = 0 \tag{1.7}$$

$$\nabla \times \boldsymbol{\mathcal{E}} = -\frac{\partial \mathbf{B}}{\partial t} \tag{1.8}$$

$$\nabla \times \mathbf{B} = \mu_0 \mathbf{j} + \mu_0 \varepsilon_0 \frac{\partial \boldsymbol{\mathcal{E}}}{\partial t} \tag{1.9}$$

where $\boldsymbol{\mathcal{E}}$ is the electric field, $\mathbf{B}$ is the magnetic field, ρ is the charge density, $\mathbf{j}$ is the current density, ε_0 electric constant, μ_0 is the magnetic constant, $\nabla\cdot$ is the divergence operator, $\nabla\times$ is the curl operator, and $\frac{\partial}{\partial t}$ is the partial derivative with respect to time. Maxwell's equations predict that the speed of light in a vacuum is a constant, denoted as $c = \frac{1}{\sqrt{\varepsilon_0 \mu_0}}$, independent of the motion of both the source and the observer. This stands in direct contrast with Galilean transformations, which imply that velocities should transform accordingly (a result easily obtained by differentiating Eqn. (1.4)). If a Galilean transformation were applied, the speed of light would be added to the relative velocity of the observer. This means that a moving observer would measure a speed of light different from c. The failure of Galilean transformations to account for the constancy of the speed

of light, experimentally confirmed by the null result of the Michelson-Morley experiment [76], underscored the need for a new theoretical framework.

In 1905, Einstein formulated the principles of special relativity [77]:

1. The laws of physics (including both mechanics and electromagnetism) must hold identically in all inertial reference frames.
2. The speed of light c is the same in all inertial reference frames.

The first principle extends Galileo's principle of relativity, while the second, introduced by Einstein, follows naturally from the first. Since Maxwell's equations must take the same form in all inertial frames, and they explicitly include the speed of light, the invariance of c is already implicitly contained within the first principle. Einstein himself later recognized the redundancy of the second postulate in his fourth paper of the same year [78]. Therefore, new transformations were required.

Consider two events, $E_1(t_1, \mathbf{r}_1)$ and $E_2(t_2, \mathbf{r}_2)$, connected by a light beam (for example, the emission and subsequent absorption of a photon). The velocity definition implies that the following relation must hold:

$$\frac{|\mathbf{r}_2 - \mathbf{r}_1|}{t_2 - t_1} = c \quad \Leftrightarrow \quad c^2(t_2 - t_1)^2 - |\mathbf{r}_2 - \mathbf{r}_1|^2 = 0. \tag{1.10}$$

Thus, if an observer is in a reference frame S, they will measure the four-distance (or spacetime interval) as:

$$s_{12}^2 = c^2(t_2 - t_1)^2 - |\mathbf{r}_2 - \mathbf{r}_1|^2. \tag{1.11}$$

This quantity must be invariant under some transformations that relate the two frames. Lorentz, based on the observation that the speed of light c must remain the same in all inertial reference frames, identified a set of transformations, known today as the *Lorentz transformations* [79], which allow one to transition from one inertial frame to another without violating the principles of relativity. These can be written as

$$\mathbf{r}' = \mathbf{r} + \frac{\gamma - 1}{v^2}(\mathbf{v} \cdot \mathbf{r})\mathbf{v} - \gamma \mathbf{v} t, \tag{1.12}$$

$$t' = \gamma\Big(t - \frac{\mathbf{v} \cdot \mathbf{r}}{c^2}\Big), \tag{1.13}$$

where $\mathbf{r}$ and $\mathbf{r}'$ denote the position vectors in frames S and S', respectively, t and t' are the corresponding times, c is the speed of light, and $\gamma = 1/\sqrt{1 - v^2/c^2}$ is the Lorentz factor. We should note that these transformations mix space and time coordinates, indicating their interdependence in special relativity. It is interesting to note that in the non-relativistic limit, $c \to \infty$, the Lorentz factor γ approaches 1 and the term $\mathbf{v} \cdot \mathbf{r}/c^2$ vanishes. Consequently, the general Lorentz transformations reduce to Eqn.(1.4), yielding the familiar Galilean transformations.

1.2.1 Relativistic dynamics

We have seen that the second principle of relativity naturally leads to the definition of the four-distance. The aim of this paragraph is to get some physical quantities that we know from the non-relativistic world. To do that, it is convenient to introduce a more compact and practical notation for further developments, based on *four-vectors*.

We define four-vectors as vectors that have three spatial and one time components

$$x^\mu = \begin{pmatrix} x^0 \\ x^1 \\ x^2 \\ x^3 \end{pmatrix} = \begin{pmatrix} ct \\ \mathbf{r} \end{pmatrix}, \tag{1.14}$$

where we have chosen supscript indexes to denote the *contravariant component* x^μ of the space-time vector. We also define the metric tensor as

$$g_{\mu\nu} = \begin{pmatrix} 1 & 0 & 0 & 0 \\ 0 & -1 & 0 & 0 \\ 0 & 0 & -1 & 0 \\ 0 & 0 & 0 & -1 \end{pmatrix}, \quad \text{or, equivalently} \quad \text{diag}(g_{\mu\nu}) = (1, -1, -1, -1). \tag{1.15}$$

By using this notation, we express the four-distance between two events x_1^μ and x_2^μ, defined as

$$\Delta x^\mu = x_2^\mu - x_1^\mu. \tag{1.16}$$

The squared spacetime interval (or four-distance) between the two events is defined as

$$s_{12}^2 = \sum_{\mu,\nu=0}^{3} g_{\mu\nu}\,\Delta x^\mu\,\Delta x^\nu = c^2(t_2 - t_1)^2 - (\mathbf{r}_2 - \mathbf{r}_1)^2. \tag{1.17}$$

The four-vector space defined by the four-vector x^μ, together with the metric $g_{\mu\nu}$, constitutes *Minkowski space*. We may define the *covariant* four-vectors using the metric tensor

$$x_\mu = \sum_{\mu,\nu=0}^{3} g_{\mu\nu}x^\nu = \begin{pmatrix} ct \\ -\mathbf{r} \end{pmatrix}. \tag{1.18}$$

Thus, lowering the indices results in a sign change of the spatial coordinates. This additional definition is very useful for defining the infinitesimal distance between two events as

$$ds^2 = \sum_{\mu\nu=0}^{3} g_{\mu\nu}dx^\mu dx^\nu = c^2dt^2 - d\mathbf{r}^2. \tag{1.19}$$

We need to make a few considerations regarding the determination of the four-velocity. In non-relativistic mechanics, as we have seen before, velocity is defined as the derivative of the position vector with respect to time. However, the non-relativistic framework assumes the existence of absolute time. In the relativistic domain, this is no longer true, and while we can still define a quantity associated with time, it must be Lorentz invariant. To achieve this, we introduce the concept of *proper time*, τ, which can be defined by rearranging Eqn. (1.19):

$$d\tau^2 = \frac{ds^2}{c^2} \Rightarrow d\tau = \gamma^{-1}dt. \tag{1.20}$$

Integrating this expression, we obtain:

$$\tau = \int_{\tau_1}^{\tau_2} d\tau = \int_{t_1}^{t_2} dt\sqrt{1 - \frac{\mathbf{v}^2}{c^2}}. \tag{1.21}$$

The proper time is the time measured by a clock moving along with an observer or a particle. Moreover, we can also provide more physical interpretations of it.

- If the object is at rest in the reference frame ($v = 0$), then $\tau = t$, meaning that the proper time coincides with the coordinate time. Since the object is not moving relative to the observer measuring t, there is no time dilation. The clock carried by the object ticks at the same rate as the coordinate time of the reference frame.

- If the object is moving ($v > 0$), then $\tau < t$, meaning that the proper time runs more slowly compared to the coordinate time measured by a stationary observer.
- In the limit $v \to c$, the proper time tends to zero: a photon, for instance, does not have a proper time in the usual sense.

Having made this necessary premise, we can avoid ambiguities and define trajectories in this Minkowski space expressed as a function of the proper time, $x^\mu(\tau)$. Therefore, we can define the four-velocity, u^μ, as the derivative of the four-position vector with respect to the proper time

$$u^\mu = \frac{dx^\mu}{d\tau} = \gamma(c, \mathbf{v}). \tag{1.22}$$

Furthermore, since the derivative of a four-vector respect to the proper time is still a four-vector, we can define the four-dimensional length of the four-velocity

$$u_{12}^2 = \sum_{\mu\nu=0}^{3} g_{\mu\nu} u^\mu u^\nu = \sum_{\mu\nu=0}^{3} u^\mu u_\mu = \gamma^2(c^2 - v^2) = c^2. \tag{1.23}$$

We can now define the four-momentum by extending its non-relativistic definition:

$$p^\mu = m u^\mu = m\gamma(c, \mathbf{v}), \tag{1.24}$$

where m is the rest mass. Enforcing

$$E = \gamma m c^2, \quad \mathbf{p} = \gamma m \mathbf{v}, \tag{1.25}$$

we may write the four-momentum in the familiar form

$$p^\mu = \left(\frac{E}{c}, \mathbf{p}\right). \tag{1.26}$$

It is important to note that these expressions are valid only for particles with non-zero rest mass ($m > 0$). For a massive particle, as the velocity approaches the speed of light ($v \to c$), the energy E diverges to infinity. This implies that accelerating a massive object to a velocity arbitrarily close to c would require an infinite amount of energy. In contrast, for massless particles with energy, such as photons, the formulas $E = \gamma m c^2$ and $\mathbf{p} = \gamma m \mathbf{v}$ would incorrectly yield zero. For such particles, the four-momentum must instead be

defined directly as

$$p^\mu = \left(\frac{E}{c}, \mathbf{p}\right), \qquad E = |\mathbf{p}|c, \tag{1.27}$$

which correctly accounts for their non-zero energy and momentum. Consequently, massless particles are necessarily constrained to travel at the speed of light, $v = c$, while massive particles can never reach this limit.

Now we have all the key quantities to derive the energy-momentum relation. Following our previous approach, we define the four-square of the four-momentum:

$$\sum_{\mu=0}^{3} p^\mu p_\mu = m^2 \sum_{\mu=0}^{3} u^\mu u_\mu = m^2 c^2. \tag{1.28}$$

This four-square can also be expressed in terms of the energy and the three-momentum as

$$\sum_{\mu=0}^{3} p^\mu p_\mu = \frac{E^2}{c^2} - |\mathbf{p}|^2, \tag{1.29}$$

where $|\mathbf{p}|^2 = p_x^2 + p_y^2 + p_z^2$ is the ordinary three-momentum squared.

By combining Eqs. (1.28) and (1.29), we obtain the *energy-momentum relation*:

$$E^2 = c^2|\mathbf{p}|^2 + m^2c^4 \quad \rightarrow \quad \begin{cases} E = +\sqrt{c^2|\mathbf{p}|^2 + m^2c^4} = +\gamma mc^2, & \text{for } E > 0, \\ E = -\sqrt{c^2|\mathbf{p}|^2 + m^2c^4} = -\gamma mc^2, & \text{for } E < 0. \end{cases} \tag{1.30}$$

Taking the square root of the energy-momentum relation yields two solutions: one positive and one negative. The negative-energy solution may seem unphysical, as classical mechanics assumes energy is continuous. In this context, since a negative energy has not been observed experimentally, we restrict ourselves to the positive-energy branch ($E > 0$), with zero probability of accessing the negative-energy part. This restriction will no longer hold in quantum theory, which will be discussed in the next section. Focusing on the positive-energy solution, we obtain

$$E = \sqrt{c^2|\mathbf{p}|^2 + m^2c^4} = mc^2\sqrt{1 + \frac{|\mathbf{p}|^2}{m^2c^2}}. \tag{1.31}$$

In the non-relativistic limit $|\mathbf{p}| \ll mc$, the expansion of the square root yields

$$\begin{aligned} E &\approx mc^2 \left(1 + \tfrac{1}{2}\tfrac{|\mathbf{p}|^2}{m^2c^2} - \tfrac{1}{8}\left(\tfrac{|\mathbf{p}|^2}{m^2c^2}\right)^2 + \cdots\right) \\ &= mc^2 + \frac{|\mathbf{p}|^2}{2m} - \frac{|\mathbf{p}|^4}{8m^3c^2} + \cdots . \end{aligned} \tag{1.32}$$

Here, the first term mc^2 is the rest energy of the particle, the second term $\frac{|\mathbf{p}|^2}{2m}$ is the familiar non-relativistic kinetic energy, and the third term $-\frac{|\mathbf{p}|^4}{8m^3c^2}$ represents the leading relativistic correction to the kinetic energy, which becomes noticeable as the particle's speed increases.

1.3 Relativistic theory of an electron

Nowadays, we know that the description of small systems, such as atoms, molecules, and subatomic particles, is entrusted to quantum mechanics, which is governed by the time-dependent Schrödinger equation [80]:

$$i\hbar\frac{\partial}{\partial t}\psi(\mathbf{r},t) = \left(-\frac{\hbar^2}{2m}\nabla^2 + V(\mathbf{r})\right)\psi(\mathbf{r},t), \tag{1.33}$$

which describes how the wavefunction $\psi(\mathbf{r},t)$ of a particle evolves over time, where i is the imaginary unit, $\hbar$ is the reduced Planck constant, $\frac{\partial}{\partial t}$ is the partial derivative with respect to time, ∇^2 is the Laplacian operator representing the sum of second spatial derivatives, m is the mass of the particle, and $V(\mathbf{r})$ is the potential energy of the particle, which, together with the kinetic energy term $-\frac{\hbar^2}{2m}\nabla^2$, governs the evolution of $\psi(\mathbf{r},t)$.

The incorporation of special relativity into the Schrödinger equation is far from straightforward. As discussed in the previous section, special relativity demands that the fundamental equations of physics be *covariant*, meaning their form must remain unchanged under Lorentz transformations. This requirement reflects the fact that space and time are not independent entities but are unified into a single spacetime framework described by four-vectors. At a glance, Eqn. (1.33) is clearly not Lorentz-covariant: the left-hand side contains a first-order time derivative, whereas the right-hand side involves a second-order spatial derivative. This asymmetry reflects the incompatibility of the Schrödinger equation with the relativistic treatment of space and time on equal footing. To make this

explicit, consider two inertial frames: the laboratory frame S and a frame S' moving with constant velocity $\mathbf{v}$ relative to S. Using Eqs.(1.12)-(1.13) and applying the chain rule, derivatives transform as

$$\frac{\partial}{\partial t} = \gamma \frac{\partial}{\partial t'} - \gamma(\mathbf{v} \cdot \nabla'), \tag{1.34}$$

$$\nabla = \nabla' + \frac{\gamma - 1}{v^2}(\mathbf{v} \cdot \nabla')\mathbf{v} - \gamma \frac{\mathbf{v}}{c^2}\frac{\partial}{\partial t'}. \tag{1.35}$$

The second derivatives then mix space and time:

$$\nabla^2 = \sum_{i=x,y,z} \frac{\partial^2}{\partial r_i^2} = \sum_{i,j=x,y,z} \left(\delta_{ij} + \frac{\gamma - 1}{v^2} v_i v_j \right) \frac{\partial^2}{\partial r_i' \partial r_j'} - 2\gamma \sum_{i=x,y,z} \frac{v_i}{c^2} \frac{\partial^2}{\partial t' \partial r_i'} + \gamma^2 \frac{v^2}{c^4} \frac{\partial^2}{\partial t'^2}. \tag{1.36}$$

This shows that, in general, the Laplacian in the moving frame S' contains mixed space-time derivatives, explicitly demonstrating that the Schrödinger equation is not invariant under general Lorentz transformations. To construct a wave equation compatible with relativity, one must ensure that its form is preserved under Lorentz transformations. This requirement leads naturally to the development of fully relativistic wave equations, such as the Klein–Gordon and Dirac equations, which will be introduced in the following sections.

1.3.1 From Schrödinger to Klein-Gordon: adapting to relativity

Having established that the Schrödinger equation is not a good starting point for the formulation of a relativistic quantum mechanics, we must look elsewhere. One possible direction is to take a classical equation that is already relativistic and "quantize" it according to the correspondence principle. Eqn. (1.30) seems to suit our needs, as it describes a relativistic energy. Therefore, we make the following substitutions

$$\mathbf{p} \to -i\hbar\boldsymbol{\nabla} \tag{1.37}$$

$$E \to i\hbar \frac{\partial}{\partial t}, \tag{1.38}$$

and by doing this substitution in Eqn. (1.30) we get

$$i\hbar \frac{\partial}{\partial t}\psi(\mathbf{r}, t) = \pm \left(\sqrt{-\hbar^2 \nabla^2 c^2 + m^2 c^4} \right) \psi(\mathbf{r}, t), \tag{1.39}$$

which is not indeed a good result, as this equation is quite hard so solve, mostly due to the presence of the square root. Therefore, Klein and Gordon proposed to use the square of the energy, giving rise to the Klein-Gordon equation [80–84]:

$$\left(\Box - \frac{m^2c^2}{\hbar^2}\right)\psi(\mathbf{r},t) = 0, \tag{1.40}$$

in which we defined the d'Alembertian

$$\Box \equiv \partial_\mu \partial^u = \frac{1}{c^2}\frac{\partial^2}{\partial t^2} - \nabla^2, \quad \partial_\mu \equiv \frac{\partial}{\partial x^\mu}, \tag{1.41}$$

where ∂_μ is the four-gradient. Since the mass term is a Lorentz scalar, the Klein–Gordon equation remains invariant under Lorentz transformations. In non-relativistic quantum mechanics, the wavefunction is associated with a probability density, typically expressed via a continuity equation. When transitioning to a relativistic framework through the Klein–Gordon equation, it is natural to ask whether a similar continuity equation still holds. To investigate this, we consider solutions of Eqn. (1.40) in the form of plane waves:

$$\psi_\pm(\mathbf{r},t) = \exp\{\frac{i}{\hbar}(\mathbf{p}\cdot\mathbf{r} \mp Et)\}, \quad E = \pm\sqrt{p^2c^2 + m^2c^4}. \tag{1.42}$$

Substituting Eqn. (1.42) into Eqn. (1.40) verifies that this is indeed a solution. We begin with the explicit Klein–Gordon equations for the wavefunction $\psi(\mathbf{r},t)$ and its complex conjugate $\psi^*(\mathbf{r},t)$:

$$\left(\partial_\mu\partial^\mu + \frac{m^2c^2}{\hbar^2}\right)\psi(\mathbf{r},t) = 0, \tag{1.43}$$

$$\left(\partial_\mu\partial^\mu + \frac{m^2c^2}{\hbar^2}\right)\psi^*(\mathbf{r},t) = 0. \tag{1.44}$$

Multiplying Eqn. (1.43) by ψ^* and Eqn. (1.44) by ψ, and subtracting the two, the mass terms cancel out and we obtain:

$$\psi^*\,\partial_\mu\partial^\mu\psi - \psi\,\partial_\mu\partial^\mu\psi^* = 0. \tag{1.45}$$

This expression can be written as a total divergence by applying the identity:

$$\partial_\mu\left(\psi^*\,\partial^\mu\psi - \psi\,\partial^\mu\psi^*\right) = 0, \tag{1.46}$$

which has the structure of a continuity equation. This suggests that the quantity inside the divergence defines a conserved current. To ensure correct physical dimensions and to recover the non-relativistic limit, we define the four-current as:

$$j^\mu = \frac{i\hbar}{2m}\left(\psi^*\,\partial^\mu\psi - \psi\,\partial^\mu\psi^*\right) = (c\rho, \mathbf{j}). \tag{1.47}$$

With this definition, the continuity equation takes the compact covariant form:

$$\partial_\mu j^\mu = 0. \tag{1.48}$$

The time component $j^0 = c\rho$ is interpreted as the probability density:

$$\rho = \frac{i\hbar}{2m}\left(\psi^*\frac{\partial\psi}{\partial t} - \psi\frac{\partial\psi^*}{\partial t}\right). \tag{1.49}$$

Since the Klein–Gordon equation is a second-order differential equation in time, it inherently involves two integration constants. This means that the initial conditions for the wavefunction $\psi(\mathbf{r}, t)$ and its time derivative $\partial_t\psi(\mathbf{r}, t)$ can be chosen independently. As a result, the probability density, can take on either positive or negative values, depending on the specific choice of these initial conditions. Moreover, by simply inserting Eqn.(1.42) into Eqn.(1.49) we get

$$\rho_+ = \frac{E}{m}|\psi_+(\mathbf{r}, t)|^2 \quad \text{(positive-energy, } E > 0) \tag{1.50}$$

$$\rho_- = -\frac{E}{m}|\psi_-(\mathbf{r}, t)|^2 \quad \text{(negative-energy, } E > 0 \text{ in magnitude).} \tag{1.51}$$

Therefore, positive-energy solutions yield a positive probability density, whereas the negative-energy solutions lead to a negative probability density. This is the biggest issue with the Klein-Gordon equation, since while we will be able to make sense of negative-energy solutions (in the next paragraph), there is no physical meaning for the probability density.

We close this section with this following remark: in the context of quantum field theory, the wavefunction $\psi(\mathbf{r}, t)$ is a scalar field. Since scalar fields have no intrinsic degrees of freedom related to spin, the Klein–Gordon equation naturally describes particles without spin (i.e., spin-0 particles). Moreover, the lack of spin implies that the field transforms trivially under spatial rotations. This simplicity makes the Klein–Gordon equation ideal for modeling particles such as the Higgs boson or other hypothetical scalar particles, where

no additional internal structure (like spin) is present [85, 86].

1.3.2 Solving the relativistic puzzle: the Dirac equation

The primary issue with the Klein–Gordon equation is that, being second-order in time, it allows for the possibility of negative probability densities. Dirac's insightful solution [2] was to linearize Eqn. (1.30), thereby seeking a first-order differential equation in time analogous to the Schrödinger equation:

$$i\hbar\frac{\partial\psi(\mathbf{r},t)}{\partial t} = \hat{h}_D\psi(\mathbf{r},t), \tag{1.52}$$

where $\hat{h}_D$ denotes the Dirac Hamiltonian, which we now derive.

First, the equation must be relativistically invariant—that is, unchanged under Lorentz transformations. This requires that Dirac's Hamiltonian be linear in the spatial derivatives, motivating the ansatz:

$$\hat{h}_D = c\,(\boldsymbol{\alpha}\cdot\mathbf{p}) + \beta\,mc^2. \tag{1.53}$$

Unlike the Schrödinger equation, the speed of light c appears explicitly, scaling both the momentum term and the rest energy term, in order to have the coefficients $\boldsymbol{\alpha}$ and β dimensionless. Dirac's aim was to find a first-order time-dependent equation whose Hamiltonian squared yields the relativistic dispersion relation, i.e Eqn.(1.30). We therefore compute the square of Eqn.(1.53)

$$\hat{h}_D^2 = c^2\sum_{i,j=1}^{3}\alpha_i p_i\alpha_j p_j + \beta^2 m^2c^4 + mc^3\sum_{i=1}^{3}\left(\alpha_i\beta+\beta\alpha_i\right), \tag{1.54}$$

and in order to reproduce Eqn.(1.30) the coefficients $\boldsymbol{\alpha}$ and β must satisfy the following relations

$$\{\alpha_i,\alpha_j\} = \alpha_i\alpha_j+\alpha_j\alpha_i = 2\delta_{ij}\mathbf{I}, \tag{1.55}$$

$$\{\alpha_i,\beta\} = \alpha_i\beta+\beta\alpha_i = 0, \tag{1.56}$$

$$\beta^2 = \mathbf{I}. \tag{1.57}$$

It is important to note that the vector $\boldsymbol{\alpha}$ can not be an ordinary numerical vector; if it were, it would imply the existence of a preferred direction—an impossibility for a free particle in an isotropic space. Therefore, $\boldsymbol{\alpha}$ must consist of $N \times N$ matrices, and similarly, β must be an $N \times N$ matrix. This immediately implies that the wave function can not be a scalar but must instead be an N-component vector:

$$(\alpha_k, \beta) \in \mathbb{R}^{N\times N} \quad \Longrightarrow \quad \psi(\mathbf{r}, t) = \begin{pmatrix} \psi_1(\mathbf{r}, t) \\ \psi_2(\mathbf{r}, t) \\ \vdots \\ \psi_N(\mathbf{r}, t) \end{pmatrix}. \tag{1.58}$$

Moreover, the Hermiticity of the Dirac Hamiltonian demands that the matrices α_i and β are themselves Hermitian. In order to find α_i and β, we can make some considerations:

- Noting that $\alpha_i^2 = \beta^2 = \mathbf{I}$, we know that they must have eigenvalues ± 1. Moreover, by simply rearranging Eqn. (1.56), we can note that they must be traceless matrices

$$\mathrm{Tr}(\alpha_i) = \mathrm{Tr}(\beta) = 0, \quad i = 1, \ldots, 3. \tag{1.59}$$

  Since the trace is the sum of the eigenvalues, the number of positive and negative eigenvalues must be equal. This means that the dimension N of the Dirac matrices must be even.

- In order for the equation to be relativistically invariant, the matrices appearing in the Hamiltonian must not act on space-time coordinates themselves. Instead, they must act on internal degrees of freedom of the wavefunction, such as spin. A natural starting point is to consider the Pauli matrices:

$$\sigma_x = \begin{pmatrix} 0 & 1 \\ 1 & 0 \end{pmatrix}, \quad \sigma_y = \begin{pmatrix} 0 & -i \\ i & 0 \end{pmatrix}, \quad \sigma_z = \begin{pmatrix} 1 & 0 \\ 0 & -1 \end{pmatrix}.$$

  These matrices, along with the 2×2 identity matrix $\mathbf{I}_{2\times 2}$, form a complete basis for the space of complex 2×2 matrices, which is a 4-dimensional complex vector space. The Pauli matrices are linearly independent and traceless, while the identity matrix has non-zero trace. Since any 2×2 complex matrix can be expressed as a linear combination of these four matrices, there are no additional 2×2 matrices that

can be added to this set while maintaining linear independence. Dirac's equation requires four matrices—three α_i and one β—that mutually anticommute and square to the identity. This is not possible within a 2-dimensional matrix representation: the Clifford algebra generated by four such elements requires matrices of at least dimension 4×4. Therefore, the wavefunction ψ must be at least a four-component object, and the matrices α_i and β must be 4×4.

- The next even matrix dimension to consider is $N = 4$, for which the space of complex 4×4 matrices has dimension 16. This provides sufficient freedom to construct four linearly independent matrices that satisfy the required anticommutation relations. Since the Clifford algebra generated by the Dirac matrices admits multiple inequivalent representations in this space, we are free to choose a convenient one. The standard choice is the so-called Dirac (or Dirac–Pauli) representation, given by:

$$\alpha_i = \begin{pmatrix} \mathbf{0}_{2\times2} & \sigma_i \\ \sigma_i & \mathbf{0}_{2\times2} \end{pmatrix}, \qquad \beta = \begin{pmatrix} \mathbf{I}_{2\times2} & \mathbf{0}_{2\times2} \\ \mathbf{0}_{2\times2} & -\mathbf{I}_{2\times2} \end{pmatrix}, \tag{1.60}$$

Note that representations are not unique because any set of matrices can be conjugated by a nonsingular (unitary, if Hermiticity is required) matrix S, yielding an equivalent representation by

$$\alpha_i \to S\alpha_i S^{-1}, \quad \beta \to S\beta S^{-1}. \tag{1.61}$$

Different representations can simplify specific problems. For instance, the Weyl representation is advantageous for studying ultrarelativistic particles like neutrinos [87]:

$$\alpha_i^{\mathrm{W}} = W^\dagger \alpha_i^{\text{D-P}} W, \quad \beta^{\mathrm{W}} = W^\dagger \beta^{\text{D-P}} W, \quad W = \frac{1}{2}\begin{pmatrix} \mathbf{I}_{2\times2} & -\mathbf{I}_{2\times2} \\ \mathbf{I}_{2\times2} & \mathbf{I}_{2\times2} \end{pmatrix}. \tag{1.62}$$

Since the Dirac matrices are 4×4 matrices, then the dimension of the wavefunction $\psi(\mathbf{r}, t)$ must be consistent and therefore, in this standard representation, $\psi(\mathbf{r}, t)$ is a 4-vector. Therefore, we conclude that the time-dependent Dirac equation reads as

$$i\hbar \frac{\partial \psi(\mathbf{r}, t)}{\partial t} = [c(\alpha \cdot \mathbf{p}) + \beta mc^2]\psi(\mathbf{r}, t). \tag{1.63}$$

In order to cast the Dirac equation in a manifestly covariant form, we rewrite Eqn. (1.63) as

$$\left(-i\hbar\,\partial_0 - i\hbar\,\alpha^i\partial_i + \beta\,mc\right)\psi(\mathbf{r},t) = 0. \tag{1.64}$$

We then introduce the gamma matrices by defining

$$\gamma^0 \equiv \beta, \quad \gamma^i \equiv \beta\,\alpha^i. \tag{1.65}$$

which satisfy the fundamental anticommutation relation

$$\{\gamma^\mu, \gamma^\nu\} \equiv \gamma^\mu\gamma^\nu + \gamma^\nu\gamma^\mu = 2g^{\mu\nu}\mathbf{I}_{4\times 4}, \tag{1.66}$$

With these definitions, the Dirac equation assumes the covariant form

$$\left(i\gamma^\mu\partial_\mu - \frac{mc}{\hbar}\right)\psi(\mathbf{r},t) = 0. \tag{1.67}$$

Following the same steps that we have carefully done in Sec.(1.3.1), we may derive the continuity equation, which reads as

$$\partial_\mu j^\mu = 0, \quad j^\mu = (j^0, \mathbf{j}) \tag{1.68}$$

where we have defined the Dirac density distribution $j^0 = c\psi(\mathbf{r},t)^\dagger\psi(\mathbf{r},t)$ and the Dirac current density $\mathbf{j} = c\psi(\mathbf{r},t)^\dagger\alpha\psi(\mathbf{r},t)$.

As we pointed out before, since the Dirac equation involves 4×4 matrices acting on the wave function $\psi(\mathbf{r},t)$, the latter must be a four-component vector:

$$\psi(\mathbf{r},t) = \begin{pmatrix}\psi^L(\mathbf{r},t)\\ \psi^S(\mathbf{r},t)\end{pmatrix} = \begin{pmatrix}\psi^L_\alpha(\mathbf{r},t)\\ \psi^L_\beta(\mathbf{r},t)\\ \psi^S_\alpha(\mathbf{r},t)\\ \psi^S_\beta(\mathbf{r},t)\end{pmatrix}, \tag{1.69}$$

where we have explicitly separated the wave function into its *large* and *small* components, $\psi^L(\mathbf{r},t)$ and $\psi^S(\mathbf{r},t)$, respectively. Each of these components is itself a two-component Pauli spinor, describing spin-up (α) and spin-down (β) components.

1.3.2.1 Time-independent Dirac equation

In quantum chemistry, it is often useful to separate the temporal and spatial dependencies of the wavefunction in order to obtain a stationary state description. We start by assuming that the four-component Dirac spinor can be written as a product of a time-dependent phase factor and a spatial part:

$$\psi(\mathbf{r}, t) = \psi(\mathbf{r})\Omega(t). \tag{1.70}$$

We should underline that this is a separation for stationary states in a given inertial frame with a time-independent Hamiltonian; it is not valid in all reference frames. Under a boost, the time and spatial coordinates mix; hence, a wavefunction that factorizes as a product of a purely time-dependent part and a purely space-dependent part in one frame will generally not have the same separable form in another frame. This means that the ansatz is not covariant. By substituting the separation ansatz in Eqn.(1.63) we get

$$\frac{\hat{h}_D\psi(\mathbf{r})}{\psi(\mathbf{r})} = \frac{i\hbar}{\Omega(t)}\frac{\partial\Omega(t)}{\partial t}. \tag{1.71}$$

For this equality to hold for all $\mathbf{r}$ and t, both sides must be equal to the same constant, which we denote by E. This gives:

$$\frac{\hat{h}_D\psi(\mathbf{r})}{\psi(\mathbf{r})} = E \quad \text{and} \quad \frac{i\hbar}{\Omega(t)}\frac{\partial\Omega(t)}{\partial t} = E.$$

Thus, we obtain the separate equations:

$$\hat{h}_D\psi(\mathbf{r}) = E\,\psi(\mathbf{r}), \quad \hat{h}_D = c(\alpha\cdot\mathbf{p}) + \beta mc^2, \tag{1.72}$$

$$i\hbar\frac{\partial\Omega(t)}{\partial t} = E\,\Omega(t), \quad \Omega(t) = \exp\{-iEt/\hbar\}. \tag{1.73}$$

Equation (1.72) is the time-independent (stationary) Dirac equation for the spatial part of the wavefunction, while Equation (1.73) governs its time evolution. Substituting the separation ansatz (1.70) into Equation (1.63) gives

$$E\begin{pmatrix}\psi^L(\mathbf{r})\\ \psi^S(\mathbf{r})\end{pmatrix} = \begin{pmatrix} mc^2 & c\,\boldsymbol{\sigma}\cdot\mathbf{p}\\ c\,\boldsymbol{\sigma}\cdot\mathbf{p} & -mc^2\end{pmatrix}\begin{pmatrix}\psi^L(\mathbf{r})\\ \psi^S(\mathbf{r})\end{pmatrix}. \tag{1.74}$$

This leads to the coupled equations:

$$E\,\psi^L(\mathbf{r}) = mc^2\,\psi^L(\mathbf{r}) + c\,\boldsymbol{\sigma}\cdot\mathbf{p}\,\psi^S(\mathbf{r}), \tag{1.75}$$

$$E\,\psi^S(\mathbf{r}) = c\,\boldsymbol{\sigma}\cdot\mathbf{p}\,\psi^L(\mathbf{r}) - mc^2\,\psi^S(\mathbf{r}). \tag{1.76}$$

Solving Eqn. (1.76) for $\psi^S(\mathbf{r})$ gives

$$\psi^S(\mathbf{r}) = R\,\psi^L(\mathbf{r}), \qquad R = \frac{c\,\boldsymbol{\sigma}\cdot\mathbf{p}}{mc^2 + E}. \tag{1.77}$$

In the non-relativistic limit, for positive energies, E is close to mc^2, and therefore in Eqn. (1.75) the term $mc^2\,\psi^L(\mathbf{r})$ dominates over the kinetic coupling term $c\,\boldsymbol{\sigma}\cdot\mathbf{p}\,\psi^S(\mathbf{r})$. This implies that $\psi^L(\mathbf{r})$ is the *large component*, while $\psi^S(\mathbf{r})$ is significantly smaller. In fact, to leading order, one obtains the approximation

$$\psi^S(\mathbf{r}) \simeq \frac{\boldsymbol{\sigma}\cdot\mathbf{p}}{2mc}\,\psi^L(\mathbf{r}). \tag{1.78}$$

For a free-particle, the four solutions can be casted in the following form [64]

$$\psi_1^L(\mathbf{r}) = \mathcal{N}\begin{pmatrix} 1 \\ 0 \\ \frac{cp_z}{E+mc^2} \\ \frac{c(p_x+ip_y)}{E+mc^2} \end{pmatrix}, \quad \psi_2^L(\mathbf{r}) = \mathcal{N}\begin{pmatrix} 0 \\ 1 \\ \frac{c(p_x-ip_y)}{E+mc^2} \\ -\frac{cp_z}{E+mc^2} \end{pmatrix}, \tag{1.79}$$

$$\psi_2^S(\mathbf{r}) = \mathcal{N}\begin{pmatrix} \frac{cp_z}{E-mc^2} \\ \frac{c(p_x+ip_y)}{E-mc^2} \\ 1 \\ 0 \end{pmatrix}, \quad \psi_2^S(\mathbf{r}) = \mathcal{N}\begin{pmatrix} \frac{c(p_x-ip_y)}{E-mc^2} \\ -\frac{cp_z}{E-mc^2} \\ 0 \\ 1 \end{pmatrix}, \tag{1.80}$$

where $\mathcal{N}$ is the normalization constant, often written as $\mathcal{N} = \sqrt{\frac{|E|+mc^2}{2|E|}}$.

1.3.2.2 Negative-energy solutions

We have seen that the Dirac equation admits two types of solutions, namely those with positive-energy and those with negative-energy, as also predicted by the Klein–Gordon

equation. Therefore, the spectrum of the eigenvalues of the Dirac Hamiltonian is

$$\left(-\infty,\, -mc^2\right] \cup \left[mc^2,\, \infty\right),$$

as reported in Figure 1.3. Thus, even if there exists a ground state for the positive-energy

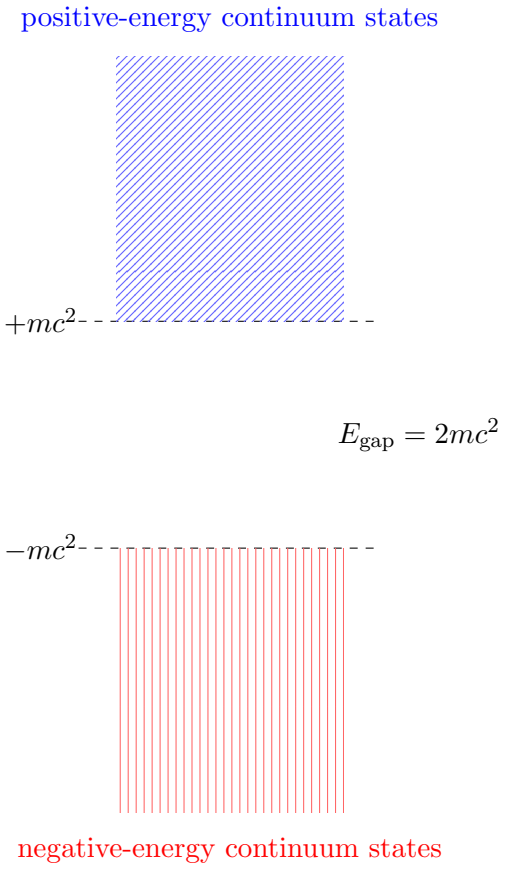

FIGURE 1.3: Representation of the Dirac sea. Horizontal dashed lines indicate $+mc^2$ and $-mc^2$. Blue and red patterned regions represent the continuum of positive- and negative-energy states. The energy gap is $2mc^2$.

solutions, this is not true for the negative-energy solutions. In classical mechanics we could simply discard the negative-energy solutions as physically unacceptable; however, in quantum mechanics this is not possible since, in principle, we have access to every state. Consequently, there is a finite probability that an electron in a positive-energy state may undergo a transition to a negative-energy state, and since these negative-energy states are in principle infinite, the electron could continue decaying indefinitely towards negative infinity, thereby not ensuring the stability of matter. To resolve this issue, Dirac proposed that all negative-energy states are already occupied by electrons, forming what is known as the *Dirac sea*. According to the Pauli exclusion principle, no two electrons can occupy the same quantum state. Therefore, if every negative-energy state is filled, an

electron in a positive-energy state is prevented from decaying into a negative-energy state, ensuring the stability of matter [3]. In this framework, a vacancy, or *hole*, in the Dirac sea—created when an electron is excited from a negative-energy state to a positive-energy state—manifests as a particle with positive-energy and opposite charge. This hole is interpreted as the *positron*, the electron's antiparticle, a prediction that was subsequently confirmed experimentally [88]. It is interesting to note that, up to this point, the Dirac equation itself does not contain any information regarding the particle's charge. In order to describe electromagnetic interactions, the particle's charge q is introduced through the principle of *minimal coupling* [89]. In covariant notation, this corresponds to replacing the canonical four-momentum $p_\mu = i\hbar\partial_\mu$ with the mechanical (or kinetic) four-momentum $\pi_\mu = p_\mu - qA_\mu$, where $A_\mu = (\varphi, -\mathbf{A})$ is the electromagnetic four-potential (see Appendix A for more details). The Dirac equation in the presence of an external electromagnetic field then reads

$$(\gamma^\mu \pi_\mu - m)\,\psi(x) = (i\hbar\gamma^\mu\partial_\mu - q\gamma^\mu A_\mu - m)\,\psi(x) = 0. \tag{1.81}$$

To reveal the connection between particles and antiparticles, we consider the complex conjugate of Eq. (1.81),

$$(-i\hbar\gamma^{\mu*}\partial_\mu - q\gamma^{\mu*}A_\mu - m)\,\psi^*(x) = 0, \tag{1.82}$$

where we used that $i^* = -i$ and $m^* = m$ is real. Multiplying through by -1 gives

$$(i\hbar\gamma^{\mu*}\partial_\mu + q\gamma^{\mu*}A_\mu + m)\,\psi^*(x) = 0. \tag{1.83}$$

At this stage, the equation for $\psi^*(x)$ resembles the original Dirac equation, but with the opposite sign of the charge term. To bring it into the canonical Dirac form, we introduce the *charge-conjugation operator* C, which generates the charge-conjugate spinor:

$$\psi_c(x) = C\,\psi^*(x). \tag{1.84}$$

Substituting this into Eq. (1.83), we obtain

$$(i\hbar\gamma^{\mu*}\partial_\mu + q\gamma^{\mu*}A_\mu + m)\,C^{-1}\psi_c(x) = 0. \tag{1.85}$$

Multiplying on the left by C and imposing this condition on the gamma matrices

$$C\gamma^{\mu *}C^{-1} = -\gamma^{\mu}, \tag{1.86}$$

we arrive at

$$(-i\hbar\gamma^{\mu}\partial_{\mu} - q\gamma^{\mu}A_{\mu} + m)\,\psi_c(x) = 0. \tag{1.87}$$

Finally, multiplying through by -1 leads to the Dirac equation for the charge-conjugate spinor:

$$(i\hbar\gamma^{\mu}\partial_{\mu} + q\gamma^{\mu}A_{\mu} - m)\,\psi_c(x) = 0. \tag{1.88}$$

Equation (1.88) shows that $\psi_c(x)$ satisfies the Dirac equation with the opposite sign of the charge, i.e., it describes the corresponding antiparticle. This construction illustrates the charge-conjugation symmetry ($\mathcal{C}$-symmetry, coined by Kramer [90]) of the Dirac equation. If we consider the electron we have $q = -e$, and therefore we get

$$(i\hbar\gamma^{\mu}\partial_{\mu} + e\gamma^{\mu}A_{\mu} - m)\,\psi(x) = 0, \quad \text{Eq. for the electron} \tag{1.89}$$

$$(i\hbar\gamma^{\mu}\partial_{\mu} - e\gamma^{\mu}A_{\mu} - m)\,\psi_c(x) = 0, \quad \text{Eq. for the positron} \tag{1.90}$$

1.4 Relativistic molecular calculations

Previously we focused on the Dirac equation as the fundamental relativistic wave equation for a single electron, which can interact with some external electromagnetic field through the minimal coupling procedure. While this provides a solid foundation for understanding relativistic effects at the one-particle level, most chemically relevant systems involve multiple electrons interacting with each other and with one or more atomic nuclei. Consequently, to account for relativistic effects in realistic molecular systems, the Dirac framework must be extended to handle many-electron wavefunctions. Moreover, we are mainly interested in electrons bound in molecules by electromagnetic forces. Within the Born–Oppenheimer approximation [91], the nuclei are treated as fixed classical sources of the electromagnetic field. As a consequence, the electrons experience a static scalar potential $\varphi(\mathbf{r})$ generated by the nuclear charges, while the magnetic effects associated with nuclear motion are neglected. Therefore, the vector potential can be set to zero,

$\mathbf{A}(\mathbf{r}) = 0$. So, the definition of the Hamiltonian for a many-particle system which, regardless of whether the case is relativistic or not, takes the simple form

$$\hat{H} = \sum_i \hat{h}_D(i) + \frac{1}{2}\sum_{ij} \hat{g}(i,j) + V_{NN}, \tag{1.91}$$

where $\hat{h}(i)$ is the mono-electronic part, $\hat{g}(i,j)$ is the two-electron interaction and V_{NN} is the classical repulsion of clamped nuclei. This separation, while practical, explicitly breaks Lorentz covariance: the nuclei are treated as fixed classical sources, thus selecting a preferred inertial frame and violating the relativistic requirement that all parts of the system transform covariantly under Lorentz transformations. Small relativistic corrections to the nucleus–nucleus interaction can be applied to refine the approximation [92].

In the relativistic context, the mono-electronic part is the usual Dirac Hamiltonian

$$\hat{h}_D = c(\alpha \cdot \mathbf{p}) + \beta mc^2 + V, \tag{1.92}$$

where the electron-nucleus interaction V is defined as

$$V(\mathbf{r}) = -e\sum_A \varphi_A(\mathbf{r}), \quad \varphi_A(\mathbf{r}_1) = \frac{1}{4\pi\varepsilon_0}\int \frac{\rho_A(\mathbf{r}_2)}{|\mathbf{r}_1 - \mathbf{r}_2|} d^3\mathbf{r}_2, \tag{1.93}$$

where e is the fundamental charge, ε_0 is the electric constant, φ_A and ρ_A are respectively the scalar potential and the charge density of each nucleus A. A few words should be devoted to the two-electron interaction in the relativistic regime.

1.4.1 Two-electron interaction

In classical electrodynamics the interaction between charged particles is described by Maxwell's equations and the Lorentz force law. In this framework, the fields and potentials are used to mediate the interaction. A moving charge generates an electric field $\boldsymbol{\mathcal{E}}$ and a magnetic field $\mathbf{B}$. These fields can be expressed in terms of the scalar potential φ and the vector potential $\mathbf{A}$, as discussed in Appendix A. In the Coulomb gauge ($\boldsymbol{\nabla} \cdot \mathbf{A} = 0$), the scalar potential for a charge distribution $\rho(\mathbf{r}, t)$ is given by:

$$\varphi(\mathbf{r}, t) = \frac{1}{4\pi\varepsilon_0}\int \frac{\rho(\mathbf{r}', t)}{|\mathbf{r} - \mathbf{r}'|} d\mathbf{r}', \tag{1.94}$$

which represents the instantaneous Coulomb potential. The vector potential is related to the current density. When taking into account the finite propagation speed of electromagnetic signals (i.e., the speed of light c), the vector potential is written as:

$$\mathbf{A}(\mathbf{r},t) = \frac{1}{4\pi\varepsilon_0 c^2}\int \frac{\mathbf{j}_\perp(\mathbf{r}',t_{\text{ret}})}{|\mathbf{r}-\mathbf{r}'|}\,d\mathbf{r}', \tag{1.95}$$

where t_{ret} is the *retarded time*, which arises from the finite speed at which electromagnetic signals propagate, which is the speed of light c. Due to this finite speed, an event occurring at time t at the source will influence an observer located at a distance r only after a delay. This delay is characterized by the retarded time t_{ret}, defined as

$$t_{\text{ret}} = t - \frac{|\mathbf{r}-\mathbf{r}'|}{c}. \tag{1.96}$$

In practical terms, when calculating the fields or potentials generated by a moving charge, one must evaluate the source's behavior at t_{ret} rather than at the current time t. The transverse current density, denoted by $\mathbf{j}_\perp$, is defined as the part of the current that is divergence-free.

The two-electron interaction in the relativistic regime can be constructed using the principle of minimal substitution [89], an approach originally introduced by Darwin [93]. Darwin considered the interaction energy between two moving classical charges expressed through the scalar and vector potentials generated by one charge at the location of the other, respectively Eqn.(1.94) and Eqn.(1.95). However, his treatment is approximate, truncated at order $1/c^2$, incorporating velocity-dependent corrections but excluding higher-order effects such as radiation. Later, Breit heuristically quantized this interaction energy by introducing relativistic velocity operators, defined as

$$\hat{v} = \frac{i}{\hbar}\left[\hat{h}_D, \hat{x}\right] = c\boldsymbol{\alpha}, \tag{1.97}$$

resulting in the Breit operator as a correction to the Dirac–Coulomb Hamiltonian, which can be expressed as

$$g_{\text{Breit}}(\mathbf{r}_1,\mathbf{r}_2) = -\frac{1}{4\pi\varepsilon_0 c^2}\frac{q_1 q_2}{r_{12}}\left[\frac{\boldsymbol{\alpha}_1\cdot\boldsymbol{\alpha}_2}{2} + \frac{(\boldsymbol{\alpha}_1\cdot\mathbf{r}_{12})(\boldsymbol{\alpha}_2\cdot\mathbf{r}_{12})}{2r_{12}^2}\right], \tag{1.98}$$

where we have defined $\mathbf{r}_{12} = \mathbf{r}_1 - \mathbf{r}_2$, $r_{12} = |\mathbf{r}_{12}|$. The first term in Eqn.(1.98) is called the Gaunt term, and describes the relativistic magnetic interaction between the electron currents (including spin contributions), whereas the second term, often called the gauge or retardation term, and accounts for the current-current interaction. It should be emphasized that this truncated interaction is not fully Lorentz invariant. A detailed analysis of the Breit interaction is extensively discussed in Saue's thesis [94].

Eqn.(1.98) can also be derived in the framework of the QED, where charged particles (such as electrons) interact by emitting and absorbing virtual photons. The virtual photon carries the momentum and energy between the interacting electrons, encapsulating the effects of the finite speed of light and the relativistic nature of the interaction. By performing a non-relativistic reduction of the scattering amplitude (i.e., expanding in powers of v/c), one recovers not only the Coulomb interaction but also additional velocity-dependent terms.

1.4.2 Relativistic basis set requirements

This section is heavily inspired by chapter 11 of Ref.[63], to which the reader is referred to for a comprehensive and complete discussion.

A fundamental tool in the framework of molecular calculations is the basis set expansion, where the electron wave functions are approximated by a linear combination of predefined functions. While the LCAO (Linear Combination of Atomic Orbitals) approach is well established in the non-relativistic framework, its development within the relativistic context has required considerably more time. As also done in the non-relativistic setup, we might expand the large and small components of the electronic wave-function

$$\psi^L(\mathbf{r}) = \sum_{\mu}^{N_L} c_\mu^L \chi_\mu^L, \quad \psi^S(\mathbf{r}) = \sum_{\mu}^{N_S} c_\mu^S \chi_\mu^S. \tag{1.99}$$

We may now insert this expansion in Eqn.(1.92), leading to

$$\begin{pmatrix} \mathbf{V}^{LL} - E\mathbf{S}^{LL} & c\mathbf{\Pi}^{LS} \\ c\mathbf{\Pi}^{SL} & \mathbf{V}^{SS} - (2mc^2 + E)\mathbf{S}^{SS} \end{pmatrix} \begin{pmatrix} \mathbf{c}^L \\ \mathbf{c}^S \end{pmatrix} = \begin{pmatrix} \mathbf{0} \\ \mathbf{0} \end{pmatrix}, \tag{1.100}$$

where we are considering the shifted Dirac equation by applying the substitution $\beta \rightarrow \beta - \mathbf{I}_{2\times 2}$. We have defined the following matrix elements

$$X_{\mu\nu}^{\lambda\lambda'} = \langle \chi_\mu^\lambda | X | \chi_\nu^{\lambda'} \rangle, \quad \lambda, \lambda' \in \{L, S\}. \tag{1.101}$$

In particular, for the operators V and $\boldsymbol{\sigma} \cdot \mathbf{p}$ and the overlap we have

$$\begin{aligned}
V_{\mu\nu}^{LL} &= \langle \chi_\mu^L | V | \chi_\nu^L \rangle, \quad V_{\mu\nu}^{SS} = \langle \chi_\mu^S | V | \chi_\nu^S \rangle, \\
S_{\mu\nu}^{LL} &= \langle \chi_\mu^L | \chi_\nu^L \rangle, \quad S_{\mu\nu}^{SS} = \langle \chi_\mu^S | \chi_\nu^S \rangle, \\
\Pi_{\mu\nu}^{LS} &= \langle \chi_\mu^L | (\boldsymbol{\sigma} \cdot \mathbf{p}) | \chi_\nu^S \rangle, \quad \Pi_{\mu\nu}^{SL} = \langle \chi_\mu^S | (\boldsymbol{\sigma} \cdot \mathbf{p}) | \chi_\nu^L \rangle.
\end{aligned}$$

It is now possible to extract the coefficient $\mathbf{c}^S$ from Eqn.(1.100). Since we are looking for the positive-energy solutions ($E > -2mc^2$) and V in negative-definite for most of the atomic and molecular systems, whereas the overlap matrix $\mathbf{S}^{SS}$ is positive-definite, the matrix $\left[(2mc^2 + E)\mathbf{S}^{SS} - \mathbf{V}^{SS}\right]$ is non-singular, and can be inverted

$$\mathbf{c}^S = \left[(2mc^2 + E)\mathbf{S}^{SS} - \mathbf{V}^{SS}\right]^{-1} c\boldsymbol{\Pi}^{SL}\mathbf{c}^L, \tag{1.102}$$

and putting it in the first equations Eqn.(1.100), we may eliminate the dependence of the small coefficient

$$(\mathbf{V}^{LL} - E\mathbf{S}^{SS})\mathbf{c}^L + c\boldsymbol{\Pi}^{LS}\left\{\left[(2mc^2 + E)\mathbf{S}^{SS} - \mathbf{V}^{SS}\right]^{-1} c\boldsymbol{\Pi}^{SL}\mathbf{c}^L\right\} = 0, \tag{1.103}$$

and by using the following identity

$$(\mathbf{A} - \mathbf{B})^{-1} = \mathbf{A}^{-1} + \mathbf{A}^{-1}\mathbf{B}(\mathbf{A} - \mathbf{B})^{-1}, \tag{1.104}$$

for the term $\left[(2mc^2 + E)\mathbf{S}^{SS} - \mathbf{V}^{SS}\right]^{-1}$ and looking at the non-relativistic limit, we end up with the following expression

$$(\mathbf{V}^{LL} - E\mathbf{S}^{LL} + \frac{1}{2m}\boldsymbol{\Pi}^{LS}[\mathbf{S}^{SS}]^{-1}\boldsymbol{\Pi}^{SL})\mathbf{c}^L = 0. \tag{1.105}$$

We may identify the corresponding kinetic energy as

$$\mathbf{T}^{LL} = \frac{1}{2m}\boldsymbol{\Pi}^{LS}[\mathbf{S}^{SS}]^{-1}\boldsymbol{\Pi}^{SL}, \tag{1.106}$$

and therefore, the specific matrix element reads

$$T_{\mu\nu}^{LL} - \frac{\hbar^2}{2m} \sum_{\eta\lambda} \langle \chi_\mu^L | (\boldsymbol{\sigma} \cdot \boldsymbol{\nabla}) | \chi_\eta^S \rangle \, [S^{SS}]_{\eta\lambda}^{-1} \, \langle \chi_\lambda^S | (\boldsymbol{\sigma} \cdot \boldsymbol{\nabla}) | \chi_\nu^L \rangle \,, \tag{1.107}$$

which is not equivalent to the non-relativistic version

$$T_{\mu\nu} = -\frac{\hbar^2}{2m} \langle \chi_\mu^L | \nabla^2 | \chi_\nu^L \rangle \equiv \frac{\hbar^2}{2m} \langle \chi_\nu^L | (\boldsymbol{\sigma} \cdot \boldsymbol{\nabla})(\boldsymbol{\sigma} \cdot \boldsymbol{\nabla}) | \chi_\nu^L \rangle \,. \tag{1.108}$$

A key aspect in recovering the non-relativistic limit correctly is the proper construction of the small-component basis functions. In an ideal (complete) basis set, the elimination of the small component in the Dirac equation would yield a kinetic energy term that exactly coincides with the familiar non-relativistic operator, Eqn.(1.108). However, achieving this correspondence depends critically on the small-component basis spanning exactly the space generated by applying the operator $\boldsymbol{\sigma} \cdot \boldsymbol{\nabla}$ to the large-component functions, i.e., the space $\{\boldsymbol{\sigma} \cdot \boldsymbol{\nabla} \, \chi_\mu^L\}$. If we choose the small-component basis functions according to

$$\chi_\mu^S = -i \, \boldsymbol{\sigma} \cdot \boldsymbol{\nabla} \, \chi_\mu^L \quad \text{or equivalently} \quad \chi_\mu^S = (\boldsymbol{\sigma} \cdot \boldsymbol{p}) \, \chi_\mu^L, \tag{1.109}$$

the so-called *kinetic balance condition* is satisfied [95]. Under this choice, the matrix elements simplify

$$\Pi^{SL} = S^{SS} \quad \text{and consequently} \quad \Pi^{LS} = 2m \, T^{LL} \,. \tag{1.110}$$

This relationship ensures that when eliminating the small component, the resulting kinetic energy matrix

$$\mathbf{T}^{LL} = \frac{1}{2m} \, \mathbf{\Pi}^{LS} \, [\mathbf{S}^{SS}]^{-1} \, \mathbf{\Pi}^{SL}, \tag{1.111}$$

corresponds directly to the non-relativistic kinetic energy operator. In practical finite-basis set calculations, if the small-component basis does not fully span the space $\{\boldsymbol{\sigma} \cdot \boldsymbol{\nabla} \, \chi_\mu^L\}$, the above matrix relation does not hold exactly. In such cases, the operator $\boldsymbol{\sigma} \cdot \boldsymbol{\nabla}$ acting through the finite basis cannot reproduce the Laplacian perfectly. This behavior can be understood in light of the general analysis of Dyall, Grant, and Wilson [96], who showed that, in a finite basis, the matrix of an operator product (such as $(\boldsymbol{\sigma} \cdot \boldsymbol{\nabla})^2$) is not identical to the product of the corresponding matrices unless the basis is closed under the action of the operators involved. In the absence of this closure, positive contributions are

systematically lost, leading precisely to the underestimation of the kinetic energy. This underestimation of the kinetic energy leads to a systematic lowering of the total energy, a phenomenon that was indeed observed in early computational studies [97, 98].

1.4.3 Relativistic Hartree-Fock theory

Our ultimate goal is to solve the many-body problem

$$\hat{H}\Psi(\mathbf{r}_1,\ldots,\mathbf{r}_N) = E\,\Psi(\mathbf{r}_1,\ldots,\mathbf{r}_N), \tag{1.112}$$

where $\Psi(\mathbf{r}_1,\ldots,\mathbf{r}_N)$ represents the many-body wave function. The inherent mathematical complexity arises from the fact that this function depends on several independent variables. It is instructive to consider the simplified case where the two-electron interaction is turned off. In this situation, the Dirac-Coulomb Hamiltonian reduces to a sum of one-electron operators, each satisfying the eigenvalue equation

$$\hat{h}_D\,\psi_i(\mathbf{r}) = \varepsilon_i\,\psi_i(\mathbf{r}), \quad i = 1,\ldots,N. \tag{1.113}$$

Consequently, the many-body wave function can be expressed as a simple product of the one-electron solutions

$$\Phi(\mathbf{r}_1,\ldots,\mathbf{r}_N) = \prod_{i=1}^{N}\psi_i(\mathbf{r}), \tag{1.114}$$

where the mono-electronic wave-functions are the orbitals [99, 100]. However, while this product form is mathematically acceptable, it fails to capture the essential physical property of antisymmetry required for fermionic wave functions. In particular, the wave function must satisfy

$$\hat{P}_{ij}\,\Phi(\mathbf{r}_i,\mathbf{r}_j) = -\Phi(\mathbf{r}_j,\mathbf{r}_i), \tag{1.115}$$

which embodies the Pauli exclusion principle. To incorporate the antisymmetry of fermionic wave functions, one typically constructs the solution as a *Slater determinant* [101]:

$$\Phi(\mathbf{r}_1,\ldots,\mathbf{r}_N) = \frac{1}{\sqrt{N!}}\begin{vmatrix} \psi_1(\mathbf{r}_1) & \psi_1(\mathbf{r}_2) & \cdots & \psi_1(\mathbf{r}_N) \\ \psi_2(\mathbf{r}_1) & \psi_2(\mathbf{r}_2) & \cdots & \psi_2(\mathbf{r}_N) \\ \vdots & \vdots & \ddots & \vdots \\ \psi_N(\mathbf{r}_1) & \psi_N(\mathbf{r}_2) & \cdots & \psi_N(\mathbf{r}_N) \end{vmatrix}, \quad \langle\psi_i|\psi_j\rangle = \delta_{ij}. \tag{1.116}$$

This guarantees that the wave function changes sign upon the exchange of any two electrons, as required by the Pauli exclusion principle.

The single-electron orbitals ψ cannot be obtained by applying the variational principle directly to the relativistic Hamiltonian. In fact, the Dirac Hamiltonian is *not lower-bounded* due to the presence of negative-energy solutions separated from the positive-energy spectrum by a gap of $2mc^2$. Naively minimizing the expectation value of the Dirac-Coulomb Hamiltonian with respect to a general trial wave function can lead to an unphysical collapse of the energy toward $-\infty$, a phenomenon known as *variational collapse* [102]. To circumvent this issue, the *minimax principle* can be employed [103]: the energy is minimized with respect to variations of the *large components* of the spinors, while simultaneously being maximized with respect to variations of the *small components*. In practice, quantum chemistry often focuses exclusively on electronic solutions. The *no-pair approximation* [104] provides a valuable simplification by projecting out the negative-energy states entirely,

$$\hat{H} \to \Lambda_+ \hat{H} \Lambda_+, \tag{1.117}$$

yielding a Hamiltonian whose spectrum is bounded from below and amenable to standard variational optimization. Therefore, the negative energy states are treated as an orthogonal complement. It is worth to mention that the division between the subspaces spanned by positive- and negative-energy orbitals depends on the specific form of the potential, meaning that projection operators cannot be defined without explicitly specifying the potential they refer to.

Therefore, one can determine the orbitals that minimize the energy while enforcing their mutual orthogonality. In first quantization, this is achieved by introducing a Lagrangian functional:

$$L^{\mathrm{HF}}[\{\psi_i\}] = E[\{\psi_i\}] - \sum_{i,j} \varepsilon_{ij} \left(\langle \psi_i | \psi_j \rangle - \delta_{ij} \right), \tag{1.118}$$

where the Lagrange multipliers ε_{ij} ensure the orthonormality of the orbitals. Requiring stationarity with respect to variations of the orbitals,

$$\frac{\delta L^{\mathrm{HF}}}{\delta \psi_i(\mathbf{r})} = 0, \tag{1.119}$$

leads to

$$\hat{F}\,\psi_i(\mathbf{r}) = \sum_j \varepsilon_{ij}\,\psi_j(\mathbf{r}), \qquad i = 1, \ldots, N, \tag{1.120}$$

where the Fock operator $\hat{F}$ is defined as

$$\hat{F} = \hat{h}_D + \sum_{k\in\mathrm{occ}} \big(\hat{J}_k - \hat{K}_k\big), \tag{1.121}$$

with $\hat{h}_D$ the one-electron Dirac operator, and $\hat{J}_k$, $\hat{K}_k$ the Coulomb and exchange operators associated with the occupied orbitals. The operators $\hat{J}_k$ and $\hat{K}_k$ are constructed from the occupied orbitals and represent the two contributions of the electron–electron interaction in the mean-field approximation:

- $\hat{J}_k$ – the *Coulomb operator* – describes the classical electrostatic potential generated by the charge distribution of orbital ψ_k. Its action on an arbitrary spinor ψ reads

$$\big(\hat{J}_k\psi\big)(\mathbf{r}) \;=\; \left[\int d^3\mathbf{r}'\,\frac{\psi_k^\dagger(\mathbf{r}')\psi_k(\mathbf{r}')}{|\mathbf{r}-\mathbf{r}'|}\right]\psi(\mathbf{r}). \tag{1.122}$$

- $\hat{K}_k$ – the *exchange operator* – has no classical analogue and originates from anti-symmetry of the Slater determinant (Pauli principle). Its action is non-local:

$$\big(\hat{K}_k\psi\big)(\mathbf{r}) \;=\; \psi_k(\mathbf{r})\int d^3\mathbf{r}'\,\frac{\psi_k^\dagger(\mathbf{r}')\psi(\mathbf{r}')}{|\mathbf{r}-\mathbf{r}'|}. \tag{1.123}$$

  This contribution yields a reduction of the Coulomb repulsion for electrons with the same spin (the so-called Fermi hole).

Equations (1.120)–(1.121) show that each electron experiences an effective single-particle Hamiltonian $\hat{F}$: the original one-electron Dirac operator $\hat{h}_D$ plus a mean-field potential built from all occupied orbitals

$$\hat{V}_{\mathrm{mf}}(\mathbf{r}) \;=\; \sum_{k\in\mathrm{occ}} \big(\hat{J}_k - \hat{K}_k\big), \tag{1.124}$$

which acts on each orbital and encodes both classical electrostatic repulsion ($\hat{J}$) and quantum exchange ($\hat{K}$). Finally, by a unitary rotation among occupied orbitals one may diagonalize the Lagrange multiplier matrix and obtain the usual canonical (relativistic)

HF equations [105]:

$$\hat{F}\,\psi_i(\mathbf{r}) = \varepsilon_i\,\psi_i(\mathbf{r}), \qquad i = 1, \ldots, N, \tag{1.125}$$

where the ε_i are the orbital energies. Introducing a basis set to expand the molecular spinors as we have done in Eqn.(1.99) we may write the relativistic Roothaan equations [106]:

$$\begin{pmatrix} \mathbf{F}^{LL} & \mathbf{F}^{LS} \\ \mathbf{F}^{SL} & \mathbf{F}^{SS} \end{pmatrix} \begin{pmatrix} \mathbf{c}_i^L \\ \mathbf{c}_i^S \end{pmatrix} = \varepsilon_i \begin{pmatrix} \mathbf{S}^{LL} & \mathbf{0} \\ \mathbf{0} & \mathbf{S}^{SS} \end{pmatrix} \begin{pmatrix} \mathbf{c}_i^L \\ \mathbf{c}_i^S \end{pmatrix} \tag{1.126}$$

where we have defined

$$\mathbf{F}^{LL} = \mathbf{V}^{LL} + \mathbf{J}^{LL} - \mathbf{K}^{LL} \tag{1.127}$$

$$\mathbf{F}^{LS} = c\mathbf{\Pi}^{LS} - \mathbf{K}^{LS} \tag{1.128}$$

$$\mathbf{F}^{SL} = c\mathbf{\Pi}^{SL} - \mathbf{K}^{SL} \tag{1.129}$$

$$\mathbf{F}^{SS} = \mathbf{V}^{SS} - 2mc^2\mathbf{S}^{SS} + \mathbf{J}^{LL} - \mathbf{K}^{LL} \tag{1.130}$$

$$\tag{1.131}$$

Because $\hat{F}$ depends on the orbitals themselves, the HF equations are solved iteratively via the Self–Consistent Field (SCF) procedure: one guesses a set of orbitals, constructs $\hat{F}$, solves the eigenproblem, and repeats until convergence.

While the Hartree-Fock method can yield energies that are more than 95% of the exact electronic energy, the representation of the total electronic wave function by a single Slater determinant is generally inadequate. The small remaining error, less than 5%, is surprisingly significant for the properties description of properties and chemical reactions. As a result, the Hartree-Fock error, well-known as the *correlation energy* [107], is commonly defined as the difference between the exact energy and the Hartree-Fock energy

$$E_{\text{corr}} = E_{\text{exact}} - E_{\text{HF}} \tag{1.132}$$

where E_{exact} is the eigenvalue associated to the exact wave function for the electronic Hamiltonian in the chosen basis set.

One of the major areas of development in theoretical chemistry focuses on accurately capturing the correlation energy, which escapes description when using the single Slater determinant approximation. This leads to the so-called *post-Hartree–Fock methods*, among

which well-known examples include Configuration Interaction (CI), Møller–Plesset perturbation theory, multireference methods, and Coupled-Cluster (CC) theory. The latter will be discussed in greater detail in the following chapter.

1.4.4 Relativistic density functional theory

Wave function methods for N-particle systems face a significant mathematical hurdle due to their dependence on $3N$ spatial variables. Density Functional Theory (DFT) offers a compelling simplification by focusing on the electron charge density $\rho(\mathbf{r})$, a quantity dependent on only three variables, regardless of the number of electrons. This density represents the probability of finding one of the N electrons within an infinitesimal volume $d^3\mathbf{r}_1$:

$$\rho(\mathbf{r}_1) = N \int |\Psi(\mathbf{r}_1, \ldots, \mathbf{r}_N)|^2 \, d^3\mathbf{r}_2 \ldots d^3\mathbf{r}_N \tag{1.133}$$

Notice that by construction, the integral of $\rho(\mathbf{r})$ over all space yields the total number of electrons N:

$$\int \rho(\mathbf{r}) \, d^3\mathbf{r} = N. \tag{1.134}$$

The foundation of modern DFT lies in the Hohenberg–Kohn (HK) theorems (1964) [108], which establish the ground-state density as the fundamental variable. The first theorem proves that the external potential $V_{\text{ext}}(\mathbf{r})$ is uniquely determined (up to a constant) by the ground-state density $\rho_0(\mathbf{r})$. The second theorem posits the existence of a universal energy functional $E[\rho]$, whose global minimum corresponds to the exact ground-state energy, achieved at the exact ground-state density. While the HK theorems demonstrate the central role of the density, they do not provide a practical method for its determination.

Kohn and Sham (KS) in 1965 [109] provided a route to calculate $\rho_0(\mathbf{r})$ by introducing a fictitious system of non-interacting electrons subjected to an effective Kohn–Sham potential $V_{\text{KS}}(\mathbf{r})$, such that its density matches that of the real, interacting system. The energy of the real system is expressed as a functional of the density:

$$E[\rho] = T_s[\rho] + J[\rho] + E_{\text{XC}}[\rho] + \int V_{\text{ext}}(\mathbf{r})\rho(\mathbf{r}) \, d^3\mathbf{r}, \tag{1.135}$$

where $T_s[\rho]$ is the exact kinetic energy of the non-interacting system, $J[\rho]$ is the classical electrostatic energy, and $E_{\text{XC}}[\rho]$ is the exchange–correlation functional, which is not known

exactly. The Kohn–Sham potential is then derived as:

$$V_{\mathrm{KS}}(\mathbf{r}) = \frac{\delta J}{\delta \rho} + \frac{\delta E_{\mathrm{XC}}}{\delta \rho} + V_{\mathrm{ext}}(\mathbf{r}). \tag{1.136}$$

Solving the single-particle Kohn–Sham equations,

$$\hat{h}^{\mathrm{KS}} \psi_i^{\mathrm{KS}}(\mathbf{r}) = \epsilon_i^{\mathrm{KS}} \psi_i^{\mathrm{KS}}(\mathbf{r}) \quad ; \quad i = 1, \ldots, N \tag{1.137}$$

allows the calculation of the electron density:

$$\rho(\mathbf{r}) = \sum_{i=1}^{N} |\psi_i^{\mathrm{KS}}(\mathbf{r})|^2. \tag{1.138}$$

As the Kohn–Sham potential depends on the density, these equations are solved iteratively using a self-consistent field (SCF) procedure. The accuracy of DFT heavily relies on the approximation chosen for the exchange–correlation functional $E_{\mathrm{XC}}[\rho]$ and its derivative, the exchange–correlation potential $V_{\mathrm{XC}} = \delta E_{\mathrm{XC}}[\rho]/\delta\rho$. Various levels of approximations for these functionals exist, often categorized within the "Jacob's ladder" framework [110].

The extension to the relativistic case is non-trivial and necessitates the framework of quantum field theory for a proper treatment, which falls outside the scope of this thesis. Nevertheless, we can provide a practical description of the relativistic extension, directing the interested reader to Ref.[111] for a comprehensive and rigorous analysis. In the relativistic domain, the electronic density $\rho(\mathbf{r})$ and the current density $\mathbf{j}(\mathbf{r})$ can be expressed in terms of Dirac spinors as follows:

$$\rho(\mathbf{r}) = -e \sum_{i}^{N} \psi_i^{\dagger}(\mathbf{r}) \psi_i(\mathbf{r}), \tag{1.139}$$

$$\mathbf{j}(\mathbf{r}) = -ec \sum_{i}^{N} \psi_i^{\dagger}(\mathbf{r}) \boldsymbol{\alpha} \psi_i(\mathbf{r}), \tag{1.140}$$

As previously encountered with the relativistic Hartree-Fock method, the concept of variational collapse arises. Consequently, this issue casts doubt on the validity of the Hohenberg-Kohn theorems in the relativistic regime. Without delving into excessive mathematical intricacies, Rajagopal and Callaway [112] demonstrated that the 4-current density $j^{\mu}(\mathbf{r})$ uniquely determines the external 4-vector potential $A^{\mu}(\mathbf{r})$ up to a gauge transformation. This allows us to express the electronic energy as a functional of $j^{\mu}(\mathbf{r})$,

denoted as $E_{el}[j^\mu]$. Analogous to the non-relativistic case, the energy functional can be written as:

$$E_{el}[j^\mu] = T[j^\mu] + V_{\text{ext}}[j^\mu] + J[j^\mu] + E_{XC}[j^\mu]. \tag{1.141}$$

Similar to the non-relativistic scenario, the exact form of the exchange-correlation energy functional $E_{XC}[j^\mu]$ remains unknown, mirroring the non-relativistic case. This involves introducing a fictitious system of non-interacting fermions that exhibits the same density as the real interacting system. For this fictitious system, the kinetic energy can be exactly calculated thought a minimization restricted to wave functions ensuring positive-energy eigenvalues to avoid variational collapse. To evaluate the electronic density $\rho(\mathbf{r})$ and the current density $\mathbf{j}(\mathbf{r})$, Dirac spinors are required. Again, Rajagopal and Callaway proposed a relativistic counterpart to the Kohn-Sham equations [112].

1.4.5 Two-component methodologies

The 4-component Dirac Hamiltonian contains both the positive and the negative-energy solutions. It is worth to note that in quantum chemistry we are mainly interested in the positive-energy ones. Therefore, it is reasonable to ask if there is a way to directly start from a 2-component Hamiltonian which only refers to the positive-energy solutions. The purpose of two–component (2C) relativistic Hamiltonians is to capture the leading-order relativistic effects (scalar–relativistic and spin–orbit coupling) in molecular electronic–structure calculations, while drastically reducing the computational cost compared to the full four–component Dirac equation, by eliminating the explicit treatment of the small components.

Two families of methods are employed for the generation of two-component Hamiltonians: those based on unitary transformations [113–117] and those relying on the elimination of the small component [118–121]. The first methodology is based on finding a unitary transformation U that eliminates the *odd* terms, that is, those that couple the large and small components, thus yielding a block-diagonal Dirac Hamiltonian

$$U^\dagger \begin{bmatrix} h_{LL} & h_{LS} \\ h_{SL} & h_{SS} \end{bmatrix} U = \begin{bmatrix} h_{++} & 0 \\ 0 & h_{--} \end{bmatrix}. \tag{1.142}$$

The second technique is based on explicitly expressing the small component ψ^S of the wavefunction in terms of the large component ψ^L by using the coupled equations

$$\begin{cases} h_{LL}\psi^L(\mathbf{r}) + h_{LS}\psi^S(\mathbf{r}) = E\psi^L(\mathbf{r}) \\ h_{SL}\psi^L(\mathbf{r}) + h_{SS}\psi^{SS}(\mathbf{r}) = E\psi^S(\mathbf{r}) \end{cases} \tag{1.143}$$

where large and small components are exactly coupled by the following relation

$$\psi^S(\mathbf{r}) = R\psi^L(\mathbf{r}), \quad R \equiv R(E) = \frac{c\boldsymbol{\sigma}\cdot\mathbf{p}}{mc^2 + E - V} \tag{1.144}$$

where R is the coupling operator previously derived (see Eqn. (1.77)), now generalized to include the potential energy term V introduced in Eqn. (1.93). Once the operator R is known, the small component ψ^S can be substituted back into the Dirac equation, leading to an effective two-component equation involving only the large component ψ^L. The corresponding wavefunction must be properly normalized using the factor $N_+ = \sqrt{1 + R^\dagger R}$.

However, a major complication arises from the fact that R depends on the total energy E, which is itself the quantity we aim to determine. This circular dependence makes the exact elimination of ψ^S impractical in most applications. To overcome this, one typically resorts to approximations of the operator R, which lead to various two-component methodologies [113, 115, 116, 122–124].

What we aim for is the development of an *exact* decoupling scheme. The historical evolution of the X2C (exact two-component) Hamiltonian, however, is not entirely straightforward, as it is difficult to attribute credit to a single work. Many authors have contributed to its development [118, 125–133], and we refer the reader to the comprehensive review by Saue [134] for a detailed discussion. The development of the exact two-component (X2C) method rests on two key insights. First, the solution of the one-electron Dirac equation is computationally inexpensive when compared to the formidable task of solving the many-electron problem. Second, the entire procedure can be formulated in the language of matrix algebra, which makes the approach both elegant and practical. Building on these observations, one arrives at a remarkably simple strategy for achieving an exact decoupling of the Dirac Hamiltonian. The procedure begins by solving the four-component one-electron Dirac equation in a finite basis, which amounts

to diagonalizing the matrix representation of h_{4c}. From the resulting eigenvectors, one can identify the matrix R that characterizes the coupling between the large and small components of the wave function. With R at hand, the unitary transformation matrix U can be constructed in a closed form. Applying this transformation to the one-electron Dirac Hamiltonian,

$$U^\dagger h_{4c} U = \begin{pmatrix} h_{X2C}^{++} & 0 \\ 0 & h_{X2C}^{--} \end{pmatrix}, \tag{1.145}$$

yields the two-component Hamiltonian h_{X2C}^{++}, which corresponds to the positive-energy part of the four-component one-electron Dirac Hamiltonian. The current one-step procedure used in the relativistic `DIRAC` program package is detailed in Ref. [134]. This formulation brings with it several notable advantages. Most importantly, the positive-energy spectrum of the original Dirac Hamiltonian is reproduced exactly within the chosen basis. The method relies solely on matrix manipulations, so no new operators need to be introduced. Furthermore, since the transformation matrix U is available explicitly, it can be applied consistently to any property operator,

$$\Omega_{2c} = [U^\dagger \Omega_{4c} U]_{++}, \tag{1.146}$$

ensuring that Hamiltonian and operators remain in the same representation. As a direct consequence, the well-known problem of *picture-change errors* [135–137] is completely avoided.

One may wonder why the two-electron part is not diagonalized in the same way as the one-electron part. If the same transformation were applied, the resulting two-electron operator would become a 4×4 matrix in the large/small component space, whose computation is significantly more demanding than a direct four-component calculation. For this reason, it is common to approximate the two-electron contribution by retaining only the $++$ block, $\tilde{g}_{++}^{++}$, which can be evaluated using standard non-relativistic two-electron repulsion integrals in combination with the X2C one-electron operator. However, this approximation implies that the spin-same-orbit (SSO) and spin-other-orbit (SOO) contributions are not correctly accounted for, since we are not using Eqn.(1.98). Conceptually, the SSO term represents the interaction between the spin of electron i and its own orbital angular momentum in the potential created by the remaining $n-1$ electrons. In contrast, the SOO term describes the interaction between the spin of electron i and the

orbital motion of a different electron j. One common scheme to address this issue is the *atomic mean-field* approach (X2C-AMFI) [138]. In X2C-AMFI, one replaces the exact two-electron spin–orbit interaction by a sum of spherically averaged atomic potentials (obtained from atomic Dirac–Fock calculations). That is, atomic spin–orbit integrals are pre-tabulated (via the AMFI code) and added to the one-electron X2C Hamiltonian. In contrast, at the correlated level, the *molecular mean-field* approach (sometimes called X2C-MMF) can be adopted [139]. It performs the X2C decoupling after an initial SCF step using the full molecular normal-ordered Fock operator. Thus, in the X2C-MMF approach, a four-component SCF calculation is first performed, and the decoupling transformation is applied to the Fock operator, hence eliminating picture-change errors in the mean-field description at the correlated level. The two-component Fock matrix is combined with the untransformed two-electron interaction, and the correlated calculation is carried out.

Chapter 2

Coupled Cluster Theory

"In theory, there is no difference between theory and practice. But, in practice, there is."

— *Yogi Berra*

The purpose of this chapter is to present the single-reference Coupled Cluster (CC) method, derive its fundamental equations, and introduce the development and application of diagrammatic techniques, particularly for high-order methods. In writing this chapter, I have relied on several key references that I consider essential for a deep and accurate understanding of the theory. Among these, the review by Crawford and Schaefer [140] has served as a guiding light in my learning process. Other invaluable sources are the comprehensive book by Helgaker, Jørgensen, and Olsen [141], and—particularly for diagrammatic techniques—include the textbook by Shavitt and Bartlett [142], and the review article by Bartlett and Musiał [143].

2.1 The electron correlation problem

One of the central challenges in electronic structure theory is the proper description of electron correlation. Electrons interact through the Coulomb force, which in this case is a purely repulsive electrostatic interaction. As a result, they tend to avoid each other in space: the presence of one electron at a given position makes it less likely to find another electron nearby. This dynamical avoidance, driven by the instantaneous positions of the electrons, is referred to as *electronic correlation*. In the mean-field picture, such as Hartree–Fock theory, the many-electron wavefunction is approximated by a single Slater determinant. Each electron is assumed to move independently in an average, or mean, potential generated by all the other electrons. As illustrated in Figure (2.1), the red dashed circle schematically represents this collective mean field produced by a group of electrons (shown as blue dots within the bubble). Rather than accounting for explicit electron–electron interactions, each electron experiences an effective potential, V_{eff}, which captures the averaged influence of the remaining electrons. This simplification reduces the complexity of the many-body problem but neglects dynamical correlation effects arising from instantaneous electron–electron repulsion.

While the mean-filed description correctly imposes the antisymmetry requirement and includes some effects of the Pauli exclusion principle (often called exchange correlation), it fails to capture the full extent of electron-electron repulsion. In particular, it neglects the dynamical adjustments of the electronic cloud that arise from the correlated motion of the electrons, resulting in an energy discrepancy known as the *correlation energy* [14]:

$$E_{\text{corr}} = E_{\text{exact}} - E_{\text{HF}}, \tag{2.1}$$

where E_{exact} is the exact electronic energy (within a given basis set) for the Hamiltonian $\hat{H}$, and E_{HF} is the corresponding Hartree-Fock energy. To go beyond this approximation and account for correlation, one must allow for a more flexible wavefunction ansatz. This is typically achieved by expressing the correlated wavefunction as a linear combination of multiple Slater determinants, where some electrons are excited from occupied to virtual orbitals. These excited determinants encode the different ways in which electrons can rearrange to better minimize their mutual repulsion, thus providing a systematic path to improving the description of the electronic structure. As shown in Figure 2.2, each electron (blue dot) interacts explicitly with all others through pairwise correlations, depicted by

the red arrows connecting every pair. Unlike the mean-field approximation, this fully connected network captures the instantaneous electron–electron interactions

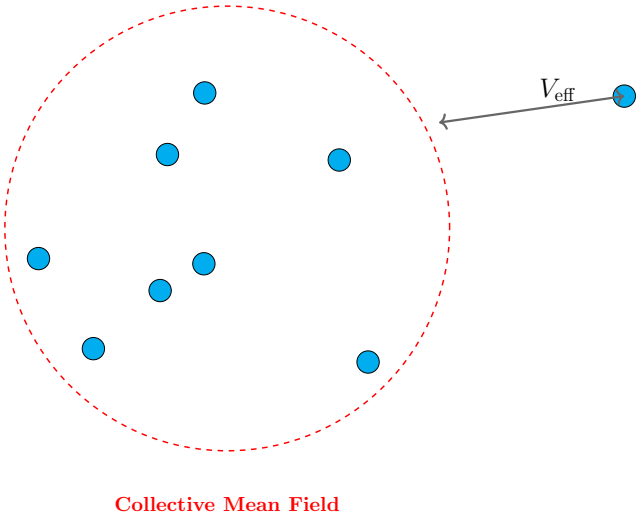

FIGURE 2.1: Schematic representation of an electronic system treated with the mean-field approach. Each blue dot represents an electron. The red dashed circle represents the collective "mean field" generated by a subset of electrons (inside the bubble), acting individually on each of them. One electron lies outside the mean-field description and is affected by the effective potential V_{eff} generated by the rest of the system.

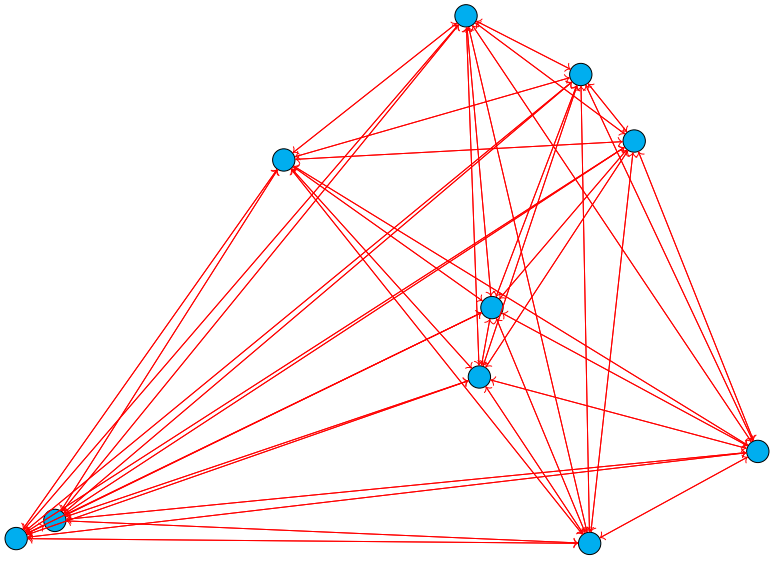

FIGURE 2.2: Schematic representation of true electronic correlation. Each blue dot represents an electron, and the red arrows indicate all pairwise interactions between them.

Electron correlation can be broadly classified into two distinct types:

1. *Static correlation* (also known as non-dynamic correlation) arises in systems where a single Slater determinant fails to provide an adequate description of the electronic

structure. This situation typically occurs in cases of near-degeneracy among electronic configurations, such as in open-shell species, bond dissociation processes, or when the highest occupied and lowest unoccupied molecular orbitals (HOMO and LUMO) are close in energy. Under these conditions, multiple electronic configurations contribute significantly to the ground state wave function, necessitating the use of so-called *multireference methods*.

2. *Dynamic correlation* describes the rapid, short-range adjustments in the motion of electrons as they avoid one another due to their instantaneous Coulomb repulsion. This type of correlation is present even in systems that are well described by a single determinant and is responsible for subtle effects such as dispersion interactions. Consequently, methods that primarily account for dynamic correlation are often referred to as *single-reference methods*.

In this thesis, we will primarily focus on dynamic correlation.

Historically, one of the earliest and most straightforward approaches to treat electron correlation beyond Hartree-Fock is the *Configuration Interaction* (CI) method [144, 145]. In CI, the exact wave function is expressed as a linear combination of Slater determinants constructed from a set of molecular orbitals:

$$|\Psi_{\mathrm{CI}}\rangle = c_0|\Phi_0\rangle + \sum_{i,a} c_i^a|\Phi_i^a\rangle + \sum_{\substack{i<j \\ a<b}} c_{ij}^{ab}|\Phi_{ij}^{ab}\rangle + \cdots , \tag{2.2}$$

where $|\Phi_0\rangle$ is the Hartree-Fock reference determinant, $|\Phi_i^a\rangle$ are singly excited determinants obtained by replacing an occupied orbital i with a virtual orbital a, $|\Phi_{ij}^{ab}\rangle$ are doubly excited determinants with two such replacements, and so forth. The *Full CI* method corresponds to including *all* possible excitations within a given one-electron basis set. This means that the wave function expansion in Eqn. (2.2) contains every possible Slater determinant that can be constructed by distributing the N electrons among the M spin-orbitals. Full CI provides the exact solution of the electronic equation within the chosen basis set, thus serving as the *gold standard* for electron correlation. The total number of determinants in Full CI is given by the binomial coefficient:

$$N_{\mathrm{det}} = \binom{M}{N} = \frac{M!}{N!\,(M-N)!}, \tag{2.3}$$

where M is the total number of orbitals and N is the number of electrons. For example, for a system with 10 electrons and 50 orbitals, the number of determinants is 4.2×10^{11}, making Full CI feasible only for very small molecules or minimal basis sets. The CI coefficients $\{c_I\}$, where the index I runs over all determinants included in the expansion, are obtained by solving the time-independent electronic equation projected onto the basis of determinants:

$$\hat{H}|\Psi_{\mathrm{CI}}\rangle = E|\Psi_{\mathrm{CI}}\rangle \quad \Rightarrow \quad \mathbf{Hc} = E\mathbf{c}, \tag{2.4}$$

where $\mathbf{H}$ is the Hamiltonian matrix with elements

$$H_{IJ} = \langle \Phi_I | \hat{H} | \Phi_J \rangle, \tag{2.5}$$

and $\mathbf{c}$ is the vector of CI coefficients. Due to the combinatorial growth of N_{det}, the dimension of $\mathbf{H}$ becomes prohibitively large for all but the smallest systems, motivating the use of truncated CI methods (e.g., CIS, CISD).

2.1.1 Size-extensivity and size-consistency

Two fundamental properties that any reliable electronic structure method should satisfy are *size-extensivity* and *size-consistency*.

1. **Size-extensivity** requires that the total energy of a system composed of N non-interacting identical subsystems scales linearly with N:

$$E(N \text{ subsystems}) = N \times E(\text{single subsystem}). \tag{2.6}$$

2. **Size-consistency** demands that the energy of two infinitely separated, non-interacting fragments A and B equals the sum of their individual energies:

$$\lim_{R_{AB} \to \infty} E(A + B) = E(A) + E(B). \tag{2.7}$$

   where $R_{AB} = |\mathbf{R}_A - \mathbf{R}_B|$ is the distance between the two fragments.

A necessary condition for size-extensivity is that the total wave function for non-interacting fragments factorizes in the appropriate antisymmetrized product space. Specifically, if

fragments A and B are spatially and electronically disjoint, the total wave function must be

$$\Psi_{AB}(\mathbf{r}_A, \mathbf{r}_B) = \Psi_A(\mathbf{r}_A) \wedge \Psi_B(\mathbf{r}_B), \tag{2.8}$$

where $\wedge$ denotes the antisymmetrized product, ensuring that the Pauli principle is respected for the full system.

Truncated CI expansions, being linear combinations of determinants, do not satisfy this multiplicative separability. Consequently, truncated CI methods such as CISD are neither size-extensive nor size-consistent. For example, if both fragments A and B require double excitations for accurate correlation, the combined system $A + B$ would require quadruple excitations to maintain proper factorization, which are absent in CISD. This leads to errors that grow with system size and incorrect dissociation limits. Such deficiencies can be partially alleviated by applying perturbative corrections, such as Davidson's correction [146]. For a comprehensive discussion on the limitations of truncated CI methods, the reader is referred to the classical textbook by Szabo and Ostlund [147].

2.1.2 Towards size-extensive wave functions: the Coupled Cluster ansatz

As discussed in the previous section, a key requirement for any robust electronic structure method is the ability to describe the energy of non-interacting systems accurately, i.e., to be size-extensive and size-consistent. While truncated CI methods fail to satisfy these properties due to the linear expansion of the wave function, a more suitable approach is based on an exponential parametrization. The exponential function naturally ensures multiplicative separability, as it satisfies the fundamental relation

$$e^{X+Y} = e^X \cdot e^Y, \quad [X, Y] = 0. \tag{2.9}$$

This observation motivates the introduction of the exponential *Coupled Cluster* (CC) ansatz [148]:

$$|\Psi_{\mathrm{CC}}\rangle = e^{\hat{T}}|\Phi_0\rangle, \tag{2.10}$$

where $|\Phi_0\rangle$ is the reference determinant (typically the Hartree-Fock determinant), and $\hat{T}$ is the cluster operator, which generates excitations out of the reference determinant. The

cluster operator is typically expressed as a sum of excitation operators of different orders:

$$\hat{T} = \hat{T}_1 + \hat{T}_2 + \hat{T}_3 + \cdots , \tag{2.11}$$

where $\hat{T}_1$ generates single excitations, $\hat{T}_2$ generates double excitations, and so on.

To illustrate how the exponential CC ansatz ensures size-extensivity and size-consistency, consider a system composed of two non-interacting subsystems A and B. The cluster operator for the combined system can be written as the sum of the cluster operators for the individual subsystems:

$$\hat{T}_{AB} = \hat{T}_A + \hat{T}_B. \tag{2.12}$$

Then, the CC wave function for the combined system is:

$$|\Psi_{\mathrm{CC}}^{AB}\rangle = e^{\hat{T}_{AB}}|\Phi_0^{AB}\rangle = e^{\hat{T}_A+\hat{T}_B}|\Phi_0^{A}\rangle \wedge |\Phi_0^{B}\rangle, \tag{2.13}$$

where we have assumed that the reference determinant for the combined system is simply the product of the reference determinants for the individual subsystems. This is not simple an approximation, as the Hartree-Fock wave-function is multiplicative-separable. Since $\hat{T}_A$ and $\hat{T}_B$ operate on different sets of electrons and therefore commute, we can rewrite the above equation as:

$$|\Psi_{\mathrm{CC}}^{AB}\rangle = e^{\hat{T}_A}e^{\hat{T}_B}|\Phi_0^{A}\rangle \wedge |\Phi_0^{B}\rangle = |\Psi_{\mathrm{CC}}^{A}\rangle \wedge |\Psi_{\mathrm{CC}}^{B}\rangle. \tag{2.14}$$

Thus, the CC wave function for the combined system factorizes into the product of the CC wave functions for the individual subsystems, demonstrating that the CC ansatz is multiplicatively separable and therefore size-extensive and size-consistent. This property holds even when the cluster operator is truncated at a certain excitation level (e.g., CCSD, which includes singles and doubles only), making CC theory a powerful and reliable tool for electronic structure calculations. The CC approach will be discussed in detail in the following chapters.

2.2 Second-quantization background

In general, many-body systems are often conveniently treated using the formalism of second quantization, and the coupled-cluster method is no exception. It is therefore necessary to briefly summarize the concepts required for the formal development of the coupled-cluster theory. More information and details can be found in Refs. [141, 142, 149].

In many-body quantum mechanics, it is often convenient to work not within a fixed number of particles, but in a more general space that accommodates varying particle numbers. This leads us to the definition of the *Fock space*. Given a set of A orthonormal spin-orbitals $\psi_1, \psi_2, \ldots, \psi_A$, the Fock space $\mathcal{F}$ is defined as the direct sum of all n-electron Hilbert spaces constructed from these spin-orbitals:

$$\mathcal{F} = \bigoplus_{n=0}^{A} \mathcal{H}^{(n)}, \tag{2.15}$$

where $\mathcal{H}^{(n)}$ denotes the antisymmetric n-particle Hilbert space (for fermions), spanned by Slater determinants constructed from n occupied spin-orbitals out of the A available. Within this framework, a Slater determinant $|\Phi\rangle$ is a basis vector in one of the $\mathcal{H}^{(n)}$ subspaces.

We introduce the *occupation number vector* (ONV). This is a binary representation that captures the occupation status of each orbital:

$$|\Phi\rangle \rightarrow |\nu_1, \nu_2, \ldots, \nu_A\rangle\,, \tag{2.16}$$

where $\nu_k \in \{0, 1\}$ indicates whether the k-th spin-orbital ψ_k is occupied ($\nu_k = 1$) or unoccupied ($\nu_k = 0$). The generic state expressed in Eqn. (2.16) can be constructed systematically by defining the so-called *creation operators*. These operators allow us to build many-body wavefunctions starting from the vacuum state $|-\rangle$, which represents the state with no particles. For a given set of spin-orbitals $\{\psi_1, \psi_2, \ldots, \psi_A\}$, we associate to each spin-orbital an operator $a_k^\dagger$ that creates a fermion in orbital ψ_k, and an operator a_k that annihilates a fermion from spin-orbital ψ_k. These operators satisfy the canonical anticommutation relations for fermions:

$$\{a_k, a_l^\dagger\} = \delta_{kl}, \quad \{a_k, a_l\} = \{a_k^\dagger, a_l^\dagger\} = 0, \tag{2.17}$$

where $\{A, B\} = AB + BA$ denotes the anticommutator. Using these operators, any occupation number vector can be constructed by successively applying creation operators to the vacuum:

$$|\nu_1, \nu_2, \ldots, \nu_A\rangle = (a_1^\dagger)^{\nu_1}(a_2^\dagger)^{\nu_2} \cdots (a_A^\dagger)^{\nu_A} |-\rangle \,, \tag{2.18}$$

where each $\nu_k \in \{0, 1\}$ determines whether the creation operator $a_k^\dagger$ acts on the vacuum or not. Due to the fermionic nature of the particles, applying a creation operator to an already occupied spin-orbital yields zero:

$$a_k^\dagger \,|\ldots, 1_k, \ldots\rangle = 0. \tag{2.19}$$

The annihilation operators a_k act as the adjoint of the creation operators, and satisfy:

$$a_k \,|\ldots, 1_k, \ldots\rangle = (-1)^{s_k} \,|\ldots, 0_k, \ldots\rangle \,, \tag{2.20}$$

where the phase factor $(-1)^{s_k}$ arises from the anticommutation relations and depends on the number of occupied spin-orbitals to the left of ψ_k in the ordering convention.

Once the Fock space formalism and the creation/annihilation operators have been introduced, the next step is to express the electronic Hamiltonian in terms of these operators using the algebra of second quantization. In Sec.(1.4), we introduced the electronic Hamiltonian within the Born–Oppenheimer approximation in Eqn. (1.91). Using the second quantized formalism, the same Hamiltonian can be written as:

$$\hat{H} = \sum_{pq} h_{pq} a_p^\dagger a_q + \frac{1}{4} \sum_{pqrs} V_{pqrs} a_p^\dagger a_q^\dagger a_s a_r, \tag{2.21}$$

where h_{pq} are the one-electron integrals, and V_{pqrs} denote the antisymmetrized two-electron integrals

$$h_{pq} = \int \psi_p^\dagger(\mathbf{r})\, \hat{h}(\mathbf{r})\, \psi_q(\mathbf{r})\, d\mathbf{r}, \tag{2.22}$$

$$V_{pqrs} = \iint \psi_p^\dagger(\mathbf{r}_1)\psi_q^\dagger(\mathbf{r}_2)\, \hat{g}(\mathbf{r}_1, \mathbf{r}_2)\, [\psi_r(\mathbf{r}_1)\psi_s(\mathbf{r}_2) - \psi_s(\mathbf{r}_1)\psi_r(\mathbf{r}_2)]\; d\mathbf{r}_1 d\mathbf{r}_2. \tag{2.23}$$

Here, $\hat{h}(\mathbf{r})$ is the one-electron operator (kinetic energy plus external potential), and $\hat{g}(\mathbf{r}_1, \mathbf{r}_2)$ is the electron–electron interaction operator.

We have seen that the algebra of the creation and annihilation operators is non-commutative and follows the anticommutation relations for fermions (Eqn.(2.17)). To systematically handle operator products, we introduce the concept of *normal ordering*. The normal ordering operation is defined such that all creation operators $a^\dagger$ are moved to the left of all annihilation operators a; each transposition contributes a minus sign due to the fermionic anti-commutation relations. By convention, normal ordering is defined with respect to the vacuum state $|-\rangle$, so that the expectation value of any normal-ordered product vanishes in this state. While this simplifies the algebra of operator expressions, the key tool for handling arbitrary operator products is *Wick's theorem* [150]. The time-independent version of the theorem states that any product of creation and annihilation operators can be expressed as a sum of normal-ordered terms plus all possible contractions between operator pairs:

$$\begin{aligned} ABC\ldots XYZ = \{ABC\ldots XYZ\}_\nu + \sum_{\text{singles}} \{\overbracket{AB}C\ldots XYZ\}_\nu \\ + \sum_{\text{doubles}} \{\overbracket{AB}\ldots\overbracket{XY}Z\}_\nu + \ldots \end{aligned} \tag{2.24}$$

where the notation $\{\ldots\}_\nu$ refer to the normal-order respect to the vacuum state. A *contraction* between two operators A and B is defined as the difference between their standard product and the corresponding normal-ordered product:

$$\overbracket{AB} = AB - \{AB\}_\nu. \tag{2.25}$$

The theorem can also be extended to the product of two second-quantized operator strings. Let $A_1A_2\ldots A_m$ and $B_1B_2\ldots B_n$ be two strings of fermionic creation or annihilation operators. Then, the product of their normal-ordered forms can be expressed as:

$$\{A_1A_2\ldots A_m\}_\nu \cdot \{B_1B_2\ldots B_n\}_\nu = \sum_{\text{all contractions}} \{A_1A_2\ldots A_mB_1B_2\ldots B_n\}_\nu, \tag{2.26}$$

where the sum runs over all possible sets of contractions between one operator from the first string and one from the second string. No contractions are allowed between operators within the same string.

In general, referring to the true vacuum state for each term can lead to extremely long strings of second-quantized operators, which would be cumbersome to manipulate and

reorder into normal-ordered form. To simplify this process, we transition to the *particle-hole formalism*. In the particle-hole formalism, instead of referring to the true vacuum, we introduce a reference state (the *Fermi vacuum*), typically a Hartree-Fock determinant or a similar Slater determinant. This reference state is used as a vacuum, and the creation and annihilation operators are treated as acting with respect to this state. From this point onward, we introduce the following notation for indexes to avoid ambiguities:

- $i, j, k, \ldots$ for occupied spin-orbitals.
- $a, b, c, \ldots$ for virtual spin-orbitals.
- $p, q, r, \ldots$ for generic spin-orbitals.

Therefore, we define normal ordering relative to a reference determinant $|\Phi_0\rangle$, where operators that annihilate $|\Phi_0\rangle$ are placed to the right. This means creation operators for occupied spin-orbitals and annihilation operators for virtual spin-orbitals appear on the right of all other operators. This definition modifies the rules defined in Eqn.(2.17): they are non-zero when an annihilation operator for an occupied spin-orbital or a creation operator for a virtual spin-orbital appears to the right:

$$\overbrace{a_i^\dagger a_j} = \delta_{ij}, \quad \overbrace{a_a a_b^\dagger} = \delta_{ab}, \tag{2.27}$$

while all the others vanish. This change is naturally interpreted in the particle-hole formalism: occupied spin-orbitals are holes and virtual spin-orbitals are particles. Operators such as a_i and $a_a^\dagger$ act as quasiparticle creation operators, while $a_i^\dagger$ and a_a act as annihilation operators. Most importantly, the expectation value of a normal-ordered operator with respect to reference state is zero. It can be shown that normal ordering a generic operator $\hat{\Omega}$ with respect to a reference state $|\Phi_0\rangle$ is equivalent to subtracting its expectation value in that state. In other words, the normal-ordered form of the operator is given by

$$\hat{\Omega}_N = \hat{\Omega} - \langle\Phi_0|\hat{\Omega}|\Phi_0\rangle\,. \tag{2.28}$$

Applying this to the electronic Hamiltonian leads to the following expression:

$$\hat{H}_N = \hat{H} - \langle\Phi_0|\hat{H}|\Phi_0\rangle = \sum_{pq} f_{pq}\{a_p^\dagger a_q\} + \frac{1}{4}\sum_{pqrs} V_{pqrs}\{a_p^\dagger a_q^\dagger a_s a_r\}, \tag{2.29}$$

which defines the *normal-ordered Hamiltonian* $\hat{H}_N$. Here, the coefficients f_{pq} correspond to the elements of the Fock matrix, while V_{pqrs} are the antisymmetrized two-electron integrals:

$$f_{pq} = h_{pq} + \sum_i \langle pi||qi\rangle\,, \qquad V_{pqrs} = \langle pq||rs\rangle = \langle pq|rs\rangle - \langle pq|sr\rangle\,,$$

where the index i runs over occupied spin-orbitals in the reference determinant $|\Phi_0\rangle$. It is somewhat interesting to note that the normal-ordered Hamiltonian is not simply the one-body and two-body parts written in normal order, but instead involves the Fock operator. The details and its derivation are provided in Appendix B.1.

With this necessary foundation in second quantization, we are now equipped to move on to the next section, where we develop the coupled cluster formalism.

2.3 Formal Coupled Cluster method

The basic assumption in Coupled Cluster (CC) theory is to construct the correlated wave function by applying an non-unitary exponential parametrization to a reference determinant, typically the Hartree–Fock (HF) ground state:

$$|\Psi_{\mathrm{CC}}\rangle = e^{\hat{T}}\,|\Phi_0\rangle\,, \tag{2.30}$$

where $|\Phi_0\rangle$ is a single Slater determinant and $\hat{T}$ is the *cluster operator*, which introduces electronic correlation into the wave function. The cluster operator is expressed as a sum over excitation operators:

$$\hat{T} = \sum_\mu t_\mu \hat{\tau}_\mu, \tag{2.31}$$

where $\hat{\tau}_\mu$ are excitation operators that promote electrons from occupied orbitals in the reference state to virtual (unoccupied) orbitals, and t_μ are the corresponding cluster amplitudes. Each $\hat{\tau}_\mu$ acts on $|\Phi_0\rangle$ to generate an excited determinant $|\Phi_\mu\rangle = \hat{\tau}_\mu\,|\Phi_0\rangle$, known as an *excited determinant*. Excited determinants refer to electronic wavefunctions in which one or more electrons are promoted from their ground-state orbitals to higher-energy orbitals. These excitations can be classified into different types depending on the number of electrons involved. A singly excited determinant involves the promotion of a single electron from one occupied orbital to a virtual orbital, while a doubly excited determinant

involves the promotion of two electrons to higher orbitals. Two examples are reported in Figures 2.3 and 2.4. According to the language of second quantization introduced in Sec. 2.2, it is clear that these excited determinants can be appropriately expressed by operators that create and annihilate electrons. We then formally define a single excitation operator as an operator composed of a creation operator and a annihilation operator; multiple pairs of these form multi-excitation operators. We may therefore write Eqn.(2.31) as

$$\hat{T} = \hat{T}_1 + \hat{T}_2 + \cdots + \hat{T}_N, \tag{2.32}$$

where we have

$$\hat{T}_1 = \sum_{ia} t_i^a \hat{a}_a^\dagger a_i, \tag{2.33}$$

$$\hat{T}_2 = \left(\frac{1}{2!}\right)^2 \sum_{ijab} t_{ij}^{ab} \hat{a}_a^\dagger \hat{a}_b^\dagger a_i a_j, \tag{2.34}$$

$$\vdots$$

$$\hat{T}_N = \left(\frac{1}{N!}\right)^2 \sum_{i_1 \ldots i_N a_1 \ldots a_N} t_{i_1 \ldots i_N}^{a_1 \ldots a_N} \prod_{k=1}^{N} \hat{a}_{a_k}^\dagger a_{i_k}. \tag{2.35}$$

The prefactors $\left(\frac{1}{N!}\right)^2$ in the definition of the cluster operators are required to avoid over-counting equivalent excitations due to the permutations of occupied indices $(i_1, \ldots, i_N)$ and virtual indices $(a_1, \ldots, a_N)$. Each excitation operator is antisymmetric with respect to these permutations, and the $N!$ factors in the denominator ensure that each unique excitation is counted only once. These excited determinants are generated by the Taylor series expansion of the operator $e^{\hat{T}}$ in Eqn.(2.30)

$$e^{\hat{T}} = \sum_{k=0}^{\infty} \frac{\hat{T}^k}{k!}, \tag{2.36}$$

and we may realize that the above expansion, acting on the reference state, will generate *connected excitations*, by means of linear clusters, whereas all the non-linear clusters will generate *disconnected excitations* which correspond to multiple independent excitations occurring simultaneously. Therefore, the exponential ansatz naturally generates both connected and disconnected excitations:

- **Connected excitations:** $\hat{T}_n|\Phi_0\rangle$

- **Disconnected excitations:** products like $\hat{T}_1^2|\Phi_0\rangle$, $\hat{T}_1\hat{T}_2|\Phi_0\rangle$, etc.

where the latter ensures the size-extensivity of the coupled cluster wavefunction [143]. We should recall that the disconnected excitations were missing in the truncated CI expansion. This is not surprising, as the CI ansatz is linear by construction and therefore incapable of generating disconnected terms.

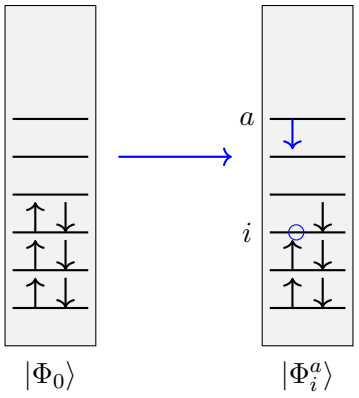

FIGURE 2.3: Singly excited determinant with an electron promoted to orbital a, starting from the reference determinant.

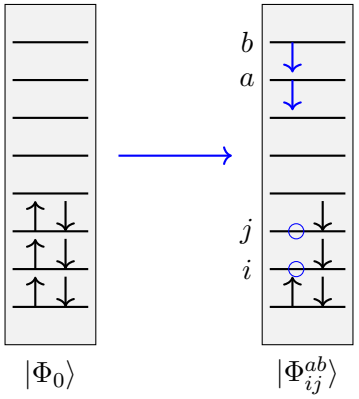

FIGURE 2.4: Doubly excited determinant with electrons promoted to orbitals a and b, starting from the Hartree-Fock determinant.

2.3.1 Coupled Cluster equations

We have seen that the wavefunction parametrization is governed by the cluster amplitudes t_μ, which are initially unknown and must be determined. In line with the general philosophy of many methods in theoretical chemistry—such as Hartree–Fock (HF), multiconfigurational self-consistent field (MCSCF), and configuration interaction (CI)—a natural first approach is the *variational principle*. In this framework, one seeks to determine the

amplitudes by minimizing the expectation value of the normal-ordered Hamiltonian:

$$E_{\mathrm{CC}} = \frac{\langle \Psi_{\mathrm{CC}} | \hat{H}_N | \Psi_{\mathrm{CC}} \rangle}{\langle \Psi_{\mathrm{CC}} | \Psi_{\mathrm{CC}} \rangle} = \frac{\langle \Phi_0 | (e^{\hat{T}})^\dagger \hat{H}_N e^{\hat{T}} | \Phi_0 \rangle}{\langle \Phi_0 | (e^{\hat{T}})^\dagger e^{\hat{T}} | \Phi_0 \rangle}. \tag{2.37}$$

However, in contrast to HF or CI, this variational formulation is not practically feasible within CC theory. The reason lies in the non-unitary exponential parametrization of the CC wavefunction: both the numerator and the denominator in Eqn. (2.37) involve non-terminating series arising from the Taylor expansion of $e^{\hat{T}}$ and its adjoint, leading to an intractable number of terms. Despite this challenge, several efforts have been made to develop *variational coupled-cluster* (VCC) formulations, which retain the exponential ansatz while addressing its variational treatment through alternative strategies [151–153].

The projected CC approach is the standard and most widely used method for determining the amplitudes in the coupled-cluster ansatz. This approach is based on inserting the CC wavefunction into the wave equation and projecting the resulting equation onto a set of reference and excited determinants. To determine the unknown cluster amplitudes, we insert the exponential ansatz into the wave equation:

$$\hat{H} e^{\hat{T}} | \Phi_0 \rangle = E_{\mathrm{CC}} e^{\hat{T}} | \Phi_0 \rangle, \tag{2.38}$$

and then project from the left onto the reference determinant and all excited determinants $|\Phi_\mu\rangle$, yielding:

$$\langle \Phi_0 | \hat{H} e^{\hat{T}} | \Phi_0 \rangle = E_{\mathrm{CC}}, \tag{2.39}$$

$$\langle \Phi_\mu | \hat{H} e^{\hat{T}} | \Phi_0 \rangle = E_{\mathrm{CC}} t_\mu \qquad \forall \mu \neq 0. \tag{2.40}$$

This set of nonlinear equations is known as the *projected coupled-cluster equations*. However, these equations are not yet in a computationally convenient form, as the amplitude equations depend explicitly on the energy. To simplify their structure, we introduce the *similarity-transformed Hamiltonian*:

$$\overline{H} = e^{-\hat{T}} \hat{H} e^{\hat{T}}, \tag{2.41}$$

and left-multiply the original wave equation by $e^{-\hat{T}}$, yielding an effective wave equation:

$$\overline{H} | \Phi_0 \rangle = E_{\mathrm{CC}} | \Phi_0 \rangle. \tag{2.42}$$

The projected equations now become:

$$\langle \Phi_0 | \overline{H} | \Phi_0 \rangle = E_{\mathrm{CC}}, \tag{2.43}$$

$$\langle \Phi_\mu | \overline{H} | \Phi_0 \rangle = 0 \qquad \forall \mu \neq 0. \tag{2.44}$$

In this form, the amplitude equations are energy-independent and benefit from an additional important property introduced by the similarity transformation, which will be discussed shortly.

A key feature of a similarity transformation is that it preserves the spectrum of an operator, as it leaves the characteristic polynomial unchanged. However, as pointed out by Monkhorst [154], a subtle but important detail arises in this formulation. Equation (2.43) is equivalent to the variational expression in Eqn. (2.37) *only* when the cluster operator $\hat{T}$ includes all possible excitations of the system. This equivalence can be shown straightforwardly using the completeness relation.

We begin by rewriting the numerator of Eqn. (2.37) as follows:

$$\begin{aligned} \langle \Phi_0 | (e^{\hat{T}})^\dagger \hat{H} e^{\hat{T}} | \Phi_0 \rangle &= \langle \Phi_0 | (e^{\hat{T}})^\dagger e^{\hat{T}} e^{-\hat{T}} \hat{H} e^{\hat{T}} | \Phi_0 \rangle \,, \quad \text{since } e^{-\hat{T}} e^{\hat{T}} = 1 \\ &= \sum_\eta \langle \Phi_0 | (e^{\hat{T}})^\dagger e^{\hat{T}} | \Phi_\eta \rangle \, \langle \Phi_\eta | e^{-\hat{T}} \hat{H} e^{\hat{T}} | \Phi_0 \rangle \,, \end{aligned} \tag{2.45}$$

where $\{|\Phi_\eta\rangle\}$ form a complete orthonormal basis. We can now separate the contribution from the reference determinant:

$$\begin{aligned} \sum_\eta \langle \Phi_0 | (e^{\hat{T}})^\dagger e^{\hat{T}} | \Phi_\eta \rangle \, \langle \Phi_\eta | \hat{\overline{H}} | \Phi_0 \rangle &= \langle \Phi_0 | (e^{\hat{T}})^\dagger e^{\hat{T}} | \Phi_0 \rangle \, \langle \Phi_0 | \hat{\overline{H}} | \Phi_0 \rangle \\ &\quad + \sum_{\eta \neq 0} \langle \Phi_0 | (e^{\hat{T}})^\dagger e^{\hat{T}} | \Phi_\eta \rangle \, \langle \Phi_\eta | \hat{\overline{H}} | \Phi_0 \rangle \,. \end{aligned} \tag{2.46}$$

If the cluster operator $\hat{T}$ spans the full excitation space, then the projected amplitude equations (Eqn. (2.44)) are satisfied, i.e., all off-diagonal terms vanish:

$$\langle \Phi_\eta | \hat{\overline{H}} | \Phi_0 \rangle = 0 \quad \forall \eta \neq 0. \tag{2.47}$$

As a result, the numerator simplifies to:

$$\langle \Phi_0 | (e^{\hat{T}})^\dagger \hat{H} e^{\hat{T}} | \Phi_0 \rangle = \langle \Phi_0 | (e^{\hat{T}})^\dagger e^{\hat{T}} | \Phi_0 \rangle \, \langle \Phi_0 | \hat{\overline{H}} | \Phi_0 \rangle \,. \tag{2.48}$$

Substituting this back into Eqn. (2.37), we obtain:

$$E_{\mathrm{CC}} = \frac{\langle\Phi_0|(e^{\hat{T}})^\dagger e^{\hat{T}}|\Phi_0\rangle\,\langle\Phi_0|\hat{\overline{H}}|\Phi_0\rangle}{\langle\Phi_0|(e^{\hat{T}})^\dagger e^{\hat{T}}|\Phi_0\rangle} = \langle\Phi_0|\hat{\overline{H}}|\Phi_0\rangle\,, \tag{2.49}$$

which coincides precisely with Eqn. (2.43). Thus, the variational and projected expressions for the coupled-cluster energy are equivalent only in the full (complete) excitation limit. In any truncated coupled-cluster model (e.g., CCSD or CCSDT), the projected and variational energies differ.

The most important reason for using the similarity-transformed Hamiltonian in CC theory is that it can be systematically expanded using the Baker–Campbell–Hausdorff (BCH) formula [155–157]:

$$\hat{\overline{H}} = \hat{H}_N + [\hat{H}_N, \hat{T}] + \frac{1}{2}[[\hat{H}_N, \hat{T}], \hat{T}] + \frac{1}{3!}[[[\hat{H}_N, \hat{T}], \hat{T}], \hat{T}] + \frac{1}{4!}[[[[\hat{H}_N, \hat{T}], \hat{T}], \hat{T}], \hat{T}]. \tag{2.50}$$

After the fourth nested commutator, all creation and annihilation operators in $\hat{H}_N$ have already been contracted with cluster operators. Therefore, the only remaining terms are commutators between cluster operators, which commute with each other. This series *naturally truncates at the fourth commutator*. The proof of the BCH expansion is reported in Appendix B.2. We can further simplify our Hamiltonian. For example, if we take the first commutator of Eqn.(2.50), we can use Wick's theorem to write

$$\begin{aligned}
[H_N, T] &= H_N T - T H_N \\
&\overset{(2.24)}{=} \{H_N T\} + \overbrace{H_N T} - \{T H_N\} - \overbrace{T H_N} \\
&= \overbrace{H_N T}.
\end{aligned} \tag{2.51}$$

The last equality follows from two key observations. First, both the normal-ordered Hamiltonian $\hat{H}_N$ and the cluster operator $\hat{T}$ contain an *even* number of creation and annihilation operators, so their product is symmetric under permutation: $\{\hat{T}\hat{H}_N\} = \{\hat{H}_N\hat{T}\}$. Second, since $\hat{T}$ is a pure excitation operator, both $\hat{T}$ and $\hat{H}_N$ are already normal-ordered, we have $\overbrace{T H_N} = 0$. One may extend the above manipulations also for the other commutators in Eqn.(2.50). This bring us at this important statement:

The only non-vanishing contributions to the coupled cluster equations are those terms in which the normal-ordered Hamiltonian $\hat{H}_N$ is contracted at least once with the cluster operators $\hat{T}$ to its right.

which is a formulation of the *connected-cluster theorem* [158, 159]. As we will see, for the energy the normal-ordered Hamitlonian will be fully contracted with the cluster operators.

Practical CC theory always involves truncating the cluster operator (e.g., at singles and doubles, CCSD), which makes the computational cost affordable. Therefore, in the following we will use the truncated cluster operator, which reads as

$$\hat{T} = \sum_{k}^{k_{\max}} \hat{T}_k, \quad \hat{T}_k = \sum_{\mu} t_{\mu;k} \hat{\tau}_{\mu;k}. \tag{2.52}$$

where the excitation operators are restricted to act only to some maximal excitation level $k_{\max}$. While the truncation of the cluster operator is well defined (e.g., retaining only singles and doubles: $\hat{T} = \hat{T}_1 + \hat{T}_2$ in the CCSD model, for instance), the choice of the projection space is more subtle. Thanks to the exponential parametrization of the wavefunction, the inclusion of only $\hat{T}_1$ and $\hat{T}_2$ still generates higher-order excitations (triples, quadruples, etc.) in the wavefunction due to the non-linear expansion of the exponential. Therefore, in principle, one could project the similarity-transformed equation onto a space that includes triple and quadruple excitations, even if $\hat{T}_3$ and $\hat{T}_4$ are not included explicitly in $\hat{T}$. However, doing so introduces a fundamental inconsistency: the number of equations becomes larger than the number of unknown amplitudes. For instance, in the CCSD model (where only $\hat{T}_1$ and $\hat{T}_2$ are present), the number of unknowns is:

$$N_{\text{unknowns}} = \dim(\text{S}) + \dim(\text{D}), \tag{2.53}$$

but if we choose to project also onto the triples and quadruples:

$$N_{\text{equations}} = \dim(\text{S}) + \dim(\text{D}) + \dim(\text{T}) + \dim(\text{Q}), \tag{2.54}$$

where S, D, T, Q denote the respective excitation spaces. Since $\hat{T}_3 = \hat{T}_4 = 0$ in the model, the corresponding residual equations can not be satisfied in general, making the system overdetermined and hence inconsistent. Therefore, the projection space must be consistent with the truncation of the cluster operator, in order to yield a system of equations that

can be solved. For a deeper mathematical understanding of the coupled-cluster equations, the reader is referred to the work of Faulstich and Oster [160], as well as to the review by Faulstich [161]. Using this truncated cluster operator, the CC equations read as

$$E_{\mathrm{CC}} = \langle \Phi_0 | \hat{\overline{H}} | \Phi_0 \rangle \,, \qquad \hat{\overline{H}} = e^{-\hat{T}} \hat{H}_N e^{\hat{T}}, \tag{2.55}$$

$$0 = \langle \Phi_{\mu;k} | \hat{\overline{H}} | \Phi_0 \rangle \,, \qquad |\Phi_{\mu;k}\rangle = \hat{\tau}_{\mu;k} \, |\Phi_0\rangle \,, \quad k \leq k_{\max} \tag{2.56}$$

As pointed out by Koch and Jørgensen [162], summing up Eqn. (2.55) and Eqn. (2.56) we get

$$\langle \Phi_{\mathrm{L}} | \hat{\overline{H}} | \Phi_{\mathrm{R}} \rangle = E_{\mathrm{CC}}, \quad |\Phi_{\mathrm{R}}\rangle = |\Phi_0\rangle \,, \quad \langle \Phi_{\mathrm{L}}| = \langle \Phi_0| + \sum_{\mu,k} \bar{t}_{\mu;k} \langle \Phi_{\mu;k}| \,, \tag{2.57}$$

$$\langle \Phi_{\mathrm{L}} | \Phi_{\mathrm{R}} \rangle = 1, \tag{2.58}$$

which clearly shows the non-Hermitian nature of the similarity-transformed Hamiltonian, since it has different right- and left- eigenvectors. The coefficients $\bar{t}_{\mu;k}$ can be in principle determined by solving the left-eigenvalue problem

$$\langle \Phi_L | \, \hat{\overline{H}} = E_{\mathrm{CC}} \, \langle \Phi_L | \,, \tag{2.59}$$

by projecting it onto $|\Phi_{\mu;k}\rangle$

$$\langle \Phi_L | \hat{\overline{H}} | \Phi_{\mu;k} \rangle = E_{\mathrm{CC}} \bar{t}_{\mu;k} \tag{2.60}$$

where we also see that we get an energy-dependent equation. However, since left and right eigenvectors share the same eigenvalue (the CC energy) we may simply consider the right-eigenvalue problem. As we will see in the next chapter, the left-eigenvalue problem is connected to the computation of properties.

One of the early successes was the Coupled Cluster with Single and Double excitations (CCSD) method ($k_{\max} = 2$), where single and double excitations are included iteratively [163], later extended to include higher-level excitations like triple (CCSDT) ($k_{\max} = 3$) [164–166], quadruple (CCSDTQ) ($k_{\max} = 4$) [167], and quintuple (CCSDTQP) ($k_{\max} = 5$) excitations [168]. The challenge with these extensions is the substantial increase in computational cost. A more cost-effective approach to include triple excitations was proposed by Noga *et al.* [164, 169], who developed the CCSDT-n family of methods, each differing

in the extent of evaluating the $\hat{T}_3$ amplitudes. An improved balance between computational cost and accuracy is achieved by methods that treat higher-order excitations perturbatively rather than iteratively. The most notable of these is the CCSD(T) method [170–173], in which single and double excitations are computed iteratively, and triple excitations are included using many-body perturbation theory. This approach provides all fourth-order corrections to CCSD and for any chosen reference determinant. Following this, similar methods have been extended to handle quadruple, quintuple, and sextuple excitations [170, 174–176].

One may wonder about the behavior of truncated coupled-cluster energies as the excitation level increases. Unlike truncated CI, truncated coupled-cluster models are not variational, and it is therefore not completely obvious how the energy should improve with excitation rank. Nevertheless, as illustrated in Figure 13.3 of Ref. [141], the CC energies decrease in a rather systematic manner, and at each truncation level the error is significantly smaller than that of the corresponding CI model. This is particularly reassuring, since the non-variational character of truncated CC provides no guarantee of such a regular convergence pattern.

We conclude this section with the following statement, as explicitly noted by Crawford [177],

> "While normal ordering, Wick's theorem, and the particle-hole formalism have substantially reduced the effort required to derive the (...) equations relative to the direct application of the second quantization anti-commutation relations, they do not go far enough by-hand derivations — especially if we wish to go beyond the CCSD approximation, or into other aspects of coupled cluster, such as excited states, analytic gradients, response properties, etc."

Therefore, in the next section, we will discuss the diagrammatic techniques that have been explicitly used in this thesis work to derive the CC equations and molecular properties.

2.4 The diagrammatic approach

Diagrammatic methods have long served as a cornerstone for the development of theoretical models in physics and chemistry. Quantum electrodynamics, the quantum theory

of electromagnetic interactions, faced enormous calculations challenges in the 1940s. Divergent integrals and the sheer number of terms arising at higher orders of perturbation theory demanded a more organized approach. The advent of diagrammatic techniques can be attributed to the seminal work of Feynman [178], who introduced Feynman diagrams to provide an intuitive and calculationally efficient method to evaluate scattering amplitudes in QED. Dyson [179] subsequently formalized the connection between Feynman diagrams and the perturbative expansion of the S-matrix. Each Feynman diagram corresponds to a mathematical term in the perturbation expansion, with specific rules governing vertices (interactions), lines (propagators), and loops (internal degrees of freedom). Inspired by developments in QED, many-body physicists adapted diagrammatic techniques to tackle problems in nuclear and condensed matter systems. Brueckner [180] and Goldstone [181] independently developed linked-cluster expansions, demonstrating that only connected diagrams contribute to observable quantities such as the ground-state energy. This realization culminated in the formulation of the *linked-cluster theorem*, a fundamental result ensuring size-extensivity—a necessary condition for the accurate description of extensive systems. Goldstone [181] introduced a time-dependent perturbation theory formalism using diagrams, later termed *Goldstone diagrams*. Simultaneously, Hugenholtz [182] developed an equivalent approach.

The CC equations can be formulated within the diagrammatic framework. In this thesis, we will use the antisymmetrized Goldstone diagrammatic formalism, as developed and popularized by Kucharski and Bartlett.

2.4.1 Diagrammatic rules

In this subsection, I present, in a schematic way, the set of rules used for the construction and interpretation of CC diagrams. It is important to emphasize that, although these rules are often applied in a learning-by-doing fashion, they are grounded in a well-established mathematical framework. Readers with a more mathematical inclination can find detailed derivations and proofs of these rules in Ref. [183]. Moreover, the coupled cluster diagrams have been generated using the `ccdiag` package [184], developed by Daniel Kats. This LaTeXpackage relies on TikZ/PGF vector graphics and represents diagrams as directed graphs. The sources that I used are listed in the bibliography [140, 142].

Determinants

The matrix elements we wish to evaluate are composed of three fundamental ingredients: determinants (in the bra and the ket), operators, and the contractions between them. We begin by representing the determinants, again employing the particle–hole formalism discussed above. The reference determinant, $|\Phi_0\rangle$, is not shown diagrammatically since it contains no internal excitations. What interests us here is the representation of excited determinants. Upward and downward lines in Figure 2.5 mark orbitals that differ from the reference determinant $|\Phi_0\rangle$. Downward arrows denote holes (occupied in $|\Phi_0\rangle$), upward arrows denote particles (unoccupied in $|\Phi_0\rangle$). Thus, the third diagram represents a single excitation from φ_i to φ_a.

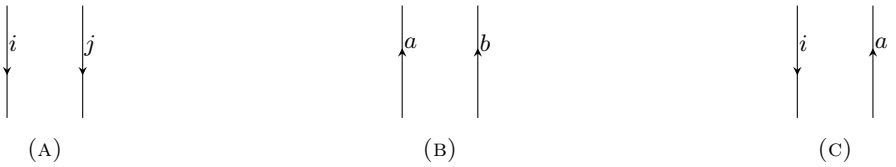

FIGURE 2.5: Coupled cluster diagrammatic topologies for excitation operators: (a) two-hole diagram representing the removal of electrons from occupied orbitals φ_i and φ_j; (b) two-particle diagram representing the addition of electrons into virtual orbitals φ_a and φ_b; (c) mixed hole–particle diagram representing a single excitation from occupied orbital φ_i to virtual orbital φ_a.

Normal-ordered Hamiltonian

We recall the normal-ordered Hamiltonian definition

$$\hat{H}_N = \hat{F}_N + \hat{V}_N = \sum_{pq} f_{pq}\{a_p^\dagger a_q\} + \frac{1}{4}\sum_{pqrs} V_{pqrs}\{a_p^\dagger a_q^\dagger a_s a_r\} \tag{2.61}$$

We shall start by the normal-ordered Fock operator. All the possible combinations of creation/annihilation operators are

$$\begin{aligned}\hat{F}_N = &\sum_{ij} f_{ij}\{a_i^\dagger a_j\} + \sum_{ia} f_{ia}\{a_i^\dagger a_a\} \\ &+ \sum_{ai} f_{ai}\{a_a^\dagger a_i\} + \sum_{ab} f_{ab}\{a_a^\dagger a_b\}\end{aligned} \tag{2.62}$$

- The *hole–hole* term $f_{ij}\{a_i^\dagger a_j\}$ and the *particle–particle* term $f_{ab}\{a_a^\dagger a_b\}$ both preserve the net number of excitations (they act entirely within the occupied or the virtual space, respectively).
- The mixed term $f_{ia}\{a_i^\dagger a_a\}$ lowers the excitation level by -1 (it removes an electron from occupied i and creates one in virtual a).
- The mixed term $f_{ai}\{a_a^\dagger a_i\}$ raises the excitation level by $+1$ (it removes an electron from virtual a and creates one in occupied i).

The one-body Fock operator $\hat{F}_N$, characterized by matrix elements f_{pq}, is represented as a single vertex with one incoming and one outgoing line. To distinguish it from other interactions introduced later, a cross ("X") is placed at the interaction vertex, and the corresponding interaction line is drawn as a dashed line. Therefore, the four contributions of Eqn.(2.62) can be draw as

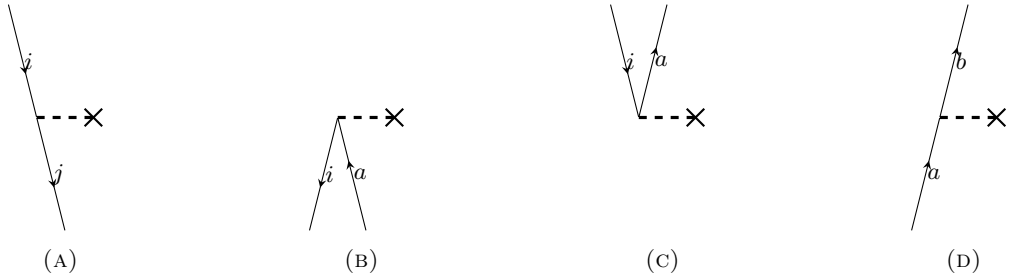

FIGURE 2.6: Diagrammatic representation of the four terms in the normal-ordered Fock operator $\hat{F}_N$ of Eqn. (2.62). Each vertex (marked with a cross) corresponds to a matrix element f_{pq}, with a single incoming and outgoing line representing the annihilation and creation operators. Diagrams (a) and (d) correspond to excitation-preserving contributions within the occupied (f_{ij}) and virtual (f_{ab}) subspaces, respectively. Diagram (b) lowers the excitation level by one (f_{ia}), while diagram (c) raises it by one (f_{ai}).

For the two-electron interaction, we have more terms

$$\begin{aligned}\hat{V}_N = &\frac{1}{4}\sum_{abcd}\langle ab||cd\rangle\,\{a_a^\dagger a_b^\dagger a_d a_c\} + \frac{1}{4}\sum_{ijkl}\langle ij||kl\rangle\,\{a_i^\dagger a_j^\dagger a_l a_k\}\\ &+\frac{1}{2}\sum_{aibc}\langle ai||bc\rangle\,\{a_a^\dagger a_i^\dagger a_c a_b\} + \frac{1}{2}\sum_{ijka}\langle ij||ka\rangle\,\{a_i^\dagger a_j^\dagger a_a a_k\}\\ &+\frac{1}{2}\sum_{abci}\langle ab||ci\rangle\,\{a_a^\dagger a_b^\dagger a_i a_c\} + \frac{1}{2}\sum_{iajk}\langle ia||jk\rangle\,\{a_i^\dagger a_a^\dagger a_j a_k\}\\ &+\frac{1}{4}\sum_{abij}\langle ab||ij\rangle\,\{a_a^\dagger a_b^\dagger a_j a_i\} + \frac{1}{4}\sum_{ijab}\langle ij||ab\rangle\,\{a_i^\dagger a_j^\dagger a_b a_a\}\\ &+\sum_{iabj}\langle ia||bj\rangle\,\{a_i^\dagger a_a^\dagger a_j a_b\},\end{aligned} \tag{2.63}$$

where the prefactors in the algebraic expression of Eqn.(2.63) arise from the antisymmetry of the operator and the corresponding electron exchange. These prefactors account for redundancies in the terms due to the indistinguishability of identical fermions, ensuring each unique physical interaction is counted only once. Again, we should note that

- The first two terms and the last one of Eqn.(2.63) preserve the net number of excitations;
- The third and fourth lower the excitation level by -1;
- The fifth and sixth raise the excitation level by +1;
- The seventh raise the excitation level by +2;
- The eighth lower the excitation level by -2.

The two-electron operator in diagrammatic representations is typically denoted by a dashed horizontal line. Lines connected to this interaction line represent the orbitals involved. All the diagrams for $\hat{V}_N$ are reported in Figure 2.7. In principle, additional diagrams for the two-electron operator could be generated. However, as previously mentioned, by exploiting the permutational symmetry of the two-electron integrals, all newly generated diagrams can be reduced to one of the nine diagrams shown in the figure.

Cluster operators

The excitation operators $\hat{T}$ are typically represented in diagrams using solid interaction lines. Each excitation level of the operator corresponds to a vertex with one incoming and one outgoing line per excitation. Since these are excitation operators, the incoming lines are associated with hole (occupied) states, while the outgoing lines correspond to particle (virtual) states. This convention reflects the nature of the excitation process: electrons are excited from occupied orbitals (holes) to virtual orbitals (particles). For example, a single excitation operator $\hat{T}_1$ is represented by a vertex with one incoming hole line and one outgoing particle line. A double excitation operator $\hat{T}_2$ would have two vertexes with one incoming hole line and one outgoing particle line for each, and so on for higher excitations.

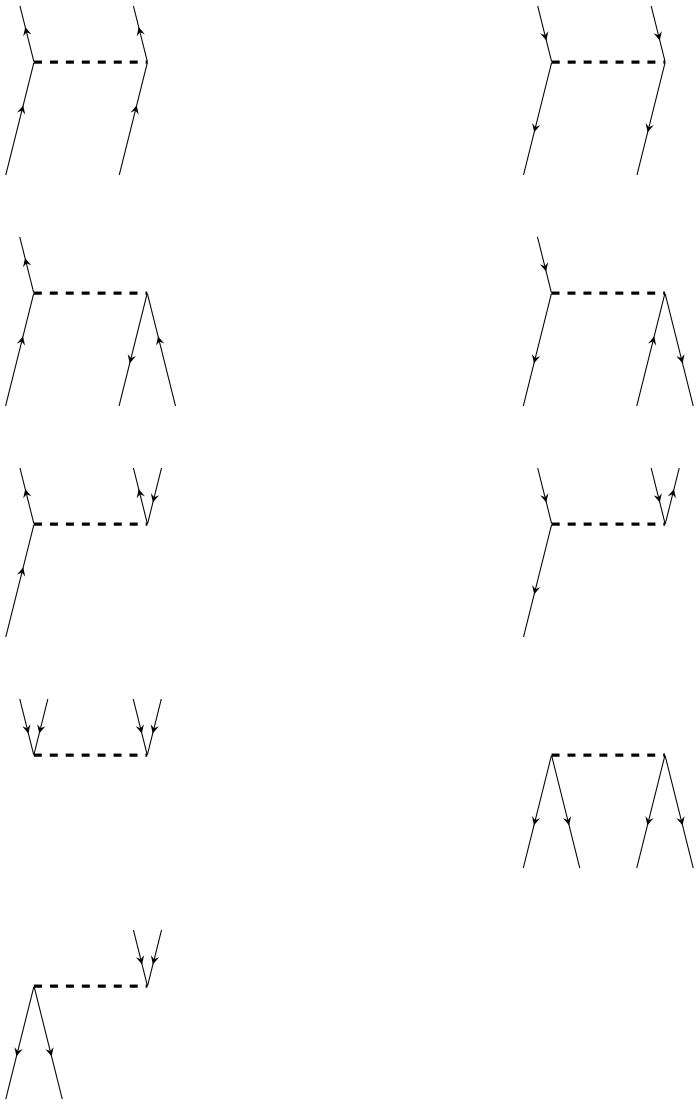

FIGURE 2.7: Normal-ordered two-electron operator $\hat{V}_N$ in diagrammatic form. In order, each diagram in the figure corresponds to each term in Eqn.(2.63).

(A) (B)

FIGURE 2.8: Diagrammatic representation of the $\hat{T}$ operators. Here, (A) represents the single excitation operator $\hat{T}_1$, while (B) corresponds to the double excitation operator $\hat{T}_2$.

Matrix elements

Our goal is to employ diagrammatic techniques to compute the matrix elements arising from the Eqn.(2.43) and Eqn.(2.44). We have previously discussed that, in general, these equations can be formally solved by performing contractions between the Hamiltonian

operator and the cluster operators. In this context, each algebraic contraction is associated with a diagrammatic *connection* between the Hamiltonian and the cluster operators. Moreover, as we have emphasized before, the same contraction logic applies: the only diagrams that will contribute to the CC equations are those in which the Hamiltonian is connected at least once to every cluster operator present (up to four, in accordance with Eqn.(2.50)).

Each diagram represents a matrix element

$$\langle \Phi_\mu | \, \hat{\overline{H}} \, | \Phi_\nu \rangle$$

between two determinants, with the bottom and top of the diagram corresponding to the ket (Φ_ν) and bra (Φ_μ) states, respectively. If the reference determinant Φ_0 appears on the right, no external lines may emanate from the bottom of the diagram. If Φ_0 appears on the left, no external lines may reach the top. Conversely, if the matrix element involves excited determinants, the diagram must contain the appropriate number of external particle and hole lines at the bottom and/or top, matching the excitation level of the bra and ket states. From these simple considerations, it is clear that the CC energy equation (Eqn. (2.43)) corresponds to *closed* diagrams, i.e., diagrams with no external lines. In contrast, the amplitude equations (Eqn. (2.44)) involve diagrams with e*upwards* lines, corresponding to the excited bra states on the left-hand side of the matrix elements.

We now begin to introduce the rules required for constructing the diagrams, and subsequently their algebraic formulation. These rules can be found in different references, such as the Bartlett and Shavitt book [142] as well the review by Crawford [177]. In the meantime, we report in Table(2.1) the list of rules that are used. Subsequently, with reference to the CCSD method, we will provide specific examples to clarify the procedure.

example: CCSD energy via diagrammatic techniques

First, we must note that, in order for a matrix element to be non-zero, the total excitation rank generated by the operators acting on the reference must match the excitation level of the bra determinant. This follows from the orthogonality of Slater determinants with different excitation levels. As an example, we may consider the CCSD approximation,

Diagrammatic Rules

Rule 1. Each interaction diagram is associated with a corresponding matrix element. For a general multi-index case, the matrix element can be written as

$$\Omega^{o_1,o_2,\ldots,o_n}_{i_1,i_2,\ldots,i_n},$$

where the sets of outgoing orbitals $\{o_1,\ldots,o_n\}$ correspond to the superscripts, and the sets of incoming orbitals $\{i_1,\ldots,i_n\}$ correspond to the subscripts.

Rule 2. All *internal lines*—that is, lines that connect two vertices within the diagram and do not extend to the top or bottom—must be summed over. This corresponds to a summation over the orbital indices associated with these internal particle or hole lines.

Rule 3. The overall sign of a diagram is given by $(-1)^{h+l}$, where h is the number of hole lines and l is the number of loops. A loop is defined as a path along directed lines that either returns to its starting point or begins and ends on external lines located on the same side of the diagram.

Rule 4. Whenever a diagram contains k or more lines that are *equivalent*—that is, they start and end at the same interaction vertices—a symmetry factor must be included in the algebraic expression. Specifically, for each set of k equivalent lines, a prefactor of $1/k!$ is applied to account for overcounting due to line permutations.

Rule 5. Any two diagrams that differ only by a permutation of internal lines connecting the same Hamiltonian vertex to the same cluster operator are considered *topologically equivalent*, and therefore contribute identically to the algebraic expression. Such diagrams must be included only *once* in the final expression to avoid overcounting.

Rule 6. Each set of k equivalent vertices—defined as operator interaction lines connected to other vertices with identical patterns of hole and particle lines—contributes a symmetry factor of $\frac{1}{k!}$ to the algebraic expression.

Rule 7. Each pair of distinct external hole or particle lines on the same side of the diagram introduces a permutation operator to ensure antisymmetry. Distinct pairs are those attached to different interaction vertices, where exchanging lines alters more than just the sign. For two sets of distinct external lines $X = \{p, q, \ldots\}$ and $Y = \{r, s, \ldots\}$ on the same side of the diagram, introduce the permutation operator

$$P\big(X/Y\big) \;=\; \sum_{p\in X}\sum_{r\in Y} P(p/r)\,,$$

which exchanges each line in X with each line in Y individually—without permuting lines within X or within Y. This guarantees antisymmetry under any single swap between the two sets.

Table 2.1: Summary of the diagrammatic rules used to evaluate matrix elements in the coupled-cluster framework. Each rule governs the construction, interpretation, and sign of the diagrams contributing to energy, amplitude equations, and properties.

where we have only $\hat{T} = \hat{T}_1 + \hat{T}_2$. The CCSD energy looks like

$$E_{\text{CCSD}} = \langle \Phi_0 | (\hat{H}_N e^{(\hat{T}_1 + \hat{T}_2)})_{\mathcal{C}} | \Phi_0 \rangle \tag{2.64}$$

where we used the notation $\mathcal{C}$ to indicate that only the connected diagrams are considered. By using the BCH expansion we get

$$\begin{aligned}
\left(\hat{H}_N e^{\hat{T}_1 + \hat{T}_2}\right)_{\mathcal{C}} &= \hat{H}_N + \left(\hat{H}_N \hat{T}\right)_{\mathcal{C}} + \frac{1}{2}\left(\hat{H}_N \hat{T} \hat{T}\right)_{\mathcal{C}} + \cdots && (2.65)\\
&= \hat{H}_N + (\hat{H}_N \hat{T}_1)_{\mathcal{C}} + (\hat{H}_N \hat{T}_2)_{\mathcal{C}} + \frac{1}{2}(\hat{H}_N \hat{T}_1 \hat{T}_1)_{\mathcal{C}} + (\hat{H}_N \hat{T}_1 \hat{T}_2)_{\mathcal{C}} && (2.66)\\
&\quad + \frac{1}{2}(\hat{H}_N \hat{T}_2 \hat{T}_2)_{\mathcal{C}} + \cdots && (2.67)
\end{aligned}$$

It is important to emphasize that in the CCSD energy expression the bra is the reference determinant, $\langle \Phi_0 |$. Hence, the combined action of the Hamiltonian and cluster operators must ultimately reproduce the reference determinant. By definition, excitation operators carry positive excitation rank—namely $+1$ for $\hat{T}_1$ and $+2$ for $\hat{T}_2$. We have seen that the $\hat{F}_N$ operator can de-excite by at most -1, while the $\hat{V}_N$ operator can de-excite by at most -2. Therefore, any term that produces a ket with excitation rank greater than 2 can not have a nonzero overlap with $\langle \Phi_0 |$, and thus does not contribute to the CCSD energy. We conclude that the only matrix element that can contribute to the CCSD are

$$E_{\text{CCSD}} = \langle \Phi_0 | (\hat{H}_N \hat{T}_1)_{\mathcal{C}} | \Phi_0 \rangle + \frac{1}{2} \langle \Phi_0 | (\hat{H}_N \hat{T}_1^2)_{\mathcal{C}} | \Phi_0 \rangle + \langle \Phi_0 | (\hat{H}_N \hat{T}_2)_{\mathcal{C}} | \Phi_0 \rangle , \tag{2.68}$$

where we omitted the expectation value involving the normal-ordered Hamiltonian, which, by definition in Eqn.(2.29), evaluates to zero. Let's pick up the first term of Eqn.(2.68)

$$\langle \Phi_0 | (\hat{H}_N \hat{T}_1)_{\mathcal{C}} | \Phi_0 \rangle \overset{(2.29)}{=} \langle \Phi_0 | (\hat{F}_N \hat{T}_1)_{\mathcal{C}} | \Phi_0 \rangle + \langle \Phi_0 | (\hat{V}_N \hat{T}_1)_{\mathcal{C}} | \Phi_0 \rangle \tag{2.69}$$

- For the matrix element $\langle \Phi_0 | (\hat{F}_N \hat{T}_1)_{\mathcal{C}} | \Phi_0 \rangle$, the cluster operator $\hat{T}_1$ creates a singly excited determinant on the right. To return to the reference determinant Φ_0 on the left, the Fock operator $\hat{F}_N$ must de-excite the determinant by one. Looking at Figure 2.6 we take the second diagram (B) and me make the connections with the $\hat{T}_1$ operator, giving the following diagram

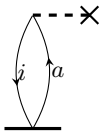

We can now obtain the algebraic expression corresponding to this diagram by applying the rules defined in Table (2.1). According to **Rule 1.**, the Fock interaction line features an incoming line labeled a and an outgoing line labeled i, leading to a matrix element f_a^i. For the cluster operator $\hat{T}_1$, we instead have an incoming line i and an outgoing line a, resulting in a matrix element t_i^a. Then, by applying **Rule 2.**, we see that both i and a are internal lines and therefore must be summed up. To determine the sign, we apply **Rule 3.**, noting that there is one closed loop and one hole line. The resulting sign is therefore $(-1)^{1+1} = +1$. We conclude that the algebraic expression corresponding to the diagram is

$$\langle \Phi_0 | (\hat{F}_N \hat{T}_1)_{\mathcal{C}} | \Phi_0 \rangle = \sum_{ia} f_a^i t_i^a, \tag{2.70}$$

which is consistent from the point of view of index contraction: since the energy is a scalar quantity and the indices i and a are both summed over, the final result is indeed a scalar. It is worth to note that by applying Wick's theorem on this matrix element we get

$$\begin{aligned}
\langle \Phi_0 | (\hat{F}_N \hat{T}_1)_{\mathcal{C}} | \Phi_0 \rangle &= \sum_{pq} f_{pq} \sum_{ia} t_i^a \, \langle \Phi_0 | \{ a_p^\dagger a_q a_a^\dagger a_i \} | \Phi_0 \rangle \\
&\overset{(2.24)}{=} \sum_{pq} f_{pq} \sum_{ia} t_i^a \, \langle \Phi_0 | \{ \overbrace{a_p^\dagger a_q a_a^\dagger} a_i \} | \Phi_0 \rangle \\
&= \sum_{pq} f_{pq} \sum_{ia} t_i^a \delta_{pi} \delta_{qa} \\
&= \sum_{ia} f_a^i t_i^a,
\end{aligned} \tag{2.71}$$

which is exactly Eqn.(2.70).

- For the matrix element $\langle \Phi_0 | (\hat{V}_N \hat{T}_1)_{\mathcal{C}} | \Phi_0 \rangle$, the cluster operator $\hat{T}_1$ generates a singly excited determinant on the right. In order to return to the reference determinant Φ_0 on the left, the operator $\hat{V}_N$ must de-excite the determinant by one. By inspecting Figure(2.7), we see that only the third and fourth diagrams correspond to such a de-excitation. In principle, therefore, connections involving these diagrams could

contribute. However, in both cases, there are open lines on the left side of the diagram, which is not allowed, since energy diagrams must be fully closed.

The second term in Eqn.(2.68) is

$$\frac{1}{2}\langle\Phi_0|(\hat{H}_N\hat{T}_1^2)_{\mathcal{C}}|\Phi_0\rangle = \frac{1}{2}\underbrace{\langle\Phi_0|(\hat{F}_N\hat{T}_1^2)_{\mathcal{C}}|\Phi_0\rangle}_{=0} + \frac{1}{2}\langle\Phi_0|(\hat{V}_N\hat{T}_1^2)_{\mathcal{C}}|\Phi_0\rangle\,. \tag{2.72}$$

The contribution involving the Fock operator vanishes. This is because the operator $\hat{T}_1^2$ generates a doubly excited determinant, while the Fock operator $\hat{F}_N$ can at most de-excite by one level. As a result, it is not capable of bringing the system back to the reference determinant $|\Phi_0\rangle$, and the corresponding matrix element is zero. The term which includes $\hat{V}_N$ is more interesting, and since there is only one diagram that is associated to a global de-excitation -2 (the eight of Figure 2.7)) we can only create one diagram. By applying

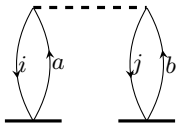

Rule 1., we observe that for the two-electron interaction operator, the lines labeled a and b are incoming, while i and j are outgoing. This corresponds to the antisymmetrized matrix element V_{ab}^{ij}. For the cluster operators, we have the amplitudes t_i^a and t_j^b. All the lines in the diagram are internal, and thus, according to **Rule 2.**, all indices are summed over. Additionally, there are two closed loops and two hole lines (i and j), leading to a sign factor of $(-1)^{2+2} = +1$, as prescribed by **Rule 3.**. Finally, we note that the two cluster vertices are equivalent. Therefore, in accordance with **Rule 6.**, a symmetry factor of $1/2$ must be included. The final algebraic expression for the diagram is thus given by

$$\frac{1}{2}\langle\Phi_0|(\hat{V}_N\hat{T}_1^2)_{\mathcal{C}}|\Phi_0\rangle = \frac{1}{2}\sum_{ijab} V_{ab}^{ij} t_i^a t_j^b. \tag{2.73}$$

We may continue with the third term of Eqn.(2.68) where again, since we have a double excitation, only the bi-electronic operator may contribute. Again, picking up the eight diagram of Figure 2.7 and using the diagrammatic form defined for $\hat{T}_2$ and connecting both we get Following the reasoning from the previous diagrams, using **Rule 1.** we obtain the matrix element V_{ab}^{ij} and the amplitude t_{ij}^{ab}. Also in this case, all lines are internal, so according to **Rule 3.**, the sign remains positive. We further note that there are two pairs

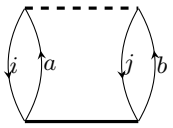

of equivalent lines — a with b, and i with j — which leads, by **Rule 4.**, to a symmetry factor of $\frac{1}{2!} \times \frac{1}{2!} = \frac{1}{4}$. The final expression is therefore given by

$$\frac{1}{2} \langle \Phi_0 | (\hat{V}_N \hat{T}_1^2)_C | \Phi_0 \rangle = \frac{1}{4} \sum_{ijab} V_{ab}^{ij} t_{ij}^{ab}. \tag{2.74}$$

We conclude that the CCSD energy expression reads

$$E_{\text{CCSD}} = \sum_{ia} f_a^i t_i^a + \frac{1}{2} \sum_{ijab} V_{ab}^{ij} t_i^a t_j^b + \frac{1}{4} \sum_{ijab} V_{ab}^{ij} t_{ij}^{ab} \tag{2.75}$$

We close this part by noting that the above expression remains unchanged even in higher-order coupled cluster methods. This is because cluster operators involving more than two-body excitations do not contribute directly to the energy expression: as previously discussed, the Hamiltonian operator contains at most two-body interactions, and thus cannot de-excite a determinant by more than two levels. However, the effect of higher-order excitations does appear in the amplitude equations, since in that case the bra state is not the reference $\langle \Phi_0 |$, but rather an excited determinant. As the energy ultimately depends on the amplitudes, it will still be indirectly affected by higher-order excitations through their influence on the solutions of the amplitude equations.

The amplitude equations are, in principle, derived using the same diagrammatic strategy discussed above for the energy expression. However, it is clear that the number of contributing terms is significantly larger. This increase arises because, unlike in the energy expression where only fully contracted (closed) diagrams contribute, the amplitude equations involve projection onto excited determinants. As a result, one must consider all diagrams that produce the appropriate excitation level in the bra state, including partially contracted terms and a wider variety of topologies. For this reason, the full set of diagrams contributing to the amplitude equations up to the CCSDT level is provided in Ref. [142].

2.5 Intermediates

Coupled cluster (CC) theory is renowned for its high accuracy in describing electron correlation, but this accuracy comes at a steep computational price. Even at the CCSD level (singles and doubles), the most expensive tensor contractions formally scale as $\mathcal{O}(N^8)$, where N denotes the total number of spin orbitals, i.e., the sum of occupied and virtual orbitals. For medium-sized molecules, the number of operations and memory requirements quickly become prohibitive. A naïve, direct translation of the diagrammatic or algebraic expressions into code would result in significant computational redundancy and an impractical scaling with system size. To address this, it is standard practice to introduce *intermediates*, that is, quantities which encapsulate repeated sub-expressions and allow the reuse of partial results across multiple terms.

The idea of intermediates originates from two key observations:

- Many terms in the CC amplitude equations share common tensor contractions. Recomputing these redundantly increases computational cost.
- By factoring out these repeated contractions and storing the results, the number of floating-point operations and the number of memory accesses can be significantly reduced.

Formally, in CC, an intermediate is defined as a tensor resulting from the contraction of Hamiltonian elements (Fock matrix or two-electron integrals) with cluster amplitudes $t_i^a, t_{ij}^{ab}, \ldots$. As an example, we consider one specific term from the T_2–equations:

$$X_{ij}^{ab} = \frac{1}{4} \sum_{klcd} \langle kl||cd\rangle \; t_{ij}^{cd} \, t_{kl}^{ab}, \tag{2.76}$$

which naïvely scales as $\mathcal{O}(o^4 v^4)$, where o denotes the number of occupied orbitals and v the number of virtual orbitals. If $N = o + v$, this corresponds roughly to $\mathcal{O}(N^8)$. To reduce this cost, we introduce the intermediate

$$W_{ij}^{kl} = \sum_{cd} \langle kl||cd\rangle \; t_{ij}^{cd}, \tag{2.77}$$

which costs only $\mathcal{O}(o^2v^4)$ to form. Once W_{ij}^{kl} is available, the original term can be rewritten as

$$X_{ij}^{ab} = \frac{1}{4}\sum_{kl} W_{ij}^{kl}\, t_{kl}^{ab}, \tag{2.78}$$

Thus, the overall cost of evaluating X_{ij}^{ab} becomes

$$\underbrace{\mathcal{O}(o^2v^4)}_{\text{forming } W} + \underbrace{\mathcal{O}(o^2v^4)}_{\text{contracting with } t} \approx \mathcal{O}(N^6), \tag{2.79}$$

instead of $\mathcal{O}(N^8)$. Thus, the introduction of intermediates lowers the computational scaling by roughly two powers of the system size.

The introduction of intermediates brings several practical benefits:

1. **Reduced operation count**: Reusing intermediates avoids recomputation of repeated tensor contractions, lowering the asymptotic scaling of the method.
2. **Modularity and maintainability**: Structuring the equations in terms of intermediates simplifies the code, facilitates debugging, and enables easier extension to higher-level methods (e.g., CCSDT, CCSDTQ).

2.6 High-order excitations

The inclusion of high-order excitations—namely triple (T_3), quadruple (T_4), and higher excitation operators—in the CC framework is crucial for achieving high accuracy in correlated electronic structure calculations. While CC with singles and doubles (CCSD) captures a large portion of the dynamic correlation energy, certain molecular properties, such as reaction barriers [185], noncovalent interactions [186], and spectroscopic constants [187], can exhibit significant sensitivity to the contribution of higher excitations. Systems with strong multireference character or near-degeneracy effects often require these contributions to avoid qualitative failures [188, 189]. The canonical example is the breaking of chemical bonds, where triple and quadruple excitations become increasingly important as static correlation grows.

From a perturbative standpoint, the leading correction beyond CCSD is typically the inclusion of triple excitations. The popular CCSD(T) method incorporates a non-iterative

treatment of T_3 amplitudes and is often referred to as the gold standard of quantum chemistry due to its excellent accuracy-to-cost ratio [172]. However, for systems where perturbative treatment is insufficient—such as stretched geometries [17, 167]—an iterative treatment of triples (CCSDT), and in some cases even quadruples (CCSDTQ), becomes necessary.

The derivation and implementation of high-order excitation operators pose significant theoretical and computational challenges:

- **Extremely complex equations:** The number of terms grows combinatorially with the excitation level, leading to hundreds or even thousands of contributions that must be accounted for explicitly.
- **Nontrivial definition of intermediates:** Identifying efficient intermediates to reduce computational scaling and redundancy is far from straightforward and often requires significant insight into the structure of the equations.
- **High risk of errors due to term and index proliferation:** The large number of similar-looking terms and repeated index patterns makes the manual derivation and implementation error-prone.
- **Challenging debugging phase:** Due to the absence of analytical benchmarks and the sheer complexity of the equations, detecting and correcting implementation bugs is often time-consuming and difficult.

Equations in high-order coupled cluster theory become too complex for manual manipulation. Diagrammatic approaches help identify equivalent terms, but symbolic automation is essential for tasks like intermediate optimization and implementing method variants.

To address these, a variety of automation tools have been developed to assist in the derivation and implementation of coupled-cluster equations. These tools can be broadly categorized by their underlying formalism: some are based on the algebra of second quantization [26, 27], others employ the generalized Wick's theorem for systematic expansion [16, 19–22, 24, 25], and many utilize diagrammatic techniques for visualizing and organizing the contributing terms [17, 23]. Modern algebraic frameworks and code generators, such as `Smith3` [23, 190], `GeCCo` [20], and `MRCC` [17, 191], have greatly streamlined the development of high-level coupled-cluster methods by automating much of this process.

However, even with such automation, the computational cost associated with evaluating and solving the resulting equations remains the principal limitation for practical applications.

Recently, the `tenpi` [28, 192] framework has been introduced as a modular and extensible platform that unifies symbolic derivation, intermediate optimization, and backend-agnostic tensor contractions. By integrating advanced algebraic tools and supporting both CPU and GPU architectures, `tenpi` aims to make the implementation and execution of high-order coupled-cluster methods more accessible and efficient.

Since the primary goal of this thesis is the generation of expectation values at arbitrary CC level using the `tenpi` toolchain, the next subsection will be devoted to providing some general aspects of how `tenpi` operates.

2.6.1 tenpi: Tensor Programming Interface

`tenpi` is an open-source modular framework for high-order coupled cluster code generation [28, 192]. It provides diagrammatic derivation, symbolic algebra, intermediate optimization, and visualization tools, with support for multiple tensor backends. Designed for efficient use on GPU-based HPC platforms, `tenpi` systematically generates tensor contractions optimized. It integrates with the ExaCorr [193] module of DIRAC [29], enabling massively parallel relativistic CC calculations using the ExaTENSOR library [194].

Most automatic CC code generators are based on formula derivation, their optimization, and the mapping to binary tensor contractions of a math library (as well `tenpi`).

Generation of the CC equations

`tenpi` is based on the diagrammatic scheme introduced by Kállay and Surján [17], where each diagram is represented as a sequence of 13 integers. The last integer designates one of the 13 possible diagrammatic representations of the normal-ordered Hamiltonian. As shown in Eqn.(3.18), the similarity-transformed Hamiltonian is naturally truncated at the fourth commutator, meaning it can be contracted with up to four different cluster operators. The remaining 12 integers are divided into four triplets, each representing a connection (i.e., a contraction in the language of Wick's theorem) between the Hamiltonian

and the $\hat{T}$ operators. In each triplet, the first index represents the excitation level of the cluster operator, the second indicates the number of connections between the Hamiltonian and this cluster operator, and the third denotes the number of particle (virtual) lines used to connect them. A schematic sketch is presented in Figure 2.12. This integer-string representation efficiently generates distinct connected diagrams and identifies equivalent ones, as two diagrams are equivalent up to a sign if their strings are identical. An example is reported in Figure 2.13. See Ref. [17] for the original and complete algorithm.

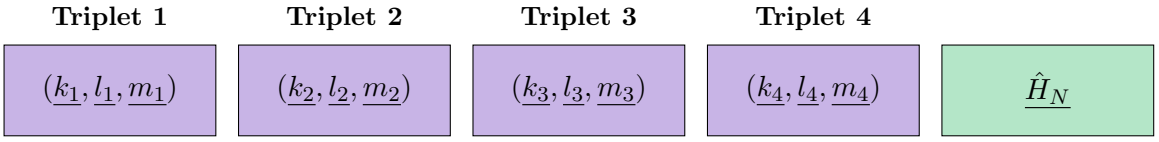

FIGURE 2.12: Schematic representation of the 13-integer string representation used in `tenpi`. The last integer specifies the diagrammatic representation of the normal-ordered Hamiltonian. The first 12 integers are grouped into four triplets, each encoding the excitation level of the corresponding cluster operator ($k_i, \quad i = 1, \ldots, 4$), number of connections between the specific $\hat{T}$ and $\hat{H}_N$ ($l_i, \quad i = 1, \ldots, 4$), and the number of connections due to particle lines ($m_i, \quad i = 1, \ldots, 4$).

`tenpi` then translates each 13-integer string into a directed graph where a nodes of the graph corresponds to a node of a CC diagram vertex and an edges correspond to particle and hole lines, i.e. the graphs are the diagrams themselves. The graph is stored as a list of edges, where one edge is determined by its starting and ending node. After this step, CC rules are applied (see Table 2.1, as well Refs. [140, 142] for a detailed discussion of CC rules), generating a list of tensor contractions. The directed-graph representation allows for intuitive implementation and easy customization of rules for different variants of CC. Intermediates are subsequently designed and optimized using OpMin [195], based on floating point operations (FLOP) count as a cost function. The correctness of the intermediate results is verified using a custom-generated, straightforward brute-force Python script. Complete source code files are generated as needed, including those for

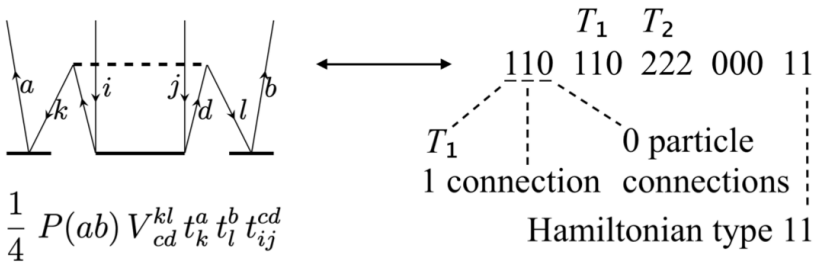

FIGURE 2.13: Figure adapted from Ref. [28] with the kind permission of the authors.

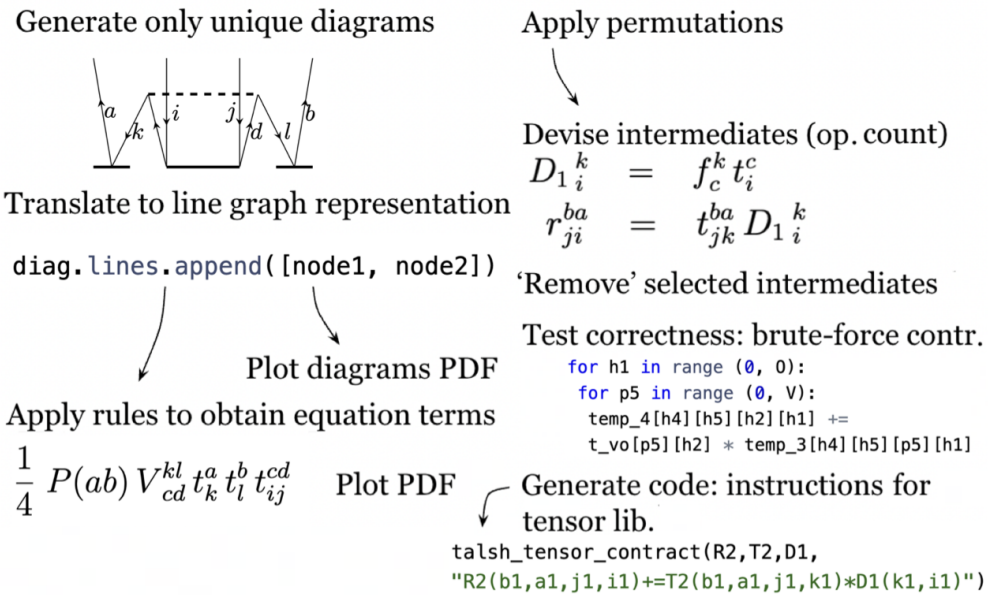

FIGURE 2.14: The tenpi workflow begins with the generation of diagrams, which are subsequently converted into a line chart format. Coupled cluster interpretation rules are then applied, and both the diagrams and the corresponding equation terms are outputted in a textbook-style PDF. Permutations are handled next, followed by code optimization through OpMin. The resulting intermediates undergo further optimization to reduce memory usage. To verify their correctness, a simple brute-force Python script generated by the system is used. At each stage, equations are displayed in a clear and readable format. Finally, the complete source code files are produced as needed (e.g., ExaTENSOR FORTRAN, NumPy Python). This entire process is fully customizable, since all steps interface with the high-level tenpi Python library.33. Figure adapted from Ref. [28] with the kind permission of the authors.

ExaTENSOR in FORTRAN, NumPy in Python, and other relevant formats. A general comprensive scheme is reported in Figure 2.14. For further details on TENPI, consult Ref. [28].

The most challenging step is the optimal design of intermediates, which were discussed in Sec. 2.5. Since finding the best set of intermediates is an NP-hard problem, that is, a problem for which no efficient algorithm is expected to yield the exact optimal solution, heuristic methods are employed. Ideally, the cost function should be the actual walltime, which refers to the real elapsed time taken to complete a computation. This depends not only on the system size but also on the specific hardware used (e.g., CPU speed, memory bandwidth) and the efficiency of the mathematical libraries employed. As this is unknown in advance, most implementations rely on a simple FLOP-based cost model, even though large-scale coupled cluster calculations are often communication-bound. In `tenpi`, the OpMin optimizer is used, which performs:

1. **Single-term optimization:** determines the contraction path that minimizes FLOPs within a term. For example, given the term

$$T_{ab}^{ij} = \sum_{kc} V_{ak}^{ic} T_{bc}^{kj}, \tag{2.80}$$

one can choose to contract over indices k or c first to minimize computational cost.

2. **Factorization:** applies distributive laws to reduce operations. For instance,

$$A_{pq}^{rs} = X_{pq}^{rs} Y_{rs}^{tu} + X_{pq}^{rs} Z_{rs}^{tu} = X_{pq}^{rs} (Y_{rs}^{tu} + Z_{rs}^{tu}), \tag{2.81}$$

reduces two contractions to one.

3. **Common subexpression elimination (CSE):** reuses repeated computations such as

$$W_{ab}^{ij} = \sum_{cd} V_{ab}^{cd} T_{cd}^{ij} \tag{2.82}$$

appearing in multiple terms, computing it once and reusing the result.

One of the biggest drawbacks of OpMin is that it does not support optimization in the presence of denominators, as encountered for example in CCSD(T) [172].

In principle, tenpi can generate CC equations for an arbitrary excitation level. However, from a practical perspective, it does not take advantage of spatial symmetry and index-permutation symmetry [190], which significantly impacts computational efficiency. As a result, excitations beyond the quintuple level are currently disabled. Efforts are underway to implement the missing symmetry support.

Chapter 3

Molecular Properties

"I think there is a moral to this story, namely that it is more important to have beauty in one's equations than to have them fit experiment."
— Paul A. M. Dirac [196]

Molecular properties are measurable physical quantities that characterize the structure, dynamics, and interactions of molecules. In this thesis, we focus on static molecular properties, which are defined in the absence of time-dependent external perturbations. In this chapter, we specifically consider one-electron properties, which depend only on one-electron operators. We will first discuss the evaluation of static molecular properties using variational wavefunctions, where expectation values can be directly computed due to the variational principle. Subsequently, we will address the more general and practically important case of non-variational wavefunctions, such as those arising in coupled cluster (CC) theory. In this context, the straightforward computation of expectation values is no longer possible, necessitating the introduction of the so-called lambda equations and the Lagrangian formalism. Special emphasis will be placed on diagrammatic techniques for the evaluation of coupled cluster expectation values, as these methods provide a systematic and efficient framework for the computation of molecular properties within the CC approach.

This chapter is based on my personal elaboration of concepts clearly presented in the books by Saue, Norman, and Ruud [197], and by Sauer [198]. I have also drawn on the notes made by Gauss [44] .

3.1 Time-independent molecular properties

Let us consider an isolated quantum system that is completely characterized by the unperturbed Hamiltonian $\hat{H}_0$. The eigenstates and eigenvalues of $\hat{H}_0$ provide a full description of the system's stationary properties in the absence of any external influences, as illustrated on the left side of Figure 3.1 by a water molecule in its equilibrium geometry. Now, suppose we introduce a static (i.e., time-independent) perturbation to the system, denoted by $\hat{V}(\boldsymbol{\varepsilon})$. This perturbation might correspond, for example, to the presence of an external electrostatic field, a geometrical distortion of the molecule, or any other static modification of the system's environment. The strength and nature of this perturbation are controlled by a set of parameters collectively indicated by the vector $\boldsymbol{\varepsilon}$. The wavy arrow in Figure 3.1 represents this perturbation acting on the system. As a result of this perturbation, the total Hamiltonian of the system can no longer be described solely by $\hat{H}_0$. Instead, the system is now governed by the perturbed Hamiltonian

$$\hat{H}(\boldsymbol{\varepsilon}) = \hat{H}_0 + \hat{V}(\boldsymbol{\varepsilon})\,, \tag{3.1}$$

which incorporates both the original dynamics and the effects of the perturbation. This new Hamiltonian $\hat{H}(\boldsymbol{\varepsilon})$ fully determines the behavior of the system in the presence of the external perturbation. The right side of Figure 3.1 shows the perturbed water molecule, where the positions of the hydrogen atoms have been slightly displaced due to $\hat{V}(\boldsymbol{\varepsilon})$, exemplifying a geometrical distortion induced by the perturbation.

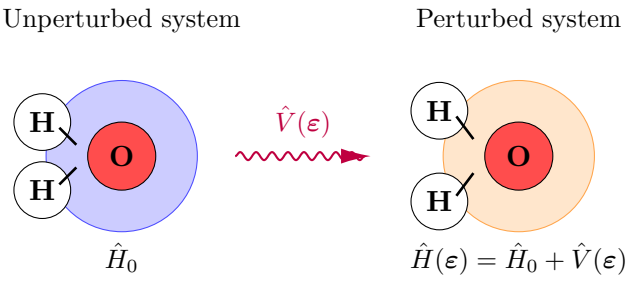

FIGURE 3.1: Sketch illustrating an isolated water molecule described by the unperturbed Hamiltonian $\hat{H}_0$ (left), a static perturbation $\hat{V}(\boldsymbol{\varepsilon})$ represented by the wavy arrow, and the resulting perturbed system governed by the total Hamiltonian $\hat{H}(\boldsymbol{\varepsilon}) = \hat{H}_0 + \hat{V}(\boldsymbol{\varepsilon})$ (right).

Our next goal is to investigate how the presence of the perturbation $\hat{V}(\boldsymbol{\varepsilon})$ affects the

physical properties of the system. To this end, we must solve the time-independent wave-equation for the perturbed system:

$$\hat{H}(\boldsymbol{\varepsilon})\,|\Psi_n\rangle = E_n(\boldsymbol{\varepsilon})\,|\Psi_n\rangle, \qquad n = 0, 1, \ldots \tag{3.2}$$

where $|\Psi_n\rangle$ and E_n denote the n-th eigenstate and eigenvalue of the perturbed Hamiltonian, respectively. In the following, we focus exclusively on the ground state of the system. For the sake of notational simplicity, the label $n = 0$ referring to the ground state will be omitted throughout.

In general, solving Eqn.(3.2) exactly for arbitrary values of $\boldsymbol{\varepsilon}$ can be extremely challenging. However, if the perturbation is sufficiently small, it is possible to obtain approximate solutions by expanding the energy as a Taylor series around $\boldsymbol{\varepsilon} = \mathbf{0}$:

$$E(\boldsymbol{\varepsilon}) = E^{(0)} + \sum_i \left.\frac{\partial E}{\partial \varepsilon_i}\right|_{\boldsymbol{\varepsilon}=0} \varepsilon_i + \frac{1}{2}\sum_{i,j} \left.\frac{\partial^2 E}{\partial \varepsilon_i \partial \varepsilon_j}\right|_{\boldsymbol{\varepsilon}=0} \varepsilon_i \varepsilon_j + \cdots \tag{3.3}$$

Here, $E^{(0)}$ is the unperturbed energy, and the derivatives of the energy with respect to the perturbation parameters $\boldsymbol{\varepsilon}$ evaluated at $\boldsymbol{\varepsilon} = 0$ are known as (static) molecular properties. For example, the first derivative corresponds to the permanent dipole moment in the case of an electric field, while the second derivative relates to the polarizability. A more complete list is reported by Gauss [44].

By analyzing these derivatives, we can systematically characterize the response of the system to external perturbations and thus gain insight into its physical and chemical properties. It is now clear that, in order to compute the time-independent molecular properties, we should be able to compute derivatives of the energy.

3.1.1 Analytical vs numerical derivatives

Our task now is to calculate the time-independent molecular properties, which, as previously discussed, can be expressed as derivatives of the energy with respect to the perturbation parameters. There are two main approaches to compute these derivatives:

1. **Numerical Differentiation:** In this approach, the derivative is estimated using numerical techniques, such as the finite difference method. To illustrate this, consider the Taylor expansion of the energy function $E(\boldsymbol{\varepsilon})$ around $\boldsymbol{\varepsilon} = 0$:

$$E(\boldsymbol{\varepsilon}) = E(0) + \left.\frac{dE}{d\boldsymbol{\varepsilon}}\right|_0 \boldsymbol{\varepsilon} + \frac{1}{2}\left.\frac{d^2E}{d\boldsymbol{\varepsilon}^2}\right|_0 \boldsymbol{\varepsilon}^2 + \frac{1}{6}\left.\frac{d^3E}{d\boldsymbol{\varepsilon}^3}\right|_0 \boldsymbol{\varepsilon}^3 + \mathcal{O}(\boldsymbol{\varepsilon}^4). \tag{3.4}$$

Evaluating at $\boldsymbol{\varepsilon} = +\Delta\boldsymbol{\varepsilon}$ and $\boldsymbol{\varepsilon} = -\Delta\boldsymbol{\varepsilon}$:

$$E(+\Delta\boldsymbol{\varepsilon}) = E(0) + \left.\frac{dE}{d\boldsymbol{\varepsilon}}\right|_0 \Delta\boldsymbol{\varepsilon} + \frac{1}{2}\left.\frac{d^2E}{d\boldsymbol{\varepsilon}^2}\right|_0 (\Delta\boldsymbol{\varepsilon})^2 + \frac{1}{6}\left.\frac{d^3E}{d\boldsymbol{\varepsilon}^3}\right|_0 (\Delta\boldsymbol{\varepsilon})^3 + \cdots, \tag{3.5}$$

$$E(-\Delta\boldsymbol{\varepsilon}) = E(0) - \left.\frac{dE}{d\boldsymbol{\varepsilon}}\right|_0 \Delta\boldsymbol{\varepsilon} + \frac{1}{2}\left.\frac{d^2E}{d\boldsymbol{\varepsilon}^2}\right|_0 (\Delta\boldsymbol{\varepsilon})^2 - \frac{1}{6}\left.\frac{d^3E}{d\boldsymbol{\varepsilon}^3}\right|_0 (\Delta\boldsymbol{\varepsilon})^3 + \cdots. \tag{3.6}$$

Subtracting and dividing by $2\Delta\boldsymbol{\varepsilon}$:

$$\frac{E(+\Delta\boldsymbol{\varepsilon}) - E(-\Delta\boldsymbol{\varepsilon})}{2\Delta\boldsymbol{\varepsilon}} = \left.\frac{dE}{d\boldsymbol{\varepsilon}}\right|_0 + \underbrace{\frac{1}{6}\left.\frac{d^3E}{d\boldsymbol{\varepsilon}^3}\right|_0 (\Delta\boldsymbol{\varepsilon})^2 + \cdots}_{\text{Error term}}. \tag{3.7}$$

A more accurate alternative is the four-point finite difference formula, which reduces the leading-order truncation error:

$$\left.\frac{dE}{d\boldsymbol{\varepsilon}}\right|_0 \approx \frac{-E(2\Delta\boldsymbol{\varepsilon}) + 8E(\Delta\boldsymbol{\varepsilon}) - 8E(-\Delta\boldsymbol{\varepsilon}) + E(-2\Delta\boldsymbol{\varepsilon})}{12\Delta\boldsymbol{\varepsilon}} + \mathcal{O}(\Delta\boldsymbol{\varepsilon}^4). \tag{3.8}$$

The accuracy of the finite difference estimate depends critically on the choice of the step size $\Delta\boldsymbol{\varepsilon}$. If $\Delta\boldsymbol{\varepsilon}$ is too large, truncation errors arising from neglected higher-order terms become significant; if it is too small, numerical round-off errors dominate. Therefore, an optimal step size exists that minimizes the total error. In practice, this optimal value depends on both the smoothness of $E(\boldsymbol{\varepsilon})$ and the numerical precision of the computation. Moreover, the extension of such numerical differentiation schemes to the evaluation of magnetic or time-dependent properties is nontrivial, due to complex-valued operators, explicit time dependence, or gauge-origin sensitivity, all of which impose additional constraints on the stability and implementation of the numerical procedure.

2. **Analytical Differentiation:** Alternatively, molecular properties can be determined analytically by directly differentiating the energy with respect to the perturbation parameter. The analytical approach offers high accuracy and, in principle,

broad applicability-including the calculation of time-dependent properties. Nevertheless, its main drawback is the complexity of implementation. The analytical form of the derivative often depends on the details of the chosen quantum chemical method, and switching between methods typically requires the derivation of new, method-specific formulas. In some cases, existing expressions can be reused, but this is not always possible. In this approach, the energy is regarded as a function of the perturbation, and its derivative is obtained using calculus. A common starting point is the Hellmann-Feynman theorem [45, 46], which, for a system described by the Hamiltonian $\hat{H}(\varepsilon) = \hat{H}_0 + \hat{V}(\varepsilon)$, relates the derivative of the ground state energy $E(\varepsilon)$ to the expectation value of the derivative of the Hamiltonian:

$$\frac{dE}{d\varepsilon} = \left\langle \Psi \left| \frac{\partial \hat{H}}{\partial \varepsilon} \right| \Psi \right\rangle . \tag{3.9}$$

However, it is important to recognize that the Hellmann-Feynman theorem is strictly valid only for exact eigenfunctions of the Hamiltonian. In practical quantum chemical calculations, the exact wave function is generally not available; instead, we rely on approximate wave functions whose accuracy depends on the computational method used. As a result, direct application of the Hellmann-Feynman theorem may not always yield reliable results, especially when the wave function is not an exact eigenstate or does not satisfy certain stationarity conditions. To overcome these limitations and obtain accurate molecular properties, it is necessary to employ more general analytical techniques, such as response theory, or to derive explicit expressions for the energy derivatives tailored to the specific quantum chemical method in use. As will be discussed in the following sections, particular attention must be paid to the distinction between variational and non-variational methods, as this has significant implications for the derivation and evaluation of analytical derivatives.

3.1.2 Variational perturbation theory

Most quantum chemical methods for determining approximate ground states, such as Hartree-Fock, Kohn-Sham DFT, MCSCF, and CI, rely on an ansatz for the wave function parameterized by a set of variational parameters. Therefore, we will refer to the

approximate wave-function as $|\Phi(\boldsymbol{\lambda})\rangle$, where $\boldsymbol{\lambda}$ is the vector containing the variational-parameters. *Variational perturbation theory* provides a systematic framework for deriving molecular properties in such cases.

Let us express the energy as a function of both the variational parameters $\boldsymbol{\lambda}$ and the perturbation strengths $\boldsymbol{\varepsilon}$:

$$E \equiv E(\boldsymbol{\lambda}, \boldsymbol{\varepsilon}). \tag{3.10}$$

Because the wave function is parameterized variationally, the energy is minimized with respect to $\boldsymbol{\lambda}$ for any fixed value of the perturbation. This leads to the variational condition:

$$\left.\frac{\partial E(\boldsymbol{\lambda}, \boldsymbol{\varepsilon})}{\partial \boldsymbol{\lambda}}\right|_{\boldsymbol{\varepsilon}} = 0, \quad \forall\, \boldsymbol{\lambda}. \tag{3.11}$$

This simply states that, for each value of the perturbation $\boldsymbol{\varepsilon}$, the energy is optimized with respect to the variational parameters. Computing the total differential of Eqn.(3.10) and making the variation of the energy respect to the perturbation explicit we find

$$\frac{dE(\boldsymbol{\lambda}, \boldsymbol{\varepsilon})}{d\boldsymbol{\varepsilon}} = \frac{dE(\boldsymbol{\lambda}, \boldsymbol{\varepsilon})}{d\boldsymbol{\varepsilon}} + \frac{\partial E(\boldsymbol{\lambda}, \boldsymbol{\varepsilon})}{\partial \boldsymbol{\lambda}} \frac{d\boldsymbol{\lambda}}{d\boldsymbol{\varepsilon}}, \tag{3.12}$$

where we see that the implicit derivative involves the response of the variational parameters due to the perturbation. Generally, one need to solve *response equations* in order to get $\frac{d\boldsymbol{\lambda}}{d\boldsymbol{\varepsilon}}$, and the number of these equations depends on the number of perturbations. However, by using Eqn.(3.11) we easily realize that for fully-variational wave-functions first-order molecular properties can be computed by using the Hellmann-Feynman theorem [45, 46]

$$\frac{dE(\boldsymbol{\lambda}, \boldsymbol{\varepsilon})}{d\boldsymbol{\varepsilon}} = \frac{\partial E(\boldsymbol{\lambda}, \boldsymbol{\varepsilon})}{\partial \boldsymbol{\varepsilon}}. \tag{3.13}$$

We should also mention that Eqn.(3.13) is true also for the situation in which the parameters $\boldsymbol{\lambda}$ do not depend on the perturbation.

To compute second-order molecular properties, i.e., the second derivative of the energy with respect to the perturbation, the situation is more involved. The total second derivative can be written as:

$$\frac{d^2E}{d\boldsymbol{\varepsilon}^2} = \frac{\partial^2 E}{\partial \boldsymbol{\varepsilon}^2} + 2\frac{\partial^2 E}{\partial \boldsymbol{\lambda} \partial \boldsymbol{\varepsilon}} \frac{d\boldsymbol{\lambda}}{d\boldsymbol{\varepsilon}} \quad + \frac{\partial^2 E}{\partial \boldsymbol{\lambda}^2} \left(\frac{d\boldsymbol{\lambda}}{d\boldsymbol{\varepsilon}}\right)^2 + \frac{\partial E}{\partial \boldsymbol{\lambda}} \frac{d^2\boldsymbol{\lambda}}{d\boldsymbol{\varepsilon}^2}. \tag{3.14}$$

For a fully variational wave function, the stationarity condition ensures that $\frac{\partial E}{\partial \boldsymbol{\lambda}} = 0$, so the last term vanishes. However, the mixed and quadratic terms involving the response of the variational parameters, $\frac{d\boldsymbol{\lambda}}{d\boldsymbol{\varepsilon}}$, generally remain and must be evaluated. Therefore, in order to compute second-order molecular properties (such as polarizabilities or force constants), it is necessary to solve the *response equations*, which provide the first-order response of the variational parameters to the perturbation. We therefore see that, in order to compute the second-derivative of the energy we need to know the first-order derivative of the parameters. As noted independently by Hylleraas [199] and and Wigner [200] ,we may generalize this concept by introducing the so-called $2n+1$ *rule*. This rule states that, for a fully variational wave function, knowledge of the response of the wave function up to order n with respect to a perturbation is sufficient to compute energy derivatives up to order $2n+1$. More specifically, if the wave function parameters $\boldsymbol{\lambda}$ are optimized variationally, then the $(2n+1)$-th derivative of the energy with respect to a perturbation can be expressed solely in terms of the wave function and its response up to order n:

$$\frac{d^{2n+1}E}{d\boldsymbol{\varepsilon}^{2n+1}} = f\left(\boldsymbol{\lambda},\ \frac{d\boldsymbol{\lambda}}{d\boldsymbol{\varepsilon}},\ \ldots,\ \frac{d^{n}\boldsymbol{\lambda}}{d\boldsymbol{\varepsilon}^{n}}\right). \tag{3.15}$$

3.2 Molecular properties using the CC wave-functions

Having established the general framework for molecular property calculations, we now focus on the computation of analytical energy derivatives using the CC wave function.

In contrast to fully variational wave functions, the CC energy is not strictly variational with respect to all wave function parameters. Consequently, the straightforward application of the Hellmann-Feynman theorem is not sufficient for the calculation of energy derivatives. When differentiating the CC energy with respect to an external perturbation $\boldsymbol{\varepsilon}$, it is essential to account explicitly for the response of the CC amplitudes to the perturbation. This requirement leads to the so-called *coupled-perturbed CC (CP-CC) equations*, which provide the first-order response of the cluster amplitudes. The total derivative of the CC energy with respect to the perturbation can be written as:

$$\frac{dE_{\mathrm{CC}}}{d\boldsymbol{\varepsilon}} = \frac{\partial E_{\mathrm{CC}}}{\partial \boldsymbol{\varepsilon}} + \frac{\partial E_{\mathrm{CC}}}{\partial \mathbf{t}}\frac{d\mathbf{t}}{d\boldsymbol{\varepsilon}} + \frac{\partial E_{\mathrm{CC}}}{\partial \boldsymbol{\kappa}}\frac{d\boldsymbol{\kappa}}{d\boldsymbol{\varepsilon}}, \tag{3.16}$$

where $\mathbf{t}$ denotes the set of cluster amplitudes and $\boldsymbol{\kappa}$ the set of orbital-rotation parameters of the MOs. The second term, which involves the amplitude response, is generally nonzero and must be evaluated by solving the CP-CC equations. The contribution arising from the response of the molecular orbital (MO) coefficients to the perturbation is neglected in this thesis. This term, which would otherwise appear in a fully relaxed treatment, is not explicitly included in our derivation. Its omission defines what is commonly referred to as the *unrelaxed* formalism [44]. This approximation is partially justified by the fact that orbital relaxation effects are, to some extent, recovered through the action of the T_1 operator in the coupled cluster framework [201]. The $\hat{T}_1$ amplitudes describe the mixing of occupied and virtual orbitals, which mimics the effect of orbital rotations induced by the perturbation. As a result, although the explicit orbital response is not included, the CC wavefunction can still capture a significant portion of the relaxation through the flexibility provided by T_1.

It is important to note that the calculation of the derivatives of the CC amplitudes with respect to an external perturbation is an extremely demanding task from a computational point of view. Solving the coupled-perturbed CC (CP-CC) equations involves the construction and inversion of large, often sparse, matrices whose dimensions scale steeply with the size of the molecular system and the level of excitation included in the CC ansatz. Moreover, the storage of the amplitude derivatives themselves can become a significant bottleneck. These derivatives are typically high-rank tensors, and their memory requirements increase rapidly with system size. For large molecules or high-level CC methods (such as CCSDT or beyond), the memory needed to store all amplitude derivatives may exceed the available resources, making such calculations challenging or even prohibitive. As we will see, this bottleneck can be avoided by introducing and solving a new set of linear equations, namely the Λ-equations. The introduction of these equations leads to a much simpler computation of coupled-cluster expectation values, as it eliminates the need to explicitly calculate the derivatives of the cluster amplitudes with respect to external perturbations.

3.2.1 Λ-equations from the direct differentiation of the energy

This derivation can be found in the original article by Salter and coworkers [202], as well as in the recent chapter by Crawford in the ESQC2024 book [177], which provides

additional details. I have chosen to reproduce this derivation here to emphasize even further the power and elegance of the formalism that will be introduced in the next subsection.

In this context, Salter, Trucks, and Bartlett [202] proposed an explicit method for computing the expectation value of an operator $\hat{\Omega}$ by directly differentiating Eqn. (2.43):

$$\frac{\partial E_{\mathrm{CC}}}{\partial \varepsilon} = \langle \Phi_0 \left| \frac{\partial \hat{\bar{H}}}{\partial \varepsilon} \right| \Phi_0 \rangle \,, \tag{3.17}$$

where ε is the perturbation strength. This expression corresponds to an *unrelaxed* formalism, since the same reference Φ_0, and hence the same orbitals, are used for all perturbations. In a *relaxed* formalism, the orbitals would respond to the perturbation, and the derivative would include additional contributions from orbital relaxation.

We need to evaluate the derivative of the similarity-transformed Hamiltonian

$$\begin{aligned} \frac{\partial \hat{\bar{H}}}{\partial \varepsilon} = \frac{\partial \hat{H}_N}{\partial \varepsilon} + \frac{\partial}{\partial \varepsilon}[\hat{H}_N, \hat{T}] + \frac{1}{2}\frac{\partial}{\partial \varepsilon}[[\hat{H}_N, \hat{T}], \hat{T}] \\ + \frac{1}{3!}\frac{\partial}{\partial \varepsilon}[[[\hat{H}_N, \hat{T}], \hat{T}], \hat{T}] + \frac{1}{4!}\frac{\partial}{\partial \varepsilon}[[[[\hat{H}_N, \hat{T}], \hat{T}], \hat{T}], \hat{T}]. \end{aligned} \tag{3.18}$$

We assume that the second-quantized operators do not depend on the field strength, nor do the cluster operators; therefore, the following expression is obtained

$$\frac{\partial \hat{H}_N}{\partial \varepsilon} = \sum_{pq} \frac{\partial f_{pq}}{\partial \varepsilon}\{a_p^\dagger a_q\} + \frac{1}{4}\sum_{pqrs} \frac{\partial V_{pqrs}}{\partial \varepsilon}\{a_p^\dagger a_q^\dagger a_s a_r\} \equiv \hat{H}_N^{(\varepsilon)}, \tag{3.19}$$

$$\frac{\partial \hat{T}}{\partial \varepsilon} = \sum_{\mu} \frac{\partial t_\mu}{\partial \varepsilon}\hat{\tau}_\mu \equiv \hat{T}^{(\varepsilon)}, \tag{3.20}$$

where we also note that the derivative of a cluster operator is still a cluster operator, and therefore

$$\left[\hat{T}, \frac{\partial \hat{T}}{\partial \varepsilon}\right] = 0. \tag{3.21}$$

Instead of computing all the terms in Eqn.(3.18), we may simply apply the product rule

$$\begin{aligned}
\frac{\partial \overline{H}}{\partial \varepsilon} &= \frac{\partial}{\partial \varepsilon}\left(e^{-\hat{T}}\hat{H}_N e^{\hat{T}}\right) \\
&= \left(\frac{\partial e^{-\hat{T}}}{\partial \varepsilon}\right)\hat{H}_N e^{\hat{T}} + e^{-\hat{T}}\left(\frac{\partial \hat{H}_N}{\partial \varepsilon}\right)e^{\hat{T}} + e^{-\hat{T}}\hat{H}_N\left(\frac{\partial e^{\hat{T}}}{\partial \varepsilon}\right) \\
&= -\hat{T}^{(\varepsilon)}e^{-\hat{T}}\hat{H}_N e^{\hat{T}} + e^{-\hat{T}}\hat{H}_N^{(\varepsilon)}e^{\hat{T}} + e^{-\hat{T}}\hat{H}_N\hat{T}^{(\varepsilon)}e^{\hat{T}} \\
&\overset{(3.21)}{=} e^{-\hat{T}}\left(\hat{H}_N^{(\varepsilon)} + [\hat{H}_N, \hat{T}^{(\varepsilon)}]\right)e^{\hat{T}} \\
&= \hat{\overline{H}}^{(\varepsilon)} + [\overline{H}_N, \hat{T}^{(\varepsilon)}].
\end{aligned} \tag{3.22}$$

Therefore the gradient of the CC energy reads as

$$\frac{\partial E_{\mathrm{CC}}}{\partial \varepsilon} = \langle\Phi_0|\hat{\overline{H}}^{(\varepsilon)}|\Phi_0\rangle + \langle\Phi_0|\left[\overline{H}, \hat{T}^{(\varepsilon)}\right]|\Phi_0\rangle\,. \tag{3.23}$$

The second term can be rearranged by introducing the completness relation $\sum_\eta |\Phi_\eta\rangle\langle\Phi_\eta| = 1$,

$$\begin{aligned}
\langle\Phi_0|\left[\overline{H}, \hat{T}^{(\varepsilon)}\right]|\Phi_0\rangle &= \langle\Phi_0|\overline{H}\hat{T}^{(\varepsilon)}|\Phi_0\rangle - \langle\Phi_0|\hat{T}^{(\varepsilon)}\overline{H}|\Phi_0\rangle \\
&= \sum_\eta\left(\langle\Phi_0|\hat{\overline{H}}\,|\Phi_\eta\rangle\langle\Phi_\eta|\,\hat{T}^{(\varepsilon)}|\Phi_0\rangle - \sum_\eta\langle\Phi_0|\hat{T}^{(\varepsilon)}\,|\Phi_\eta\rangle\langle\Phi_\eta|\,\hat{\overline{H}}|\Phi_0\rangle\right) \\
&= \langle\Phi_0|\hat{\overline{H}}\,|\Phi_0\rangle\langle\Phi_0|\,\hat{T}^{(\varepsilon)}|\Phi_0\rangle + \sum_{\eta\neq 0}\langle\Phi_0|\hat{\overline{H}}\,|\Phi_\eta\rangle\langle\Phi_\eta|\,\hat{T}^{(\varepsilon)}|\Phi_0\rangle \\
&\quad - \langle\Phi_0|\hat{T}^{(\varepsilon)}\,|\Phi_0\rangle\langle\Phi_0|\,\hat{\overline{H}}|\Phi_0\rangle - \sum_{\eta\neq 0}\langle\Phi_0|\hat{T}^{(\varepsilon)}\,|\Phi_\eta\rangle\langle\Phi_\eta|\,\hat{\overline{H}}|\Phi_0\rangle\,,
\end{aligned} \tag{3.24}$$

where in the second step of Eqn.(3.24) we have extracted the $\eta = 0$ term from the summation. We note that certain terms in Eqn.(3.24) vanish for the following reasons:

- The term

$$\langle\Phi_0|\hat{T}^{(\varepsilon)}|\Phi_0\rangle = 0, \tag{3.25}$$

  is zero because $\hat{T}^{(\varepsilon)}$ is an excitation operator. When acting on the reference state in the ket, it generates an excited Slater determinant that is orthogonal to the bra.

- The term

$$\sum_{\eta\neq 0}\langle\Phi_0|\hat{T}^{(\varepsilon)}|\Phi_\eta\rangle\langle\Phi_\eta|\hat{\overline{H}}|\Phi_0\rangle = 0, \quad \forall\eta, \tag{3.26}$$

also vanishes because $\langle\Phi_0|\hat{T}^{(\varepsilon)}|\Phi_\eta\rangle$ is zero. This is due to the fact that $\hat{T}^{(\varepsilon)}$ increases the excitation level of the already excited determinant in the ket, resulting in a determinant orthogonal to the reference bra.

and by simply noting that

$$\langle\Phi_\eta|\hat{T}^{(\varepsilon)}|\Phi_0\rangle = \frac{\partial t_\eta}{\partial \varepsilon} \equiv t_\eta^{(\varepsilon)}, \tag{3.27}$$

the gradient of the CC energy will be

$$\frac{\partial E_{\mathrm{CC}}}{\partial \varepsilon} = \langle\Phi_0|\hat{\overline{H}}^{(\varepsilon)}|\Phi_0\rangle + \sum_{\eta\neq 0}\langle\Phi_0|\hat{\overline{H}}|\Phi_\eta\rangle\, t_\eta^{(\varepsilon)}. \tag{3.28}$$

We see that the computation of the CC energy gradient requires the knowledge of the derivatives of the amplitudes, in principle. Pragmatically, if the amplitude equations provide us the amplitudes, the derivative of amplitude equations will provide us the derivatives of the amplitudes. By taking the derivative of Eqn.(2.44) we get

$$\langle\Phi_\eta|\hat{\overline{H}}^{(\varepsilon)}|\Phi_0\rangle + \langle\Phi_\eta|\left[\hat{\overline{H}}, \hat{T}^{(\varepsilon)}\right]|\Phi_0\rangle = 0. \tag{3.29}$$

As we have done previously, we can massage the second term by introducing the completeness relation

$$\begin{aligned}
\langle\Phi_\eta|\left[\hat{\overline{H}}, \hat{T}^{(\varepsilon)}\right]|\Phi_0\rangle &= \langle\Phi_\eta|\hat{\overline{H}}\hat{T}^{(\varepsilon)}|\Phi_0\rangle - \langle\Phi_\eta|\hat{T}^{(\varepsilon)}\hat{\overline{H}}|\Phi_0\rangle \\
&= \sum_{\eta'}\langle\Phi_\eta|\hat{\overline{H}}\,|\Phi_{\eta'}\rangle\,\langle\Phi_{\eta'}|\,\hat{T}^{(\varepsilon)}|\Phi_0\rangle - \sum_{\eta'}\langle\Phi_\eta|\hat{T}^{(\varepsilon)}\,|\Phi_{\eta'}\rangle\,\langle\Phi_{\eta'}|\,\hat{\overline{H}}|\Phi_0\rangle \\
&= \langle\Phi_\eta|\hat{\overline{H}}\,|\Phi_0\rangle\,\langle\Phi_0|\,\hat{T}^{(\varepsilon)}|\Phi_0\rangle + \sum_{\eta'\neq 0}\langle\Phi_\eta|\hat{\overline{H}}\,|\Phi_{\eta'}\rangle\,\langle\Phi_{\eta'}|\,\hat{T}^{(\varepsilon)}|\Phi_0\rangle \\
&\quad - \langle\Phi_\eta|\hat{T}^{(\varepsilon)}\,|\Phi_0\rangle\,\langle\Phi_0|\,\hat{\overline{H}}|\Phi_0\rangle - \sum_{\eta'\neq 0}\langle\Phi_\eta|\hat{T}^{(\varepsilon)}\,|\Phi_{\eta'}\rangle\,\langle\Phi_{\eta'}|\,\hat{\overline{H}}|\Phi_0\rangle\,.
\end{aligned} \tag{3.30}$$

Again, we may get few simplifications

- The term

$$\langle\Phi_0|\hat{T}^{(\varepsilon)}|\Phi_0\rangle = 0, \tag{3.31}$$

for the reason described above.

- The term

$$\sum_{\eta' \neq 0} \langle \Phi_\eta | \hat{T}^{(\varepsilon)} | \Phi_{\eta'} \rangle \langle \Phi_{\eta'} | \hat{\overline{H}} | \Phi_0 \rangle = 0, \quad \forall\, \eta', \tag{3.32}$$

  is always zero for the following reasons. When η' belongs to the excitation manifold, the amplitude equations are satisfied, and thus $\langle \Phi_{\eta'} | \hat{\overline{H}} | \Phi_0 \rangle = 0$. On the other hand, if η' is outside the excitation manifold, the term $\langle \Phi_{\eta'} | \hat{\overline{H}} | \Phi_0 \rangle$ may in general be nonzero, but $\langle \Phi_\eta | \hat{T}^{(\varepsilon)} | \Phi_{\eta'} \rangle$ is always zero. This is because, when η is outside the excitation manifold, the action of the cluster operator on $|\Phi_{\eta'}\rangle$ produces a determinant with a higher excitation level, which will also lie outside the excitation manifold and thus be orthogonal to the bra $\langle \Phi_\eta |$.

We also note

$$\begin{aligned} &\langle \Phi_0 | \hat{\overline{H}} | \Phi_0 \rangle = E_{\mathrm{CC}}, \\ &\langle \Phi_{\eta'} | \hat{T}^{(\varepsilon)} | \Phi_0 \rangle \overset{(3.27)}{=} t_{\eta'}^{(\varepsilon)}, \\ &\langle \Phi_\eta | \hat{T}^{(\varepsilon)} | \Phi_0 \rangle \overset{(3.27)}{=} t_{\eta}^{(\varepsilon)}. \end{aligned} \tag{3.33}$$

Therefore, the derivative of the amplitude equations reads as

$$\langle \Phi_\eta | \hat{\overline{H}}^{(\varepsilon)} | \Phi_0 \rangle + \sum_{\eta' \neq 0} \langle \Phi_\eta | \hat{\overline{H}} | \Phi_{\eta'} \rangle \, t_{\eta'}^{(\varepsilon)} - E_{\mathrm{CC}} t_\eta^{(\varepsilon)} = 0 \tag{3.34}$$

We can write the last term using the following trick

$$t_\eta^{(\varepsilon)} = \sum_{\eta'} t_{\eta'}^{(\varepsilon)} \delta_{\eta\eta'} = \sum_{\eta'} t_{\eta'}^{(\varepsilon)} \langle \Phi_\eta | \Phi_{\eta'} \rangle, \tag{3.35}$$

and so

$$\langle \Phi_\eta | \hat{H}^{(\varepsilon)} | \Phi_0 \rangle + \sum_{\eta' \neq 0} \langle \Phi_\eta | \hat{\overline{H}} - E_{\mathrm{CC}} | \Phi_{\eta'} \rangle \, t_{\eta'}^{(\varepsilon)} = 0, \tag{3.36}$$

$$\sum_{\eta' \neq 0} \langle \Phi_\eta | \hat{\overline{H}} - E_{\mathrm{CC}} | \Phi_{\eta'} \rangle \, t_{\eta'}^{(\varepsilon)} = - \langle \Phi_\eta | \hat{H}^{(\varepsilon)} | \Phi_0 \rangle . \tag{3.37}$$

To solve for $t_{\eta'}^{(\varepsilon)}$, we multiply from the left by the inverse of the matrix $\langle \Phi_\eta | \hat{\overline{H}} - E_{\mathrm{CC}} | \Phi_{\eta'} \rangle$. The inverse, if it exists, must satisfy:

$$\sum_{\eta'} \langle \Phi_\eta | \hat{\overline{H}} - E_{\mathrm{CC}} | \Phi_{\eta'} \rangle \left[\langle \Phi_{\eta'} | \hat{\overline{H}} - E_{\mathrm{CC}} | \Phi_{\eta''} \rangle^{-1} \right] = \delta_{\eta\eta''}. \tag{3.38}$$

Introducing the matrix elements

$$A_{\eta\eta'} = \langle \Phi_\eta | \hat{\overline{H}} - E_{\mathrm{CC}} | \Phi_{\eta'} \rangle \,, \quad [\mathbf{A}^{-1}]_{\eta\eta'} \text{ its inverse.} \tag{3.39}$$

Multiplying both sides of Eqn. (3.37) by $[\mathbf{A}^{-1}]_{\eta\eta'}$ and summing over η' gives

$$\sum_{\eta' \neq 0} [\mathbf{A}^{-1}]_{\eta\eta'} \sum_{\eta'' \neq 0} A_{\eta'\eta''} \, t_{\eta''}^{(\varepsilon)} = - \sum_{\eta' \neq 0} [\mathbf{A}^{-1}]_{\eta\eta'} \, \langle \Phi_{\eta'} | \hat{H}^{(\varepsilon)} | \Phi_0 \rangle \,, \tag{3.40}$$

$$\sum_{\eta'} [\mathbf{A}^{-1}]_{\eta\eta'} A_{\eta'\eta''} = \delta_{\eta\eta''}. \tag{3.41}$$

The left-hand side simplifies to $t_\eta^{(\varepsilon)}$, yielding the final solution:

$$t_\eta^{(\varepsilon)} = - \sum_{\eta' \neq 0} [\mathbf{A}^{-1}]_{\eta\eta'} \, \langle \Phi_{\eta'} | \hat{H}^{(\varepsilon)} | \Phi_0 \rangle \,. \tag{3.42}$$

Therefore, the CC gradient expression becomes

$$\frac{\partial E_{\mathrm{CC}}}{\partial \varepsilon} = \langle \Phi_0 | \hat{\overline{H}}^{(\varepsilon)} | \Phi_0 \rangle - \sum_{\eta\eta'} \langle \Phi_0 | \hat{\overline{H}} | \Phi_\eta \rangle \, [\mathbf{A}^{-1}]_{\eta\eta'} \, \langle \Phi_{\eta'} | \hat{\overline{H}}^{(\varepsilon)} | \Phi_0 \rangle \,. \tag{3.43}$$

To obtain a nonzero contribution from the last term, we define a de-excitation operator

$$\langle \Phi_0 | \hat{\Lambda} | \Phi_{\eta'} \rangle \equiv \sum_\eta \langle \Phi_0 | \hat{\overline{H}} | \Phi_\eta \rangle \, [\mathbf{A}^{-1}]_{\eta\eta'}, \quad \hat{\Lambda} = \sum_\eta \lambda_\eta \hat{\tau}_\eta^\dagger. \tag{3.44}$$

Multiplying from the right by $A_{\eta\eta'}$ gives

$$\sum_{\eta'} \langle \Phi_0 | \hat{\Lambda} | \Phi_{\eta'} \rangle \, A_{\eta'\eta} = - \langle \Phi_0 | \hat{\overline{H}} | \Phi_\eta \rangle \,. \tag{3.45}$$

We also note that

$$\langle \Phi_0 | \hat{\Lambda} | \Phi_0 \rangle = 0, \tag{3.46}$$

$$\langle \Phi_0 | E_{\mathrm{CC}} | \Phi_\eta \rangle = 0, \tag{3.47}$$

and therefore

$$\langle \Phi_0 | (1 + \hat{\Lambda}) (\hat{\overline{H}} - E_{\mathrm{CC}}) | \Phi_\eta \rangle = 0. \tag{3.48}$$

This is a system of *perturbation independent* linear equations, that we need only solve once for the λ_η amplitudes. We can formally eliminate the energy

$$\begin{aligned}
(\hat{\overline{H}} - E_{\mathrm{CC}})\,|\Phi_\eta\rangle &= (\hat{\overline{H}} - E_{\mathrm{CC}})\hat{\tau}_\eta\,|\Phi_0\rangle \\
&= \hat{\overline{H}}\hat{\tau}_\eta\,|\Phi_0\rangle - E_{\mathrm{CC}}\hat{\tau}_\eta\,|\Phi_0\rangle \\
&= \hat{\overline{H}}\hat{\tau}_\eta\,|\Phi_0\rangle - \hat{\tau}_\eta\left(E_{\mathrm{CC}}\,|\Phi_0\rangle + \sum_{\eta'\neq 0}|\Phi_{\eta'}\rangle\,\langle\Phi_{\eta'}|\,\hat{\overline{H}}\,|\Phi_0\rangle\right) \\
&= \hat{\overline{H}}\hat{\tau}_\eta\,|\Phi_0\rangle - \hat{\tau}_\eta\left(\langle\Phi_0|\hat{\overline{H}}|\Phi_0\rangle\,|\Phi_0\rangle + \sum_{\eta'\neq 0}|\Phi_{\eta'}\rangle\,\langle\Phi_{\eta'}|\,\hat{\overline{H}}\,|\Phi_0\rangle\right) \\
&= \hat{\overline{H}}\hat{\tau}_\eta\,|\Phi_0\rangle - \hat{\tau}_\eta\left(|\Phi_0\rangle\,\langle\Phi_0| + \sum_{\eta'\neq 0}|\Phi_{\eta'}\rangle\,\langle\Phi_{\eta'}|\right)\hat{\overline{H}}\,|\Phi_0\rangle \\
&= [\hat{\overline{H}}, \hat{\tau}_\eta]\,|\Phi_0\rangle\,.
\end{aligned} \tag{3.49}$$

and therefore the lambda equations can be written as

$$\langle\Phi_0|(1+\hat{\Lambda})[\hat{\overline{H}}, \hat{\tau}_\eta]|\Phi_0\rangle = 0. \tag{3.50}$$

The energy gradient can be written as

$$\begin{aligned}
\frac{\partial E_{\mathrm{CC}}}{\partial \boldsymbol{\varepsilon}} &= \langle\Phi_0|\hat{\overline{H}}^{(\boldsymbol{\varepsilon})}|\Phi_0\rangle + \sum_\eta \langle\Phi_0|\hat{\Lambda}\,|\Phi_\eta\rangle\,\langle\Phi_\eta|\,\hat{\overline{H}}|\Phi_0\rangle \\
&= \langle\Phi_0|(1+\hat{\Lambda})\hat{\overline{H}}^{(\boldsymbol{\varepsilon})}|\Phi_0\rangle\,.
\end{aligned} \tag{3.51}$$

3.2.2 Λ-equations from the Lagrangian framework

We have seen in the previous subsection that deriving the Λ-equations through direct differentiation of the energy leads to the Λ-equations in a rather unnatural and complicated manner. Helgaker [203] and Jørgensen [47] introduced a powerful Lagrangian formalism to compute energy derivatives for non-variational wave functions, such as those arising in CC theory. The Lagrangian formalism introduces a generalized energy functional, or Lagrangian, that depends not only on the wave function parameters (e.g., the cluster amplitudes $\mathbf{t}$) but also on a set of Lagrange multipliers $\bar{\mathbf{t}}$ (often called $\boldsymbol{\lambda}$ in the literature). The Lagrangian is constructed such that it is stationary with respect to both sets

of parameters:

$$L_{\mathrm{CC}}(\boldsymbol{\varepsilon}, \boldsymbol{t}, \bar{\boldsymbol{t}}) = E_{\mathrm{CC}} + \sum_{\eta,k} \bar{t}_{\eta;k} \langle \Phi_{\eta;k} | \hat{\overline{H}} | \Phi_0 \rangle \,, \quad k \leq k_{\max}. \tag{3.52}$$

By simply defining a de-excitator operator $\hat{\Lambda}$ as

$$\hat{\Lambda} = \sum_{k}^{k_{\max}} \hat{\Lambda}_k, \quad \hat{\Lambda}_k = \sum_{\eta} \bar{t}_{\eta;k} \hat{\tau}^{\dagger}_{\eta;k}, \tag{3.53}$$

defined as a linear combination of de-excitator operators $\hat{\tau}^{\dagger}_{\eta;k}$ associated to the de-excitation manifold corresponding to the cluster operator $\hat{T}$, and $\bar{t}_{\eta;k}$ are the multipliers, we see that Eqn.(3.52) may be written as

$$L_{\mathrm{CC}}(\boldsymbol{\varepsilon}, \boldsymbol{t}, \bar{\boldsymbol{t}}) = \langle \Phi_0 | (1 + \hat{\Lambda}) \hat{\overline{H}} | \Phi_0 \rangle = \langle \Phi_{\mathrm{L}} | \hat{\overline{H}} | \Phi_{\mathrm{R}} \rangle \,, \tag{3.54}$$

which is exactly Eqn.(2.57). We should note that this definition of the Lagrangian overlooks orbital relaxation, but which is assumed to be partially accounted for by the $\hat{T}_1$ operator [201, 204]. By taking the total differential of the above Lagrangian and explicitly expressing its variation with respect to the perturbation, we obtain:

$$\frac{dL^{\mathrm{CC}}}{d\boldsymbol{\varepsilon}} = \frac{\partial L^{\mathrm{CC}}}{\partial \boldsymbol{\varepsilon}} + \frac{\partial L^{\mathrm{CC}}}{\partial \mathbf{t}} \frac{d\mathbf{t}}{d\boldsymbol{\varepsilon}} + \frac{\partial L^{\mathrm{CC}}}{\partial \bar{\mathbf{t}}} \frac{d\bar{\mathbf{t}}}{d\boldsymbol{\varepsilon}}. \tag{3.55}$$

We note that if the last two terms in Eqn.(3.55) vanish, first-order molecular properties can be obtained simply by evaluating the explicit derivative of the coupled-cluster energy. To ensure this, we impose stationarity of the Lagrangian with respect to both $\mathbf{t}$ and $\bar{\mathbf{t}}$, which leads to the following variational conditions:

$$\frac{\partial L_{\mathrm{CC}}}{\partial \bar{t}_{\nu;k}} = \langle \Phi_{\nu;k} | \hat{\overline{H}} | \Phi_0 \rangle = 0 \quad k \leq k_{\max}, \tag{3.56}$$

$$\frac{\partial L_{\mathrm{CC}}}{\partial t_{\nu;k}} = \langle \Phi_0 | (1 + \hat{\Lambda}) [\hat{\overline{H}}, \hat{\tau}_{\nu;k}] | \Phi_0 \rangle = 0 \quad k \leq k_{\max}, \tag{3.57}$$

where Eqn.(3.56) are the usual amplitudes equations defined previously in Eqn.(2.56), and Eqn.(3.57) are the $\Lambda-$equations, a linear set of equations for the multipliers [205]. We should note that Eqns.(3.57) are the Λ-equations derived before (see Eqn.(3.50)), but now obtained in a much faster, more intuitive, and generalizable way.

When calculating the derivative of the energy with respect to an external perturbation

$\boldsymbol{\varepsilon}$, one differentiates the Lagrangian instead of the original energy. Because the Lagrangian is stationary with respect to both $\mathbf{t}$ and $\bar{\mathbf{t}}$, implicit derivatives of these parameters with respect to $\boldsymbol{\varepsilon}$ do not contribute, and the total derivative reduces to partial derivatives:

$$\frac{dE_{\mathrm{CC}}}{d\boldsymbol{\varepsilon}} = \frac{\partial L^{\mathrm{CC}}}{\partial \boldsymbol{\varepsilon}} = \langle \Phi_0 | (1 + \hat{\Lambda}) \frac{\partial \overline{H}}{\partial \boldsymbol{\varepsilon}} | \Phi_0 \rangle \,. \tag{3.58}$$

This approach allows the analytic evaluation of energy derivatives for non-variational wave functions, bypassing the need to solve for the response of the wave function parameters to the perturbation.

We pointed out in Sec.2.3.1 the existence of a connection between the left-eigenvalue problem reported in Eqn.(2.60) and the computation of properties. To see this, we first expand the commutator in Eqn.(3.57) and insert a resolution of identity on the right-hand side

$$\langle \Phi_L | \hat{\overline{H}} | \Phi_{\nu;k} \rangle = \langle \Phi_L | \hat{\tau}_{\nu;k} \hat{\overline{H}} | \Phi_0 \rangle \tag{3.59}$$

$$= \sum_{m=0}^{N} \sum_{\eta} \langle \Phi_L | \hat{\tau}_{\nu;k} | \Phi_{\eta;m} \rangle \langle \Phi_{\eta;m} | \hat{\overline{H}} | \Phi_0 \rangle \tag{3.60}$$

$$= \langle \Phi_L | \Phi_{\nu;k} \rangle \, E_{\mathrm{CC}}. \tag{3.61}$$

We then recover Eqn.(2.60) since only the term with $m = 0$ will survive. We may conclude that the lambda equations are the left-eigenvalue equations of the similarity-transformed Hamiltonian projected onto the excitation manifold. It should be noted that these latter equations, for first-order properties, do not depend on the perturbations, so we only need to solve these equations once.

Similarly to what was done previously, for the multipliers we may invoke the $(2n + 2)$ rule: the knowledge of the n-th derivative of the multipliers is sufficient to determine the $(2n + 2)$-th derivative of the CC Lagrangian [206].

$$\frac{d^{2n+2} L_{\mathrm{CC}}}{d\boldsymbol{\varepsilon}^{2n+2}} = f\left(\bar{\boldsymbol{t}}, \frac{d\bar{\boldsymbol{t}}}{d\boldsymbol{\varepsilon}}, \ldots, \frac{d^n \bar{\boldsymbol{t}}}{d\boldsymbol{\varepsilon}^n}\right). \tag{3.62}$$

In Appendix C we explicitly show the $2n + 2$ rule in action and provide an overview of the calculation of second-order molecular properties using the Lagrangian formalism.

A significant difference between Eqn.(3.56) and Eqn.(3.57) is that the latter are not

fully connected, meaning they consist of disconnected diagrams. To see this, we reformulate the left-hand side of Eqn.(3.59) as

$$\langle \Phi_L | \hat{\overline{H}} | \Phi_{\nu;k} \rangle = \langle \Phi_0 | \hat{\overline{H}} | \Phi_{\nu;k} \rangle + \langle \Phi_0 | [\hat{\Lambda}, \hat{\overline{H}}] | \Phi_{\nu;k} \rangle + \langle \Phi_0 | \hat{\overline{H}} \hat{\Lambda} | \Phi_{\nu;k} \rangle \,. \tag{3.63}$$

Inserting a resolution of identity in the final term, we obtain [142]

$$\begin{aligned} \frac{\partial L_{\mathrm{CC}}}{\partial t_{\nu;k}} = 0 = \langle \Phi_0 | \hat{\overline{H}} | \Phi_{\nu;k} \rangle + \langle \Phi_0 | [\hat{\Lambda}, \hat{\overline{H}}] | \Phi_{\nu;k} \rangle \\ + \sum_{m \neq 0}^{N} \sum_{\eta} \langle \Phi_0 | \hat{\overline{H}} | \Phi_{\eta;m} \rangle \langle \Phi_{\eta;m} | \hat{\Lambda} | \Phi_{\nu;k} \rangle \,, \quad k \leq k_{\max} \end{aligned} \tag{3.64}$$

where the term with $m = 0$ was cancelled by the right-hand side of Eqn.(3.59). Clearly, the Λ_1-equations are fully connected since the last term in Eqn. (3.64) is then equal to zero; however, starting from the Λ_2 equations onward, we begin to encounter disconnected terms. This result is somewhat surprising, as the $\hat{\Lambda}$-equations play a central role in the computation of molecular properties, which are required to be fully connected in order to ensure size-extensivity. As we will see shortly, however, the disconnected nature of the $\hat{\Lambda}$-equations does not compromise the size-extensivity of the resulting properties.

3.2.3 A diagrammatic perspective on the $\Lambda-$equations

We have previously shown how diagrammatic techniques can be effectively employed to derive the energy equations. In principle, we aim to adopt the same strategy for molecular properties. The first step in this direction is therefore to derive the $\hat{\Lambda}$-equations diagrammatically. In general, all the rules discussed in Sec.2.1 still apply; however, we now face the additional task of representing the de-excitation operator in diagrammatic form. This operator will be depicted essentially as a flipped version of a T diagram (as reported in Figure 3.2), placed above both the T and $\hat{H}$ diagrams. By convention, de-excitation operators are always depicted by a solid interaction line drawn above the vertex. In this case, we will have a particle line entering the vertex and a hole line exiting

In principle, one can derive the $\hat{\Lambda}$-equations from scratch using diagrammatic techniques. However, it is instructive to note that Kállay and co-workers [207] succeeded in deriving the $\hat{\Lambda}$-equations (for arbitrary excitation level) solely from the knowledge of the energy equations at arbitrary order. First, it is important to note that the full

(A) (B)

FIGURE 3.2: Diagrammatic representation of the $\hat{\Lambda}$ operators. Here, (A) represents the single de-excitation operator, while (B) corresponds to the double de-excitation operator.

CC Lagrangian in Eqn.(3.54) is defined as a scalar quantity, with both the bra and the ket states built upon the reference determinant. This implies that no open (free) lines can appear in any of its diagrams. Therefore, the generation of the CC Lagrangian is based on capping the original amplitude equations with a de-excitation operator $\hat{\Lambda}$ from above, thereby closing all the open upward lines, as exemplified by the central diagram in Figure 3.3. To obtain the working equations, we apply the standard two variational conditions: the stationarity of the Lagrangian with respect to both the Lagrange multipliers (the $\hat{\Lambda}$-amplitudes) and the cluster amplitudes (the $\hat{T}$-amplitudes). The $\hat{\Lambda}$-amplitudes appear linearly in the Lagrangian. This translates diagrammatically to the presence of at most one $\hat{\Lambda}$ diagram per diagram in the CC Lagrangian. Taking the derivative of the Lagrangian with respect to a specific $\hat{\Lambda}$-amplitude thus removes that particular Lagrange multiplier, and diagrammatically corresponds to removing the $\hat{\Lambda}$ interaction line, i.e going from the top to the middle diagram in Figure 3.3. In contrast, the $\hat{T}$-amplitudes appear nonlinearly in the Lagrangian, so that multiple $\hat{T}$ operators (up to four) can appear in each CC Lagrangian diagram. When taking the first derivative with respect to one particular $\hat{T}$-amplitude, the derivative removes the corresponding $\hat{T}$ interaction line individually. Consequently, if a given CC Lagrangian diagram contains n $\hat{T}$ operators, it will generate n separate diagrams in the resulting $\hat{\Lambda}$-equations, each associated with the removal of one $\hat{T}$ interaction line from the original diagram, i.e going from the bottom to the middle diagram in Figure 3.3. For full details of these operations and their diagrammatic representation, please refer to Ref. [207]. In Section 6.2.1, I will present the strategy we followed to compute coupled-cluster expectation values for CC wave functions of arbitrarily high excitation rank.

Unlike the energy equations, the $\hat{\Lambda}$-equations turn out to be disconnected, as highlighted in Eqn.(3.64). In particular, the last term is the source of this disconnection, since $\hat{\Lambda}$ and $\overline{\hat{H}}$ are not connected by construction. This naturally leads to the question of which Hamiltonian diagrams give rise to these disconnected contributions in the $\hat{\Lambda}$-equations.

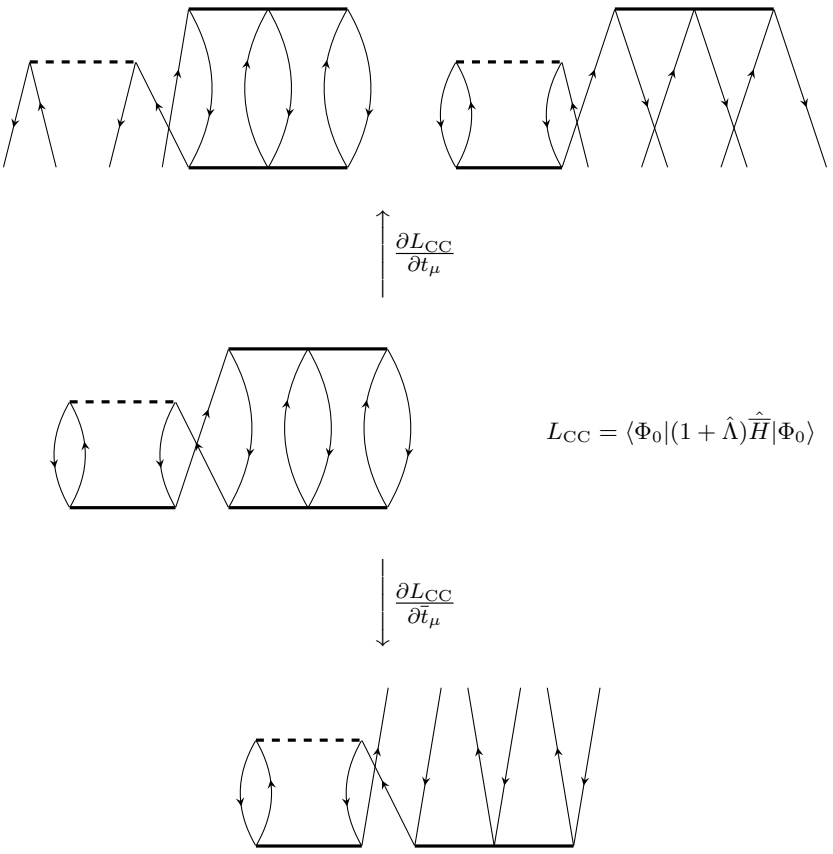

FIGURE 3.3: Diagrammatic structure of the coupled-cluster Lagrangian: the central diagram is obtained by capping all open lines in the amplitude equations with the de-excitation operator $\hat{\Lambda}$; the downward arrow indicates differentiation with respect to the multipliers $\bar{t}_\mu$, and the upward arrow indicates differentiation with respect to the cluster amplitudes t_μ.

This diagrammatic framework allows us to explicitly show from which amplitude equations the disconnected diagrams in the $\hat{\Lambda}$ equations originate. To do so, we recall that the normal-ordered Hamiltonian $\hat{H}_N$ must be connected to all possible cluster operators $\hat{T}$ (up to four clusters at most). Disconnected diagrams can only occur when the $\hat{\Lambda}$-operator is not directly connected to the Hamiltonian, which limits the possible elements to those given in Figure 3.4, having *no* upward lines and an *even* number of downward lines. In order to be disconnected upon removal of a $\hat{T}$-interaction line, the $\hat{\Lambda}$ has to be connected to that $\hat{T}$ only, hence by an *even* number of connections, while the $\hat{T}$ at the same time must be connected to the Hamiltonian. A comprehensive example is shown in Figure 3.5. This excludes disconnected diagrams from the $\hat{\Lambda}_1$-equations, as we concluded by more elaborate means in Eqn.(3.64). More generally, we also learn that at least one downward external line must emanate from the Hamiltonian, as indicated by the commutator appearing in Eqn.(3.57).

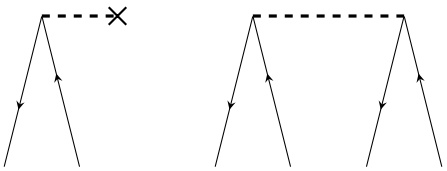

FIGURE 3.4: Elements of the Hamiltonian contributing to disconnected diagrams in the $\hat{\Lambda}$-equations.

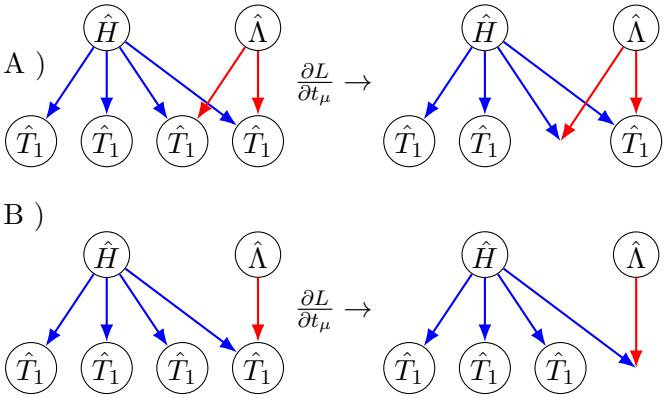

FIGURE 3.5: Diagrammatic illustration of the origin of disconnected terms in the $\hat{\Lambda}$ equations. In A), $\hat{H}_N$ and $\hat{\Lambda}$ share multiple $\hat{T}$ operators, so removing one $\hat{T}$ does not disconnect the diagram. In B), they share only a single $\hat{T}$ operator, and its removal leads to a disconnected diagram.

3.2.4 Expectation values

Having introduced the Λ-equations, we are now in the proper framework to derive the explicit form of expectation values within coupled-cluster theory. Once Eqs.(2.44) and (3.57) are satisfied, the derivative of the CC energy with respect to an external perturbation ε_A becomes

$$\frac{dE_{\mathrm{CC}}}{d\varepsilon_A} = \frac{\partial L^{\mathrm{CC}}}{\partial \varepsilon_A} = \langle \Phi_0 | (1 + \hat{\Lambda}) \frac{\partial \hat{\overline{H}}}{\partial \varepsilon_A} | \Phi_0 \rangle \,, \tag{3.65}$$

where we still refer to the perturbed Hamiltonian defined in Eqn.(3.1). We note that the unperturbed Hamiltonian $\hat{H}_0$ does not depend on ε_A, hence

$$\frac{\partial \hat{\overline{H}}(\boldsymbol{\varepsilon})}{\partial \varepsilon_A} = \underbrace{\frac{\partial \hat{\overline{H}}_0}{\partial \varepsilon_A}}_{=0} + \frac{\partial \hat{\overline{V}}(\boldsymbol{\varepsilon})}{\partial \varepsilon_A}. \tag{3.66}$$

Assuming a linear perturbation of the form

$$\hat{V}(\boldsymbol{\varepsilon}) = \sum_X \varepsilon_X \hat{H}_X, \tag{3.67}$$

we obtain

$$\frac{\partial \hat{V}(\boldsymbol{\varepsilon})}{\partial \varepsilon_A} = \sum_X \frac{\partial \varepsilon_X}{\partial \varepsilon_A} \hat{H}_X = \sum_X \delta_{AX} \hat{H}_X = \hat{H}_A. \tag{3.68}$$

Assuming that the perturbation operator $\hat{H}_A$ is a general one-body operator, we write

$$\hat{H}_A = \sum_{pq} h_{pq;A} \{a_p^\dagger a_q\}, \tag{3.69}$$

where curly brackets denote normal ordering. Substituting this into Eqn.(3.65), we obtain

$$\frac{dE_{\mathrm{CC}}}{d\varepsilon_A} = \frac{\partial L^{\mathrm{CC}}}{\partial \varepsilon_A} = \sum_{pq} h_{pq;A} \left\langle \Phi_0 | (1 + \hat{\Lambda}) e^{-\hat{T}} \{a_p^\dagger a_q\} e^{\hat{T}} | \Phi_0 \right\rangle . \tag{3.70}$$

We may then define the *one-body CC response density matrix* as

$$\gamma_{pq}^{\mathrm{CC}} = \left\langle \Phi_0 | (1 + \hat{\Lambda}) e^{-\hat{T}} \{a_p^\dagger a_q\} e^{\hat{T}} | \Phi_0 \right\rangle , \tag{3.71}$$

which encapsulates the linear response of the coupled-cluster wavefunction to one-body perturbations. We therefore conclude that the evaluation of CC expectation values reduces to the computation of the trace of the product between the one-body perturbation integrals and the CC response density matrix. Explicitly,

$$\frac{dE_{\mathrm{CC}}}{d\varepsilon_A} = \frac{\partial L^{\mathrm{CC}}}{\partial \varepsilon_A} = \sum_{pq} h_{pq;A} \, \gamma_{pq}^{\mathrm{CC}} = \mathrm{Tr}\left[\mathbf{h}^A \boldsymbol{\gamma}^{\mathrm{CC}}\right] , \tag{3.72}$$

where $\mathbf{h}^A$ is the matrix representation of the one-body perturbation operator $\hat{H}_A$ in the orbital basis, and $\boldsymbol{\gamma}^{\mathrm{CC}}$ is the corresponding CC response density matrix.

3.2.4.1 Comments on the size-extensivity

The disconnected nature of the lambda equations will not affect the size-extensivity of properties. By reconsidering again

$$\left.\frac{dL_{\mathrm{CC}}}{d\varepsilon_A}\right|_{\boldsymbol{\varepsilon}=\mathbf{0}} = \left\langle \Phi_0 | (1 + \hat{\Lambda}) \hat{\overline{H}}_A | \Phi_0 \right\rangle , \tag{3.73}$$

we can introduce a commutator in the right-hand side of Eqn.(3.73)

$$\langle\Phi_0|(1+\hat{\Lambda})\hat{\overline{H}}_A|\Phi_0\rangle = \langle\Phi_0|\hat{\overline{H}}_A + [\hat{\Lambda},\hat{\overline{H}}_A]|\Phi_0\rangle + \underbrace{\langle\Phi_0|\hat{\overline{H}}_A\hat{\Lambda}|\Phi_0\rangle}_{=0}, \tag{3.74}$$

where the last term is strictly zero since it has $\hat{\Lambda}$ acting on $|\Phi_0\rangle$. We therefore conclude that

$$\left.\frac{dL_{\mathrm{CC}}}{d\varepsilon_A}\right|_{\boldsymbol{\varepsilon}=\mathbf{0}} = \langle\Phi_0|\hat{\overline{H}}_A + [\hat{\Lambda},\hat{\overline{H}}_A]|\Phi_0\rangle\,, \tag{3.75}$$

which means that calculating first-order molecular properties requires only connected terms, as required for size-extensivity.

3.2.5 One-body CC response density matrix

The determination of the one-body CC response density matrix can be done by Wick's theorem or by the diagrammatic approach.

$$\begin{aligned}\gamma_{pq}^{\mathrm{CC}} &= \langle\Phi_0|(1+\hat{\Lambda})e^{-\hat{T}}\{a_p^\dagger a_q\}e^{\hat{T}}|\Phi_0\rangle \\ &= \langle\Phi_0|e^{-\hat{T}}\{a_p^\dagger a_q\}e^{\hat{T}}|\Phi_0\rangle + \langle\Phi_0|\hat{\Lambda}e^{-\hat{T}}\{a_p^\dagger a_q\}e^{\hat{T}}|\Phi_0\rangle.\end{aligned} \tag{3.76}$$

We may use the BCH expansion in order to expand the term $e^{-\hat{T}}\{a_p^\dagger a_q\}e^{\hat{T}}$, and since the operator $\{a_p^\dagger a_q\}$ contains two second-quantized operators, the BCH expansion will be exactly truncated at the second commutator

$$e^{-\hat{T}}\{a_p^\dagger a_q\}e^{\hat{T}} = \{a_p^\dagger a_q\} + [\{a_p^\dagger a_q\},\hat{T}] + \frac{1}{2}[[\{a_p^\dagger a_q\},\hat{T}],\hat{T}]. \tag{3.77}$$

and so

$$\begin{aligned}\langle\Phi_0|e^{-\hat{T}}\{a_p^\dagger a_q\}e^{\hat{T}}|\Phi_0\rangle = \langle\Phi_0|\{a_p^\dagger a_q\}|\Phi_0\rangle + \langle\Phi_0|[\{a_p^\dagger a_q\},\hat{T}]|\Phi_0\rangle \\ +\frac{1}{2}\langle\Phi_0|[[\{a_p^\dagger a_q\},\hat{T}],\hat{T}]|\Phi_0\rangle.\end{aligned} \tag{3.78}$$

As an example, we shall see the case for $\hat{T}_1$ and $\hat{\Lambda}_1$. For the first term, the only non zero contribution is

$$\begin{aligned}
\langle\Phi_0|e^{-\hat{T}}\{a_p^\dagger a_q\}e^{\hat{T}}|\Phi_0\rangle &= \sum_{ia} t_i^a \langle\Phi_0|[\{a_p^\dagger a_q\},\{a_a^\dagger a_i\}]|\Phi_0\rangle \\
&= \sum_{ia} t_i^a \langle\Phi_0|\{\overbrace{a_p^\dagger a_q a_a^\dagger a_i}\}|\Phi_0\rangle \\
&= \sum_{ia} t_i^a \delta_{qa}\delta_{pi}\delta_{p\in i}\delta_{q\in a} \\
&= t_i^a,
\end{aligned} \tag{3.79}$$

whereas, for the second one we get

$$\begin{aligned}
\langle\Phi_0|\hat{\Lambda}e^{-\hat{T}}\{a_p^\dagger a_q\}e^{\hat{T}}|\Phi_0\rangle = \langle\Phi_0|\hat{\Lambda}\{a_p^\dagger a_q\}|\Phi_0\rangle + \langle\Phi_0|\hat{\Lambda}[\{a_p^\dagger a_q\},\hat{T}]|\Phi_0\rangle \\
+\frac{1}{2}\langle\Phi_0|\hat{\Lambda}[[\{a_p^\dagger a_q\},\hat{T}],\hat{T}]|\Phi_0\rangle,
\end{aligned} \tag{3.80}$$

and for $\hat{\Lambda}_1$ we get

$$\begin{aligned}
\langle\Phi_0|\hat{\Lambda}_1\{a_p^\dagger a_q\}|\Phi_0\rangle &= \sum_{ia} \bar{t}_a^i \langle\Phi_0|\{a_i^\dagger a_a\}\{a_p^\dagger a_q\}|\Phi_0\rangle \\
&= \sum_{ia} \bar{t}_a^i \langle\Phi_0|\{\overbrace{a_i^\dagger a_a a_p^\dagger a_q}\}|\Phi_0\rangle \\
&= \sum_{ia} \bar{t}_a^i \delta_{qi}\delta_{pa}\delta_{p\in a}\delta_{q\in i} \\
&= \overline{t_a^i}.
\end{aligned} \tag{3.81}$$

When including double excitations, the algebraic structure of the expressions involved becomes increasingly intricate and less amenable to direct manipulation. In contrast, the diagrammatic approach offers a more intuitive and systematic framework for constructing the one-body CC response density matrix.

The first step is to understand how this object can be represented diagrammatically. Since the response density matrix involves a one-body operator, we can exploit the fact that such operators have already been treated in diagrammatic terms—most notably in the case of the Fock operator. This is also the strategy adopted by Kállay and Gauss [207]. The key idea is to use the Fock operator as a proxy for a general one-body operator during the diagrammatic construction. Once the full diagrammatic and algebraic form has been derived using the Fock operator as a placeholder, we can simply replace (or remove)

the Fock-specific contributions—namely the Fock matrix elements—and substitute in the desired one-body operator integrals. This can also be viewed as taking the derivative of the Fock operator with respect to f_{pq}. This strategy streamlines the derivation without loss of generality. As an example, we may consider again Eqn.(3.81) and we may simply substitute the term $\{a_p^\dagger a_q\}$ by $\hat{F}_N = \sum_{pq} f_{pq}\{a_p^\dagger a_q\}$. We recognize that the matrix element in Eqn.(3.81) is non-zero if and only if $\hat{F}_N$ is able to excite by one the reference state, and therefore we get the following diagram

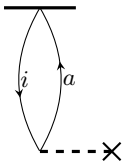

$$\langle \Phi_0 | \hat{\Lambda}_1 \hat{F}_N | \Phi_0 \rangle = \sum_{ia} \bar{t}_a^i f_i^a.$$

After doing that, me may simply remove the Fock operator (as well the Fock matrix element), getting,

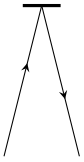

$$\langle \Phi_0 | \hat{\Lambda}_1 \{a_p^\dagger a_q\} | \Phi_0 \rangle = \bar{t}_a^i.$$

The same approach can be in principle adopted also per the two-body CC response density matrix, which is defined as

$$\Gamma^{\mathrm{CC}}_{pqrs} = \langle \Phi_0 | (1 + \hat{\Lambda}) e^{-\hat{T}} \{a_p^\dagger a_q^\dagger a_s a_r\} e^{\hat{T}} | \Phi_0 \rangle \,, \tag{3.82}$$

by using the normal-ordered two-electron operator $\hat{V}_N$.

Finally, it is worth discussing the elephant in the room, i.e that the one-particle density matrix obtained from truncated CC methods is generally *non-Hermitian*. This arises because the left and right CC wavefunctions are not simply complex conjugates in truncated

CC. Therefore, for practical calculations, is necessary to symmetrize it

$$\tilde{\gamma}_{pq}^{\mathrm{CC}} = \frac{1}{2}\left(\gamma_{pq}^{\mathrm{CC}} + \gamma_{qp}^{*\mathrm{CC}}\right). \tag{3.83}$$

However, in the limit of the full *full coupled-cluster method* (Full CC, formally equivalent to full configuration interaction), all excitations are included, and the exact left and right wavefunctions coincide, making $\boldsymbol{\gamma}^{\mathrm{CC}}$ Hermitian. As recently exploited by Weflen and coworkers [208], the apparent non-Hermitian nature of the one-particle density matrix in truncated coupled-cluster (CC) methods, usually considered a disadvantage, can actually be used to an advantage. By considering the *anti-symmetrized* density matrix, $\underline{\gamma}$, as

$$\underline{\gamma}_{pq}^{\mathrm{CC}} = \frac{1}{2}\left(\gamma_{pq}^{\mathrm{CC}} - \gamma_{qp}^{*\mathrm{CC}}\right). \tag{3.84}$$

we can compute the Frobenius norm of it, defining

$$||\underline{\gamma}||_F = \sqrt{\sum_{ij} |\underline{\gamma}_{oo}(i,j)|^2 + \sum_{ia} |\underline{\gamma}_{ov}(i,a)|^2 + \sum_{ai} |\underline{\gamma}_{vo}(a,i)|^2 + \sum_{ab} |\underline{\gamma}_{vv}(a,b)|^2}, \tag{3.85}$$

where we have defined the occupied-occupied (oo), occupied-virtual (ov), virtual-occupied (vo) and virtual-virtual (vv) blocks of the density matrix. The diagnostic factor is computed as

$$\text{diagnostic-factor} = \frac{||\underline{\gamma}||_F}{\sqrt{N_{el}}}, \tag{3.86}$$

where N_{el} is the number of correlated electrons. The asymmetry of the reduced one-particle density matrix can serve as a diagnostic indicator of both the intrinsic difficulty of a correlated electronic problem and the performance of a given CC approximation. In the limit of full coupled-cluster theory, the wavefunction is exact and the density matrix is Hermitian, while deviations from Hermiticity in truncated CC reflect the approximation and can therefore provide useful quantitative insight into the quality of the calculation. One may wonder about the applicability of this diagnostic factor in relativistic calculations. In fact, I have implemented its evaluation for high-order CC methods in ExaCorr [193], within a private version of the `DIRAC` program package [29], and computed the diagnostic factor for the Be atom, accurately reproducing the values reported in the original work [208]. A paper presenting the results for relativistic systems is currently in preparation and will not be included in this thesis.

Chapter 4

Nuclear Electric Quadrupole Interaction

The nuclear electric quadrupole interaction originates from the coupling between the nuclear electric quadrupole moment (NQM) and the electric field gradient (EFG) generated by the electronic cloud surrounding the nucleus. This interaction is non-zero only for nuclei with spin quantum number $I > 1/2$, which possess an a non-spherical charge distribution and hence a finite quadrupole moment. The quadrupole interaction manifests itself in measurable spectroscopic features, such as the splitting or shifting of nuclear energy levels, and plays a key role in techniques like nuclear magnetic resonance (NMR), nuclear quadrupole resonance (NQR), and Mössbauer spectroscopy. From a theoretical perspective, it provides a direct link between nuclear and electronic properties. While the EFG is crucial for determining physical observables such as the nuclear quadrupole moment—through the combination with known quadrupole coupling constants—it also carries significant chemical information. As emphasized by the Dailey–Townes model, the EFG reflects the local electronic structure and bonding environment, and thus serves as a sensitive probe of chemical bonding and electron distribution near the nucleus.

In this chapter, we provide a detailed theoretical and computational analysis of the EFG and its role in the nuclear quadrupole interaction. Most of the theoretical background reported in this chapter comes from the books listed in bibliography [197, 198] and from our recent paper [209].

4.1 Electrostatic interaction energy

The electrostatic interaction energy between a probe charge distribution $\rho(\mathbf{r})$ and the electrostatic potential $\varphi(\mathbf{r})$ generated by a distinct source charge distribution $\rho(\mathbf{r}')$ is given by

$$E_{\text{int}} = \int \rho(\mathbf{r})\,\varphi(\mathbf{r})\,d^3r, \tag{4.1}$$

where $\mathbf{r}$ denotes the coordinates of the observation points at which the probe charge distribution is located. The electrostatic potential generated by the source distribution is given by the Coulomb expression

$$\varphi(\mathbf{r}) = \frac{1}{4\pi\varepsilon_0}\int \frac{\rho(\mathbf{r}')}{|\mathbf{r}-\mathbf{r}'|}\,d^3r', \tag{4.2}$$

where $\mathbf{r}'$ runs over the coordinates of the source charge distribution. A sketch is reported in Figure 4.1.

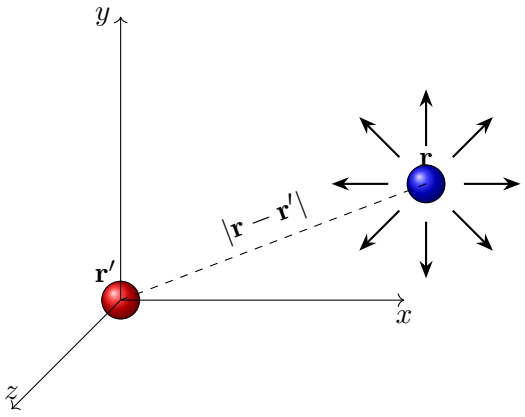

FIGURE 4.1: Schematic representation of a source point $\mathbf{r}'$ and a probe point $\mathbf{r}$. The dashed line indicates the distance between source and probe, while the arrows at the probe represent the electric field vectors generated by the source. The axes indicate the Cartesian reference frame.

When the observation point $\mathbf{r}$ is located far from the source region, such that $|\mathbf{r}'| \ll |\mathbf{r}|$ for all $\mathbf{r}'$ where $\rho(\mathbf{r}')$ is nonzero, it is convenient to expand the Coulomb kernel $|\mathbf{r}-\mathbf{r}'|^{-1}$ in a Taylor series in powers of $\mathbf{r}'$ around the origin. This yields the multipole expansion

$$\frac{1}{|\mathbf{r}-\mathbf{r}'|} = \sum_{n=0}^{\infty} \frac{(-1)^n}{n!} r'_{\alpha_1}\cdots r'_{\alpha_n}\,\frac{\partial^n}{\partial r_{\alpha_1}\cdots\partial r_{\alpha_n}}\frac{1}{|\mathbf{r}|}, \tag{4.3}$$

where repeated Cartesian indices imply summation over x, y, z. Inserting Eq. (4.3) into Eq. (4.2) and interchanging summation and integration leads to the standard multipole

expansion of the electrostatic potential

$$\varphi(\mathbf{r}) = \frac{1}{4\pi\varepsilon_0}\sum_{n=0}^{\infty}\frac{(-1)^n}{n!}Q^{[n]}_{\alpha_1\cdots\alpha_n}\frac{\partial^n}{\partial r_{\alpha_1}\cdots\partial r_{\alpha_n}}\frac{1}{|\mathbf{r}|}, \tag{4.4}$$

where the Cartesian multipole moments of the source charge distribution, defined with respect to the origin, are given by

$$Q^{[0]} = \int \rho(\mathbf{r}')\, d^3r' \qquad \text{(monopole)}, \tag{4.5}$$

$$Q^{[1]}_{\alpha} = \int r'_{\alpha}\, \rho(\mathbf{r}')\, d^3r' \qquad \text{(dipole)}, \tag{4.6}$$

$$Q^{[2]}_{\alpha\beta} = \int r'_{\alpha}r'_{\beta}\, \rho(\mathbf{r}')\, d^3r' \qquad \text{(quadrupole)}, \tag{4.7}$$

$$Q^{[3]}_{\alpha\beta\gamma} = \int r'_{\alpha}r'_{\beta}r'_{\gamma}\, \rho(\mathbf{r}')\, d^3r' \qquad \text{(octupole)}. \tag{4.8}$$

The expansion in Eq. (4.4) expresses the electrostatic potential at large distances in terms of the multipole moments of the source charge distribution.

We should recall that, in the static case, the electric field is related to the potential by Eqn.(A.9)

$$\mathcal{E}^{[n]}_{\alpha;\beta_1\cdots\beta_n} = \frac{\partial^n \mathcal{E}_{\alpha}(\mathbf{r})}{\partial r_{\beta_1}\cdots\partial r_{\beta_n}} = -\frac{\partial^{n+1}\varphi(\mathbf{r})}{\partial r_{\alpha}\partial r_{\beta_1}\cdots\partial r_{\beta_n}}, \tag{4.9}$$

Unless otherwise specified, all electric field components and their derivatives are evaluated at the origin, $\mathbf{r} = \mathbf{0}$, which is chosen as the reference point for the multipole expansion. Note that the semicolon notation for the electric field derivatives is used to emphasize that the partial derivatives of the electric field components are not generally symmetric under the exchange of indices α and β; that is,

$$\mathcal{E}^{[1]}_{\alpha;\beta} = \frac{\partial \mathcal{E}_{\alpha}}{\partial r_{\beta}} \neq \frac{\partial \mathcal{E}_{\beta}}{\partial r_{\alpha}} = \mathcal{E}^{[1]}_{\beta;\alpha}, \tag{4.10}$$

Therefore, substituting this expansion into Eqn. (4.1), the interaction energy can be expressed as a series of contributions from successive multipole orders:

$$E_{\text{int}} = Q^{[0]}\varphi(\mathbf{0}) - Q^{[1]}_{\alpha}\mathcal{E}_{\alpha}(\mathbf{0}) - \frac{1}{2}Q^{[2]}_{\alpha\beta}\mathcal{E}^{[1]}_{\alpha;\beta}(\mathbf{0}) - \frac{1}{3!}Q^{[3]}_{\alpha\beta\gamma}\mathcal{E}^{[2]}_{\alpha;\beta\gamma}(\mathbf{0}) + \ldots \tag{4.11}$$

In this thesis, we focus on the quadrupole term:

$$E_{E_2} = -\frac{1}{2}\sum_{\alpha\beta} Q^{[2]}_{\alpha\beta}\mathcal{E}^{[1]}_{\alpha;\beta}(\mathbf{0}). \tag{4.12}$$

4.2 Nuclear electric quadrupole moment interaction

We are now in the appropriate framework to define the *Nuclear Electric Quadrupole Moment Interaction*. To this end, we consider a particular nucleus K and associate to it a charge density $\rho_n^K(\mathbf{r})$. This nucleus will experience an external electrostatic potential generated by the charge distribution of the surrounding electrons ($\rho_e(\mathbf{r})$) and of any other nuclei present in the system ($\rho_n^A(\mathbf{r})$). Therefore, as we pointed out in Eqn. (4.12), the electric quadrupole moment of a nucleus K couples to the electric field gradient (EFG) at the nuclear position, here conveniently located at the origin and generated by the surrounding charges.

The nuclear electric quadrupole interaction energy reads as

$$E^K_{E2} = -\frac{1}{2}\sum_{\alpha\beta} Q^{[2]}_{\alpha\beta}\mathcal{E}^{[1]}_{\alpha;\beta}; \quad Q^{[2]}_{\alpha\beta} = \int r_\alpha r_\beta \rho_n^K(\mathbf{r})\, d^3\mathbf{r}. \tag{4.13}$$

Components $\mathcal{E}^{[1]}_{\alpha;\beta}$ of the electric field gradient are generated by the charge densities associated with electrons and other nuclei

$$\rho(\mathbf{r}) = \rho_e(\mathbf{r}) + \sum_{A\neq K}\rho_n^A(\mathbf{r}), \tag{4.14}$$

and can therefore be expressed as

$$\mathcal{E}^{[1]}_{\alpha;\beta} = \left.\frac{\partial \mathcal{E}_\alpha}{\partial r_\beta}\right|_{\mathbf{r}=\mathbf{0}} = -\left.\frac{\partial^2\varphi}{\partial r_\alpha \partial r_\beta}\right|_{\mathbf{r}=\mathbf{0}} = -\chi^{[1]}_{\alpha\beta} + \frac{1}{3\varepsilon_0}\delta_{\alpha\beta}\rho_e(\mathbf{0}), \tag{4.15}$$

where appears the *traceless* part of the *negative* electric field gradient

$$\chi^{[1]}_{\alpha\beta} = \frac{1}{4\pi\varepsilon_0}\int \rho(\mathbf{r})\frac{3r_\alpha r_\beta - \delta_{\alpha\beta}r^2}{r^5} d^3\mathbf{r}. \tag{4.16}$$

Due to its importance, we explicitly derive Eqn.(4.15) in Appendix D.1. The above interaction, Eqn.(4.13), is expressed in terms of components $Q^{[2]}_{\alpha\beta}$ of the *Cartesian* electric quadrupole moment tensor. In terms of the *traceless* electric quadrupole moment tensor

[210]

$$\Theta^{[2]}_{\alpha\beta} = \frac{3}{2}\left(Q^{[2]}_{\alpha\beta} - \delta_{\alpha\beta}\frac{1}{3}\sum_{\gamma} Q^{[2]}_{\gamma\gamma}\right), \tag{4.17}$$

the interaction reads

$$E^{K}_{E2} = \frac{1}{3}\sum_{\alpha\beta}\Theta^{[2]}_{\alpha\beta}\chi^{[1]}_{\alpha\beta} - \frac{1}{6}\sum_{\alpha} Q^{[2]}_{\alpha\alpha}\sum_{\beta}\mathcal{E}^{[1]}_{\beta;\beta}. \tag{4.18}$$

The second term, denoted the Poisson term, contains the divergence of the electric field at the nuclear position

$$\sum_{\beta}\mathcal{E}^{[1]}_{\beta;\beta} = (\nabla\cdot\mathcal{E})|_{\mathbf{r}=\mathbf{0}} = -\nabla^2\varphi(\mathbf{r})\big|_{\mathbf{r}=\mathbf{0}} = \rho_e(\mathbf{0})/\varepsilon_0 \neq 0, \tag{4.19}$$

which by Gauss's law equals the source density at the expansion point divided by the electric constant ε_0. In many cases the source density is zero at the expansion point, such that the quadrupole interaction is fully described in terms of the traceless form, hence showing its utility. For nuclear quadrupole coupling, though, this is not the case, since the electronic charge density ρ_e can not be expected to be zero at the nuclear origin. However, since the Poisson term is a product of two traces, it is perfectly isotropic and can in practice be dropped since it does not contribute to hyperfine splittings. This can be seen explicitly by noting that, using angular momentum algebra, the components of the traceless nuclear electric quadrupole moment for a nuclear spin state $|I, m_I\rangle$ can be expressed in terms of nuclear spin operators as (see for instance Appendix G of Ref. [197])

$$\Theta^{[2]}_{\alpha\beta} = \frac{eQ}{\hbar^2 I(2I-1)}\langle I, m_I|\frac{1}{2}(3\hat{I}_\alpha\hat{I}_\beta - \delta_{\alpha\beta}\hat{I}^2)|I, m_I\rangle. \tag{4.20}$$

In the above expression appears the electric quadrupole moment Q of the nucleus, defined by $eQ = 2\Theta_{zz}$ where e is the fundamental charge. By similar arguments one finds that

$$\sum_{\alpha} Q^{[2]}_{\alpha\alpha} = \frac{eQ}{\hbar^2 I(2I-1)}\langle I, m_I|\hat{I}^2|I, m_I\rangle = \frac{eQ(I+1)}{(2I-1)}. \tag{4.21}$$

The interaction energy associated with a specific nuclear spin level can thereby be expressed as

$$E_{E2}(I, m_I) = \frac{eQ}{\hbar^2 6I(2I-1)}\sum_{\alpha\beta}\langle I, m_I|(3\hat{I}_\alpha\hat{I}_\beta - \delta_{\alpha\beta}\hat{I}^2)|I, m_I\rangle\chi^{[1]}_{\alpha\beta} - \frac{1}{6\varepsilon_0}\frac{eQ(I+1)}{(2I-1)}\rho_e(\mathbf{0}), \tag{4.22}$$

where the latter term is independent of the azimuthal quantum number m_I, hence do not contribute to hyperfine splittings. It should be noted that the above expression ignores electron-nucleus overlap effects [211, 212]. Furthermore, Sternheimer pointed out that the presence of a nuclear electric quadrupole moment should induce a quadrupole in the electron cloud, for instance the atomic core, which were thought to otherwise not contribute to the E_{E2} interaction [213]. At first sight the resulting Sternheimer shielding appears to be not included in our methodology, but this is not the case, as explained in Appendix D.2.

Dropping the Poisson term, the expression can be further simplified by transforming to a principal axis system, where the electric field gradient tensor becomes diagonal. In this frame we get

$$E_{E_2}(I, m_I) = \frac{eQ}{6\hbar^2 I(2I-1)} \sum_{\alpha} \langle I, m_I | (3\hat{I}_\alpha^2 - \hat{I}^2) \chi^{[1]}_{\alpha;\alpha} | I, m_I \rangle \,, \tag{4.23}$$

and without losing generality we can assume $|\chi^{[1]}_{z;z}| > |\chi^{[1]}_{y;y}| > |\chi^{[1]}_{x;x}|$. Introducing the asymmetry parameter η and the electric field gradient q as

$$\eta = \frac{(\chi^{[1]}_{x;x} - \chi^{[1]}_{y;y})}{\chi^{[1]}_{z;z}} \;;\; eq = \chi^{[1]}_{z;z}, \tag{4.24}$$

we get

$$E_{E_2} = \frac{e^2 Qq}{4\hbar^2 I(2I-1)} \langle I, m_I | (3\hat{I}_z^2 - \hat{I}^2) + \eta(\hat{I}_x^2 - \hat{I}_y^2) | I, m_I \rangle \,, \tag{4.25}$$

and by introducing the ladder operators $\hat{I}_+$ and $\hat{I}_-$ we get

$$E_{E_2} = \frac{e^2 Qq}{4\hbar^2 I(2I-1)} \langle I, m_I | (3\hat{I}_z^2 - \hat{I}^2) + \frac{\eta}{2}(\hat{I}_+^2 + \hat{I}_-^2) | I, m_I \rangle \,. \tag{4.26}$$

One should note that the definition of the asymmetry parameter η is sometimes given in terms of the absolute values of the diagonal components of the EFG tensor. However, this is not strictly necessary. Indeed, in order to satisfy the traceless condition

$$\chi^{[1]}_{xx} + \chi^{[1]}_{yy} + \chi^{[1]}_{zz} = 0, \tag{4.27}$$

together with the ordering convention

$$|\chi^{[1]}_{zz}| \geq |\chi^{[1]}_{yy}|, \geq |\chi^{[1]}_{yy}|, \tag{4.28}$$

the two smaller components, $\chi^{[1]}_{xx}$ and $\chi^{[1]}_{yy}$, must necessarily share the same sign. By additionally imposing

$$|\chi^{[1]}_{yy}| \geq |\chi^{[1]}_{xx}|, \tag{4.29}$$

one ensures that the asymmetry parameter is positive and constrained to the interval $\eta \in [0, 1]$. It should be emphasized, however, that in the limiting case $\eta \to 1$ the sign of the quadrupole splitting cannot be determined unambiguously. Achieving $\eta = 1$ requires the condition

$$\chi^{[1]}_{xx} = 0, \quad \chi^{[1]}_{yy} = -\chi^{[1]}_{zz}, \tag{4.30}$$

which corresponds to a maximal anisotropy of the EFG tensor. In this situation, a degeneracy arises between the $\chi^{[1]}_{yy}$- and $\chi^{[1]}_{zz}$-axes, such that the orientation of the principal axes system cannot be uniquely defined.

Focusing on atoms and linear systems, we have $\eta = 0$. Therefore, interaction energy reads

$$E_{E2}\left(I, m_I\right) = \frac{e^2 qQ}{4I\left(2I-1\right)}\left[3m_I^2 - I\left(I+1\right)\right]. \tag{4.31}$$

From axial symmetry it follows that $\chi^{[1]}_{xx} = \chi^{[1]}_{yy} = -\frac{1}{2}\chi^{[1]}_{zz}$. The interaction of the electric quadrupole results in a division of the $(2I+1)$ magnetic substates, but it does not alter the average energy of the nuclear spin levels. If $\eta = 0$, the substates sharing the same magnitude of $|m_I|$ stay at the same energy level. We shall note that m_I is a good quantum number, and the usual magnetic dipole transition rules can be applied. Thus, we can define the transition energies between two nuclear energy levels E_m and $E_{m\pm1}$ as

$$\Delta E_{m\pm1,m} = E_{m\pm1} - E_m = \nu_Q(2m_I \pm 1), \tag{4.32}$$

where we have defined the frequency of absorption

$$\nu_Q = \frac{3e^2qQ}{4I(2I-1)h}. \tag{4.33}$$

As a concrete example, we shall consider nuclear states with spin $I = 3/2$, such as in the case of ^{201}Hg. The quadrupole interaction causes the splitting between the states

$|3/2, \pm 3/2\rangle$ and $|3/2, \pm 1/2\rangle$, and using Eqn.(4.31)) we get two nuclear energy levels

$$E_{\pm 3/2} = \frac{e^2 Qq}{4}, \tag{4.34}$$

$$E_{\pm 1/2} = -\frac{e^2 Qq}{4}. \tag{4.35}$$

Combining Eqn.(4.32) and Eqn.(4.33) we may see that the NQCC is easily related with the frequency of absorption

$$\Delta E_{\pm 3/2, \pm 1/2} = \frac{1}{2} e^2 qQ = h\nu_Q. \tag{4.36}$$

Thus, for the a nucleus with $I = 3/2$ we are expecting only one NQR transition, and the knowledge of ν_Q reveals the NQCC through Eqn.(4.36). The measure $\Delta E_{m\pm 1,m}$, frequently denoted as ΔE_Q, is known as the *quadrupole splitting*. It offers insights into both bond characteristics and the local symmetry at the examined site.

For a generic system $\eta \neq 0$, and therefore Eqn.(4.26) contains off-diagonal terms. From basic rules of angular momentum algebra, we find

$$\langle I, m|\hat{H}_Q|I, m'\rangle = \frac{e^2 qQ}{4I(2I-1)}\Big[\big(3m^2 - I(I+1)\big)\delta_{m,m'} + \frac{\eta}{2}\big(f_+(I,m')\,\delta_{m,m'+2} + f_-(I,m')\,\delta_{m,m'-2}\big)\Big], \tag{4.37}$$

where we have defined

$$f_+(I,m') = \sqrt{\big(I(I+1) - m'(m'+1)\big)\big(I(I+1) - (m'+1)(m'+2)\big)}, \tag{4.38}$$

$$f_-(I,m') = \sqrt{\big(I(I+1) - m'(m'-1)\big)\big(I(I+1) - (m'-1)(m'-2)\big)}. \tag{4.39}$$

Again, for the $I = 3/2$ case, using Eqn.(4.37), the matrix representation of the nuclear quadrupole Hamiltonian is

$$\langle \hat{H}_Q \rangle = \frac{e^2 qQ}{12} \begin{pmatrix} 3 & 0 & \sqrt{3}\eta & 0 \\ 0 & -3 & 0 & \sqrt{3}\eta \\ \sqrt{3}\eta & 0 & -3 & 0 \\ 0 & \sqrt{3}\eta & 0 & 3 \end{pmatrix}. \tag{4.40}$$

We can exactly diagonalize it, leading to the following energy levels

$$E_{\pm 3/2} = h\nu_Q \left(1 + \frac{\eta^2}{3}\right)^{1/2} \tag{4.41}$$

$$E_{\pm 1/2} = -h\nu_Q \left(1 + \frac{\eta^2}{3}\right)^{1/2}, \tag{4.42}$$

which gives the unique allowed transition frequency

$$\Delta E_{\pm 3/2, \pm 1/2} = 2h\nu_Q \left(1 + \frac{\eta^2}{3}\right)^{1/2}, \tag{4.43}$$

in line with the results reported by Townes and Dailey [214], Pound [215] and Gütlich [216]. Again, only one transition is expected for this system. However, in such situation we have two unknowns (η and eq), and so the NQCC can not be obtained from direct NQR experiments. Ruby and Flinn [217] suggested the possibility of applying a very small magnetic field in order to remove the degeneracy of the energy levels in the Mossbauer spectrum; the theory was developed by Collins [218] and numerically by Gabriel and Ruby [219]. The same approach was then applied also in NQR by Brooker and Creel [220]. Consequently, for $I = 3/2$, four potential transitions become observable, enabling the determination of ν_Q and η.

The first section of the Applications part of this thesis is devoted to the study of the electric field gradient at nuclear centers in molecules, with particular attention to the chemical insight that can be extracted from it, as suggested by the Dailey–Townes model [61]. This model will be shown to correspond to a specific approximation within the framework of projection analysis for expectation values [221, 222], providing a useful interpretative tool for understanding electronic structure contributions.

4.3 Dailey–Townes model

The Dailey-Townes model [61] provides a simple framework for interpreting nuclear quadrupole coupling constants in molecules from the perspective of valence electron distributions. The model relates the electric field gradient at a nucleus primarily to the population and anisotropy of its valence p-orbitals, assuming spherical core orbitals contribute negligibly. In the following, this model will be derived and discussed.

The electric field gradient q at the position of nucleus K in an N-electron molecule can be obtained as an expectation value

$$\langle e\hat{q}_K \rangle = \underbrace{\left\langle \sum_{i=1}^{N} \frac{-e}{4\pi\varepsilon_0} \left[\frac{3z_{iK}^2 - r_{iK}^2}{r_{iK}^5} \right] \right\rangle}_{\text{Electronic: } eq_K^e} + \underbrace{\sum_{A \neq K} \frac{Z_A e}{4\pi\varepsilon_0} \left[\frac{3Z_{AK}^2 - R_{AK}^2}{R_{AK}^5} \right]}_{\text{Nuclear: } eq_K^n}, \tag{4.44}$$

where the nuclear contribution eq_K^n (not considering rovibrational degrees of freedom [223–225]) is a simple scalar. At the self-consistent field (SCF) level, the electronic contribution is

$$\langle e\hat{q}_K^e \rangle = \sum_{i}^{N} \langle \psi_i^{\text{MO}} | e\hat{q}_K^e | \psi_i^{\text{MO}} \rangle. \tag{4.45}$$

4.3.1 Projection analysis

As we shall see, the Dailey-Townes model is founded on contributions from individual atomic shells. Therefore, our analysis is conducted using the projection analysis [221, 226], which expresses molecular orbitals as a linear combination of atomic orbitals (LCAO)

$$|\psi_i^{\text{MO}}\rangle = \sum_{A} \sum_{p \in A} c_{p,i}^{A} |\psi_p^{A}\rangle + |\psi_i^{\text{pol}}\rangle, \tag{4.46}$$

very much in line with common chemical thinking [227, 228]. It should be stressed that these are pre-calculated orbitals of the atoms constituting the molecule. By default, the expansion is limited to atomic orbitals occupied in the atomic ground state. The orthogonal complement ψ_i^{pol} is denoted the polarization contribution. Significant polarization complicates analysis and may be a sign that important contributions from other AOs are missing. The polarization contribution can be completely eliminated by transformation to intrinsic atomic orbitals (IAOs) [229]. However, in the present setting the polarization contribution carries its name aptly since it provides a precise definition of the difference between the molecular space and the superposition of the free atomic ones. Inserting the expansion Eqn. (4.46) into the above expectation value, Eqn. (4.45) provides a decomposition into intra-atomic and inter-atomic contributions, as well as contributions associated with polarization

$$\langle e\hat{q}_K^e \rangle = \sum_{A} \langle e\hat{q}_K^e \rangle_{\text{intra}}^{(A)} + \sum_{A} \sum_{B \neq A} \langle e\hat{q}_K^e \rangle_{\text{inter}}^{(A,B)} + \langle e\hat{q}_K^e \rangle_{\text{pol}}. \tag{4.47}$$

In passing, we note that if $e\hat{q}^e_K$ above is replaced by the identity operator, we obtain a decomposition of the integrated density (electrons) in line with Mulliken population analysis [230], with net populations given by intra-atomic contributions and gross populations defined in the usual way as

$$g(A) = \langle 1 \rangle^{(A)}_{\text{intra}} + \frac{1}{2} \sum_A \sum_{B \neq A} \langle 1 \rangle^{(A,B)}_{\text{inter}}. \tag{4.48}$$

Further decomposition in terms of atomic orbitals gives effective electronic configurations of atoms within the molecule. A crucial difference with respect to Mulliken population analysis, though, is that projection analysis is very stable with respect to a change of basis [221].

If we now focus on the intra-atomic contribution $\langle e\hat{q}^e_K \rangle^{(K)}_{\text{intra}}$ to eq^e_K from the same center, it can be written as

$$\langle e\hat{q}^e_K \rangle^{(K)}_{\text{intra}} = \underbrace{\sum_{p \in K} D^{KK}_{pp} \langle \psi^K_p | e\hat{q}^e_K | \psi^K_p \rangle}_{\text{principal}} + \underbrace{\sum_{p \in K} \sum_{(q \neq p) \in K} D^{KK}_{pq} \langle \psi^K_q | e\hat{q}^e_K | \psi^K_p \rangle}_{\text{hybridization}}, \tag{4.49}$$

where appears a density matrix

$$D^{AB}_{pq} = \sum_i^N c^A_{pi} c^{B*}_{qi}, \tag{4.50}$$

built from the expansion coefficients of Eqn. (4.46). We distinguish between principal contributions, which would also contribute to the atomic expectation value, and hybridization contributions, which arises due to the mixing of orbitals of a given atom within the molecule [231].

4.3.2 Decomposition of the EFG in terms of reference orbitals

Since the matrix elements of $\langle e\hat{q}^e_K \rangle^{(K)}_{\text{intra}}$ are limited to atomic orbitals of the same center, much information is provided by taking into account the structure of the atomic orbitals. Throughout this work we shall mostly limit attention to the case where spin-orbit interaction is not included, in line with the Dailey–Townes model. The general form of

scalar-relativistic, as well as non-relativistic, atomic orbitals is

$$\psi_{n\ell m} = R_{n\ell}(r)\, Y_{\ell m}(\theta, \phi)\,. \tag{4.51}$$

Placing the nucleus K at the origin, the electronic EFG operator can be expressed as

$$\frac{3z^2 - r^2}{r^5} = \frac{3\cos^2\theta - 1}{r^3} = \frac{2}{r^3} C_0^2(\theta, \phi)\,, \tag{4.52}$$

where appears a component of the spherical harmonic tensor [232, 233]

$$C_m^\ell(\theta, \phi) = \left(\frac{4\pi}{2\ell + 1}\right)^{1/2} Y_{\ell m}(\theta, \phi)\,. \tag{4.53}$$

Matrix elements can then be factorized into radial and angular parts

$$\langle \psi^K_{n\ell m} | e\hat{q}^e_K | \psi^K_{n'\ell' m'} \rangle_{r,\theta,\phi} = -\frac{2e}{4\pi\varepsilon_0} \langle R_{n\ell} | r^{-3} | R_{n'\ell'} \rangle_r \langle Y_{\ell m} | C_0^2 | Y_{\ell' m'} \rangle_{\theta,\phi}. \tag{4.54}$$

From consideration of angular momentum and parity we obtain the following selection rules

$$\ell' \in \{|\ell - 2|\,, \ell, \ell + 2\} \quad \wedge \quad m' = m. \tag{4.55}$$

Furthermore, within an atomic shell ($\ell' = \ell$) matrix elements are given by

$$\langle \psi^K_{n\ell m} | e\hat{q}^e_K | \psi^K_{n\ell m'} \rangle_{r,\theta,\phi} = -\frac{2e}{4\pi\varepsilon_0} \langle r^{-3} \rangle \frac{\ell(\ell + 1) - 3m^2}{(2\ell - 1)(2\ell + 3)} \delta_{mm'}. \tag{4.56}$$

We note in particular the appearance of the inverse cubic radial expectation value $\langle r^{-3} \rangle$, which shows that the EFG probes the core region around the nucleus, making it sensitive to relativistic effects.

The chemical interest of the EFG arises from Unsölds theorem, [60] which essentially states that a closed atomic shell is spherically symmetric. Its contribution to the EFG expectation value is thereby zero, that is,

$$\sum_{m=-\ell}^{\ell} |Y_{\ell m}(\theta, \phi)|^2 = \frac{2\ell + 1}{4\pi} \quad \Rightarrow \quad \sum_{m=-\ell}^{\ell} \langle Y_{\ell m} | C_0^2 | Y_{\ell m} \rangle_{\theta,\phi} = 0. \tag{4.57}$$

(We note in passing that the left-hand side of the above equations shows the utility of the normalization chosen for the spherical harmonic tensors, Eqn. (4.53).) This observation

suggests that core orbitals do not contribute to the EFG expectation value. Instead, the operator $e\hat{q}^e_K$ samples the inner tails of valence orbitals, making it sensitive to electron correlation. The need to properly account for both relativity and electron correlation makes the accurate calculation of the EFG quite challenging, as illustrated by the determination of the NQM of ^{197}Au [234, 235] and ^{209}Bi [32, 236–241]. An exemplary recent recent calculation has been reported by Skripnikov and Barzakh [242].

The basis of the Dailey–Townes (DT) model is the above observation that the EFG is sensitive to deviations from spherical symmetry. Such deviations can be induced by chemical bonding. Since core orbitals as well as valence s-orbitals are not expected to contribute and that positive and negative charge on other centers possibly cancel out (*vide infra*), Dailey and Townes suggested that the EFG is entirely due to the contribution of valence p-orbitals on the atom of interest. In the present notation their approximation therefore reads

$$\langle e\hat{q}_K\rangle \approx \langle e\hat{q}^e_K\rangle^{(K)}_{\text{intra}} \approx \frac{2e}{4\pi\varepsilon_0}\langle r^{-3}\rangle_{np} \times \frac{2}{5}\left(n_x + n_y - 2n_z\right); \quad n_\alpha = D^{KK}_{np_\alpha;np_\alpha}, \tag{4.58}$$

where we used Eqn. (4.56).

The angular part of Eqn. (4.54) may be evaluated using angular momentum algebra, notably the Wigner–Eckart theorem [243]. The same tools may be used when extending the formalism to include spin-orbit interaction [244]. We start from the general form of 4-component atomic orbitals

$$\psi_{njm_j} = \begin{bmatrix} R^L_{n\kappa}(r)\,\xi_{\kappa,m_j}(\theta,\phi) \\ iR^S_{n\kappa}(r)\,\xi_{-\kappa,m_j}(\theta,\phi) \end{bmatrix}, \tag{4.59}$$

with real scalar radial functions for the large (L) and small (S) components and 2-component complex angular functions. The angular functions are defined in terms of quantum numbers j,m_j,ℓ and κ, with the sign of $\kappa = 2(\ell - j)(j + 1/2)$ indicating from which orbital angular momentum ℓ the total angular momentum j is generated [244, 245]. Intra-atomic matrix elements over the EFG operator are given by

$$\begin{aligned}\langle\psi^K_{njm_j}|e\hat{q}^e_K|\psi^K_{n'j'm'_j}\rangle_{r,\theta,\phi} \;=\; & -\frac{2e}{4\pi\varepsilon_0}\langle R^L_{n\kappa}|r^{-3}|R^L_{n'\kappa'}\rangle_r\langle\xi_{\kappa,m_j}|C^2_0|\xi_{\kappa',m'_j}\rangle_{\theta,\phi} \\ & -\frac{2e}{4\pi\varepsilon_0}\langle R^S_{n\kappa}|r^{-3}|R^S_{n',\kappa'}\rangle_r\langle\xi_{-\kappa,m_j}|C^2_0|\xi_{-\kappa'm'_j}\rangle_{\theta,\phi}.\end{aligned} \tag{4.60}$$

However, complete factorization into radial and angular parts is possible since the angular integrals are independent of the sign of κ [244]. Again, from consideration of angular momentum and parity, we find that $p_{3/2;m_j}$ couples to $p_{1/2;m_j}$, $p_{3/2;m_j}$, $f_{5/2;m_j}$ and $f_{7/2;m_j}$. Likewise, $p_{1/2;m_j}$ couples to $p_{3/2;m_j}$ and $f_{5/2;m_j}$, but not itself. The latter follows from the same argument as used above to conclude that nuclear spin $I > 1/2$ is required to have a nuclear electric quadrupole moment; a $p_{1/2}$-orbital, just like $s_{1/2}$, has a spherical density.

We shall again be specifically interested in matrix elements within an atomic shell characterized by (large component) orbital angular momentum ℓ. Possible values of total angular momentum are then $j = \ell + 1/2\eta$, where $\eta = \pm 1$. Matrix elements are given by

$$\langle \psi^K_{n,\ell+1/2\eta_1,m_j} | e\hat{q}^e_K | \psi^K_{n\ell+1/2\eta_2,m'_j} \rangle_{r,\theta,\phi} = -\frac{2e}{4\pi\varepsilon_0} \langle r^{-3} \rangle_{\eta_1,\eta_2} \delta_{m_j,m'_j} A_{\eta_1,\eta_2;m_j}. \tag{4.61}$$

It should be noted that with the introduction of spin-orbit interaction, the operator $e\hat{q}^e_K$ is no longer diagonal within an atomic shell of given orbital angular momentum ℓ, since there is now generally coupling between the SO-components of $j = \ell \pm 1/2$. Radial factors are given by

$$\langle r^{-3} \rangle_{\eta_1,\eta_2} = \langle R^L_{n\kappa_1} | r^{-3} | R^L_{n\kappa_2} \rangle_r + \langle R^S_{n\kappa_1} | r^{-3} | R^S_{n\kappa_2} \rangle_r; \quad \kappa_i = -\eta_i \left[\ell + \frac{1}{2}(\eta_i + 1) \right], \tag{4.62}$$

whereas angular factors are given by

$$A_{\eta_1,\eta_2;m_j} = \langle \ell + 1/2\eta_1, m_j | C^{(2)}_0 | \ell + 1/2\eta_2, m_j \rangle_{\theta,\phi}. \tag{4.63}$$

Specifically, one has

$$\begin{aligned}
A_{--;m_j} &= \frac{(2\ell+1)(2\ell-1) - 12m_j^2}{4(2\ell+1)(2\ell-1)}; \qquad 2\ell \geq 3 \\
A_{+-;m_j} &= -\frac{3m_j\sqrt{(2\ell+1)^2 - 4m_j^2}}{(2\ell+1)(2\ell-1)(2\ell+3)}; \qquad \ell \geq 1 \\
A_{++;m_j} &= \frac{(2\ell+1)(2\ell+3) - 12m_j^2}{4(2\ell+1)(2\ell+3)}; \qquad 2\ell \geq 1
\end{aligned} \tag{4.64}$$

In passing, we note that the sign of the mixed angular factor $A_{+-;m_j}$ depends on the sign of m_j. Under time reversal, the two-component angular functions ξ_{κ,m_j} transform as

$$\mathcal{K}\xi_{\kappa,m_j} = \mathrm{sgn}(\kappa)(-1)^{m_j+1/2}\xi_{\kappa,-m_j}; \quad \mathcal{K} = -i\sigma_y\mathcal{K}_0, \tag{4.65}$$

This implies that

$$\begin{aligned} \mathcal{K}\langle \ell+1/2, m_j|C_0^{(2)}|\ell-1/2, m_j\rangle_{\theta,\phi} &= -\langle \ell+1/2, -m_j|C_0^{(2)}|\ell-1/2, -m_j\rangle_{\theta,\phi} & (4.66)\\ &= \langle \ell+1/2, m_j|C_0^{(2)}|\ell-1/2, m_j\rangle_{\theta,\phi}, & (4.67)\end{aligned}$$

which is the expected behavior from a time-symmetric operator (more information about time-reversal symmetry can be found in the Appendix D.3). Casimir does not explicitly give the above matrix elements [232]. Rather, he considers the expectation value of $e\hat{q}_K^e$ for states $|J, M_J = J\rangle$ arising from s, ℓ-configurations, e.g the excited ^{3}L (5s5d) state of indium, starting either from LS-coupling (§9), or from jj-coupling (§15). In the latter case his expressions are consistent with the above matrix elements.

Part II

Applications

Chapter 5

Beyond the Dailey-Townes Model: Chemical information from the Electric Field Gradient

The results presented in this chapter are based on the following work:

> Gabriele Fabbro, Johann Pototschnig, and Trond Saue, "Beyond the Dailey–Townes Model: Chemical Information from the Electric Field Gradient," *The Journal of Physical Chemistry A*, vol. 129, pp. 1006–1025, Jan. 2025. https://doi.org/10.1021/acs.jpca.4c06884

In this project, I performed all the calculations, carried out the data analysis, and wrote the first draft of the manuscript.

Abstract

In this work, we reexamine the Dailey–Townes model by systematically investigating the electric field gradient (EFG) in various chlorine compounds, dihalogens, and the uranyl ion (UO_2^{2+}). Through the use of relativistic molecular calculations and projection analysis, we decompose the EFG expectaton value in terms of atomic reference orbitals. We show how the Dailey–Townes model can be seen as an approximation to our projection analysis. Moreover, we observe for the chlorine compounds that, in general, the Dailey-Townes model deviates from the total EFG value. We show that the main reason for this is that the Dailey–Townes model does not account for contributions from the mixing of valence p-orbitals with subvalence ones. We also find a non-negligible contribution from core polarization. This can be interpreted as Sternheimer shielding, as discussed in an appendix. The predictions of the Dailey–Townes model are improved by replacing net populations by gross ones, but we have not found any theoretical justification for this. Subsequently, for the molecular systems X–Cl (where X = I, At, and Ts), we find that with the inclusion of spin-orbit interaction, the (electronic) EFG operator is no longer diagonal within an atomic shell, which is incompatible with the Dailey–Townes model. Finally, we examine the EFG at the uranium position in UO_2^{2+}, where we find that about half the EFG comes from core polarization. The other half comes from the combination of the U ≡ O bonds and the U($6p$) orbitals, the latter mostly non-bonding, in particular with spin-orbit interaction included. The analysis was carried out with molecular orbitals localized according to the Pipek–Mezey criterion. Surprisingly, we observed that core orbitals are also rotated during this localization procedure, even though they are fully localized. We show in an appendix that, using this localization criterion, it is actually allowed.

5.1 Introduction

In 1935 Schüler and Schmidt [246] reported clear deviations from the Landé interval rule, associated with the nuclear magnetic dipole moment, in the hyperfine splittings of the atomic spectra of the two naturally occurring isotopes of europium, ^{151}Eu and ^{153}Eu, both with nuclear spin I=5/2. They argued that these perturbations were due to a nuclear property beyond the little that was known at the time (mass, charge, mechanical and magnetic moment as well as volume (isotope shift)), namely a non-spherical nuclear charge distribution [247]. They assumed an ellipsoid shape, and noted in a subsequent publication, citing Delbrück, that this corresponds to a quadrupole [248, 249]. Soon thereafter the underlying theory was worked out by Casimir [232, 250].

Nuclear electric quadrupole moments (NQMs) have played an important role in our understanding of nuclear structure. Upon inspection of quadrupole moments known at the time (1949), Townes *et al.* [251] found clear disagreements with the spherical nuclear shell model [252, 253], in particular in regions far away from closed shells. Reconciliation required the development of theories of nuclear deformation [254–258].These refinements also introduce a distinction between the intrinsic nuclear electric quadrupole moment Q_0, reflecting the nuclear deformation [211], and the spectroscopic nuclear electric quadrupole moment Q, observed in the laboratory frame.

Tables of (spectroscopic) nuclear electric quadrupole moments (NQMs) have been provided at regular intervals by Pyykkö [49, 238, 259], likewise by Stone.[260, 261] The latest compilation by Stone [53] lists for each isotope the method used for the determination of the nuclear electric quadrupole moment, and therefore allows to make statistics on the many experimental methods employed. If we consider all isotopes, then the dominant experimental methods are collinear laser spectroscopy [262, 263] (23.5%), Coulomb excitation reorientation [264] (12.9%) and time-dependent perturbed angular correlation [52] (9.9%). However, these are methods mostly used for short-lived species [52]. If we restrict attention to stable isotopes, then the dominant methods are atomic beam magnetic resonance (32.1%), muonic X-ray hyperfine structure [265] (25.6%) and molecular spectroscopy (12.8 %).

The basic interaction is the coupling of the NQM with the electric field gradient generated by electrons and other nuclei in the vicinity of the target nucleus. A direct determination of the nuclear electric quadrupole moment eQ is possible by combining nuclear quadrupole coupling constants (NQCC) e^2qQ/h obtained from experiment with accurate calculations of the electric field gradient (EFG) eq

$$\text{NQCC [in MHz]} = 234.9647 \times Q[\text{in b}] \times q \left[\text{in } E_h/a_0^2\right] \tag{5.1}$$

(see, for instance, Ref. [266]). Once such a value is known, NQMs of other isotopes of the same element may be obtained from ratios of NQCCs, under the assumption of an ideal point-like nucleus [262].

The electric field gradient is highly sensitive to small changes in the charge distribution around the nucleus which can occur, for example, in the formation of a chemical bond. It can therefore give us chemical information, as pointed out by Dailey and Townes [61]. In a 1949 paper, focusing on halogen compounds, these authors proposed that the electric field gradient at a given nuclear position is determined by the partially occupied valence p orbitals of the same atom. This in turn suggested that information about these populations could be inferred from knowledge of atomic and molecular NQCCs [267]. Subsequent refinements have been proposed in the literature [268–272]. A detailed study of the chemical information associated with the electric field gradient has been reported by Autschbach and co-workers [273].

In the present work we show that the Dailey–Townes model can be formulated as a particular approximation to projection analysis [221], providing a decomposition of expectation values in terms of atomic reference orbitals. This allows a detailed study of the validity of the Dailey–Townes model. Our exploration begins with a comprehensive examination of compounds featuring Cl in diverse molecular systems, as explored in the seminal work of Dailey and Townes [61]. These include Cl_2, ICl, ClCN, CH_3Cl, and NaCl. Subsequently, we extend our investigation to dihalogens of chlorine, X−Cl, where X=I, At, Ts. Finally, we shall consider a molecule where bonding is dominated by d- and f-orbitals, namely uranyl, which also features a subvalence $6p$-hole, contributing significantly to the EFG.

5.2 Computational Details

We performed all calculations with the DIRAC program for relativistic molecular calculations [274, 275], employing a value of 137.035 999 8 $a_0 E_h/\hbar$ for the speed of light. A Gaussian model for the nuclear charge distribution was employed throughout our calculations, using the parameters of Ref. [276]. We have carried out relativistic Kohn–Sham calculations [277, 278] based on the 4-component Dirac-Coulomb Hamiltonian, using the GGA (Generalized Gradient Approximation) exchange-correlation functional PBE [279]. To establish a connection with the Dailey–Townes model, the calculations were initially performed including only scalar relativistic effects, with the spin-orbit interaction omitted as described in Ref. [280]. The spin-orbit interaction was then included in a subsequent step. All the halogens were equipped with a dyall.3zp basis set [281], suitable for SCF calculations. For $UO_2{}^{2+}$, we have used the slightly larger dyall.v3z basis set for all atoms [282, 283]. Molecular orbitals were localized using the Pipek-Mezey criterion [284] combined with an exponential parametrization and a trust region minimization method. For the dihalogen compounds, we have calculated and used the bond distances reported in Table 5.1. The bond distance 1.7044 Å of $UO_2{}^{2+}$ was taken from Ref. [285] .

	FCl	Cl_2	BrCl	ICl	AtCl	TsCl
no-SO	1.664	2.043	2.186	2.322	2.419	2.521
SO	1.665	2.026	2.182	2.374	2.523	2.712

TABLE 5.1: Optimized bond distances (in Å) for chlorine dihalogens. The distances were calculated using 4-component Dirac-Coulomb Hamiltonian with DFT/PBE, with and without spin-orbit (SO) interaction.

5.3 Results

5.3.1 Chlorine compounds

In this section we will examine the chemical information that can be obtained from the electric field gradient in some chlorine compounds, most of which are present in the original paper of Dailey and Townes [61] (ICl, ClCN, CH_3Cl and NaCl), but also including Cl_2. We start by considering the chlorine atom itself. In Table 5.2 we present the matrix elements $\langle e\hat{q}_{\mathrm{Cl}} \rangle_{ii}$ of individual orbitals obtained from a PBE calculation using fractional occupation corresponding to the ground state configuration [Ne]$3s^2 3p^5$; this occupation is

reported as Case I in the Table. We first note that the values of the matrix elements are consistent with Eq. (4.56), giving inverse cubic radial expectation values $\langle r^{-3}\rangle$ of 101.98 a_0^{-3} and 7.512 a_0^{-3}, respectively, for the 2p and 3p shells. We also observe that summing expectation values within an atomic shell indeed gives zero in accordance with Unsöld's theorem.

Orbital	$\langle e\hat{q}_{\mathrm{Cl}}\rangle_{ii}$	Case I	Case II
1s	0.000	2.000	2.000
2s	0.000	2.000	2.000
$2p_x$	40.792	2.000	2.000
$2p_y$	40.792	2.000	2.000
$2p_z$	-81.584	2.000	2.000
Total		0.000	0.000
3s	0.000	2.000	2.000
$3p_x$	3.005	1.670	2.000
$3p_y$	3.005	1.670	2.000
$3p_z$	-6.010	1.670	1.000
Total		0.000	6.010

TABLE 5.2: Interatomic contributions $\langle e\hat{q}_{\mathrm{Cl}}\rangle^{\mathrm{Cl}}$ calculated from matrix elements and net occupations. Two sets of occupations are considered: Case I is the fractional occupation of the atomic ground state, whereas Case II is the idealized occupation in Cl_2. All values of eq_{Cl} are in atomic units (E_h/ea_0^2).

We next turn to molecular species. In Table 5.3 we have listed the title molecules ClX according to the Pauling electronegativity difference $\Delta\chi_{\mathrm{Cl-X}}$. For the chlorine molecule one would ideally expect an occupation corresponding to Case II of Table 5.2. The sum of matrix elements $\langle e\hat{q}_{\mathrm{Cl}}\rangle_{ii}$ weighted by this occupation gives the value

$$eq_{\mathrm{Cl}}\,[\mathrm{Cl_2}] = \frac{2e}{4\pi\varepsilon_0}\langle r^{-3}\rangle_{3p} \times \frac{4}{5} = 6.010 E_h/ea_0^2 \tag{5.2}$$

which is remarkably close to the total value $eq_{\mathrm{Cl}}^{SCF} = 6.075\ \mathrm{E}_h/ea_0^2$ reported in Table 5.3. However, the actual net populations of the chlorine 3p orbitals obtained in our calculations are somewhat different, due to overlap and hybridization. They are reported in Table 5.3, giving a Dailey–Townes value eq_{Cl}^{DT} of 7.345 E_h/ea_0^2. Generally, for the molecules in Table 5.3, we expect that with increasing positive electronegativity difference $\Delta\chi_{Cl-X}$, leading to increased charge transfer towards the chlorine atom, the electric field gradient should decrease towards zero as we go to the limiting case of a chlorine anion. This is indeed what we see for the calculated total values eq_{Cl}, whereas the values eq_{Cl}^{DT} obtained using the Dailey–Townes model of Eq. (4.58) are often in significant error and even unable to give the right trend.

Molecule	$\Delta\chi_{Cl-X}$	n($3p_x$)	n($3p_y$)	n($3p_z$)	eq_{Cl}^{DT}	eq_{Cl}
Cl_2	0.00	2.034	2.034	0.812	7.345	6.075
		1.992	1.992	1.017	5.861	
ICl	0.50	2.030	2.030	1.048	5.902	4.736
		1.990	1.990	1.240	4.507	
ClCN	0.61	1.902	1.902	0.855	6.295	4.340
		1.897	1.897	1.154	4.468	
CH_3Cl	0.61	2.049	2.056	1.036	6.115	4.017
		1.978	1.978	1.240	4.436	
NaCl	2.23	1.976	1.976	1.830	0.871	0.575
		1.975	1.975	1.873	0.614	

TABLE 5.3: Calculated values (in E_h/ea_0^2) of the electric field gradient at the nuclear position Cl of molecules ClX. The molecules are listed according to the difference $\Delta\chi_{Cl-X}$ in electronegativity on the Pauling scale . The value eq_{Cl} refers to the calculated total electric field gradient, including nuclear contributions, whereas eq_{Cl}^{DT} is obtained with the Dailey–Townes model, that is, according to Eq. (4.58). We also give the net populations on chlorine, obtained from projection analysis, used to calculate eq_{Cl}^{DT}. For each molecule, we give in the second line the numbers obtained when net populations are replaced by gross populations. These calculations were performed in the absence of spin-orbit interaction.

Orb	ε	Sym	I	Cl	I($5s$)	I($5p$)	Cl($3s$)	Cl($3p$)
29	-0.791	σ	0.392	1.598	0.320	0.071	1.554	0.044
30	-0.642	σ	1.560	0.438	1.553	0.006	0.360	0.078
31	-0.395	σ	0.798	1.172	0.091	0.708	0.056	1.117
32	-0.326	π	0.558	1.428	0.000	0.558	0.000	1.429
33	-0.326	π	0.558	1.428	0.000	0.558	0.000	1.429
34	-0.243	π	1.436	0.560	0.000	1.436	0.000	0.560
35	-0.243	π	1.436	0.560	0.000	1.436	0.000	0.560

TABLE 5.4: Projection analysis of canonical molecular orbitals for ICl. We report the gross populations for I and Cl (columns 4 and 5) as well as valence orbitals (columns 6-9). Orbital energies ε are given in E_h.

Orb	$\langle\varepsilon\rangle$	Sym	I	Cl	I($5s$)	I($5p$)	Cl($3s$)	Cl($3p$)
29	-0.916	σ	0.754	1.210	0.005	0.747	0.011	1.199
30	-1.275	σ	2.020	-0.022	1.963	0.056	-0.003	-0.016
31	-1.463	σ	-0.002	2.018	-0.004	-0.017	1.963	0.056
32	-0.533	π	2.004	-0.004	0.000	2.004	0.000	-0.009
33	-0.533	π	2.004	-0.004	0.000	2.004	0.000	-0.009
34	-0.605	π	-0.002	1.998	0.000	-0.009	0.000	1.999
35	-0.605	π	-0.002	1.998	0.000	-0.009	0.000	1.999

TABLE 5.5: Projection analysis of localized molecular orbitals for ICl. $\langle\varepsilon\rangle$ refers to the expectation value (in E_h) of the converged Kohn-Sham operator. We report the gross populations for I and Cl (columns 4 and 5) as well as valence orbitals (columns 6-9).

In order to understand the limited success of the Dailey–Townes model, we shall single out the ICl molecule for detailed analysis. This molecule was also scrutinized by Dailey and Townes, but within the framework of valence bond theory [286]. They considered

bonding to be mediated by a single σ-bond; starting from a Heitler–London covalent form they considered the effect of hybridization, overlap and ionicity. We, on the other hand, work within the setting of molecular orbital (MO) theory. Upon inspection of the canonical MOs (cf. Table 5.4), we find, somewhat to our surprise, a more complicated picture, with seven MOs having significant gross population on both centers. However, upon localization, limited to the valence orbitals of Table 5.4, we recover the bonding picture discussed by Dailey and Townes (cf. Table 5.5). The now single σ bonding orbital is almost exclusively spanned by p_z orbitals on the two centers

$$\psi_{29} \approx a\ \mathrm{Cl3p}_z + b\ \mathrm{I5p}_z, \quad \begin{cases} a &= 0.703 \\ b &= -0.514 \end{cases} . \tag{5.3}$$

According to the Dailey–Townes model, Eq. (4.58), we then get

$$eq_{\mathrm{Cl}}\,[\mathrm{ICl}] = \frac{2e}{4\pi\varepsilon_0}\langle r^{-3}\rangle_{3p} \times \frac{4}{5}(2-2a^2) = (2-2a^2)eq_{\mathrm{Cl}}\,[\mathrm{Cl_2}]\,, \tag{5.4}$$

where the right-hand side refers to the expression in Eq. (5.2). The ICl bonding σ-orbital, Eq. (5.3), to a very good approximation, involves only p_z orbitals from the two centers. This is in vivid contrast to Dailey and Townes who suggested significant s hybridization on the chlorine center, on the order of 20%, in order to accommodate their model with experimental data [61]. A different point of view was taken by Gordy [287, 288], who suggested that one could ignore overlap when evaluating the electric field gradient. This would imply that the net populations appearing in the Dailey–Townes model, Eq. (4.58), are replaced by gross populations. Indeed, if we proceed in this manner, we get much better agreement with the calculated total values eq_{Cl}, as shown in Table 5.3 (second row for each molecule). In the case of ICl we could then combine the normalization $a^2+b^2=1$, which is clearly not true, with the definition of ionicity [288]

$$\beta = a^2 - b^2 \tag{5.5}$$

to rewrite Eq. (5.4) as

$$\beta = 1 - \frac{eq_{\mathrm{Cl}}\,[\mathrm{ICl}]}{eq_{\mathrm{Cl}}\,[\mathrm{Cl_2}]} \tag{5.6}$$

For the left-hand side, using the coefficients from Eq. (5.3), we get 0.230, whereas the right-hand side, using the calculated total values eq_{Cl} from Table 5.3, gives 0.220. Although the agreement is intriguing, we can see no obvious justification for the overlap neglect

by Gordy. A better line of argument was provided by Cotton and Harris [268]: They split (the valence) inter-atomic contributions $\langle e\hat{q}^e_K\rangle^{(K,A)}_{\text{inter}}$ in two equal parts. One part is combined with the inter-atomic contribution $\langle e\hat{q}^e_K\rangle^{(A)}_{\text{intra}}$ as well as the nuclear contribution from the same center A and their sum assumed to be zero. For the second part, they assume a Mulliken-type relation [289, 290]

$$\langle\psi^A_p|e\hat{q}^e_K\psi^K_q\rangle \approx \langle\psi^A_p|\psi^K_q\rangle\langle\psi^K_q|e\hat{q}^e_K|\psi^K_q\rangle. \tag{5.7}$$

Inserted back into the expansion Eq. (G) one indeed gets a modified version of the Dailey–Townes model, now based on gross populations.

		$\langle e\hat{q}^{\text{el}}_{\text{Cl}}\rangle^{(\text{Cl})}_{\text{princ}}$	$\langle e\hat{q}^{\text{el}}_{\text{Cl}}\rangle^{(\text{Cl})}_{\text{hyb}}$	$\langle e\hat{q}^{\text{el}}_{\text{Cl}}\rangle^{(\text{Cl})}_{\text{intra}}$	$\langle e\hat{q}^{\text{el}}_{\text{Cl}}\rangle^{(\text{I})}_{\text{intra}}$	$\langle e\hat{q}^{\text{el}}_{\text{Cl}}\rangle^{(\text{Cl})}_{\text{inter}}$	$\langle e\hat{q}^{\text{el}}_{\text{Cl}}\rangle^{(\text{Cl})}_{\text{pol}}$	$\langle e\hat{q}^{\text{el}}_{\text{Cl}}\rangle^{(\text{Cl})}$
I core		-0.000	-0.000	-0.000	-1.089	-0.000	-0.000	-1.091
Cl core		0.000	0.0455	0.045	0.000	0.000	0.155	0.2003
Valence	σ bond	-5.952	-0.568	-6.520	-0.019	-0.026	-0.302	-6.866
	σ n.b	-0.362	0.013	-0.349	-0.038	0.008	-0.024	-0.403
	π n.b	12.205	-0.060	12.145	-0.056	0.001	-0.449	11.641
	Total valence	5.891	-0.616	5.276	-0.113	-0.017	-0.775	4.372

TABLE 5.6: Decomposition of electronic contribution to the EFG at the position of Cl in ICl using the projection analysis for each group of MOs. All values are reported in E_h/ea_0^2. Adding the nuclear contribution of 1.255 E_h/ea_0^2 gives the total contribution of 4.736 E_h/ea_0^2. n.b=non-bonding.

Let us now consider the complete decomposition of the EFG according to Eq. (G). This is shown in Table 5.6. We have divided the MOs into three groups: i) core orbitals on iodine, ii) core orbitals on chlorine and iii) valence orbitals, the latter corresponding to the MOs shown in Table 5.5. For the valence orbitals we further distinguish between the bonding σ-orbital (MO 29), non-bonding ones (MOs 30 and 31) as well-as non-bonding π-orbitals (MOs 32 – 35). The EFG given by the Dailey–Townes model is the Cl principal contribution $\langle e\hat{q}^{\text{el}}_{\text{Cl}}\rangle^{(\text{Cl})}_{\text{princ}}$ 5.891 E_h/ea_0^2 arising from the valence orbitals. This number is slightly different from the value 5.902 E_h/ea_0^2 reported Table 5.3; this is because the net populations reported in that Table are accumulated over all MOs of the molecule. It is of interest to note that the valence non-bonding σ-orbitals contribute -0.362 E_h/ea_0^2 to $\langle e\hat{q}^{\text{el}}_{\text{Cl}}\rangle^{(\text{Cl})}_{\text{princ}}$, although Table 5.5 suggests that MOs 30 and 31 essentially correspond to I5s and Cl3s, respectively. However, Table 5.5 also shows participation of Cl3p_z to these orbitals; it is minute, but enough to explain the cited contribution.

Let us now consider what further contributions beyond the Dailey–Townes model that

are needed to arrive at the total EFG of 4.736 E_h/ea_0^2. From Table 5.6 we see that the iodine intra-atomic contribution $\langle e\hat{q}^{\mathrm{el}}_{\mathrm{Cl}}\rangle^{(\mathrm{I})}_{\mathrm{intra}}$ from core and valence sum up to -1.202 E_h/ea_0^2, which is clearly not a small number. However, this contribution is to a large extent cancelled by the nuclear contribution of 1.255 E_h/ea_0^2. This can be understood from a Taylor-expansion of the operator $e\hat{q}^e_K$ about another center ($A \neq K$)

$$\langle\psi^A_p|e\hat{q}^e_K|\psi^A_q\rangle = -\frac{e}{4\pi\varepsilon_0}\left[\frac{3Z^2_{AK}-R^2_{AK}}{R^5_{AK}}\right]\delta_{pq} + \sum_\alpha \left.\frac{\partial e\hat{q}^e_K}{\partial r_{A;\alpha}}\right|_{\mathbf{r}_{A;\alpha}=\mathbf{0}} \langle\psi^A_p|r_{A;\alpha}|\psi^A_q\rangle + \ldots \quad (5.8)$$

The zeroth-order terms corresponds exactly to a nuclear contribution of Eq.(4.44), but with opposite sign. Further terms in the expansion involve matrix elements $\langle\psi^A_p|x^i_A y^j_A z^k_A|\psi^A_q\rangle$ of increasing Cartesian powers $i+j+k=\ell$ balanced against increasing inverse powers of $R^{-(3+\ell)}_{AK}$. In less mathematical terms, the electron cloud of the iodine atom, seen from the chlorine atom, appears as a point-like charge which thereby gives an electronic contribution of the same magnitude as the nuclear one, but of opposite sign.

Further inspection of Table 5.6 shows that there is a Cl hybridization contribution $\langle e\hat{q}^{\mathrm{el}}_{\mathrm{Cl}}\rangle^{(\mathrm{Cl})}_{\mathrm{hyb}}$ from valence of -0.616 E_h/ea_0^2, most of which comes from the bonding σ-orbital. This is somewhat surprising, since Eq. (5.3) is a faithful description of this orbital. However, our projection analysis shows that there is a contribution from $\mathrm{Cl2p}_z$, with a very small coefficient of $-5.94\cdot10^{-2}$, but it multiplies a large matrix element ($\langle\mathrm{Cl3}p_z|e\hat{q}^e_K|\mathrm{Cl2}p_z\rangle = 21.182E_h/ea_0^2$) and the $\mathrm{Cl3p}_z$ coefficient ($a=0.703$) to give an important contribution.

A final significant contribution is that of polarization $\langle e\hat{q}^{\mathrm{el}}_{\mathrm{Cl}}\rangle^{(\mathrm{Cl})}_{\mathrm{pol}}$, summing up to -0.619 E_h/ea_0^2. When projection analysis is used to decompose the integrated number density according to Eq. (4.48), significant polarization is an indication that some important atomic orbital contribution is missing. However, this is not the case for the present systems. The polarization contribution is only large for the electronic EFG expectation value and not for populations. We will therefore claim that the polarization contribution provides a precise definition of the deformation of atomic densities that occur when atoms are brought together to form a molecule.

Our observations concerning the ICl molecule are valid for all the studied molecules, as seen from Table 5.7. We note that:

	$\langle e\hat{q}^{\mathrm{el}}_{\mathrm{Cl}}\rangle^{(\mathrm{Cl})}_{\mathrm{intra}}$	$\langle e\hat{q}^{\mathrm{el}}_{\mathrm{Cl}}\rangle^{(\mathrm{Cl})}_{\mathrm{princ}}$	$\langle e\hat{q}^{\mathrm{el}}_{\mathrm{Cl}}\rangle^{(\mathrm{Cl})}_{\mathrm{hyb}}$	$\langle e\hat{q}^{\mathrm{el}}_{\mathrm{Cl}}\rangle^{(\mathrm{Cl}X)}_{\mathrm{inter}}$	$\langle e\hat{q}^{\mathrm{el}}_{\mathrm{Cl}}\rangle_{\mathrm{pol}}$	$\langle e\hat{q}^{\mathrm{el}}_{\mathrm{Cl}}\rangle^{(\mathrm{X})}_{\mathrm{intra}}$	$e\hat{q}^{\mathrm{nucl}}_{\mathrm{Cl}}$	$\langle e\hat{q}_{\mathrm{Cl}}\rangle$
Cl_2	6.662	7.320	-0.659	-0.020	-0.618	-0.539	0.591	6.075
ICl	5.319	5.890	-0.571	-0.017	-0.619	-1.202	1.255	4.736
ClCN	5.114	6.223	-1.109	-0.062	-0.852	-0.364	0.504	4.340
CH_3Cl	5.146	6.082	-0.936	-0.033	-1.153	-0.301	0.359	4.018
NaCl	0.769	0.874	-0.105	0.002	-0.213	-0.219	0.240	0.579

TABLE 5.7: Decomposition of the electric field gradient at the nuclear position of Cl in molecules Cl–X using projection analysis. All values are expressed in atomic units (E_h/ea_0^2). $\langle e\hat{q}^{\mathrm{el}}_{\mathrm{Cl}}\rangle^{(\mathrm{X})}_{\mathrm{intra}}$ is the sum of all intra-atomic contributions coming from the other atoms present in the molecule.

- The expectation value $\langle e\hat{q}_{\mathrm{Cl}}\rangle$ is dominated by the intra-atomic contribution $\langle e\hat{q}^{\mathrm{el}}_{\mathrm{Cl}}\rangle^{(\mathrm{Cl})}_{\mathrm{intra}}$, in particular the principal contribution $\langle e\hat{q}^{\mathrm{el}}_{\mathrm{Cl}}\rangle^{(\mathrm{Cl})}_{\mathrm{princ}}$, which is essentially the Dailey–Townes model.

- The hybridization contribution $\langle e\hat{q}^{\mathrm{el}}_{\mathrm{Cl}}\rangle^{(\mathrm{Cl})}_{\mathrm{hyb}}$ can be significant. It arises from mixing of valence p orbitals with subvalence ones, even by very small amounts, and typically reduces the Dailey–Townes value by 10-15 %.

- Inter-atomic contributions $\langle e\hat{q}^{\mathrm{el}}_{\mathrm{Cl}}\rangle^{(\mathrm{Cl}X)}_{\mathrm{inter}}$ are generally small and can be ignored. They therefore do not distinguish between the Dailey–Townes model [61] and the refinements proposed by Cotton and Harris [268].

- Intra-atomic contributions $\langle e\hat{q}^{\mathrm{el}}_{\mathrm{Cl}}\rangle^{(\mathrm{X})}_{\mathrm{intra}}$ from other centers are not negligible, but to a large extent cancelled by corresponding nuclear contributions $e\hat{q}^{\mathrm{nucl}}_{\mathrm{Cl}}$. We may expect that the combined contribution can be calculated as a nuclear contribution, but replacing nuclear charges by atomic partial ones.

- Polarization contributions $\langle e\hat{q}^{\mathrm{el}}_{\mathrm{Cl}}\rangle_{\mathrm{pol}}$ may be important and have a clear physical interpretation.

So far we only considered scalar relativistic effects in our calculations. Let us now investigate the effect of spin-orbit coupling. For p-shells the non-zero angular factors of Eq. (4.64) are $A_{+-;\pm 1/2} = \mp\sqrt{2}/5$, $A_{++,\pm 1/2} = 1/5$ and $A_{++,\pm 3/2} = -1/5$. In Table 5.9 we show atomic matrix elements $\langle e\hat{q}_{\mathrm{Cl}}\rangle_{ii}$ obtained in the same manner as in Table 5.2, but now with spin-orbit interaction included. The values are consistent with the expression given in Eq. (4.61). For instance, the matrix elements for $3p_{3/2;1/2}$ and $3p_{3/2;3/2}$ both imply an inverse cubic radial expectation value $\langle r^{-3}\rangle_{3p;++} = 7.455 a_0^{-3}$. As already discussed, the

expectation value $\langle r^{-3}\rangle_{3p;--}$ is not accessible from the EFG due to spherical symmetry of the $p_{1/2}$ orbital density. Direct calculation gives $\langle r^{-3}\rangle_{3p;--} = 10.850 a_0^{-3}$, which is a 45% increase with respect to $\langle r^{-3}\rangle_{3p;++}$. In comparison the radial expectation value $\langle r\rangle_{3p;--} = 1.834 a_0$ is only -0.53% smaller than $\langle r\rangle_{3p;+-} = 1.844 a_0$. The EFG operator, due to its inverse cubic radial dependency, is clearly very sensitive to changes in orbital size due to spin-orbit interaction. This is the origin of the spin-orbit tilting discussed by Pyykkö and Seth [59].

	$\langle e\hat{q}^{\mathrm{el}}_{\mathrm{Cl}}\rangle^{(\mathrm{Cl})}_{\mathrm{intra}}$	$\langle e\hat{q}^{\mathrm{el}}_{\mathrm{Cl}}\rangle^{(\mathrm{Cl})}_{\mathrm{princ}}$	$\langle e\hat{q}^{\mathrm{el}}_{\mathrm{Cl}}\rangle^{(\mathrm{Cl})}_{\mathrm{hyb}}$	$\langle e\hat{q}^{\mathrm{el}}_{\mathrm{Cl}}\rangle^{(\mathrm{Cl}X)}_{\mathrm{inter}}$	$\langle e\hat{q}^{\mathrm{el}}_{\mathrm{Cl}}\rangle_{\mathrm{pol}}$	$\langle e\hat{q}^{\mathrm{el}}_{\mathrm{Cl}}\rangle^{(\mathrm{X})}_{\mathrm{intra}}$	$e\hat{q}^{\mathrm{nucl}}_{\mathrm{Cl}}$	$\langle e\hat{q}_{\mathrm{Cl}}\rangle$
ICl	5.319	5.890	-0.571	-0.017	-0.619	-1.202	1.254	4.735
	5.237	1.741	3.496	-0.016	-0.575	-1.127	1.174	4.693
AtCl	5.073	5.595	-0.522	-0.016	-0.608	-1.733	1.780	4.495
	4.365	1.233	3.132	-0.010	-0.544	-1.534	1.567	3.844
TsCl	4.690	5.177	-0.487	-0.015	-0.615	-2.122	2.165	4.102
	3.050	0.773	2.276	-0.007	-0.506	-1.713	1.739	2.561

TABLE 5.8: Decomposition of the electric field gradient at the nuclear position of Cl in molecules Cl–X using projection analysis. All values are in atomic units (E_h/ea_0^2). The second line for each molecule gives the decomposition upon inclusion of spin-orbit interaction.

Orbital	$\langle e\hat{q}_{\mathrm{Cl}}\rangle_{ii}$
$1s_{1/2;1/2}$	0.000
$2s_{1/2;1/2}$	0.000
$2p_{1/2;1/2}$	0.000
$2p_{3/2;1/2}$	-40.500
$2p_{3/2;3/2}$	40.500
$3s_{1/2;1/2}$	0.000
$3p_{1/2;1/2}$	0.000
$3p_{3/2;1/2}$	-2.982
$3p_{3/2;3/2}$	2.982

TABLE 5.9: Atomic matrix elements $\langle e\hat{q}_{\mathrm{C}}\rangle^{\mathrm{Cl}}$ in the presence of spin-orbit coupling. All values of eq_{Cl} are in atomic units (E_h/ea_0^2).

The mixed value $\langle r^{-3}\rangle_{3p;+-} = 7.542 a_0^{-3}$ does not contribute to atomic expectation values, but can be expected to contribute significantly to molecular expectation values and, in our terminology, as a hybridization contribution. For instance, using the notation of Pyykkö and Seth [59], the contribution from chlorine to the σ-bond of ICl can be expressed as

$$3p_\sigma(1/2) = -\sqrt{\frac{1}{3}}3p_{1/2;1/2} + \sqrt{\frac{2}{3}}3p_{3/2;1/2}, \tag{5.9}$$

giving rise to an EFG expectation value

$$\langle 3p_\sigma(1/2)|e\hat{q}^e_{\mathrm{Cl}}|3p_\sigma(1/2)\rangle = -\frac{2e}{4\pi\varepsilon_0}\left(\frac{4}{15}\langle r^{-3}\rangle_{3p;+-} + \frac{2}{15}\langle r^{-3}\rangle_{3p;++}\right). \tag{5.10}$$

Note, however, that this reduces to the scalar-relativistic expectation value

$$\langle 3p_z\alpha|e\hat{q}^e_{\mathrm{Cl}}|3p_z\alpha\rangle = -\frac{2e}{4\pi\varepsilon_0} \times \frac{2}{5}\langle r^{-3}\rangle_{3p} \tag{5.11}$$

only when the radial matrix elements $\langle r^{-3}\rangle_{p;+-}$ and $\langle r^{-3}\rangle_{p;++}$ coincide.

In Table 5.8 we show the decomposition of the calculated electric field gradient at the nuclear position of Cl in the interhalogens X−Cl, (X=I, At, Ts), without and with spin-orbit interaction included. We recall that the calculations were carried out at the corresponding optimized equilibrium distances, as seen in Table 5.1. When spin-orbit interaction is included, the hybridization contribution $\langle e\hat{q}^{\mathrm{el}}_{\mathrm{Cl}}\rangle^{(\mathrm{Cl})}_{\mathrm{hyb}}$ is systematically larger than the principal contribution $\langle e\hat{q}^{\mathrm{el}}_{\mathrm{Cl}}\rangle^{(\mathrm{Cl})}_{\mathrm{princ}}$. Closer inspection shows that both contributions are dominated by the 3*p*-shell of chlorine. In ICl the sum of the two contributions, the total intra-atomic contribution $\langle e\hat{q}^{\mathrm{el}}_{\mathrm{Cl}}\rangle^{(\mathrm{Cl})}_{\mathrm{intra}}$, is only slightly affected by the spin-orbit interaction and the redistribution between principal and hybridization contributions simply reflects the change of coupling regime of the underlying atomic reference orbitals. However, replacing iodine by the heavier halogens astatine and tennessine a genuine spin-orbit effect on $\langle e\hat{q}^{\mathrm{el}}_{\mathrm{Cl}}\rangle^{(\mathrm{Cl})}_{\mathrm{intra}}$ comes into play, induced by the heavier atom, as also seen on the optimized bond distances in Table 5.1. Furthermore, as seen in Table 5.10, if we instead focus on the electric field gradient at the heavier atom X of these compounds, the hybridization contribution is overtaken by the principal contribution. Finer scrutiny shows that these contributions are dominated by the valence *p*-shell of the heavy atom. Keeping in mind that the EFG operator probes the vicinity of the target atom, this can be seen as the transition from LS coupling to jj coupling on the heavy atom. It should also be noted that the decomposition is invariant to a rotation among the occupied molecular orbitals. We may also note that a bond length extension of 7.5% for TsCl, induced by spin-orbit interaction, translates into a 19.7% reduction of the nuclear EFG-contributions $e\hat{q}^{\mathrm{nucl}}_{\mathrm{Cl}}$ and $e\hat{q}^{\mathrm{nucl}}_{\mathrm{X}}$, again showing the sensitivity of the EFG-operator.

Finally, before closing this Section, we summarize in Table 5.11 calculated values of the EFG at the Cl position in different dihalogens using different Hamiltonians. Starting

	$\langle e\hat{q}_{\mathrm{X}}^{\mathrm{el}}\rangle_{\mathrm{intra}}^{(\mathrm{X})}$	$\langle e\hat{q}_{\mathrm{X}}^{\mathrm{el}}\rangle_{\mathrm{princ}}^{(\mathrm{X})}$	$\langle e\hat{q}_{\mathrm{X}}^{\mathrm{el}}\rangle_{\mathrm{hyb}}^{(\mathrm{X})}$	$\langle e\hat{q}_{\mathrm{X}}^{\mathrm{el}}\rangle_{\mathrm{inter}}^{(\mathrm{Cl}X)}$	$\langle e\hat{q}_{\mathrm{X}}^{\mathrm{el}}\rangle_{\mathrm{pol}}$	$\langle e\hat{q}_{\mathrm{X}}^{\mathrm{el}}\rangle_{\mathrm{intra}}^{(\mathrm{Cl})}$	$e\hat{q}_{\mathrm{X}}^{\mathrm{nucl}}$	$\langle e\hat{q}_{\mathrm{X}}\rangle$
ICl	19.772	22.052	-2.281	-0.031	-1.234	-0.382	0.402	18.527
	19.012	8.317	10.694	-0.027	-0.960	-0.360	0.376	18.041
AtCl	40.908	45.453	-4.544	0.011	-1.957	-0.342	0.356	38.976
	31.424	17.386	14.038	0.013	-1.002	-0.306	0.314	30.443
TsCl	91.377	101.123	-9.744	-0.039	-3.832	-0.305	0.314	87.515
	44.895	28.910	15.984	-0.025	-0.781	-0.252	0.252	44.089

TABLE 5.10: Decomposition of the electric field gradient at the nuclear position of X in molecules X−Cl using projection analysis. Each value is expressed in atomic units (E_h/ea_0^2). The second line for each molecule gives the decomposition upon inclusion of spin-orbit interaction.

from non-relativistic values, the inclusion of scalar-relativistic effects increase the EFG, whereas the further inclusion of spin-orbit effects reduces it. For the heaviest systems the overall relativistic effect is a reduction of the non-relativistic value. These results are in line with those obtained by Aucar *et al.* at both the HF and DFT level [291].

	eq_{Cl}^{NR}	eq_{Cl}^{SR}	eq_{Cl}^{SO}	Δ_{SR-NR}	Δ_{SO-SR}	Δ_{SO-NR}
FCl	7.622	7.709	7.707	0.087	-0.002	0.085
Cl_2	6.007	6.076	6.037	0.069	-0.039	0.03
BrCl	5.502	5.567	5.532	0.065	-0.035	0.03
ICl	4.649	4.736	4.693	0.088	-0.044	0.044
AtCl	4.318	4.496	3.844	0.178	-0.652	-0.474
TsCl	3.719	4.102	2.561	0.383	-1.541	-1.158

TABLE 5.11: Calculated values in E_h/ea_0^2 of the electric field gradient at the Cl position in different dihalogens. The values are reported at the non-relativistic level (eq_{Cl}^{NR}), adding scalar relativistic effects (eq_{Cl}^{SR}) and finally also spin-orbit interaction (eq_{Cl}^{SO}).

5.3.2 Uranyl

In order to go beyond the realm of the Dailey–Townes model, we have chosen to study the electric field gradient at the position of uranium in uranyl [$UO_2{}^{2+}$]. In this widely studied molecule [292–295] bonding is mediated primarily by the uranium $5f$ and $6d$ orbitals. An intriguing feature of the electronic structure of uranyl is the presence of the so-called $6p$-hole. Veal and co-workers in 1975 reported an X-ray photoemission spectroscopy study of hexavalent uranium compounds, most of which contained the uranyl unit, and observed a splitting of the $6p_{3/2}$ level that depended strongly on the separation between uranium and the nearest-neighbour oxygens, and which they therefore attributed to ligand-field splitting [296]. Subsequent calculations showed that the interaction is even stronger [297–304]; U $6p$ and O 2s combine to form molecular orbitals. This is also in line

with Grechukhin and co-workers who attributed the presence of a O $2s$ peak in the ^{235}U internal conversion spectrum of uranium trioxide to appreciable hybridization of these orbitals with U $6p$ [305]. Further insight was provided by a polarized X-ray spectroscopic study of a single crystal of $Cs_2UO_2Cl_4$ by Denning and co-workers, where a weak band in the O Kα emission spectrum was interpreted as revealing O $2p$ character in the $\sigma_{1/2}$ component of the U $6p_{3/2}$ orbital [294, 306].

At the relativistic Hartree–Fock level, the radial expectation value of uranium $6p$ extends beyond that of $5f$ [307]. The subvalence character of the U $6p$ orbital has been invoked to explain the relativistic bond length *extension* of uranyl [308], as well as the observation that the molecule is linear [300], in contrast to the bent structure of transition metal dioxo ions, as well as isoelectronic ThO_2, although the latter explanation has been refuted by Wadt [309]. Of particular interest in the present work is the 1986 suggestion by Larsson and Pyykkö that the electric field gradient at the position of uranium in uranyl arises essentially from the $6p$-hole [303] .

The NQCC has not been measured for the bare uranyl unit, but has been extracted from the Mössbauer spectrum of the $2^+ \rightarrow 0^+$ γ-transition of ^{234}U in nonmagnetic uranyl rubidium nitrate $[(UO_2)Rb(NO_3)_3]$; assuming axial symmetry. Monard *et al.* report $(3/8)e^2qQ = (-60.1 \pm 0.3)$ mm/s [310]. The authors also provided an estimate of eq: The intrinsic nuclear quadrupole moment Q_0 can be extracted from the electric quadrupole transition probability $B(E2; 0^+ \rightarrow 2^+)$. For ^{234}U, Ford *et al.* reported $Q_0 = (10.19 \pm 0.13)$ b [311]. Assuming an axially symmetric nuclear deformation with the nuclear spin having a well-defined direction with respect to the symmetry axis of the deformation (strong coupling [52, 257]), this translates into a spectroscopic (molecular-frame) quadrupole moment of $Q = (-2.91 \pm 0.04)$ b. Using this value, Monard *et al.* suggested an electric field gradient $eq = (8.14 \pm 0.13) \times 10^{18}$ V/cm^2 (corresponding to $(8.38 \pm 0.13)\ E_h/ea_0^2$). Repeating their calculation, we arrive at a somewhat lower electric field gradient, $eq = 7.99 \times 10^{18}$ V/cm^2 (or 8.22 E_h/ea_0^2). Reproducing their value requires selecting a γ-transition energy E_γ=4.431 keV instead of the value E_γ=4.3491 keV used by the authors and taken from Ref. [312] (the modern value is E_γ=4.34981 keV [313]).

Larsson and Pyykkö made the following suggestion [303]: suppose that the entire electric field gradient of uranyl rubidium nitrate $[(UO_2)Rb(NO_3)_3]$ comes from the diagonal element $\langle e\hat{q}^e_U \rangle_{ii}$ with $i = U\ 6p_{3/2;1/2}$, that they in atomic units express as $(3/5)\langle r^{-3} \rangle_{++}$,

and that notably Sternheimer shielding (core polarization) is ignored. Taking the HF radial expectation value [307] $\langle r^{-3}\rangle_{++} = 80.61 a_0^{-3}$, they then found that the matrix element evaluates to 48.37 E_h/ea_0^2 and that this would require a $6p_{3/2;1/2}$-hole of $0.17e$. In a subsequent paper Pyykkö and Seth point out that the angular factor was wrong [59]; it should be $(2/5)\langle r^{-3}\rangle_{++}$, now requiring a $6p_{3/2;1/2}$-hole of $0.26e$. Strictly speaking, though, the matrix element comes with a negative sign; it should be

$$\langle U\ 6p_{3/2;1/2}|e\hat{q}^e_U|U\ 6p_{3/2;1/2}\rangle = -\frac{2e}{4\pi\varepsilon_0}\langle r^{-3}\rangle_{++} \times (1/5) \tag{5.12}$$

This disagrees with the sign of eq as reported by Monard and co-workers. There are many instances, with ^{57}Fe as a prominent example, where the Mössbauer spectrum is invariant under a change of sign of eq, and so the sign of eq can only be deduced by special techniques, such as the application of a magnetic field [314]. However, in the case of ^{234}U the $2^+ \rightarrow 0^+$ γ-transition gives a three-line Mössbauer spectrum with an energy splitting ratio of 3:1 and relative line intensities of 2:2:1 [310, 315], and so there is indeed a problem of sign. A 4-component relativistic HF study by de Jong and co-workers [316] showed a positive value ($eq = 2.7\ E_h/ea_0^2$), with important contributions beyond that of the $U(6p)$ core-hole, although the latter dominated the distance-dependence of the EFG, in line with the suggestion by Larsson and Pyykkö [303]. Upon inclusion of negative point charges to simulate the effect of equatorial ligands, the authors observed a significant increase ($eq = 6.6\ E_h/ea_0^2$). These calculations employed a default U–O bond length of 1.78 Å, in line with the experimental one for $[(UO_2)Rb(NO_3)_3]$. Subsequent calculations have shown that the inclusion of electron correlation by the Kohn–Sham approach invariably makes the electric field gradient *negative*, whereas the inclusion of explicit equatorial ligands brings it back to a positive value [317–319]. The latter observation was also confirmed by a recent CCSD/X2C-AMFI study on the uranyl tris-nitrate complex ($[(UO_2)(NO_3)_3]^-$), albeit using a rather small basis [193].

Our investigation begins with an assessment of the electronic structure of uranyl. In Table 5.12 the electronic configurations of the atoms within the molecule in a purely ionic perspective is contrasted with what is actually extracted from our PBE calculations using projection analysis. In the latter case, we see that the effective charge on uranium is +2.46e, with and without SO, whereas the oxygens each carry small negative charges of -0.08e. There is, however, some uncertainty in these partial charges since the polarization contribution is -0.30e and represents charge not attributed to any center. Switching to

intrinsic atomic orbitals (IAOs) [229], the polarization contribution is eliminated, and the partial charges are +2.38e and -0.19e for U and O, respectively. Looking at the effective electron configuration of uranium in the molecule, we find that the U($5f$) and U($6d$) orbitals exhibit partial occupation and, most notably, we observe a U($6p$)-hole of 0.28e; upon inclusion of spin-orbit interaction, most of the hole (0.25e) is located on the U($6p_{3/2}$) orbital.

Atom		Charge	Occupation of atomic orbitals
U	Ionic	+6	$[\mathrm{Hg}]6p^6 5f^0 6d^0 7s^0$
	Calculated	+2.46	$[\mathrm{Hg}]6p^{5.72} 5f^{2.74} 6d^{1.05} 7s^{0.05}$
	– with SOC	+2.46	$[\mathrm{Hg}]6p_{1/2}^{1.94} 6p_{3/2}^{3.75} 5f_{5/2}^{1.23} 5f_{7/2}^{1.49} 6d_{3/2}^{0.48} 6d_{5/2}^{0.60} 7s_{1/2}^{0.05}$
O	Ionic	-2	$1s^2 2s^2 2p^6$
	Calculated	-0.08	$1s^2 2s^{1.9} 2p^{4.41}$

TABLE 5.12: Analysis of the electronic structure of UO_2^{2+} from the purely ionic point of view to that obtained from the results conducted with DFT using projection analysis. The polarization contribution is -0.30e.

Table 5.13 shows the distribution of the U($6p$)-hole over molecular orbitals, again using projection analysis. We do indeed observe significant mixing of U($6p$) with O($2s/2p$)-orbitals in MOs σ_2, σ_4 and σ_7, which, for instance, is in line with the observations of Denning and co-workers [294, 306]. However, these are *canonical* MOs, with well-defined energies and symmetries and, as stressed by Mulliken [99], although such spectroscopic MOs, as he called them, are well suited for the understanding of electronic spectra and ionization, they do not allow one to "see" chemical bonds. In order to describe and understand chemical bonding, Mulliken advocated the use of maximally localized MOs, that is, in his terminology, *chemical* MOs. We therefore carried out localization using the Pipek-Mezey criterion [284], which minimizes the number of centers spanned by each MO. Somewhat to our surprise, we found that the localization procedure also induced rotations involving core orbitals, although these are already perfectly localized. After investigation of the gradient of the Pipek-Mezey functional with respect to orbital rotation, as detailed in Appendix E.1, we found that this is actually not excluded. As a pragmatic solution we therefore limited the localization procedure to the 12 canonical MOs of Table 5.13. The gross populations, from projection analysis, of the resulting localized orbitals are shown in Table 5.14. The orbitals have been ordered according to approximate orbital energies $\langle\varepsilon\rangle$, obtained as expectation values of the converged Kohn–Sham operator. Table 5.14 suggests triple bonds between uranium and each oxygen (O_1:$\{\sigma_5, \pi_3, \pi_4\}$, O_2:$\{\sigma_6, \pi_5, \pi_6\}$, mainly involving U($5f$)/U($6d$) and O($2p$), albeit with a non-negligible contribution from U($6p$).

	ε (E_h)	6s	6p	5f	6d	7s	O_1 2s	O_1 2p	O_2 2s	O_2 2p
σ_1	-2.343	1.926					0.019	0.018	0.019	0.018
σ_2	-1.644		1.080	0.035			0.349	0.089	0.349	0.089
π_1	-1.432		1.964					0.016		0.016
π_2	-1.432		1.964					0.016		0.016
σ_3	-1.374	0.044			0.155	0.002	0.850	0.023	0.850	0.023
σ_4	-1.124		0.530	0.080			0.593	0.098	0.593	0.098
π_3	-0.863				0.389			0.767		0.767
π_4	-0.863				0.389			0.767		0.767
π_5	-0.851		0.022	0.730				0.620		0.620
π_6	-0.851		0.022	0.730				0.620		0.620
σ_6	-0.833	0.017			0.084	0.044	0.077	0.821	0.077	0.821
σ_7	-0.806		0.142	1.162			0.018	0.324	0.018	0.324
Sum		1.987	5.724	2.737	1.017	0.046	1.906	4.179	1.906	4.179

TABLE 5.13: Gross population from projection analysis in canonical orbitals of uranyl.

This is in line with previous studies [285, 318]. Interestingly, the U($6p$) contribution is significantly reduced upon inclusion of spin-orbit interaction, underlining the necessity of also considering the role of SO when investigating bonds involving heavy elements, as discussed by Knecht *et al.* in the context of the U_2 dimer [66].

	$\langle\varepsilon\rangle$	6s	6p	5f	6d	7s	O_1 2s	O_1 2p	O_2 2s	O_2 2p
σ_1	-3.429	1.021	0.791	0.251	0.010		-0.021	-0.054		
σ_2	-3.429	1.021	0.791	0.251	0.010				-0.021	-0.054
π_1	-2.827		1.990	0.007				-0.007		
π_2	-2.827		1.990	0.007						-0.007
σ_3	-2.577	-0.003	-0.023	-0.003	0.004	0.018	1.921	0.083		
σ_4	-2.577	-0.003	-0.023	-0.003	0.004	0.018			1.921	0.083
σ_5	-2.116	-0.024	0.108	0.391	0.123	0.004	0.009	1.322		0.021
σ_6	-2.116	-0.024	0.108	0.391	0.123	0.004		0.021	0.009	1.322
π_3	-1.733		-0.002	0.354	0.195			1.404		0.002
π_4	-1.733		-0.002	0.354	0.195			1.404		0.002
π_5	-1.733		-0.002	0.354	0.195			0.002		1.404
π_6	-1.733		-0.002	0.354	0.195			0.002		1.404
Sum		1.988	5.724	2.708	1.054	0.044	1.909	4.177	1.909	4.177

TABLE 5.14: Gross population from projection analysis with localized orbitals in uranyl. $\langle\varepsilon\rangle$ refers to the expectation value (in E_h) of the converged Kohn-Sham operator.

We now turn to the analysis of the electric field gradient at the nuclear position of uranium in UO_2^{2+}. Table 5.16 shows a decomposition of the total EFG from projection analysis, with and without spin-orbit interaction. It can be seen that the intra-atomic contribution from uranium is quite small, some 10-15% of the total value, arising in part

	ω	$\langle\varepsilon\rangle$	$6s_{1/2}$	$6p_{1/2}$	$6p_{3/2}$	$5f_{5/2}$	$5f_{7/2}$	$6d_{3/2}$	$6d_{5/2}$	$7s_{1/2}$	O_1 $2s_{1/2}$	$2p_{1/2}$	$2p_{3/2}$	O_2 $2s_{1/2}$	$2p_{1/2}$	$2p_{3/2}$
42	1/2	-3.422	1.021	0.203	0.587	0.106	0.145		0.006		-0.021	-0.021	-0.034	-0.001		
43	1/2	-3.422	1.02	0.203	0.587	0.106	0.145		0.006		-0.001			-0.021	-0.021	-0.034
44	1/2	-3.156		1.514	0.480	0.004	0.012					-0.003	-0.003		-0.003	-0.003
45	3/2	-2.634			1.984	0.010	0.017									
46	3/2	-2.577		-0.005	-0.018			0.002	0.003	0.019	1.920	0.030	0.053			
47	3/2	-2.577		-0.005	-0.018			0.002	0.003	0.019				1.920	0.030	0.053
48	1/2	-2.027		-0.018	0.061	0.348		0.190			0.002		0.013	0.006		1.314
49	1/2	-2.027		-0.018	0.061	0.348		0.190			0.006		1.314	0.002		0.013
50	1/2	-1.822		-0.006	0.024	0.027	0.323	0.036	0.133			1.385	0.018		0.006	
51	1/2	-1.822		-0.006	0.024	0.027	0.323	0.036	0.133			0.006			1.385	0.018
52	3/2	-1.731				0.131	0.226	0.047	0.143				0.003			1.410
53	3/2	-1.731				0.131	0.226	0.047	0.143				1.410			0.003
Sum			2.042	1.862	3.772	1.238	1.417	0.550	0.570	0.038	1.906	1.397	2.774	1.906	1.397	2.774

TABLE 5.15: Gross population from projection analysis in localized orbitals in uranyl with SOC. $\langle\varepsilon\rangle$ refers to the expectation value (in E_h) of the converged Kohn-Sham operator.

from significant cancellation between the principal and hybridization contribution. Interestingly, these contributions change sign upon inclusion of spin-orbit interaction; we shall return to this later on. In line with what we have already seen for the chlorine compounds, the nuclear contribution is practically eliminated by the principal contribution of the oxygen atoms: $0.958 - 2 \times 0.457 = 0.044 \mathrm{E}_h/ea_0^2$. The inter-atomic contributions are small, albeit not negligible. What is really striking in Table 5.16 is the polarization contribution, which completely dominates the total EFG. We have previously pointed out that a significant polarization contribution obscures projection analysis and may indicate that further atomic orbitals should be included in the analysis. However, in the present context we argue that the polarization contribution provides a precise measure of the contribution to the EFG arising from the deformation of atoms upon forming the molecule. This is vividly brought out by Table 5.17 which shows the contribution to the EFG from groups of localized MOs, specifying for each group the fraction arising from polarization. It can be seen that almost half of the polarization contribution comes from the core orbitals, which were not included in the localization procedure. From the inverse cubic radial dependency of EFG matrix elements it follows that even slight core polarization may give significant contributions to the total EFG. For instance, the lowest occupied MO (LOMO), which is essentially $U(1s)$, contributes 0.108 E_h/ea_0^2. Inspection shows that the $U(1s)$ orbital is polarized by d orbitals (*ungerade* orbitals like p are not allowed due to inversion symmetry) and that the EFG contribution arises from the matrix elements coupling s with d.

In Table 5.16 we provide a different decomposition of the EFG, now in terms of groups

			without SO	with SO
intra-atomic	U	Principal	2.093	-3.501
		Hybridization	-2.673	2.365
	O_1	Principal	-0.457	-0.454
		Hybridization	0.021	0.018
	O_2	Principal	-0.457	-0.454
		Hybridization	0.021	0.018
inter-atomic	O_1-U		0.296	0.299
	O_2-U		0.296	0.299
	O_1-O_2		-0.002	-0.002
	Total		0.590	0.596
Polarization			-6.400	-6.813
Total electronic			-7.262	-8.226
Total nuclear			0.958	
Total EFG			-6.304	-7.269

TABLE 5.16: Decomposition of EFG at the position of uranium in UO_2^{2+} with and without spin-orbit interaction (SO). All values are reported in E_h/ea_0^2

of Pipek–Mezey localized MOs. We have also added Table 5.18 which gives a further decomposition of uranium intra-atomic contributions to each group of MOs. For the moment, let us focus in the numbers obtained without inclusion of SO: It will be seen from Table 5.16 that about half of the polarization contribution (and the EFG) comes from the core region. Clearly, the large core polarization masks the information about chemical bonding suggested by the Dailey–Townes model. Continuing our analysis, the non-bonding $O(2p)$ (lone pairs) contributes -1.246 E_h/ea_0^2, of which -0.418 E_h/ea_0^2 comes from polarization and -0.676 E_h/ea_0^2 from a minute contribution from $U(6p)$ and $U(5p)$ (cf. Table 5.18); as we have seen, the intra-atomic electronic oxygen contributions are essentially canceled by the nuclear ones. Table 5.16 furthermore shows that the non-bonding $U(6p)$ gives a very large *positive* contribution, whereas the U≡O bonds a somewhat larger *negative* contribution. In fact, their sum basically complements the contribution from core polarization to give the full EFG. Upon inclusion of SO the overall picture is very little changed, but, in Tables 5.16 and 5.18 one observes an approximate permutation of principal and hybridization contributions. This mainly arises from the fact, already mentioned, that $p_{1/2}$ orbitals do not contribute to atomic EFG expectation values, only through coupling with other AOs, principally $p_{3/2}$.

The numbers of Table 5.16 can to some extent be compared with an analysis of uranyl (and uranyl complexes) in terms of natural localized molecular orbitals (NLMOs)[320] provided by Aquino and co-workers [318]. The decomposition of the EFG expectation

	without SO		with SO	
	$\langle e\hat{q}^e_U\rangle_{ii}$	Polarization	$\langle e\hat{q}^e_U\rangle_{ii}$	Polarization
Core	-3.287	-3.107 (94.55%)	-3.552	-3.112 (87.61%)
Non-bonding U(6p)	29.761	4.802 (16.12 %)	28.354	4.190(14.78%)
Non-bonding O($2p$)	-1.246	-0.418 (33.60 %)	-1.287	-0.446 (34.88 %)
U≡O_1	-16.245	-3.838(23.63%)	-15.871	-3.722 (23.44 %)
U≡O_2	-16.245	-3.838 (23.63%)	-15.871	-3.722 (23.44 %)
Electronic: $\langle e\hat{q}^e_U\rangle$	-7.262	-6.400 (88.14%)	-8.227	-6.811 (82.79%)
Nuclear: $e\hat{q}^n_U$	0.958			
Total $\langle e\hat{q}_U\rangle$	-6.304		-7.269	

TABLE 5.17: All contributions of eq_U (in E_h/ea_0^2) from the localized MOs of $UO_2{}^{2+}$. The core region starts from U($1s$) and ends at U($5d$).

	without SO		with SO	
	$\langle e\hat{q}^e_U\rangle_{\text{princ}}$	$\langle e\hat{q}^e_U\rangle_{\text{Hyb}}$	$\langle e\hat{q}^e_U\rangle_{\text{princ}}$	$\langle e\hat{q}^e_U\rangle_{\text{Hyb}}$
Core	0.475	-0.372	0.219	-0.376
Non-bonding U(6p)	18.813	6.058	5.536	18.542
Non-bonding O($2p$)	-2.859	2.183	-0.885	0.196
U≡O_1	-7.167	-5.271	-4.184	-7.999
U≡O_2	-7.167	-5.271	-4.184	-7.999
Total	2.095	-2.673	-3.498	2.364

TABLE 5.18: Principal and hybridization contributions of eq_U (in E_h/ea_0^2) from the localized MOs of uranyl. The core region starts from U($1s$) and ends at U($5d$).

value reported in Table 10 of their paper is based on scalar-relativistic calculations using the zeroth-order regular approximation (ZORA), the B3LYP functional and a bond length of 1.78 Å. Their total value eq=-7.406 E_h/ea_0^2 is comparable to our scalar-relativistic value of -6.304 E_h/ea_0^2. At this level of theory, the NLMOs split into doubly occupied Lewis NLMOs and vacant non-Lewis ones. The expectation value is then expressed as Eq. (4.45) in terms of the former set. In order to avoid "large opposing nuclear and electronic" [273] contributions, the authors directly include nuclear contributions into the electronic expectation value through the substitution

$$e\hat{q}^e_K \rightarrow e\hat{q}^e_K + \frac{1}{N} eq^n_K. \tag{5.13}$$

However, in our opinion, this even distribution of nuclear contributions over NLMOs fails to bring out the near perfect cancellation of electronic and nuclear contributions from the atoms surrounding the nucleus of interest, as revealed by our projection analysis. The EFG decomposition of Aquino *et al.* [318] agrees with ours in terms of sign. Magnitudes are indeed smaller, but this can not be explained alone by the inclusion of nuclear contributions, since it is significantly smaller (0.958 E_h/ea_0^2) than the individual differences we

observe.

5.4 Conclusions

This work presents a detailed study of the Dailey–Townes model of electric field gradients (EFG) at nuclear positions in molecular systems and the chemical information that they carry. The basic premise of the model is the sensitivity of the EFG to deviations of spherical symmetry, such as induced by chemical bonding. Dailey and Townes proposed that the EFG could be estimated from the occupations and atomic EFG matrix elements of the valence AOs on the center of interest. Dailey and Townes had p-bonding in mind when they formulated their model, but it can also accommodate the dominant bonding contributions from d- and f-orbitals, as seen in uranyl. The Dailey–Townes model can be seen as a particular approximation to the decomposition of the EFG expectation value by projection analysis [221, 222]. We have carried out such analysis for a number of halogen compounds, many of them included in the 1949 paper by Dailey and Townes, as well as uranyl. Overall, we find that the Dailey–Townes model in its pure form is too rough an approximation. Replacing net populations by gross populations improves the agreement with total SCF values, but we have found no valid theoretical justification for this. In more detail, we find that the intra-atomic contributions to the electronic EFG operator $e\hat{q}^e_K$ from centers other than the center K of interest is significant, but to a large extent cancelled by corresponding nuclear contributions, in line with the arguments of Dailey and Townes. Inter-atomic contributions are generally small, at least for the studied halogen compounds. However, hybridization contributions from the same center (K), which do not contribute to atomic expectation values, can be significant (-15%). With increasing nuclear charge and number of electrons, core polarization reach the same order of magnitude as the EFG contributions associated with bonding, as dramatically seen in uranyl. A particular feature of uranyl is the $6p$-hole. Upon localization, we find the uranium $6p$-orbitals to be mostly non-bonding, in particular upon inclusion of spin-orbit interaction. Their large positive contribution combined with the somewhat larger negative contribution from the U≡O bonds combine to give the other half of the total EFG.

We have also investigated relativistic effects. The inclusion of scalar relativistic effect does not fundamentally change the premises of the model. However, with the inclusion

of spin-orbit interaction, the electronic EFG operator $e\hat{q}^e_K$ is no longer diagonal in the space of atomic orbitals of given orbital angular momentum ℓ. We note in particular that $p_{1/2}$-orbitals, having a spherically symmetric density, have a zero EFG expectation value. The coupling between orbitals of $j = \ell \pm 1/2$, such as $p_{1/2}$ and $p_{3/2}$ becomes important, as manifested by important hybridization contributions. One could imagine rotating back from $|j, m_j\rangle$ eigenfunctions to $|\ell, m_\ell, s, m_s\rangle$ ones, but this is only possible when the radial functions of AOs of $j = \ell \pm 1/2$ are identical, which will progressively no longer be the case as one descends the periodic table, and, in the language of Pyykkö and Seth [59], lead to spin-orbit tilting.

We believe that our detailed analysis of the electric field gradient at nuclear positions will be useful when setting up a computational protocol for accurate calculations of the EFG, a necessary ingredient for the direct determination of nuclear electric quadrupole moments from experiment. There are still a number of elements for which a reference eq is not yet established [53]. We have therefore developed tools for the generation of high-order relativistic coupled cluster code [28] for the calculation of analytic derivatives of the coupled cluster energy, which will be the subject of the next chapter.

Chapter 6

Highly Accurate Expectation Values Using High-Order Relativistic Coupled Cluster Theory

The results presented in this chapter are based on the following work:

> Gabriele Fabbro, Jan Brandejs, and Trond Saue, "Highly Accurate Expectation Values Using High-Order Relativistic Coupled Cluster Theory," *The Journal of Physical Chemistry A*, vol. 129, pp. 7360–7372, 2025. DOI: 10.1021/acs.jpca.5c02844.

In this project, I derived the equations for the Λ amplitudes and the density matrices at arbitrary coupled-cluster (CC) level, formulated them within the `tenpi` framework, and implemented the CCSDT and CCSDTQ expectation values in the `DIRAC` program. I also developed and implemented the ro-vibrational corrections, carried out all calculations and the data analysis, and wrote the manuscript.

Abstract

This work presents a framework for the automatic generation of analytic one-electron first derivatives of the energy for general coupled-cluster models, implemented using the TENPI toolchain. We report the first implementation of expectation values for CCSDT and CCSDTQ methods within the DIRAC program package for relativistic molecular calculations. As pivotal calculations, we focus on the electric field gradient (EFG) evaluated at the lithium nucleus in LiX (X = H, F, Cl) compounds, enabling the extraction of the nuclear electric quadrupole moment $Q(^7\mathrm{Li})$, and at the aluminum nucleus in AlY (Y =H, F, Cl, Br) compounds, for the determination of $Q(^{27}\mathrm{Al})$. These high-order methods are applied to compute corrections for triple and quadruple excitations for the EFG, a crucial quantity for determining nuclear quadrupole moments. We obtain $Q(^{27}\mathrm{Al}) = 0.146598 \pm 0.000001$ b, in excellent agreement with the recommended value, and $Q(^7\mathrm{Li}) = -0.038624 \pm 0.000292$ b, which is smaller than the currently recommended value, that indicates the need for further investigation.

6.1 Introduction

The atomic nucleus, while often simplified as a point charge in basic atomic models, possesses a complex internal structure that can manifest in various electromagnetic moments. Among these, the nuclear electric quadrupole moment (NQM) stands out as a fundamental property that describes the deviation of the nuclear charge distribution from perfect spherical symmetry. This characteristic is inherent to nuclei with a spin quantum number greater than one-half ($I > 1/2$). The determination of nuclear quadrupole moments (NQMs) is particularly valuable, as they directly influence hyperfine parameters in rotational spectroscopy. For instance, the newly obtained data for bromine were employed in the assignment of its rotational spectra [321, 322], and analogous applications exist for iodine [323]. Also, the determination of the nuclear quadrupole moment plays a crucial role in advancing our understanding of nuclear structure and the distribution of charge within nuclei [52, 53, 324–328]. One of the key mechanisms for the accurate determination of the (spectroscopic-)nuclear quadrupole moment is based on the interaction between the NQM and the electric field gradient (EFG) at the nuclear position, and it can be quantified by the nuclear quadrupole coupling constant (NQCC), defined as

$$\text{NQCC [in MHz]} = 234.9647 \times Q[\text{in b}] \times q \left[\text{in } E_h/a_0^2\right] \tag{6.1}$$

where eQ represents the nuclear electric quadrupole moment of the isotope and eq denotes the electric field gradient along the molecular axis at the location of the nucleus, computed using molecular electronic structure theory. Several experimental techniques exist for the accurate determination of NQCCs, which have been cataloged by Stone [53], and on which we recently performed a statistical analysis [209]. On the other hand, the accurate determination of the EFG is challenging, since it is quite sensitive to the basis set quality, as clearly show by van Stralen and Vissher [329]. Moreover, at the SCF-level, in the absence of polarization, the EFG is zero for core shells. Instead, it samples the inner tails of valence orbitals, making it sensitive to electron correlation effects.

Coupled Cluster (CC) theory [15, 140] is highly regarded as the standard in quantum chemistry [330, 331] because it can systematically capture electronic correlation [14]. Moreover, the inherent multiplicative-separable characteristic of the CC wave function leads to size-extensivity and size-consistency [15, 140, 332–335], an essential feature for accurately describing realistic systems. The computation of properties within the CC

framework can be traced back to 1969 by Čížek [336], where he showed how expectation values can be computed by factorizing the numerator in order to remove all the disconnected diagram contributions. However, the expression provided by Čížek was problematic due to the enormous quantity of terms, since there was not a natural truncation of the cluster expansion. A few years later Monkhorst [154] provided a strategy for the computation of properties (both time dependent and independent) with the usage of the similarity-transformed Hamiltonian, which provides, using the Baker–Campbell–Hausdorff expansion, a natural truncation of terms, still completely connected. In the 1980s, analytic energy gradients were developed by Adamowicz and Bartlett [205]. Bartlett and co-workers provided general diagrammatic and algebraic expressions for the analytical derivatives of CC and MBPT wave functions [337]. After a few years, Salter and co-workers [204] showed the expressions for the energy derivatives and response density for the CCSD method [163] . Until then, the bottleneck in the calculation of molecular properties at the CC level was the requirement for amplitude derivatives, and thus the need to solve the response equations for each field strength. Salter and co-workers showed that it is possible to rearrange the CC equations to yield a single set of linear, perturbation-independent equations, namely the $\Lambda-$*equations* [202]. Helgaker and Jørgensen provided a more natural framework to recover these equations [47, 338]. They observed that by introducing a Lagrangian and by enforcing its stationarity with respect to the field strengths, it becomes possible to get the $\Lambda-$equations, and therefore calculate first- and second-order molecular properties without the need to explicitly compute the derivatives of the cluster amplitudes (*vide infra*). The Lagrangian approach has been a fertile ground for the calculation of molecular properties at the CC level, both for ground [48, 339, 340] and excited states [162, 341–343]. Later on, Kállay and co-workers developed analytic first and second derivatives for general coupled-cluster excitation level, based on the Lagrangian formalism [207, 344] .

In addition to correlation effects, the EFG is highly sensitive to relativistic effects [5, 58, 59, 134, 345–348], as it is proportional to the inverse cubic radial expectation value, $\langle r^{-3} \rangle$ (see, for instance, Ref. [197]). This proportionality highlights that the EFG probes the core region surrounding the nucleus, where relativistic effects are particularly pronounced, especially for heavy elements (typically with $Z > 40$). The increased number of electrons in heavy atoms further amplifies the importance of electronic correlation effects, making both relativistic and correlation contributions critical for accurately determining the EFG.

The primary challenge in studying systems with heavy atoms is that electron correlation effects and relativistic effects are non-additive and must be treated simultaneously [349].

Although alternative approaches incorporate relativistic effects via perturbation theory [350–352], the most natural inclusion is obtained by using a four-component Dirac–Coulomb (DC) Hamiltonian. In the DIRAC program package [29] first-order properties at the relativistic CCSD level were implemented by Shee and co-workers [353] in the RELCCSD module [354–356], which benefits from point-group symmetry [29]. More recently, Pototschnig and co-workers implemented relativistic coupled-cluster algorithms, including the CCSD analytic gradient, optimized for modern heterogeneous high-performance computing infrastructures, with support for GPU co-processing via the ExaTENSOR library [357].

Contributions from excitations beyond doubles may be required for an accurate description of the target property. An example of that is provided by the determination of the NQM of ^{27}Al, where Pernpointner and Visscher showed that the inclusion of perturbative triple excitations can still effect the EFG [358]. Stopkowicz and Gauss also showed how triple and quadruple excitations can affect the NQM of sulfur isotopes [359]. Therefore, the development of a general-order program arose for the generation of high-order CC equations. This need stems from the complexity and difficulty of explicitly programming and debugging the various matrix elements associated with excitations higher than doubles. Several approaches can be employed to derive systematically the CC equations: by directly applying second-quantization rules [26, 27], some rely on Wick's theorem [150], which decomposes products of operators into sums of contractions [16, 19–22, 24, 25], while others utilize a diagrammatic approach [142], where the equations are derived graphically [17, 23]. The major advantage of using diagrams over second-quantized algebra and Wick's theorem is that they are easier to inspect and interpret, and are therefore less prone to errors. Moreover, it is more easy to generate unique diagrams and identify those that are equivalent. Recently, Brandejs and co-workers introduced tenpi [28, 192], an open-source toolchain designed for the development of CC methods, integrated within the DIRAC program package [29]. tenpi builds upon the diagrammatic approach of Kállay and Surján [17], which is in turn based on the Kucharski-Bartlett diagrams [167], but extends it with advanced features such as global optimization of intermediates, a Python-based user interface, a visualization module, and a code generator. On the output, tenpi supports

several tensor libraries including ExaTENSOR as well as the standard tensor interface TAPP (Tensor Algebra Processing Primitives) [360].

In this work, we developed and implemented high-order relativistic CC expectation values within the DIRAC program package [29], focusing on the CCSDT and CCSDTQ methods. The equations were derived and generated using the tenpi toolchain and subsequently implemented in the ExaCorr module in DIRAC [357]. To validate our protocol, we performed non-relativistic calculations and compared the results with those obtained using the well-established MRCC program [191]. Furthermore, as sample applications, we computed the EFG in the LiX (X=H, F, Cl) and AlY (Y=H, F, Cl, Br) series of systems to extract the NQMs of ^{7}Li and ^{27}Al, comparing these with the standard reference values [49, 361].

6.2 Implementation

In this section we will focus on the derivation and implementation of the expression for the $\Lambda-$equations and one-body density matrix.

The ExaCorr module in DIRAC [357] provides X2C relativistic CCD/CC2/CCSD/CCSD(T) methods, based on the math libraries TAL-SH [362] and ExaTENSOR [194, 357] developed by Lyakh. The CC code is unrestricted and so can in principle be applied to any system dominated by a single reference, but in the present work received orbitals obtained by Kramers-restricted HF [363]. Recently, Brandejs and co-workers also implemented high-order CC energy methods, i.e CCSDT and CCSDTQ in ExaCorr [28]. The equations and the optimized codes were obtained using the tenpi toolchain.

6.2.1 Generation of the $\Lambda-$equations and density matrices

Compared to Kállay algorithm discussed in Sec. 3.2.3 [207], in our approach we generate the lambda equations directly from matrix elements produced by Eq.(3.57) that incorporate both the similarity–transformed Hamiltonian and the $\hat{\Lambda}$ operator. Although we also close the amplitude diagrams with the $\hat{\Lambda}$ operator from above, our integer string encoding remains unmodified. In our method the Λ diagrams are obtained by simply appending $\hat{\Lambda}$ to the amplitude diagrams, thereby preserving the original structure and streamlining the

generation process. Once these connections are established, tenpi processes the diagrams as described in Sec. 2.6.1, with subsequent factorization and reordering to ensure efficient contraction of intermediates.

In the tenpi toolchain [28], the $\Lambda-$equations are generated by the `getLambdaEquations` function, which constructs diagrammatic contributions for the left eigenvalue problem of simlarity-transformed Hamiltonian. The procedure takes as input the excitation levels to include, the maximum excitation rank allowed in the diagrams, and a flag `doCCD` to enable CCD-specific simplifications. First, the function constructs the appropriate strings representing matrix elements of the form $\langle 0L_1L_2\ldots|He^T|\mu\rangle$, where μ ranges over the desired excitation ranks. For example, in the case of CCSD, μ spans the single and double excitation manifolds. If the user selects the CCD variant, certain contributions like $\langle 0L_1|He^T|S\rangle$ are deliberately excluded.

For the generation of the one-body density matrices, we follow the idea proposed by Kállay [207], noting that Eqn.(3.71) fundamentally involves, in addition to the $\hat{\Lambda}$ operator and $\overline{\hat{H}}$, a one-electron operator $\{a_p^\dagger a_q\}$. Therefore, to represent this one-electron operator, in tenpi we replace $\{a_p^\dagger a_q\}$ by $\hat{F} = \sum_{pq} f_{pq}\{a_p^\dagger a_q\}$, and once the diagrams are generated, we remove the matrix element f_{pq}. Again, once the diagrams and the algebraic expressions are generated, they are processed by tenpi as explained in Sec.2.6.1.

The generation of the $\Lambda-$equations involving excitations beyond doubles (i.e., triples and quadruples) took longer than expected due to several bugs. As widely documented in the literature [15, 140, 142], each pair of equivalent lines (i.e., lines beginning at the same horizontal interaction line and ending at the same interaction line) contributes a factor of $1/2$ to the algebraic representation of a diagram. This rule accounts for the fact that, both in the amplitude equations (of any order) and in the $\Lambda-$equations (up to double excitations), at most *pairs* of equivalent lines are encountered. However, in the specific case of the $\Lambda-$equations (as well as for density matrices), the inclusion of triple and higher excitations requires an extension of the equivalent line rule. In these cases, groups of three, four, or more equivalent lines can appear, as seen for example in the upper left diagram of Figure (3.3). Consequently, if n is the number of equivalent lines, a factor of $1/n!$ must be applied to the algebraic representation of the diagram. This rule is also mentioned in a footnote of Ref. [140]. An example of this is provided in Figure 6.1 by one of the diagrams arising from the Λ CCSDT equations, which contains a contraction

between $\hat{T}_3$ and $\hat{\Lambda}_3$. In this example, we observe three equivalent hole lines (red lines in Figure 6.1) and two equivalent particle lines (blue lines in Figure 6.1). Therefore, applying the correct rule yields

$$\frac{1}{n_h!} \times \frac{1}{n_\mathrm{p}!} = \frac{1}{3!} \times \frac{1}{2!} = \frac{1}{12}.$$

For clarity, note that if the original rule—namely, that each pair of equivalent lines contributes a factor of 1/2—were mistakenly applied even when more than two lines are present, then for three equivalent hole lines one would count

$$\binom{3}{2} = 3 \quad \text{pairs},$$

leading to a factor of

$$\left(\frac{1}{2}\right)^3 = \frac{1}{8}.$$

For the two equivalent particle lines, the factor remains 1/2. Together, this would yield a total factor of

$$\frac{1}{8} \times \frac{1}{2} = \frac{1}{16}.$$

Thus, using the incorrect rule would yield a factor of $\frac{1}{16}$ instead of the correct $\frac{1}{12}$, thereby underscoring the necessity of applying the extension $1/n!$ for groups of n equivalent lines.

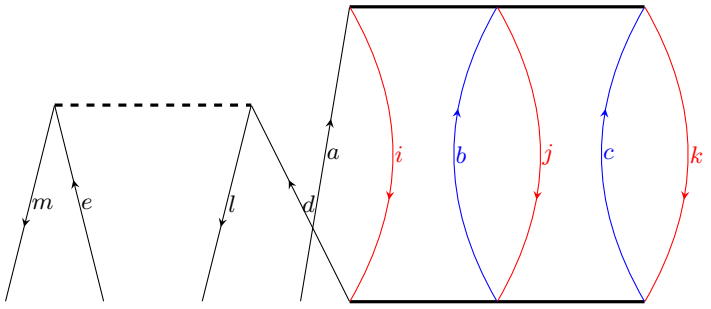

FIGURE 6.1: One of the diagrams that appears in the Λ-CCSDT equations.

During CCSDT/Q intermediate optimization, we found that Opmin's integer-only `math.gcd` [364] python function caused instability during factorization when non-integer floating-point prefactors were present. We implement the following sequence to fix this: i) compute the least common multiple (LCM) across all prefactor denominators, ii) scale each tensor contraction by that LCM to yield integer prefactors, iii) run Opmin, iv) divide the results by the LCM to restore the original scale.

6.3 Computational Details

All calculations were performed with development versions of the DIRAC [29] and the TAL-SH library. Details on the particular revisions used in the calculations described below are given in the respective output files that are provided within a separate repository [365]. In this study, we mainly use the exact two-component (X2C) Hamiltonian with molecular mean-field correction [139]. The Gaussian model of nuclei has been employed for all the molecules using the parameters of Ref. [276]. We performed all calculations including the Gaunt interaction at the SCF level, as well as the $\langle SS|SS\rangle$ class of two-electron integrals.

Our first goal was to verify the correctness of the new high-order CC expectation values. To do so, we first implemented the CCSD model using the autogenerated code from tenpi and compared it with the hand-coded implementation already present in ExaCorr [357]. Once this validation was completed, to further assess the correctness of the CCSDT and CCSDTQ expectation values, we compared the results of the new implementations using TAL-SH to those obtained with the MRCC quantum chemistry package [191], using a non-relativistic Hamiltonian.

To define the active space, we employ the notation AS(k,n), where k represents the number of electrons and n the number of active Kramers pairs (occupied plus virtual), that is, the spinors of each pair are related by time-reversal symmetry.

For the non-relativistic calculations, we have considered the computation of the dipole moment of LiH in a 6-31G basis [366, 367] at an internuclear distance of 3.015 a_0 [368]. Subsequently, a more relevant application of our high-order CC expectation values code is the determination of the nuclear quadrupole moment (NQM) of ^{7}Li and ^{27}Al from molecular data. To determine $Q(^7\text{Li})$, we considered three molecules: LiH, LiF, and LiCl. The experimental equilibrium bond distances of these molecules, 3.015 a_0, 2.9553 a_0, and 3.81852 a_0, respectively, were taken from Ref.[369]. For all the lithium compounds we took the dyall.ae4z [283] basis set, where the latter was augmented with a tight p-exponent with value $435.417100a_0^{-2}$ and with a tight d-exponent with value $62.168460a_0^{-2}$, as explained in Sec.6.3.1. For all three molecules, CCSD calculations were performed correlating all electrons. The active space was defined by including the full set of available virtual orbitals.

For the AlY (Y = H, F, Cl, Br) calculations, we used the equilibrium distances 3.1129 a_0, 3.1263 a_0, 4.0241 a_0 and 4.3372 a_0. For the CCSD calculations, we employed the basis dyall.aae4z [282], which was augmented by a p-exponent with value 24750.350000 a_0^{-2}, a d-exponent with value 1233.029836 a_0^{-2} and a f-exponent with value 548.276242 a_0^{-2} as explained in Sec.6.3.1.

For all the systems, to compute the triple and quadruple corrections, we used a slightly smaller basis, dyall.v3z [282, 283].

6.3.1 Basis set and Active space

Since basis sets are generally optimized for energy rather than properties, and because we start from basis sets already optimized for correlated calculations, we investigated the convergence of our basis set with respect to the EFG at the SCF level.

Tables 6.1–6.2 report the experimental values of the nuclear quadrupole coupling constants, along with their associated uncertainties. To ensure that the computational error does not exceed the relative uncertainties, we require that the relative change in q due to basis set augmentation remains below the experimental relative uncertainty associated to the NQCCs. For the lithium systems, we found that the smallest relative uncertainty is associated to ^{7}Li^{1}H, which is 0.0072%, and therefore we require that, in order to ensure that the accuracy of the extracted quadrupole moment Q depends only on the experimental error, the accuracy of the EFG must be determined with a relative uncertainty lower than 0.0072%, whereas for the aluminum systems, we found that the smallest relative uncertainty is associated with ^{27}Al^{35}Cl, which is 0.0089%.

Molecule	NQCC (MHz)	Relative Uncertainty (%)
^{7}Li^{1}H ($\nu = 0$, $J = 1$)	0.346750 ± 0.000025 [370]	0.0072
^{7}Li^{1}H ($\nu = 1$, $J = 1$)	0.332 ± 0.005 [370]	1.5060
^{7}Li^{2}H ($\nu = 0$)	0.349 ± 0.001 [370]	0.2865
^{7}Li^{19}F ($\nu = 0$)	0.4156 ± 0.0004 [370]	0.0963
^{7}Li^{19}F ($\nu = 1$)	0.4061 ± 0.0006 [370]	0.1477
^{7}Li^{19}F ($\nu = 2$)	0.3965 ± 0.0008 [370]	0.2016
^{7}Li^{35}Cl ($\nu = 0$)	0.24993 ± 0.00050 [370]	0.2000
^{7}Li^{35}Cl ($\nu = 1$)	0.2446 ± 0.0020 [370]	0.8179

TABLE 6.1: NQCC and relative error with respect to uncertainty for the lithium systems.

We employ the following protocol: We first add exponents in an even-tempered manner until satisfactory convergence of the EFG is achieved. However, this typically leads to

Molecule	NQCC (MHz)	Relative Uncertainty (%)
$^{27}Al^{1}H$	-48.59 ± 0.70 [371]	1.44
$^{27}Al^{2}H$	-48.48 ± 0.88 [371]	1.815
$^{27}Al^{19}F$, R_e	-37.75 ± 0.08 [372]	0.212
$^{27}Al^{19}F$ ($v = 0$)	-37.53 ± 0.12 [372]	0.320
$^{27}Al^{35}Cl$ ($v = 0$)	-30.4081 ± 0.0027 [372]	0.0089
$^{27}Al^{79}Br$ ($v = 0$)	-28.0059 ± 0.0035 [373]	0.0125

TABLE 6.2: NQCC and relative error with respect to uncertainty for the aluminum systems.

very large basis sets, which are prohibitively expensive for high-order CC calculations; therefore, we then perform a line search to optimize a single exponent against the reference value obtained with the large basis set. This procedure ensures an optimal compromise between computational cost and EFG accuracy.

The s exponents were omitted because projection analyses [209, 221] show that s orbitals, being spherically symmetric, contribute negligibly to the EFG. Furthermore, our previous work [209] demonstrated near-complete cancellation between electronic and nuclear contributions from surrounding nuclei. The dominant effect is orbital polarization by ligands, so we focus on the most polarized systems, LiF and AlF.

Starting from dyall.ae4z (19s10p5d3f) for Li and dyall.aae4z (25s15p10d7f5g) for Al, we added one p-exponent (435.417100 a_0^{-2}) and one d-exponent (62.168460 a_0^{-2}) to Li—yielding a 19s11p6d3f set—and one p-exponent (24750.350000 a_0^{-2}), one d-exponent (1233.029836 a_0^{-2}), and one f-exponent (548.276242 a_0^{-2}) to Al—yielding a 25s16p11d8f5g set. The addition of d-type exponents led to slow EFG convergence for both systems—unexpectedly also in Li, which lacks occupied d orbitals—due to the EFG operator coupling functions differing by two units of angular momentum. In the Supporting Information file, we provide basis set augmentation details for EFG calculations for LiF (Table S1) and AlF (Table S2).

Since the current high-order expectation-values module runs entirely on a single compute node, it is constrained by the available RAM on that node; hence, we can not include a very large number of virtual spinors without exceeding the memory capacity of the Olympe machine that we are currently using [374]. One of the future goals we are already working on is the transition to multiple-nodes using the Cyclops library [375].

Moreover, ExaCorr currently does not exploit point-group symmetry and index permutation symmetry of tensors [357]. So, the major disadvantage is that the active space (AS) is relatively small.

Therefore, we have used a composite approach in order to determine the EFG at the lithium and aluminum nuclear positions. An exemplary instance of such a procedure at the CC level was proposed recently by Skripnikov in the context of determining the nuclear magnetic and electric quadrupole moments of polonium isotopes [242], as well also the determination of the nuclear electric quadrupole moment of isotopes ^{33}S and ^{35}S by Stopkowicz and Gauss [359]. The strategy adopted was to obtain an accurate EFG value evaluated at the CCSD level using the RELCCSD [29, 353, 355] module (which benefits from point-group symmetry) with a large active space and a sufficiently extended basis set, and then subsequently calculate the corrections arising from triple and quadruple excitations. We have estimated the triple and quadrupole correction by performing calculations on a smaller basis set, the dyall.v3z [283]. Therefore, the contribution of triple excitations can then be estimated as

$$T = \langle q \rangle_{\mathrm{CCSDT}}^{\mathrm{dyall.v3z}} - \langle q \rangle_{\mathrm{CCSD}}^{\mathrm{dyall.v3z}}, \tag{6.2}$$

using the same active space for the CCSD and CCSDT calculations, as well for the quadruples

$$Q = \langle q \rangle_{\mathrm{CCSDTQ}}^{\mathrm{dyall.v3z}} - \langle q \rangle_{\mathrm{CCSDT}}^{\mathrm{dyall.v3z}}, \tag{6.3}$$

where $\langle q \rangle$ represents the electric field gradient expectation value. This approximate contribution can then be added to the value computed with a *large* basis set, determinate as explained above

$$\langle \Omega \rangle_{\mathrm{Q(T(CCSD))}} = \langle \Omega \rangle_{\mathrm{CCSD}}^{\mathrm{opt\text{-}basis}} + T + Q, \tag{6.4}$$

where opt-basis is the optimized basis discussed before, i.e 19s11p6d3f for Li and 25s16p11d8f5g for Al.

At the CCSD level, we fully correlated all electrons in LiX (X = H, F, Cl) systems owing to their small size. For AlY (Y=H, F, Cl, Br), however, memory constraints forced us to apply an energy cutoff when selecting virtual orbitals—a critical choice for accurate EFGs. The energy cutoff should be chosen so as not to completely eliminate correlation functions. Pernpointner and Visscher showed that excluding orbitals above 4.5 E_h (AlF,

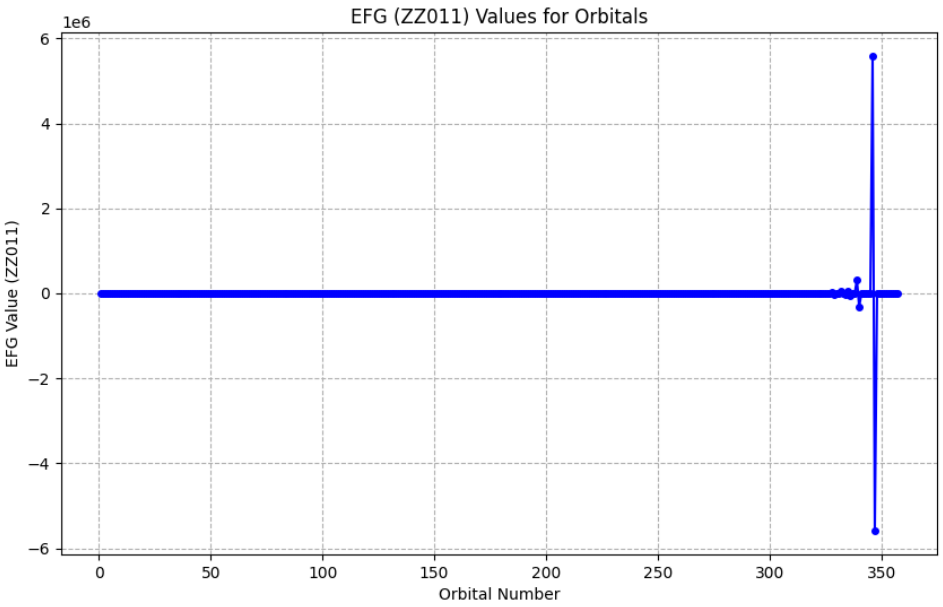

FIGURE 6.2: Contribution to the EFG from the HF orbitals in AlF molecule.

AlCl) and 4.4 E_h (AlBr) avoids sharp EFG oscillations [358]. A contribution to such unstability is as follows: Figure 6.2, we report the contributions of the Hartree–Fock orbitals to the electric field gradient in AlF. A pronounced oscillation of the order of $10^6\, E_h/ea_0^2$, attributable primarily to orbitals 346 and 347, is observed, which swamps all the other contributions. Projection analysis [221] reveals that these orbitals correspond to aluminum $p_{3/2}$-type spinors, with $|m_j| = 1/2$ and $3/2$. Notably, orbital 346 contributes $5562233.8\, E_h/ea_0^2$, while orbital 347 contributes $-5562392.7\, E_h/ea_0^2$. In the free atom, these contributions should cancel [209], but in the molecule their net contribution to the EFG is $-158.9\, E_h/ea_0^2$. The effect is therefor due to polarization of these core-like virtual orbitals in the molecule. In fact, orbital 345, identified as the partner $p_{1/2}$ spinor, contributes $156.3\, E_h/ea_0^2$, which almost cancels out the residual contributions from orbitals 346 and 347, but not entirely. It follows that noise may be introduced in the correlated calculations if the energy threshold only partially includes an atom-like shell.

For AlF, we observed that the EFG stabilizes once a threshold of 45 E_h is reached. Extending the energy cutoff beyond this threshold does not result in any significant variation in the EFG, nor does it affect the final quadrupole moment. We retained this cutoff also for AlCl and AlBr to keep the calculations computationally feasible without compromising on the correlation of inner-shell electrons.

When employing higher-order coupled-cluster methods, it was necessary to impose tighter restrictions on the number of correlated electrons and orbitals to ensure computational feasibility. For the triple and quadruple excitation corrections, however, the objective was to estimate their magnitude rather than achieve full numerical convergence. Given the relatively small size of the active space, we chose to specify the number of Kramers pairs involved rather than report energy thresholds. Table 6.3 summarizes the active spaces, reporting the number of correlated electrons and the number of Kramers pairs used for each system and method.

		LiX			AlY		
	LiH	LiF	LiCl	AlH	AlF	AlCl	AlBr
CCSD	(4, 140)	(12, 206)	(20, 283)	(14, 199)	(22, 237)	(30, 280)	(48, 292)
CCSDT	(4, 39)	(6, 34)	(6, 34)	(6, 34)	(6, 34)	(6, 34)	(6, 34)
CCSDTQ	(4, 10)	(6, 9)	(6, 9)	(6, 9)	(6, 9)	(6, 9)	(6, 9)

TABLE 6.3: For each molecule and each method, the number of correlated electrons and the number of Kramers pairs used in the active space are reported.

6.3.2 Determination of nuclear electric quadrupole moments Q

Nuclear electric quadrupole moments (NQMs) are extracted using linear regression based on (6.1). Experimental and theoretical uncertainties are incorporated using Orthogonal Distance Regression [376]. The error analysis is detailed in the Supporting Information file.

6.4 Results & Discussion

6.4.1 Correctness: dipole moment of LiH

To confirm the correctness of our high-order coupled-cluster expectation value code, we compared the ground-state coupled cluster dipole moment of LiH from tenpi (this work) with those from the MRCC package [191, 207, 377] and, where feasible, with the DIRAC code (using the hand-coded one) [357]. From Table 6.4 we see that, at SCF level, dipole moments computed with DIRAC and MRCC are virtually identical and indicate that both codes yield equivalent SCF-level results, thus providing a solid baseline for subsequent correlated methods. For the CCSD method, the dipole moments computed with DIRAC using both the tenpi autogenerated code and the hand-coded (hc) implementation are

exactly the same. The MRCC package produces a minute difference (on the order of 10^{-8}), which is negligible and demonstrates that our autogenerated code is fully consistent with the handwritten implementation as well as with an independent reference from MRCC. At higher levels of theory, i.e., CCSDT (including triple excitations) and CCSDTQ (including quadruple excitations), the dipole moments from DIRAC (tenpi) and MRCC remain in excellent agreement in the convergence threshold limit.

method	**code**	**convergence**	**Total dipole moment** $[E_h/ea_0]$
SCF	DIRAC		-2.33268232
SCF	MRCC		-2.33268233
CCSD	DIRAC tenpi	0.6E-09	-2.16553800
CCSD	DIRAC hc	0.6E-09	-2.16553800
CCSD	MRCC	1.3E-10	-2.16553802
CCSDT	DIRAC tenpi	0.9E-09	-2.16528064
CCSDT	MRCC	1.8E-10	-2.16528066
CCSDTQ	DIRAC tenpi	0.6E-09	-2.16527943
CCSDTQ	MRCC	2.1E-10	-2.16527945

TABLE 6.4: Convergence of the final error shown in the run and Total dipole moment for Different Methods and Codes for LiH. hc=hand-coded.

6.4.2 Nuclear Electric Quadrupole Moments of ^{7}Li

Pioneering values of the EFG for lithium were obtained using the restricted Hartree-Fock (RHF) [378, 379] and Configuration-Interaction (CI) calculations [380, 381]. A significant improvement in the calculation of the EFG at the lithium nucleus was provided by Green [382], who used a CI wavefunction including 200 determinants. However, as pointed out shortly thereafter by Sundholm and co-workers [383], the value reported by Green might not have been sufficiently accurate due to basis set incompleteness. Moreover, Green's calculations relied on the Hellmann-Feynman theorem [45, 46] applied to a limited CI function, potentially introducing inaccuracies in the correlation correction to q.

To address these issues, Sundholm and co-workers used a hybrid approach that combined fully numerical solutions of the HF equations with discrete basis set calculations for correlation corrections. Additionally, Sundholm and co-workers ensured that their wavefunctions satisfied the Hellmann-Feynman theorem by employing a full CI approach within the chosen active space, leading to more accurate correlation corrections and incorporating rovibrational effects. Their work provided a benchmark for the EFG, refining $Q(^7\mathrm{Li})$ to $-0.0406\,\mathrm{b}$ [383].

Shortly thereafter, Diercksen and co-workers extended the analysis to lithium fluoride (LiF) [384]. Their findings reinforced the molecular value of $Q(^7\mathrm{Li})$ as $-0.04055(80)$ b, consistent with results obtained from LiH [383], subsequently confirmed by Urban and Sadlej, also including the LiCl molecule in the analysis [369, 385], getting $Q(^7\mathrm{Li})$=0.0406 b. This value was later adopted as the reference by Pyykkö [386].

Recently, Guan and co-workers [387], using an optical Ramsey technique combined with bound-state quantum electrodynamics theory, determined the quadrupole moment of ^{7}Li as $Q(^7\mathrm{Li})$ = -0.0386(5) b, which clearly deviates from the currently accepted one [369].

On our side, we aim to shed light on this discrepancy through the methodology previously discussed, which combines state-of-the-art relativistic coupled-cluster calculations with an accurate treatment of rovibrational effects. The details on the incorporation of the rovibrational effects are detailed in Appendix F.

We have reported in Table 6.5 the different values of the EFG evaluated at the lithium position for the three different systems LiH, LiF and LiCl. Table 6.5 reveal that inclusion of electron correlation through CCSD introduces modest corrections that slightly adjust the HF values; the additional full triples corrections further refine the results, although the full quadruple corrections are negligible, indicating that higher-order correlation effects beyond triples are minimal.

	LiH		LiF		LiCl	
	EFG	Q	EFG	Q	EFG	Q
HF	-0.039726	-0.037148	-0.049030	-0.036075	-0.027471	-0.038721
+ CCSD	0.001020	-0.002578	0.002742	-0.002137	-0.000316	0.000440
+ correction for full triples	0.000051	0.001549	0.000279	-0.000232	0.000275	-0.000382
+ corrections for full quadruples	0.000000	0.000000	0.000000	0.000000	0.000000	0.000000
final value	-0.038655	-0.038177	-0.046009	-0.038444	-0.027512	-0.038663

TABLE 6.5: Individual contributions to the EFG (E_h/ea_0^2) at the Li position for the systems LiX (X = H, F, Cl) and the derived values for the ^{7}Li quadrupole moment (Q, in mb).

To better relate our theoretical EFG results with the experimental nuclear quadrupole coupling constants, we took into account the rovibrational contributions, as detailed in Appendix F. In this context, the rovibrationally averaged EFGs were computed using the utility program VIBCAL included in the DIRAC program package. In order to compute these quantities, for each molecule a potential energy surface (PES) and a corresponding

property surface (PS) were generated by sampling multiple points along the molecular coordinates at the CCSD+T+Q level of theory, using Eqn.(6.4). The individual electronic contributions are summarized in Table 6.5, while the final rovibrationally averaged values are reported in Table 6.6. For the extraction of the nuclear quadrupole moments in Table 6.5, however, we used the NQCCs reported in Table 6.1, specifically the $\nu = 0$ values. These NQCCs already include rovibrational effects, so strictly speaking, combining them with purely electronic EFGs is not fully consistent. Nevertheless, this strategy provides an "electronic" estimate of Q, which can be compared across different computational protocols without the additional variability introduced by vibrational averaging. Moreover, looking at Eqn.(F.36) we see that, setting $\nu = 0$ and $J = 0$, we loose the third term, but only partially the second and fourth terms, that are corrections to the purely electronic value.

The vibrational corrections, although modest, lead to non-negligible adjustments of the final electronic values. For example, in the case of LiH (for $\nu = 0$, $J = 1$), the vibrationally averaged EFG is $-0.037682\,E_h/ea_0^2$, compared to the electronic final value of $-0.038655\,E_h/ea_0^2$, corresponding to a reduction of approximately 2.5% in magnitude. Correspondingly, the derived nuclear quadrupole moment increases in absolute value by about 2.6% (from -0.038177 b to -0.039163 b). Similar, albeit slightly smaller, adjustments are observed for LiF and LiCl, with vibrational corrections leading to changes on the order of 1.7–1.9% in the EFGs and comparable variations in the quadrupole moments.

Molecule	ν, J	EFG (E_h/ea_0^2)	Q (b)
^{7}Li^{1}H	$\nu = 0$, $J = 1$	−0.037 682	−0.039 163
^{7}Li^{1}H	$\nu = 1$, $J = 1$	−0.035 923	−0.039 333
^{7}Li^{2}H	$\nu = 0$	−0.037 766	−0.039 329
^{7}Li^{19}F	$\nu = 0$	−0.045 475	−0.038 895
^{7}Li^{19}F	$\nu = 1$	−0.044 433	−0.038 898
^{7}Li^{19}F	$\nu = 2$	−0.043 440	−0.038 847
^{7}Li^{35}Cl	$\nu = 0$	−0.027 206	−0.039 098
^{7}Li^{35}Cl	$\nu = 1$	−0.026 649	−0.039 064

TABLE 6.6: (Ro-)vibrationally averaged EFGs and corresponding NQMs for ^{7}Li.

In Figure 6.3, a linear regression was performed between the experimental nuclear quadrupole coupling constants and the calculated electric field gradients, as defined in Eq. (6.1). This best-fit procedure yields a value of $Q(^{7}\mathrm{Li}) = -0.0386$ b, which is slightly

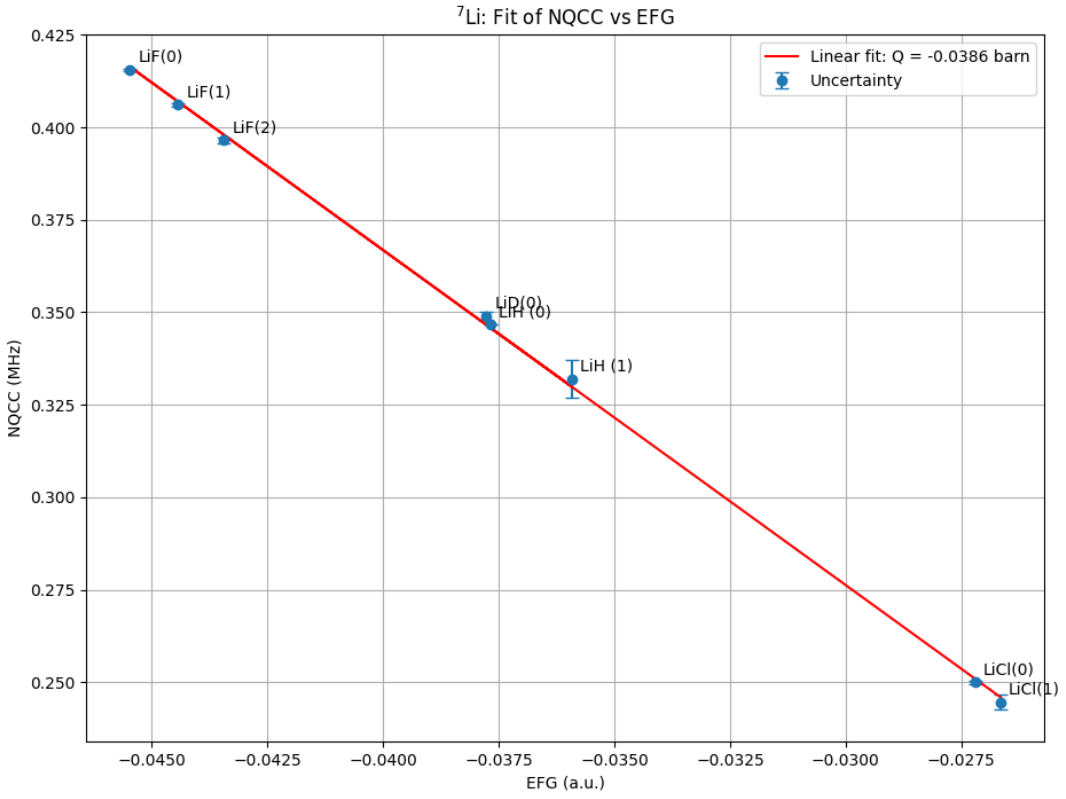

FIGURE 6.3: Linear fit of the nuclear quadrupole coupling constant (NQCC) as a function of the electric field gradient (EFG) for the ^{7}Li nuclei in different compounds. The value of Q is determined from the slope and is expressed in barns, with uncertainties on the NQCC values.

lower than the currently recommended molecular value of −0.0406 b but identical to the value reported by Guan and co-workers [387], even if obtained by a different route.

In order to understand this discrepancy, we made a comparison between our EFG values respect to those reported by Urban and Sadlej [369]. At the Hartree–Fock level, the difference is on the order of 0.0002 E_h/ea_0^2. The basis set we employed differs from that used by Urban and Sadlej. The basis set used by Urban and Sadlej for LiH is 13s8p6d2f, contracted to 9s6p3d1f, while for LiF and LiCl, they employed the 13s8p6d2f basis set, which, after contraction, becomes 8s5p3d1f. In our case, the same uncontracted basis set was used for all three systems, belonging to the dyall family, which is optimized for relativistic calculations. We selected the dyall.ae4z basis set as our starting point, which explicitly corresponds to 19s10p5d3f, and we did not contract it. As discussed in the previous section, we added a p- and d-tight exponents, resulting in a 19s11p6d3f basis set. This basis set was chosen as it allows achieving EFG convergence on the order of 10^{-6} E_h/ea_0^2. with respect to the increase of the basis set exponents. At the CCSD level the

discrepancy increases to approximately 0.0005 E_h/ea_0^2. The electrons of Li have always been fully correlated in Urban and Sadlej calculations, whereas for F and Cl, the electrons in the K and L shells have been left uncorrelated. However, there is no information regarding the number of virtual orbitals that were included in the correlation. We may therefore assume that all the virtual orbitals were correlated. In our case, in the CCSD calculation with the 19s11p6d3f basis set, we have correlated all electrons of the atoms and considered all the virtual orbitals. Since our basis set is optimized for properties and because we have correlated a larger number of electrons in the investigated systems (by considering all available virtual orbitals in the active space), we believe that our CCSD value is more accurate than previous results.

However, the most significant deviation arises in the estimation of the contribution from triple excitations, which reaches values as large as 0.002 E_h/ea_0^2. for LiF and LiCl. In their paper they used the T(CCSD) method, which is an approximation to reduce the computational cost of including triple excitations. This method is based on the calculation of the contribution of triple excitations to the energy using a fourth-order perturbation theory expression to evaluate the triple excitation [165]. In contrast, we employ the full CCSDT method without any approximation, except for the limited number of correlated electrons and virtual orbitals, as we pointed out in Table 6.3. A further inspection reveals that using a smaller basis set, while retaining all virtual orbitals in the active space, still yields corrections of the same order of magnitude as those reported in Table 6.5. Therefore, we argue that their estimate of the contribution from triple excitations is too high by approximately one order of magnitude compared to our fully iterative treatment.

We shall conclude by noting that the recent results provided by Guan and co-workers, based on high-precision measurements of hyperfine splittings in the 2^3P_J state of $^7Li^+$ [387], provide a value of $Q(^7\text{Li})$ =-0.0386(5) b, which is in perfect agreement with our value (without including QED corrections), and therefore we believe that the currently accepted value of the quadrupole moment should be revisited.

6.4.3 Nuclear Quadrupole Moment of ^{27}Al from molecular data

The reference value of the nuclear quadrupole moment of ^{27}Al is 0.1466 ± 0.0010b, as reported by Kellö and co-workers [388], based on atomic and molecular calculations. This was later confirmed by Pernpointner and Visscher via a four-component relativistic

CCSD(T) finite-field calculation, yielding 0.1460 ± 0.0004b [358]. Both studies considered the AlY (Y = F, Cl) systems, and Pernpointner and Visscher additionally included AlBr to assess relativistic contributions to $Q(^{27}\mathrm{Al})$. Brown and Wasylishen [389] reported a larger value, $Q(^{27}\mathrm{Al}) = 0.149 \pm 0.002$b (the uncertainty stemming mainly from experimental error), based on EFG calculations in AlH and AlD [371]. More recently, Aerts and Brown [390] proposed a revised value $Q(^{27}\mathrm{Al}) = 0.1482 \pm 0.0005$b, neglecting relativistic effects but including vibrational averaging.

Given these recent results, which differ from previous findings, the necessity of further investigating the quadrupole moment of ^{27}Al becomes evident. Moreover, as previously shown, triple excitations still have a non-negligible impact on the value of $Q(^{27}\mathrm{Al})$. We will consider the systems AlY (Y=H, F, Cl, Br) and employ the methodology previously discussed, where we will compute the reference value at the CCSD level with a sufficiently large active space and an extended basis set, before introducing triple and quadruple corrections. Finally, we will compute the vibrationally-averaged electric field gradient.

Table 6.7 details the stepwise contributions to the electric-field gradient (EFG) at the aluminum nucleus and the corresponding derived values of the nuclear quadrupole moment (NQM) for the series AlY (Y = H, F, Cl, Br). The starting Hartree–Fock values show significant deviation from the final results, highlighting the critical role of correlation effects. The inclusion of CCSD-level correlation already improves the EFG and Q values significantly.

Triple excitations introduce non-negligible corrections to the EFG (ranging from approximately 0.006 to 0.009 E_h/ea_0^2), which systematically affect the computed quadrupole moments by about 1 mb, underlining their importance even at this level of theory. Quadruple corrections are smaller, but still contribute meaningfully in the lighter systems.

Overall, the data confirm that an accurate determination of the NQM requires the inclusion of triple excitations and vibrational effects, especially for the light ligands.

In Figure 6.4 we made a linear regression of the experimental nuclear quadrupole coupling constants versus the calculated electric field gradients (according to Eq. (6.1)) which yielded a best fit $Q(^{27}\mathrm{Al}) = 0.1466$ b, which shows perfect agreement with previous studies [358, 388]. The slightly higher values obtained by Brown and Wasylishen [389] can be essentially attributed to the inaccuracy of the experimental NQCCs, which, in

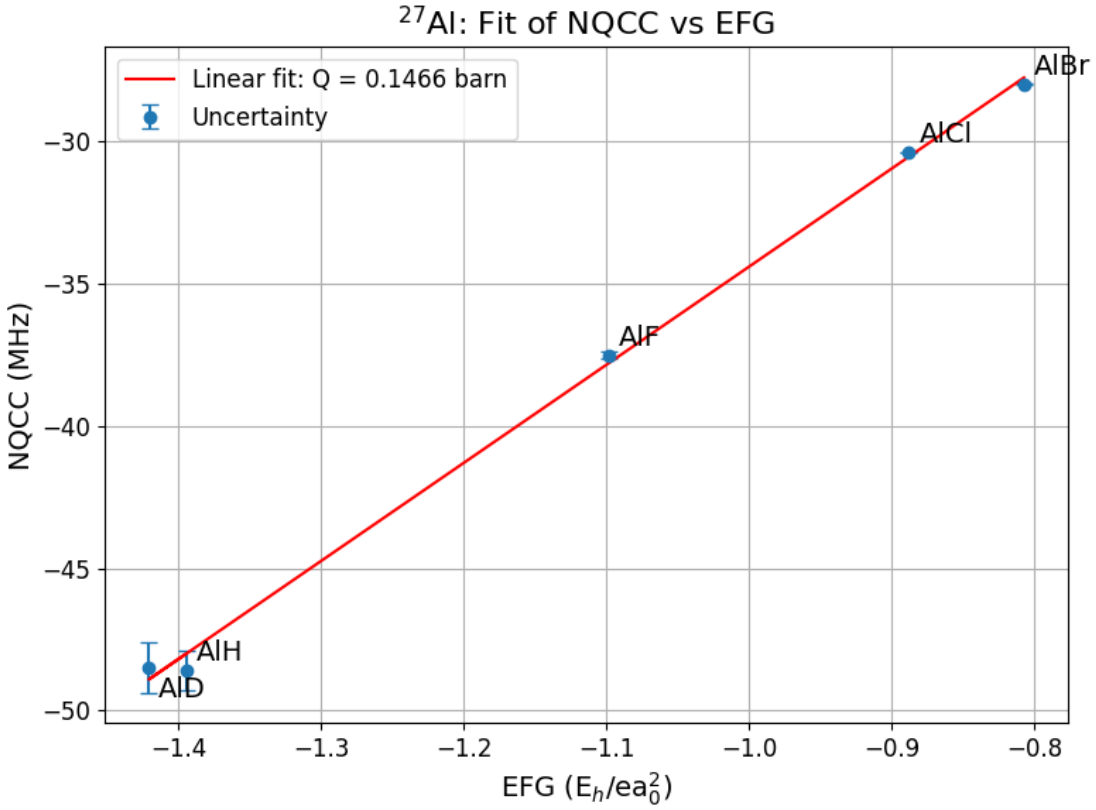

FIGURE 6.4: Linear fit of the nuclear quadrupole coupling constant (NQCC) as a function of the electric field gradient (EFG) for the ^{27}Al nuclei in different compounds. The value of Q is determined from the slope and is expressed in barns, with uncertainties on the NQCC values.

the AlY series (Y = H, F, Cl, Br), are affected by the largest uncertainties, as shown in Table 6.2. In our case, since we include a larger number of systems—many of which have more precisely determined NQCCs—and take into account the experimental uncertainties through linear regression, we obtain a quadrupole moment that is consistent with the accepted reference value. More recent studies have proposed a slightly higher value, such as $Q(^{27}\text{Al}) = 0.1482$b by Aerts and Brown [390], but it is important to note that their approach neglected relativistic effects and do not present a basis set convergence test, which we claim is quite important, as clearly demonstrated by van Stralen and Visscher [329]. In contrast, our methodology explicitly accounts for these corrections.

Error Analysis in the Determination of Electric Field Gradients

As explained in Section 6.3.2, experimental and theoretical uncertainties are incorporated in our values of nuclear electric quadrupole moments using Orthogonal Distance Regression [376]. Experimental values of NQCC, with uncertainties included, are given in Table I and II of the main text. The uncertainty in the calculated electric field gradients (EFGs), q, arises from four independent sources:

1. *CCSD active-space truncation.* In the AlY systems, a virtual orbital cutoff was applied to reduce computational cost. We conservatively estimate the residual uncertainty as
$$\delta_1 = 0.0010 \text{ E}_\text{h}/ea_0^2.$$

2. *Incomplete basis and treatment of triple (and higher) excitations.* The CCSDT–CCSD correction provides an upper bound on the triple excitation contribution:
$$\delta_2 = |q_\text{CCSDT} - q_\text{CCSD}|,$$
which we shall assume covers basis-set incompleteness and higher excitations.

3. *Neglect of the gauge-dependent Breit term.* Our calculations do not include the full Breit term, only the dominant Gaunt term and only in a mean-field fashion at the correlated level. Based on the effect of the Gaunt term at the SCF level for the heaviest molecule AlBr of our set, we assign a small static uncertainty:
$$\delta_3 = 0.0002 \text{ E}_\text{h}/ea_0^2.$$

4. *Rovibrational averaging.* The difference between the static (electronic) and vibrationally averaged EFG is used directly:
$$\Delta_\text{vib} = |q_\text{rovib} - q_\text{elec}|,$$
typically on the order of 0.001 E_h/ea_0^2.

These theoretical uncertainties combine in quadrature to yield the total theoretical uncertainty:
$$\Delta q_\text{theory} = \sqrt{\delta_1^2 + \delta_2^2 + \delta_3^2 + \Delta_\text{vib}^2}.$$

Example: Error for AlCl

For AlCl ($v = 0$), we computed:

$$q_{\text{final}} = -0.88278 \text{ E}_\text{h}/ea_0^2.$$

The error components are:

$$\begin{aligned}
\delta_1 &= 0.00100 \text{ E}_\text{h}/ea_0^2 \quad \text{(CCSD active-space)}, \\
\delta_2 &= 0.00321 \text{ E}_\text{h}/ea_0^2 \quad \text{(triple excitations)}, \\
\delta_3 &= 0.00020 \text{ E}_\text{h}/ea_0^2 \quad \text{(Breit/Gaunt)}, \\
\Delta_{\text{vib}} &= 0.00100 \text{ E}_\text{h}/ea_0^2 \quad \text{(rovibrational)}.
\end{aligned}$$

Combining in quadrature:

$$\Delta q_{\text{theory}} = \sqrt{(0.00100)^2 + (0.00321)^2 + (0.00020)^2 + (0.00100)^2} = 0.00350 \text{ E}_\text{h}/ea_0^2.$$

Thus, the final theoretical result for AlCl is:

$$q_{\text{final}} = -0.88278 \pm 0.00350 \text{ E}_\text{h}/ea_0^2.$$

We followed the same procedure for all the molecules investigated. The overall results are reported in Table 6.8. By using Orthogonal Distance Regression (ODR) we get

$$\text{NQCC}_{\text{Li}} = (-9.075308 \pm 0.068706) \cdot q_{\text{calc}} + (0.003400 \pm 0.002523) \text{ MHz}$$

and

$$\text{NQCC}_{\text{Al}} = (34.445457 \pm 0.000208) \cdot q_{\text{calc}} - (-0.000338 \pm 0.000190) \text{ MHz}$$

and the extracted NQMs are

$$Q(^7\text{Li}) = -0.038624 \pm 0.000292 \quad \text{b} \quad ; \quad Q(^{27}\text{Al}) = 0.146598 \pm 0.000001 \quad \text{b}.$$

6.5 Conclusions

In this work, we implemented CCSDT and CCSDTQ expectation values within the DIRAC quantum chemistry program [29]. We demonstrated how the implementation can be efficiently carried out using the tenpi toolchain [28] for the generation of $\Lambda-$equations and density matrices. To validate the CCSDT and CCSDTQ expectation value codes, we considered the LiH system and computed its dipole moment at the non-relativistic level from CCSD up to CCSDTQ, finding excellent agreement with the well-established MRCC quantum chemistry program [191].

A more significant application was the accurate calculation of the quadrupole moment for the nuclei ^{7}Li and ^{27}Al from molecular data. We have performed a detailed analysis of the electric field gradients at the lithium and aluminum nuclei for the series of LiX (X = H, F, Cl) and AlY (Y = H, F, Cl, Br) compounds. By employing CCSD calculations with an extended basis set, further corrected through the inclusion of full triple and quadruple excitations and vibrational averaging, we derived the corresponding nuclear quadrupole moments. For the lithium atom, we found a value of $Q(^{7}\mathrm{Li}) = -0.0387\,\mathrm{b}$, slightly lower than the currently accepted reference value, but in perfect agreement with Guan and co-workers [387]. For aluminum, our final data yield a value of $Q(^{27}\mathrm{Al}) = 0.1466\,\mathrm{b}$, in excellent agreement with the molecular values reported by Kellö *et al.* [391] and confirmed by Pernpointner and Visscher [358].

At present, our implementation faces three main bottlenecks that limit its scalability and overall efficiency: (i) the restriction to a single node, and since we are not exploiting (ii) point-group symmetry and (iii) index anti-symmetry of tensors. These limitations hinder both performance and memory efficiency, especially when tackling larger molecular systems or higher-order correlation methods. To address these issues, we are actively working on several fronts. First, we are transitioning towards a distributed-memory, multi-node implementation based on the Cyclops Tensor Framework [375]. Second, we are implementing point-group symmetry to reduce the number of independent amplitudes and integrals, which will also allow us to exploit the permutation antisymmetry of tensors, thus accelerating calculations and reducing memory requirements. These developments are expected to significantly improve the computational efficiency and make high-accuracy methods feasible for larger and more complex molecular systems. However, these technical developments go beyond the scope of the present work.

The implementation of CCSDT and CCSDTQ expectation values in DIRAC represents a further step forward in the HAMP-vQED project [392]. Combined with the inclusion of QED effects, on which we are currently working [393–395], this will enable the highly accurate calculation of molecular properties.

	AlH		AlD		AlF		AlCl		AlBr	
	EFG	Q	EFG	Q	EFG	Q	EFG	Q	EFG	Q
HF	-1.472185	0.140450	-1.472185	0.140450	-1.192554	0.134721	-0.981921	0.131798	-0.906967	0.131418
CCSD	-1.4208798	0.145542	-1.4208798	0.145542	-1.106585	0.145188	-0.897732	0.144158	-0.828187	0.143919
+ correction for full triples	0.008609	0.001154	0.008609	0.001154	0.008726	0.001154	0.006460	0.001045	0.005803	0.001015
+ corrections for full quadruples	0.000405	0.000042	0.000405	0.000042	0.000022	0.000003	0.000024	0.000004	0.000005	0.000000
+ vibrational corrections	0.017228	0.001809	0.012242	0.000947	-0.000217	-0.000029	0.003110	0.000509	0.0148850	0.002672
final value	-1.394638	0.148547	-1.399624	0.147685	-1.098055	0.146315	-0.888138	0.145716	-0.807495	0.147607

TABLE 6.7: Individual contributions to the EFG (in E_h/ea_0^2) at the Al position for the systems AlY (Y = H, D, F, Cl, Br) and the derived values for the ^{27}Al quadrupole moment (Q, in mb).

TABLE 6.8: Final electric (excluding experimental NQCC error). All values in E_h/ea_0^2.

Molecule	q_{final}	Δq_{theory}
LiH ($\nu = 0, J = 1$)	-0.03768	0.00105
LiH ($\nu = 1, J = 1$)	-0.03592	0.00099
LiF ($\nu = 0$)	-0.04548	0.00110
LiF ($\nu = 1$)	-0.04443	0.00108
LiF ($\nu = 2$)	-0.04344	0.00105
LiCl ($\nu = 0$)	-0.02721	0.00087
LiCl ($\nu = 1$)	-0.02665	0.00085
AlH ($\nu = 0$)	-1.41062	0.02610
AlF ($\nu = 0$)	-1.08954	0.00906
AlCl ($\nu = 0$)	-0.88278	0.00350
AlBr ($\nu = 0$)	-0.81304	0.01403

Chapter 7

The nuclear electric quadrupole moment of ^{87}Sr from highly accurate molecular relativistic calculations

The results presented in this chapter are based on the following work:

> Gabriele Fabbro, Jan Brandejs, and Trond Saue, "The nuclear electric quadrupole moment of ^{87}Sr from highly accurate molecular relativistic calculations," Submitted to *The Journal of Physical Chemistry*, , arXiv:2602.00855.

In this project, I proposed the idea, performed all the calculations, carried out the data analysis, and wrote the manuscript.

Abstract

The nuclear electric quadrupole moment (NQM) of ^{87}Sr has recently been revisited using high-precision relativistic atomic calculations [B. Lu *et al.*, Phys. Rev. A **100**, 012504 (2019)], indicating that the currently accepted value should be revised and that their result may serve as a new reference. In the present work, we determine the NQM of ^{87}Sr from the molecular method, by combining the experimentally measured nuclear quadrupole coupling constants (NQCCs) of SrO and SrS with highly accurate relativistic calculations of the electric field gradient (EFG) at the Sr nucleus. Electronic correlation is treated at the CCSD(T), CCSD-T and CCSD$\tilde{\text{T}}$ levels. The iterative T contribution of the latter, composite scheme was obtained using a newly implemented parallel scheme where the distributed memory tensor library Cyclops Tensor Framework (CTF) was made available to the DIRAC code for relativistic molecular calculations through TAPP, the new community standard for tensor operations. All correlated calculations are performed using the exact two-component molecular mean-field Hamiltonian (X2Cmmf). The Gaunt two-electron interaction is incorporated, an even-tempered optimized quadruple-ζ quality basis set is employed, and vibrational corrections are accounted for. Our best result is $Q(^{87}\text{Sr}) = 0.33666 \pm 0.00258$ b, which is about 10% larger than currently accepted standard value, while it is in excellent agreement with recent determinations [Y.-B. Tang, Phys. Rev. A **113**, 022812 (2026)].

7.1 Introduction

The nuclear electric quadrupole moment (NQM), eQ, plays a key role in a wide range of physical phenomena, particularly in the interpretation of hyperfine interactions in spectroscopy [52, 238, 396, 397]. A non-zero quadrupole moment occurs only for nuclei with spin quantum number $I \geq 1$, manifesting as a deformation of the nuclear charge distribution. Its direct experimental determination is challenging [398]. However, one may use the fact that the NQM interacts with the electric field gradient (EFG) generated by surrounding electrons and other charges (i.e., nuclei). In the principal-axis frame, the EFG is characterized by its largest component, eq, and an asymmetry parameter, which vanishes for linear molecules and atoms [399]. The resulting nuclear quadrupole interaction splits the nuclear energy levels, with the splitting proportional to the product of the nuclear quadrupole moment (NQM) and the electric field gradient, according to

$$\text{NQCC [MHz]} = 234.9647 \times Q(X)\,\text{[b]} \times q(X)\,[E_\text{h}/a_0^2], \tag{7.1}$$

where X denotes the nucleus under investigation. Experimentally, this effect is quantified by the nuclear quadrupole coupling constant (NQCC), which directly reflects the interaction strength. Owing to the multiplicative nature of the quadrupole interaction, the determination of nuclear quadrupole moments relies on both accurate experimental measurements of nuclear quadrupole coupling constants and high-level calculations of electric field gradients (EFGs). The *direct method* determines Q for a single nucleus using Eq. (7.1), combining the measured NQCC with the calculated EFG. This approach, however, can be highly sensitive to small inaccuracies in the EFG, especially when its value is close to zero, as even minor errors in electron correlation contributions can lead to large relative deviations [400]. In contrast, the *indirect method* estimates Q by analyzing NQCCs across a series of molecules. Here, Q is extracted from a linear regression of the experimental NQCCs against the corresponding calculated EFGs. By leveraging multiple molecules, this procedure reduces the impact of systematic errors and is generally more robust to small inaccuracies in the EFG of any individual system [56, 57]. Nonetheless, obtaining accurate EFGs remains a significant challenge in quantum-chemical calculations. This is because the EFG is highly sensitive to several factors. First, relativistic effects play a crucial role because the EFG depends on the electronic density close to the target nucleus, being proportional to $\langle r^{-3} \rangle$ (see, for instance, Refs. 197 and 209) ;

even small relativistic contractions or expansions of inner orbitals can significantly alter this expectation value. Second, electron correlation strongly influences the EFG [401]. According to Unsöld's theorem [60], closed atomic shells, such as we may expect from core orbitals, do not contribute to the EFG, unless they are polarized. Consequently, a proper description of electron correlation, particularly in the valence region, is essential to capture the correct anisotropy of the electronic density. Finally, the choice of basis set critically affects the results: since the EFG is determined by the electronic density near the nucleus and in the bonding region, an insufficiently flexible basis—especially in the core and polarization functions—can lead to large errors [58, 59, 329, 353, 358, 402, 403].

The quadrupole moment of strontium (Z = 38) is of interest due to the widespread use of Sr isotopes in optical clocks, cold-atom experiments, and precision measurements probing fundamental symmetries [404–406]. Among the naturally occurring isotopes, ^{84}Sr, ^{86}Sr, and ^{88}Sr have nuclear spin zero and therefore $Q(^{84,86,88}\mathrm{Sr}) = 0$. The nuclear electric quadrupole moment is thus relevant only for the odd-A isotopes and certain excited states. In particular, the ground states of ^{83}Sr, ^{85}Sr, and ^{87}Sr, with spins $I = 7/2^+$, $9/2^+$, and $9/2^+$, respectively, possess finite quadrupole moments [407]. Sahoo *et al.* combined the precisely measured hyperfine constant of the $4d\,^2D_{5/2}$ level in $^{87}\mathrm{Sr}^+$ with a relativistic coupled-cluster calculation of eq for that state, finding $Q(^{87}\mathrm{Sr}) = 0.305 \pm 0.002$ b [408]. This was a significant revision from earlier estimates by around 10% [409, 410], and has been adopted as the recommended value by Pyykkö [398]. More recently, Lu and co-workers revisited the NQM of ^{87}Sr [411]. Using high-precision multi-configuration relativistic Hartree-Fock calculations to obtain electric field gradients at the Sr position, combined with experimental hyperfine constants of the $5s5p\ ^3P_{1,2}$ states of neutral Sr, they obtained $Q(^{87}\mathrm{Sr}) = 0.328 \pm 0.004$ b. This result differs from the previously recommended value but is in excellent agreement with earlier determinations by Mårtensson-Pendrill [409], and by Yu *et al.* [410], and was proposed as the new reference value. Recently, an extraction of $Q(^{87}\mathrm{Sr})$ was reported by Tang [412], based on a relativistic hybrid configuration-interaction plus coupled-cluster (CI+CC) approach to calculate the electric field gradients for low-lying states of the neutral atom. By combining these EFGs with experimental electric quadrupole hyperfine-structure constants, Tang reported a value of $Q(^{87}\mathrm{Sr}) = 0.336 \pm 0.004$ b, which is approximately 10% higher than the currently recommended value.

The availability of nuclear quadrupole coupling constants for two molecules, $^{87}\mathrm{Sr}^{16}\mathrm{O}$

(−42.729(37) MHz) [413] and ^{87}Sr^{32}S (−21.959(85) MHz) [414], now enables the determination of the ^{87}Sr nuclear electric quadrupole moment using the molecular approach. To our knowledge, no extraction of $Q(^{87}\mathrm{Sr})$ was performed from these values. Indeed, in 2017, Pyykkö emphasized that these molecular constants had not yet been utilized for determining $Q(^{87}\mathrm{Sr})$ [238].

The aim of this work is to extract the nuclear quadrupole moment of ^{87}Sr from highly-accurate molecular relativistic relativistic calculations of the EFG, combined with the molecular data [413, 414].

7.2 Computational Details

All computations were carried out using the DIRAC program package [29]. The ID of the specific git commits of DIRAC utilized in this work are documented in the respective output files, which are made available in a dedicated online repository [415]. In this study, we mainly use the exact two-component molecular mean-field Hamiltonian (X2Cmmf) [139]. The initial four-component Hartree–Fock (HF) calculations explicitly included scalar relativistic effects, spin–orbit interactions, as well as the Gaunt term and the SS integrals. Any calculations performed without one or more of these contributions are explicitly indicated in the text. For spin-free calculations, the spin-orbit interaction was eliminated as described in Ref. 280. For all molecular systems, we adopted the Gaussian nuclear charge distribution model, using the parameter set from Ref. 276. For all atoms, we initially employed the dyall.ae4z basis set [283]. To assess the convergence of the EFG with respect to basis set extension, we subsequently augmented the Sr basis with two additional d-tight functions (exponents: 1.45205990×10^4 and 6.52893664×10^3) in an even-tempered manner, performing this augmentation at the SCF level (see Sec. 7.3.2).

We employed coupled-cluster (CC) [15, 140] methods to compute the electric field gradient at the nucleus and to extract the nuclear quadrupole moment of ^{87}Sr. For all CC schemes used in this work, the starting point was an iterative CCSD calculation performed with the RELCCSD module, which benefits from the exploitation of point-group symmetry [29, 353, 354]. Subsequently, triple excitations were accounted for using two complementary approaches. In the first, perturbative scheme, CCSD(T) [170–173] and CCSD–T [416] expectation values were evaluated using a finite-difference approach.

The second scheme, that we denote CCSD$\tilde{\text{T}}$, is a composite method in which triple-excitation corrections are obtained analytically from fully iterative CCSDT calculations performed using smaller basis sets and active spaces. The resulting T correction is then added to the CCSD value evaluated with a larger basis set and an active space sufficient to ensure convergence of the investigated property, thereby yielding the final CCSD$\tilde{\text{T}}$ result. This approach was employed in our previous work [403], where it enabled a reliable determination of the nuclear electric quadrupole moments of ^{27}Al and ^{7}Li.

Finally, we considered the vibrational corrections to the electronic values by employing the utility program VIBCAL, which is part of the DIRAC code [29] and which was used previously for estimating the vibration contribution to the EFG [403].

We determined $Q(^{87}\text{Sr})$ by combining the NQCCs listed in Table 7.1 with the computed EFGs, according to Eq. (7.1).

Molecule	ν	NQCC (MHz)	Bond length (Å)
^{87}SrO	0	−42.729 [413]	1.91983 [368]
^{87}SrS	0	−21.959 [414]	2.4405 [368]

TABLE 7.1: Nuclear quadrupole coupling constants (NQCC) for SrO and SrS, vibrational quantum numbers ν, and bond lengths.

7.2.1 CCSD(T) & CCSD-T

The CCSD(T) method [170–173], as implemented in the RELCCSD module [354, 355], provides a perturbative treatment of triple excitations that incorporates the dominant contributions up to fifth order in many-body perturbation theory. Owing to its favourable balance between accuracy and computational cost, CCSD(T) has long been regarded as the *de facto* standard for high-accuracy quantum-chemical calculations and is frequently referred to as the "gold standard" of electronic-structure theory [15, 140]. For many ground-state properties, this approach captures the vast majority of the correlation effects associated with triple excitations, making it both efficient and broadly applicable.

An alternative perturbative treatment is provided by the CCSD-T method, which extends the CCSD(T) formalism by incorporating a wider class of disconnected triple excitations, again up to fifth order in perturbation theory [416]. From a formal standpoint, CCSD-T is the most complete of the commonly used non-iterative triples corrections, since

it includes terms that are omitted in CCSD(T) and that become non-negligible in systems exhibiting stronger electron correlation or near-degeneracy effects. Extensive benchmark studies have demonstrated the practical importance of these additional terms for electric-field-gradient calculations [345, 402, 416–419].

Expectation values at the CCSD(T)/CCSD-T level were obtained using a finite-field procedure, in which the property is evaluated as the numerical derivative of the electronic energy with respect to an externally applied electric-field gradient. All finite-field calculations were performed using relaxed Hartree–Fock orbitals in order to ensure a consistent treatment of orbital relaxation effects across the different field strengths.

The reliability of the finite-field approach critically depends on the magnitude of the applied perturbation. If the field is chosen too small, numerical noise arising from the energy evaluation may obscure the physical response; if it is too large, higher-order nonlinearities contaminate the numerical derivative. After performing several tests with different field strengths, we found that $\varepsilon = \pm 10^{-7}$ offers an optimal balance between numerical stability and maintaining the linear-response regime. Such values were successfully used in other NQM determinations [417, 418, 420, 421]. The correlation contribution to the HF reference EFG is obtained from the antisymmetric energy difference,

$$q_{\mathrm{el,corr}} \approx \left. \frac{E_{\mathrm{corr}}(\varepsilon) - E_{\mathrm{corr}}(-\varepsilon)}{2\varepsilon} \right|_{\varepsilon=0}, \tag{7.2}$$

which isolates the first-order response of the correlation energy with respect to the external field. The final EFG value is obtained by adding the above correlated term, $q_{\mathrm{el,corr}}(X)$, to the HF value $q_{\mathrm{el,HF}}(X)$, since it has been observed that the electron correlation contribution to the EFG is essentially linear [422, 423].

The definition of an appropriate active space is a crucial prerequisite for obtaining reliable coupled-cluster results on heavy diatomic systems. In the present work, the active space was selected by in-depth analysis of the convergence behavior of the EFG in the SrO molecule. To this end, we performed a systematic series of CCSD calculations in which the number of virtual orbitals included in the correlation treatment was gradually increased while keeping all electrons correlated. After an analysis (see below, Figure 7.1), an energy cutoff of 50 E_h was adopted as a balanced and computationally efficient choice for defining the active virtual space in all subsequent calculations for both SrO and SrS.

CCSD, CCSD(T) and CCSD-T calculations were performed on the CALMIP supercomputing center (Centre de Calcul Intensif des Midi-Pyrénées) in Toulouse, France. The calculations were run on the Olympe partition of CALMIP, which comprises high-performance compute nodes each equipped with dual Intel Skylake 6140 processors at 2.3 GHz (36 physical cores per node) and 192 GB of DDR4 main memory.

7.2.2 CCSDT̃

The CCSDT̃ composite method was employed in our previous work [403]. In summary, it is based on evaluating the T corrections using a smaller basis set (dyall.v3z basis set [283] in our case) and a reduced active space,

$$T_{\text{iter}} = \langle q \rangle_{\text{CCSDT}}^{\text{dyall.v3z}} - \langle q \rangle_{\text{CCSD}}^{\text{dyall.v3z}}, \tag{7.3}$$

This correction is then added to the reference value obtained at the CCSD level

$$\langle q \rangle_{\text{CCSD}\tilde{\text{T}}} = \langle q \rangle_{\text{CCSD}}^{\text{opt-basis}} + T_{\text{iter}}, \tag{7.4}$$

with a basis guaranteeing the convergence of both the EFG, as well as the active space. The fully iterative CCSDT method [28, 164–166] and the respective expectation values counterpart [403, 424], is currently available in the ExaCorr [357] module of DIRAC, thanks to the tenpi code generator [28], based on a scheme introduced by Kallay and Surjan [17]. The CC implementation is unrestricted and can, in principle, be applied to any system well described by a single-reference wave function; in this work, however, all calculations are based on Kramers-restricted HF orbitals [363].

For the CCSDT calculations, correlation was restricted to the four highest-lying occupied Kramers pairs (i.e two spinors related by time-reversal symmetry); the same choice was adopted for both SrO and SrS. In addition, 97 virtual Kramers pairs were included in the correlation treatment for both molecules. Using the dyall.v3z basis set, this choice corresponds to an energetic cutoff of approximately 3.8 E_{h} for the virtual space in SrO, while a slightly higher cutoff of about 4.3 E_{h} was required for SrS. This choice was motivated both by computational cost considerations and by the need to avoid truncating virtual shells midway, which could otherwise lead to rapid and unphysical oscillations in the computed EFG values [403].

CCSDT calculations were performed on the Genoa partition of the French Adastra supercomputer, which packs 192 cores of a dual AMD EPYC 9654 chip with 768 GB of random access memory (RAM) into each node. The 544 nodes of Genoa partition are connected with 4x25GB/s Cray Slingshot-11 interconnects.

7.2.3 Massively parallel tensor operations

The T corrections are obtained from the fully-iterative CCSDT method [164–166], which was made possible thanks to the recent adoption of a standard tensor contraction interface into DIRAC. The Tensor Algebra Processing Primitives (TAPP) is a newly published standard [425] C-API (application programming interface) enabling programs to call one of the multiple supported tensor libraries without the need of changing the code when switching between the libraries. DIRAC is the first quantum chemistry package to use TAPP. Specifically, TAPP opened the way for the support of cutting-edge tensor libraries like TBLIS [426] and cuTENSOR [427], built on the shared-memory parallelization model. One of the present authors (J.B.) have further extended TAPP to a distributed memory multi-node variant [428]. This allows any program using TAPP to operate on tensors too large to fit into the RAM of one computational node. Such tensor operations require specialized distributed memory libraries like the Cyclops Tensor Framework (CTF) [375], used in the present work. CTF is built around an advanced communication-minimizing parallelization scheme. Recently, we have used CTF to demonstrate excellent weak scaling performance with CCSDT and CCSDTQ tensor contractions on up to 130 Frontier supercomputer nodes [28].

The present work is the first to implement CTF-based massive parallelization with the new molecular properties module in DIRAC [403], and the first to use the French national HPC platform Adastra for such purpose.

TAPP is a C-API which passes calls from DIRAC Fortran to Cyclops C++ code. To enable distributed memory operations, the TAPP specification had to be modified to eschew direct pointers to tensor data, as the data are scattered across multiple nodes. Instead, we extended the tensor metadata object "tensor_info" to include a universally unique identifier (UUID) of the tensor, which is used to retrieve the corresponding CTF tensor instantiated in our C++ worker code that wraps CTF. Except for the small modification, the wrapper implements the standard TAPP interface.

Additional development was required to align the different parallelization schemes. In DIRAC, the master MPI process assigns tasks to worker processes, whereas CTF assumes a symmetric parallelization with the same call from all the processes simultaneously. Our wrapper of CTF implements message passing from the master process of DIRAC to dedicated CTF worker processes.

All above tensor interface components are not restricted to DIRAC. The code is portable and openly accessible under a permissive license to anyone in the community seeking to use massively parallel tensor libraries in their application code through a fixed API [428].

7.3 Results and Discussion

7.3.1 Bonding analysis

Both molecules in this study, SrO and SrS, display ionic bonding, as inferred from projection analysis [221]. The EFG at the Sr nucleus is thereby not induced by covalent bonding, but by polarization by the partner anion. Using Intrinsic Atomic Orbitals [229], which assures that the HF molecular orbitals (MOs) are fully spanned by the precomputed occupied orbitals of the constituent atoms, hence removing any polarization contribution, we find that the charge of Sr is +1.98e and +1.81e in SrO and SrS, respectively. Interestingly, in SrO we observe a mixing of Sr 4p and O 2s orbitals in canonical MOs, but upon localization according to the Pipek–Mezey criterion [284], it goes away. In the terminology of Neidig *et al.* this is overlap-driven covalency [429], but clearly does not constitute true chemical bonding.

7.3.2 Basis set and active space choice

Basis sets are optimized for energies rather than properties; it is therefore necessary to verify the stability of the molecular property with respect to basis-set extension. The convergence test was performed only on the SrO molecule, which is the most ionic system. As discussed in our previous work [209], the EFG at the X nucleus is predominantly determined by the orbitals centered on that nucleus. Furthermore, we showed that contributions from surrounding nuclei largely cancel out, leaving orbital polarization by the

ligands as the dominant effect. For this reason, our study focuses on the most polarized systems. The basis-set study was carried out at the HF-level, since we assume that the basis sets are already well equipped with correlation functions.

In our augmentation study, we progressively added higher–angular–momentum functions (p, d, f, etc.) to the uncontracted `dyall.ae4z` basis set [283] until the change in the computed electric–field gradient became negligible. As shown in Table 7.2, the most substantial corrections were observed upon the addition of d-type functions, particularly up to $2d$. Notably, the addition of the third set of d-type functions ($3d$) leads to a relative change of just 0.012%, which is well below both the experimental uncertainty $\delta_{\text{exp}} = 0.087\%$. Therefore, we chose to truncate the augmentation at $3d$, as any further addition of d-functions did not result in consistent improvements and would only increase computational cost without gaining accuracy. The subsequent addition of f-tight functions did not modify the EFG.

EFG ref. (E_h/ea_0^2)	Exp.	EFG (E_h/ea_0^2)	Change (%)
-0.50244	–	–	–
	1p	-0.50245	0.002
-0.50245	–	–	–
	1d	-0.50040	0.405
	2d	-0.49736	0.608
	3d	-0.49742	0.012
-0.49736	1f	-0.49740	0.007
	2f	-0.49738	0.005

TABLE 7.2: Effect of p-, d-, and f-type basis augmentations on the EFG at the Sr position in SrO at the DCG-HF level.

For the correlation space, we adopted an energy-based virtual orbital cutoff rather than orbital-specific selection to avoid abrupt electric field gradient oscillations, as discussed in our previous work [403]. We considered the SrO molecule and increased systematically the number of virtual orbitals included in the active space by energy cutoff. Looking at the plot reported in Figure 7.1, we observed that the EFG value converges as the number of virtual spinors increases. In particular, once the energy threshold reaches 150 E_h, further inclusion of virtual spinors has a negligible effect: increasing the cutoff from 150 E_h to 200 E_h changes the EFG by only 0.02%, which is smaller than the experimental uncertainty. However, still the energy threshold 150 E_h is computational demanding. By applying an energy cutoff of 150 E_h for the virtual orbitals, we obtain a value of $eq = -0.49997\ E_h/ea_0^2$. In comparison, a more restrictive cutoff of 50 E_h yields $eq = -0.50010\ E_h/ea_0^2$. The relative difference between these two values is approximately 0.03%, which is notably smaller than the experimental relative uncertainty reported for

the nuclear quadrupole coupling constants of SrO and SrS. This indicates that, for both molecular systems, adopting a cutoff of 50 E_h for the virtual orbitals is sufficient to guarantee that the truncation error in the EFG remains negligible and does not affect the subsequent determination of the nuclear quadrupole moments.

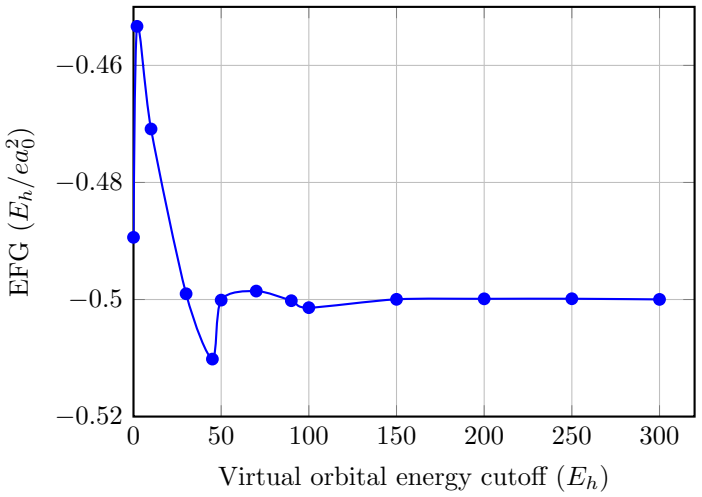

FIGURE 7.1: Electric field gradient (EFG) of the SrO molecule as a function of the virtual orbital energy cutoff, computed at the equilibrium geometry at the DCG-CCSD level.

7.3.3 Electric field gradient analysis

The data in Table 7.3 reveal clear and quantifiable trends in how relativistic and correlation effects affect the electric field gradients and nuclear quadrupole moments of SrO and SrS. Starting from the non-relativistic HF reference, the inclusion of relativistic effects (4c-DC-HF) reduces the magnitude of the EFG by 2.0% in SrO and by 14.0% in SrS, resulting in increases of 2.0% and 16.3% in the corresponding quadrupole moments. Introducing the Gaunt interaction (4c-DCG-HF) produces an additional reduction of 1.6% (SrO) and 1.4% (SrS) in the EFG magnitudes, with the associated Q values increasing by the same percentages. This trend is consistent with previous observations on heavy-element systems. Pernpointner [430] reported that for light systems such as AlF and AlCl the Gaunt contribution is negligible, whereas in strongly relativistic systems like TlH, it leads to a pronounced EFG shift of approximately 0.1 E_h/ea_0^2. Compared to these studies, SrO and SrS represent intermediate cases: the Gaunt term has a small but non-negligible effect, larger than in light systems but smaller than in strongly relativistic systems, reflecting the moderate relativistic character of strontium. One should note that

the gauge-dependent term in the full Breit operator often contributes negligibly [346]; since the Gaunt contribution is only of the order of 1.5–1.6% for both systems, we expect this additional term to be even smaller [57].

Electron correlation at the CCSD level modifies the relativistic HF picture in a system-dependent way. For SrO, CCSD increases the magnitude of the EFG by 2.2% relative to 4c-DCG-HF, whereas SrS shows a substantially larger 14.2% decrease in magnitude. The quadrupole moments reflect these changes, decreasing by 2.1% in SrO and increasing by 16.7% in SrS. This contrasting behaviour highlights the different sensitivity of the two chalcogenides to dynamical correlation. Triple excitations have a significant quantitative impact when assessed relative to CCSD. The perturbative triples correction, CCSD(T), reduces the EFG magnitude by 9.8% in SrO and by 2.4% in SrS compared to CCSD. The associated quadrupole moments decrease by 8.9% (SrO) and 2.3% (SrS), confirming that perturbative triples systematically lower both EFG and Q. The CCSD-T method partially counteracts this trend. Relative to CCSD, the EFG magnitudes change by only 6.4% in SrO and 2.7% in SrS, corresponding to quadrupole variations of +2.3% (SrO) and +2.8% (SrS). These results indicate that CCSD-T introduces corrections of opposite sign to CCSD(T). The CCSD$\tilde{\text{T}}$ method exhibits the largest deviations from the CCSD reference among the correlated approaches considered. For SrO, the inclusion of iterative triples leads to an increase in the magnitude of the EFG by approximately 4.3% (i.e., a more negative value) relative to CCSD, while the nuclear quadrupole moment is reduced by about 4.2%. In contrast, for SrS the effect of iterative triples is more pronounced in the opposite direction: the EFG magnitude is reduced by roughly 9.3%, whereas the quadrupole moment increases by about 10.3% with respect to CCSD.

Overall, the results demonstrate that relativistic effects modify the EFGs by up to about 15%, while dynamical electron correlation may further alter them by up to 17%. The inclusion of triple excitations, in particular through the CCSD$\tilde{\text{T}}$ treatment, affects both EFGs and quadrupole moments by up to ∼10%–13%, with a notably stronger impact observed for SrO than for SrS. These findings confirm that reliable predictions of quadrupole moments in alkaline-earth chalcogenides require a fully relativistic framework combined with a high-level correlated treatment.

	SrO		SrS	
Method	EFG	Q	EFG	Q
HF (no-rel)	−0.507 17	0.358 56	−0.374 80	0.249 35
4c-DC-HF	−0.497 30	0.365 68	−0.322 25	0.290 01
4c-DCG-HF	−0.489 38	0.371 60	−0.317 80	0.294 07
X2Cmmf-G-CCSD[a)]	−0.500 10	0.363 63	−0.272 54	0.342 91
X2Cmmf-G-CCSD(T)[a)]	−0.549 26	0.331 09	−0.279 05	0.334 91
X2Cmmf-G-CCSD-T[a)]	−0.532 10	0.341 76	−0.265 18	0.352 42
X2Cmmf-G-CCSD$\tilde{\text{T}}$[b)]	−0.521 82	0.348 50	−0.247 18	0.378 09

TABLE 7.3: EFG (in E_h/ea_0^2) and quadrupole moments (in b) for SrO and SrS at the equilibrium geometries. *a*) calculations were performed with the *opt* basis set, correlating all occupied orbitals and all virtual orbitals up to 50 E_h. *b*) The iterative T contribution was obtained using the `dyall.v3z`, correlating the four highest-lying occupied Kramers pairs and the lowest 97 virtual Kramers pairs.

7.3.4 Quadrupole moment analysis

In Table 7.4 we list the quadrupole moments Q of ^{87}Sr in SrO and SrS obtained at different levels of theory. In addition, we list the average value $\overline{Q}$, and the corresponding Mean Absolute Deviation (MAD) [431]. Ideally, the MAD should be zero since the quadrupole moment is a nuclear property independent of the chemical environment. The Table shows a clear hierarchy in the ability of different levels of theory to produce internally coherent quadrupole moments for the two chalcogenides. The non-relativistic HF values exhibit the largest deviation (MAD = 0.0546 b), reflecting the well-known imbalance in describing heavy-element systems without relativistic and correlation effects. Introducing relativistic effects (4c-DC-HF) reduces the MAD by approximately 30%, while the inclusion of the Gaunt term yields a very similar level of internal consistency.

Electron correlation dramatically enhances consistency. At the CCSD level, the MAD drops to 0.0102 b, representing an 80% reduction relative to the relativistic HF values. This demonstrates that dynamical correlation is essential to obtain comparable quadrupole moments for SrO and SrS. Among all methods considered, CCSD(T) yields the smallest deviation (MAD = 0.00191 b), almost an order of magnitude smaller than CCSD and more than 25 times smaller than non-relativistic HF. This confirms that perturbative triples not only improve absolute accuracy (as shown in the EFG analysis) but also produce highly balanced predictions across different chemical environments.

The CCSD-T method gives a slightly larger MAD (0.00567 b), still significantly smaller than at the HF or even CCSD level, but clearly less uniform than CCSD(T). Finally,

the CCSD$\tilde{\text{T}}$ method yields a MAD of 0.01480 b, indicating that, while this approach introduces substantial and physically meaningful corrections to the absolute EFGs and quadrupole moments, it also amplifies the difference between SrO and SrS. This results in a slightly less homogeneous description across the two systems. This behavior may be traced back to the limited virtual space used in these calculations. As we have observed in Figure 7.1, converged EFGs require a virtual space cutoff of at least approximately 50 E_h, which is not achievable in the current CCSDT calculations due to computational constraints. Consequently, the contribution of the triple excitations cannot be fully captured by the restricted virtual space employed here, leading to a partial representation of their effect.

The MAD analysis shows that relativistic HF reduces the inconsistency between the two systems, electron correlation is crucial to obtain tightly clustered quadrupole moments, and perturbative triples [CCSD(T)] provide the most balanced description across the SrX series.

Method	$Q(^{87}\text{Sr})$[SrO]	$Q(^{87}\text{Sr})$[SrS]	$\overline{Q}(^{87}\text{Sr})$	MAD
HF (no-rel)	0.358 56	0.249 35	0.303 96	0.054 61
4c-DC-HF	0.365 68	0.290 01	0.327 85	0.037 84
4c-DCG-HF	0.371 60	0.294 07	0.332 84	0.038 76
X2Cmmf-G-CCSD	0.363 63	0.342 91	0.353 27	0.010 18
X2Cmmf-G-CCSD(T)	0.331 09	0.334 91	0.333 00	0.001 91
X2Cmmf-G-CCSD-T	0.341 76	0.352 42	0.347 09	0.005 67
X2Cmmf-G-CCSD$\tilde{\text{T}}$	0.348 50	0.378 09	0.363 30	0.014 80

TABLE 7.4: Quadrupole moments Q of ^{87}Sr in SrO and SrS, their average $\overline{Q}$, and the corresponding Mean Absolute Deviation (MAD) across different relativistic and correlated methods. All values are reported in barns.

From the above analysis, we take the CCSD(T) value as the most reliable estimate. This conclusion is supported by its exceptionally low MAD, which indicates the most internally consistent description across the SrX series, together with the well-established accuracy of the perturbative triples correction in capturing the dominant contributions beyond CCSD. Unlike the CCSD$\tilde{\text{T}}$ method, here we were able to employ a larger active space, including all occupied orbitals and all virtual orbitals up to 50 E_h.

Finally, vibrational corrections were included and computed at the CCSD level using the utility program `VIBCAL` [29], accounting for cubic anharmonicities. The results are reported in Table 7.5.

The vibrational analysis was performed by constructing, for each molecule, both a potential energy surface (PES) and a corresponding property surface (PS). These surfaces were generated by sampling multiple points along the molecular coordinate at the CCSD level, employing the optimized basis set and the converged active space defined by an energy cutoff of 50 E_h for the virtual orbitals, as discussed in Sec.7.3.2. In addition to the equilibrium geometry, four displaced geometries were considered, obtained by varying the molecular coordinate by ± 0.005 Å. This resulted in a total of five geometries per molecule used to construct the PES and PS required for the vibrational treatment. One may question the use of the CCSD method for estimating vibrational contributions, given that the electronic EFG values were obtained at the CCSD(T) level. It should be noted, however, that for each molecule this analysis would require at least five CCSD(T) property calculations per geometry. When further accounting for the two finite-field points needed, two molecular systems, and five geometries per molecule, the total number of CCSD(T) calculations would amount to 20, rendering such an approach computationally too expensive. Importantly, the vibrational contributions reported in Table 7.5 are relatively small, amounting to 0.00905 E_h/ea_0^2 for SrO and 0.00296 E_h/ea_0^2 for SrS. These values are of the same order of magnitude as the estimated uncertainties in the electronic EFGs for both molecules (see Section 7.3.5). Consequently, any potential improvement gained by performing the vibrational analysis at the CCSD(T) level instead of CCSD is expected to be minor and well within the overall uncertainty of the final EFG values.

Molecule	ν	$\mathrm{EFG}_{\mathrm{CCSD(T)}}$	$\Delta\mathrm{EFG}_{\mathrm{vib}}$	$\mathrm{EFG}_{\mathrm{final}}$	$Q_{\mathrm{final}}(^{87}\mathrm{Sr})$
SrO	0	-0.54926	0.00905	-0.54021	0.33663
SrS	0	-0.27905	0.00296	-0.27757	0.33670

TABLE 7.5: CCSD(T) EFGs, vibrational corrections, final EFGs and final quadrupole moments for SrO and SrS. All the values are reported in E_h/ea_0^2.

7.3.5 Error estimation

In order to determine the uncertainty of our results, we identified the sources of error in the calculation of the EFG for the two molecules SrO and SrS.

1. **Basis set**: From our augmentation study (Table 7.2), the largest contributions to the EFG at the Sr position arise from the addition of d-type functions, particularly

the first two sets (1d: 0.405%, 2d: 0.608%). After the third set of d-functions (3d), the EFG changes by only 0.012%, and the subsequent inclusion of higher d and f-type functions results in variations below 0.02%, which are likely dominated by numerical noise rather than systematic basis set incompleteness. From these observations, we estimate the error due to the incomplete basis set to be approximately $\Delta_{\mathrm{BSIE}} \sim 6 \times 10^{-5}\ E_h/ea_0^2 \quad (\sim 0.012\%)$

2. **Active space**: At the CCSD level we correlated all electrons and included virtual orbitals up to 50 E_h. Based on this convergence behavior, we estimate the error introduced by truncating the active space at 50 E_h to be $\Delta_{\mathrm{AS}} \sim 1.3\times10^{-4}\ E_h/ea_0^2 \quad (\sim 0.03\%)$.

3. **Gauge term effects in the full Breit two-electron interaction**: In our calculations, we include the Gaunt term, which represents the magnetic interactions between electrons at the leading order in the Breit operator. Belpassi and coworkers performed a detailed analysis of the full, untruncated Breit interaction, and observed that the gauge terms reduce the magnetic (Gaunt) contribution by roughly one quarter in the AuF molecule [57]. Since Sr is considerably lighter than Au, we expect relativistic terms to be less pronounced. Therefore, applying the AuF ratio to SrO likely provides a conservative upper bound for the uncertainty. The resulting estimate of the gauge contribution is 0.002 E_{h}/ea_0^2 for SrO and 0.001 E_{h}/ea_0^2 for SrS, respectively.

4. **High-order correlation effects**: Assessing the impact of electron correlation beyond the CCSD(T) level is inherently difficult, as the contribution of higher-order excitations is not straightforward to quantify. While CCSD(T) typically offers a marked improvement over CCSD, comprehensive benchmarks at levels exceeding CCSD(T) are relatively rare. Following the reasoning of Van Stralen and Visscher [329], who build upon earlier work by Bieroń *et al.* [432], we adopt a conservative estimate that higher-order excitations contribute approximately 1% to the EFG. This value is therefore used as an uncertainty associated with neglected correlation effects beyond CCSD(T).

5. **Higher-order anharmonic contributions:** Contributions beyond cubic order are expected to be at least one order of magnitude smaller than the cubic anharmonic

contributions, which in our case were on the order of 10^{-4} E_h/ea_0^2, and are therefore anticipated to be around 10^{-5} E_h/ea_0^2.

Based on the above analysis, we report the CCSD(T) values with their estimated uncertainties as -0.54021 ± 0.00585 E_h/ea_0^2 for SrO and -0.27757 ± 0.00302 E_h/ea_0^2 for SrS. Since SrO and SrS provide two independent estimates of the same nuclear quadrupole moment, the final value of $Q(^{87}\mathrm{Sr})$ was obtained as an inverse-variance–weighted average of the two molecular determinations, giving $Q(^{87}\mathrm{Sr}) = 0.33666 \pm 0.00258$ b. This result is slightly above the value reported by Lu and co-workers [411], but it is in excellent agreement with the recent determination by Tang [412], $Q(^{87}\mathrm{Sr}) = 0.336 \pm 0.004$ b, as both values are fully consistent within their respective uncertainties.

7.4 Conclusions

In this work, the nuclear electric quadrupole moment (Q) of ^{87}Sr was determined using a highly accurate molecular relativistic approach that combines experimentally measured nuclear quadrupole coupling constants (NQCCs) of SrO and SrS with electric field gradients (EFGs) computed at various coupled-cluster levels, including CCSDT, CCSD-T, and CCSD$\tilde{\mathrm{T}}$ within an exact two-component molecular mean-field Hamiltonian (X2Cmmf). The treatment explicitly incorporates important effects such as relativistic effects, the Gaunt two-electron interaction and vibrational corrections, while carefully optimizing basis sets and active spaces to ensure convergence and reliability. Electron correlation is captured comprehensively through the inclusion of triple excitations, assessed via perturbative and iterative schemes, thanks to the recent multi-node extension of our module for high-order CC energies and expectation values, made possible by the TAPP interface connecting the Cyclops CTF library with the DIRAC program. We have shown that the inclusion of triple excitations (either perturbative or iterative) is essential for the accurate determination of the EFG in SrO and SrS.

Since we used three different methods to estimate the contribution of triple excitations (CCSD(T), CCSD-T, and CCSD$\tilde{\mathrm{T}}$), we employed the MAD to determine which provided the best value. We found that the best result is produced by CCSD(T). This greater internal consistency of CCSD(T) compared to CCSD$\tilde{\mathrm{T}}$ is likely due to the fact that the active space we employed is sufficiently large to ensure convergence of the EFG

with respect to further enlargement. In contrast, with CCSD$\tilde{\text{T}}$, although the multi-node extension allowed for an increase in the active space compared to the single-node version, it is still limited both in the choice of electrons to correlate and in the virtual space. This limitation is also certainly due to the fact that point-group symmetry is not currently implemented in the ExaCorr module of DIRAC, where we perform high-order CC calculations. In contrast, CCSD(T) is implemented in the RELCCSD module of DIRAC, which benefits from point-group symmetry. A future development we are actively pursuing is the introduction of point-group symmetry in ExaCorr.

Our best CCSD(T) value is $Q(^{87}\text{Sr}) = 0.33666 \pm 0.00258$ b, slightly above the value proposed by Lu and co-workers [411], $Q(^{87}\text{Sr}) = 0.328 \pm 0.004$ b. Lu et al. employed a multiconfiguration Dirac-Hartree-Fock (MCDHF) and relativistic configuration interaction (RCI) framework on the neutral Sr atom, focusing on the $5s5p\,^3P_{1,2}$ states and systematically accounting for electron correlations via single and double excitations from an extensive multireference space. However, they did not explicitly include triple excitations, which are essential for accurate determination of EFGs, as we have shown.

In contrast, Tang employed a hybrid configuration-interaction plus coupled-cluster (CI+CC) approach on the low-lying states of the neutral Sr atom to compute electric-field gradients, which were then combined with experimental hyperfine constants to extract $Q(^{87}\text{Sr}) = 0.336 \pm 0.004$ b [412]. This method explicitly accounts for core-core, core-valence, and valence-valence correlations and incorporates relativistic effects. While Tang's approach is atom-centered and relies on atomic CI+CC calculations, our method instead uses molecular EFGs from two different molecules, SrO and SrS, combined with experimentally measured NQCCs, providing two independent estimates of $Q(^{87}\text{Sr})$ in distinct chemical environments. By probing the nucleus within a chemical context, our approach naturally incorporates bonding effects and electron correlation in a realistic molecular setting, allowing us to cross-check the consistency of $Q(^{87}\text{Sr})$ across multiple environments and thereby reduce potential systematic errors that may arise in purely atomic calculations. Despite these methodological differences, both atomic and molecular approaches converge to essentially the same value within uncertainties, highlighting the robustness and reliability of current high-accuracy theoretical determinations of the nuclear quadrupole moment of ^{87}Sr and providing a strong cross-validation between atomic and molecular data.

Chapter 8

Summary, Conclusions and Perspectives

> *"The reward of the young scientist is the emotional thrill of being the first person in the history of the world to see something or to understand something."*
> — *Cecilia Payne-Gaposchkin*

This doctoral thesis is dedicated to the implementation of high-order Coupled Cluster expectation values, with a particular focus on the accurate determination of the electric field gradient (EFG). The work is structured in two main parts: Part I (*Theory*) lays out the foundational concepts and methodological developments, whereas Part II (*Applications*) presents computational results and practical implementations.

A central aspect of the thesis is the effective management of the complexity of high-order CC equations. The thesis emphasizes how manual derivations and implementations are prone to errors due to the proliferation of terms and index complexity. The diagrammatic approach aids in identifying equivalent terms, but symbolic automation is essential for intermediate optimization and method variant implementation. The `tenpi` framework is introduced as a modular and extensible platform that unifies symbolic derivation, intermediate optimization, and backend-independent tensor contractions.

The conclusions of this thesis are primarily drawn from the applications presented in Part II, where the analysis of the electric field gradient (EFG) at the nuclear positions enabled us to extract both chemically and physically relevant information.

Chapter 5 examined the use of the EFG to extract chemical information, going beyond the Dailey-Townes model. We therefore revisited the Dailey–Townes model for interpreting the electric field gradient (EFG) at nuclear positions in molecules. We showed that this model can be viewed as an approximation to our more general projection analysis of the EFG expectation value. Through a systematic study of halogen compounds and uranyl, we demonstrated that the original Dailey–Townes approach, which is based solely on valence p orbital populations, is often too crude. In particular, we found that hybridization effects involving subvalence orbitals play a significant role and cannot be neglected. Furthermore, we highlighted the growing importance of core polarization with increasing nuclear charge. As one descends the periodic table, the electronic response of inner-shell electrons to the molecular environment becomes more pronounced, leading to EFG contributions that can rival or even exceed those associated with chemical bonding. This phenomenon is especially evident in uranyl, where core polarization determines half of the observed EFG. Finally, we analyzed relativistic effects in detail. Scalar relativistic corrections preserve the structure of the Dailey–Townes model, but spin-orbit coupling breaks the diagonal character of the EFG operator in the atomic angular momentum basis. The mixing between $p_{1/2}$ and $p_{3/2}$ orbitals becomes essential, with $p_{1/2}$ orbitals — despite their spherical charge density and vanishing EFG contribution — playing an indirect role through hybridization. These findings underline the limits of simplified models and the need for a more complete quantum-chemical treatment of EFGs in chemically and relativistically complex systems.

Chapter 6 detailed the single-node implementation of high-order expectation values at the CCSDT (Coupled Cluster with singles, doubles, and triples) and CCSDTQ (including quadruples) levels within the `DIRAC` quantum chemistry program. This development was enabled by the `tenpi` toolchain, which facilitates the automated generation of high-order coupled-cluster equations. We derived the Λ-equations and the corresponding one-body density matrices for arbitrary excitation levels, and implemented the resulting CCSDT and CCSDTQ expectation-value expressions within `DIRAC`. The correctness of the implementation was verified by computing the non-relativistic dipole moment of LiH at various levels of theory, from CCSD up to CCSDTQ, obtaining results in excellent agreement with those from the `MRCC` program. Beyond this methodological validation, a central application was the high-accuracy determination of the nuclear electric quadrupole moments of ^{7}Li and ^{27}Al. Leveraging the theoretical infrastructure developed earlier, we carried out

coupled-cluster calculations of the electric field gradient (EFG) at the nuclei of interest across the LiX (X = H, F, Cl) and AlY (Y = H, F, Cl, Br) molecular series. Particular care was taken to ensure the reliability of the computed EFGs: we systematically investigated the basis-set convergence and its influence on the EFG, and explicitly accounted for scalar relativistic effects as well as spin–orbit coupling where relevant. In addition, vibrational and rotational corrections were derived and implemented within `DIRAC`, enabling ro-vibrational averaging of the EFGs. Starting from CCSD calculations with large basis sets and progressively incorporating corrections from full triple and quadruple excitation effects, as well as vibrational and rotational contributions, we obtained refined and reliable values of the nuclear quadrupole moments: $Q(^{7}\mathrm{Li}) = -0.038624 \pm 0.000292$ b and $Q(^{27}\mathrm{Al}) = 0.146598 \pm 0.000001$ b.

Finally, in Chapter 7, we determined the nuclear electric quadrupole moment Q of ^{87}Sr using high-accuracy molecular relativistic calculations on SrO and SrS combined with experimental nuclear quadrupole coupling constants. Our approach incorporates relativistic effects, the Gaunt interaction, vibrational corrections, and a thorough treatment of electron correlation through triple excitations, using CCSD(T), CCSD-T and CCSD$\tilde{\mathrm{T}}$, where the iterative T contribution of the latter, composite scheme was obtained using a newly implemented parallel scheme where the distributed memory tensor library Cyclops Tensor Framework (CTF) was made available to the DIRAC code for relativistic molecular calculations through TAPP, the new community standard for tensor operations. We found that CCSD(T) provides the most reliable estimate, yielding $Q(^{87}\mathrm{Sr}) = 0.33666 \pm 0.00258$ b, in excellent agreement with recent atomic CI+CC results and slightly above previous estimates. By using two distinct molecules, our molecular approach captures bonding effects and allows cross-validation of $Q(^{87}\mathrm{Sr})$ in different chemical environments, highlighting the robustness and reliability of current high-accuracy theoretical determinations.

Future directions of this research are manifold and aim at extending both the capabilities and the applicability of the methodologies developed in this thesis. From a computational perspective, the present thesis represents a significant step forward, as it enabled the evaluation of coupled-cluster expectation values at the CCSDT and CCSDTQ levels within a fully parallel multi-node framework. This development constitutes an important improvement, allowing the treatment of larger active spaces than previously accessible in single-node implementations. However, while the multi-node strategy significantly alleviates computational bottlenecks, it is not by itself sufficient to fully overcome

the limitations imposed by the steep scaling of high-order coupled-cluster methods. A crucial further improvement in computational efficiency therefore lies in the implementation of point-group symmetry and index permutation symmetry within the `ExaCorr` module. At present, the absence of symmetry exploitation increases both the memory requirements and the computational cost, and ultimately restricts the size of the active space that can be treated. Incorporating symmetry will drastically reduce the number of independent amplitudes and electron-repulsion integrals, leading to substantially more efficient and scalable high-order coupled-cluster calculations. In the longer term, from a methodological perspective, it is envisaged to broaden the scope of the `tenpi` toolchain. So far, the `tenpi` framework has proven effective for the automated derivation and implementation of energy and expectation value equations. However, its potential extends well beyond these applications. Future developments may include the automated generation of response properties, such as linear and quadratic response functions, as well as the implementation of equation-of-motion coupled-cluster (EOM-CC) methods, thereby enabling the study of excitation spectra and time-dependent phenomena at high levels of correlation. Moreover, we aim to extend the framework to support orbital-relaxed coupled-cluster properties, where the orbitals themselves are allowed to respond to external perturbations. This is particularly relevant for the accurate calculation of magnetic properties, where the contribution from negative-energy (positronic) states plays a non-negligible role. Implementing the orbital relaxation mechanism at the CC level would thus constitute a major step toward the systematic treatment of relativistic magnetic response. Finally, we are also interested in developing efficient implementations of perturbative corrections to the CC wave-function, namely CCSD(T) and CCSDT(Q). These models strike a favorable balance between accuracy and computational cost, and are expected to be essential for extending high-accuracy calculations to heavier systems and larger basis sets.

Appendix A

Complements to Chapter 1

A.1 Electromagnetic Potentials

Maxwell's equations[73] in differential form (SI units) are:

$$\nabla \cdot \mathbf{E} = \frac{\rho}{\varepsilon_0}, \tag{A.1}$$

$$\nabla \cdot \mathbf{B} = 0, \tag{A.2}$$

$$\nabla \times \mathbf{E} = -\frac{\partial \mathbf{B}}{\partial t}, \tag{A.3}$$

$$\nabla \times \mathbf{B} = \mu_0 \mathbf{j} + \mu_0 \varepsilon_0 \frac{\partial \mathbf{E}}{\partial t}. \tag{A.4}$$

To simplify Maxwell's equations, we express the electric and magnetic fields in terms of a scalar potential φ and a vector potential $\mathbf{A}$. Equation (A.2) involves the divergence of the magnetic field. If $\mathbf{B}$ is written as the curl of a vector field, then this equation is automatically satisfied, since the divergence of a curl vanishes identically. We therefore define:

$$\mathbf{B} = \nabla \times \mathbf{A}. \tag{A.5}$$

Moreover, this definition is not unique: the magnetic field remains unchanged under the transformation

$$\mathbf{A} \to \mathbf{A}' = \mathbf{A} + \nabla \chi, \tag{A.6}$$

where $\chi(\mathbf{r}, t)$ is an arbitrary scalar function. This is known as a *gauge transformation*, and reflects the gauge freedom inherent in the potentials. Having introduced Eq. (A.5),

we next consider Faraday's law, Eq. (A.3), and define the electric field accordingly:

$$\mathbf{E} = -\nabla\varphi - \frac{\partial \mathbf{A}}{\partial t}. \tag{A.7}$$

Substituting this into Eq. (A.3), we find that the law is identically satisfied, as the curl of a gradient vanishes.

Under a gauge transformation of the vector potential $\mathbf{A} \to \mathbf{A}+\nabla\chi$, the scalar potential must transform as

$$\varphi \to \varphi' = \varphi - \frac{\partial \chi}{\partial t}, \tag{A.8}$$

in order for the electric field $\mathbf{E}$ to remain invariant. Indeed, substituting both transformed potentials into Eq. (A.7), we find:

$$\mathbf{E}' = -\nabla\left(\varphi - \frac{\partial \chi}{\partial t}\right) - \frac{\partial}{\partial t}\left(\mathbf{A} + \nabla\chi\right) = -\nabla\varphi - \frac{\partial \mathbf{A}}{\partial t} = \mathbf{E} \tag{A.9}$$

Therefore, the electromagnetic fields $\mathbf{E}$ and $\mathbf{B}$ are invariant under the simultaneous transformations:

$$\mathbf{A}' = \mathbf{A} + \nabla\chi, \tag{A.10}$$

$$\varphi' = \varphi - \frac{\partial \chi}{\partial t}. \tag{A.11}$$

We now substitute both potentials into Eq. (A.4):

$$\nabla \times \mathbf{B} = \nabla \times (\nabla \times \mathbf{A}) = \nabla(\nabla \cdot \mathbf{A}) - \nabla^2\mathbf{A},$$

and:

$$\frac{\partial \mathbf{E}}{\partial t} = -\frac{\partial}{\partial t}\left(\nabla\varphi + \frac{\partial \mathbf{A}}{\partial t}\right) = -\nabla\frac{\partial \varphi}{\partial t} - \frac{\partial^2 \mathbf{A}}{\partial t^2}.$$

So, the Ampère–Maxwell equation becomes:

$$\nabla(\nabla \cdot \mathbf{A}) - \nabla^2\mathbf{A} = \mu_0\mathbf{j} - \mu_0\varepsilon_0\nabla\frac{\partial \varphi}{\partial t} - \mu_0\varepsilon_0\frac{\partial^2 \mathbf{A}}{\partial t^2}. \tag{A.12}$$

Rewriting:

$$\nabla^2\mathbf{A} - \mu_0\varepsilon_0\frac{\partial^2 \mathbf{A}}{\partial t^2} - \nabla\left(\nabla \cdot \mathbf{A} + \mu_0\varepsilon_0\frac{\partial \varphi}{\partial t}\right) = -\mu_0\mathbf{j}. \tag{A.13}$$

From Gauss's law, using Eq. (A.7), we also find:

$$-\nabla^2\varphi - \frac{\partial}{\partial t}(\nabla \cdot \mathbf{A}) = \frac{\rho}{\varepsilon_0}. \tag{A.14}$$

There are several possible choices of gauge for the scalar and vector potentials. Two of the most commonly used are the Lorenz gauge,

$$\nabla \cdot \mathbf{A} + \mu_0\varepsilon_0\frac{\partial\varphi}{\partial t} = 0, \tag{A.15}$$

and the Coulomb gauge,

$$\nabla \cdot \mathbf{A} = 0. \tag{A.16}$$

In the present notes, the equations simplify considerably by choosing the *Lorenz gauge*. Substituting Eqn.(A.16) into Eqs. (A.14) and (A.13), we obtain wave equations for the potentials:

$$\Box\varphi = \frac{\rho}{\varepsilon_0}, \tag{A.17}$$

$$\Box\mathbf{A} = \mu_0\mathbf{j}, \tag{A.18}$$

where $\Box = \nabla^2 - \frac{1}{c^2}\partial^2/\partial t^2$ is the d'Alembert operator. These equations describe the propagation of the scalar and vector potentials in space and time, sourced respectively by charge and current densities.

In the framework of special relativity, the scalar and vector potentials are unified into the four-potential:

$$A^\mu = \left(\frac{\varphi}{c}, \mathbf{A}\right), \tag{A.19}$$

where $\mu = 0, 1, 2, 3$, $A^0 = \varphi/c$, and $A^i = A_i$ for $i = 1, 2, 3$. The four-current is defined as:

$$j^\mu = (c\rho, \mathbf{j}), \tag{A.20}$$

ensuring that both charge and current densities are treated on equal footing under Lorentz transformations. Furthermore, the Lorenz gauge condition becomes a manifestly Lorentz-invariant expression:

$$\partial_\mu A^\mu = 0. \tag{A.21}$$

Under this gauge, the wave equation for the four-potential reads:

$$\Box A^{\mu} = \mu_0 j^{\mu}. \tag{A.22}$$

Appendix B

Complements to Chapter 2

B.1 Normal-ordered Hamiltonian

one-electron part

We begin with the one-body part

$$\hat{h} = \sum_{pq} h_{pq} a_p^\dagger a_q, \tag{B.1}$$

and we apply the Wick's theorem (Eq.(2.24)):

$$\begin{aligned} \hat{h} &= \sum_{pq} h_{pq} \left(\{a_p^\dagger a_q\} + \{\overbrace{a_p^\dagger a_q}\} \right) \\ &= \sum_{pq} h_{pq} \{a_p^\dagger a_q\} + \sum_{pq} h_{pq} \delta_{pq} \delta_{p \in i} \end{aligned} \tag{B.2}$$

where we used Eq.(2.27), and therefore

$$\hat{h} = \sum_{pq} h_{pq} \{a_p^\dagger a_q\} + \sum_{i} h_{ii} \tag{B.3}$$

Two-electron part

We start from

$$\hat{g} = \frac{1}{4} \sum_{pqrs} V_{pqrs} a_p^\dagger a_q^\dagger a_s a_r, \tag{B.4}$$

and we may write the product of second-quantized operators using again Wick's theorem (Eq.(2.24)):

$$\begin{aligned} a_p^\dagger a_q^\dagger a_s a_r &= \{a_p^\dagger a_q^\dagger a_s a_r\} + \{\overbrace{a_p^\dagger a_q^\dagger} a_s a_r\} + \{\overbrace{a_p^\dagger a_q^\dagger a_s} a_r\} + \{a_p^\dagger \overbrace{a_q^\dagger a_s} a_r\} \\ &+ \{a_p^\dagger \overbrace{a_q^\dagger a_s a_r}\} + \{\overbrace{a_p^\dagger a_q^\dagger} \overbrace{a_s a_r}\} + \{\overbrace{a_p^\dagger \overbrace{a_q^\dagger a_s} a_r}\} \\ &= \{a_p^\dagger a_q^\dagger a_s a_r\} - \delta_{ps}\delta_{p\in i}\{a_q^\dagger a_r\} + \delta_{pr}\delta_{p\in i}\{a_q^\dagger a_s\} + \delta_{qs}\delta_{q\in i}\{a_p^\dagger a_r\} \\ &- \delta_{qr}\delta_{q\in i}\{a_p^\dagger a_s\} + \delta_{pr}\delta_{qs}\delta_{p\in i}\delta_{q\in j} - \delta_{ps}\delta_{qr}\delta_{p\in i}\delta_{q\in j} \end{aligned} \tag{B.5}$$

where we used Eq.(2.27). We may now substitute all the terms of Eq.(B.5) in (B.4):

$$\begin{aligned} \hat{g} = &\frac{1}{4}\sum_{pqrs}\langle pq||rs\rangle \{a_p^\dagger a_q^\dagger a_s a_r\} - \frac{1}{4}\sum_{qri}\langle iq||ri\rangle \{a_q^\dagger a_r\} + \frac{1}{4}\sum_{qsi}\langle iq||is\rangle \{a_q^\dagger a_s\} + \frac{1}{4}\sum_{ipr}\langle pi||ri\rangle \{a_p^\dagger a_r\} \\ &- \frac{1}{4}\sum_{psi}\langle pi||is\rangle \{a_p^\dagger a_s\} + \frac{1}{4}\sum_{ij}\langle ij||ij\rangle - \frac{1}{4}\sum_{ij}\langle ij||ji\rangle . \end{aligned} \tag{B.6}$$

Now we can use the antisymmetry of the two-electron integrals

$$\langle pq||rs\rangle = -\langle pq||sr\rangle = -\langle qp||rs\rangle = \langle qp||sr\rangle . \tag{B.7}$$

Looking at the second, third and fifth terms we get

$$-\tfrac{1}{4}\sum_{qri}\langle iq||ri\rangle = \tfrac{1}{4}\sum_{qri}\langle qi||ri\rangle = \tfrac{1}{4}\sum_{pri}\langle pi||ri\rangle \tag{B.8}$$

$$\tfrac{1}{4}\sum_{qsi}\langle iq||is\rangle = \tfrac{1}{4}\sum_{qsi}\langle qi||si\rangle = \tfrac{1}{4}\sum_{pri}\langle pi||ri\rangle \tag{B.9}$$

$$-\tfrac{1}{4}\sum_{psi}\langle pi||is\rangle = \tfrac{1}{4}\sum_{psi}\langle pi||si\rangle = \tfrac{1}{4}\sum_{pri}\langle pi||ri\rangle \tag{B.10}$$

where we used the fact that summed indices can be renamed. We may realize that these three terms are exactly the fourth term in Eq.(B.6), and therefore these can be grouped into a single term $\sum_{pri}\langle pi||ri\rangle \{a_p^\dagger a_r\}$ by removing the 1/4 factor. The last two terms of Eq.(B.6) can be written as a single term

$$\frac{1}{4}\sum_{ij}\langle ij||ij\rangle - \frac{1}{4}\sum_{ij}\langle ij||ji\rangle = \frac{1}{2}\sum_{ij}\langle ij||ij\rangle . \tag{B.11}$$

Therefore, the normal-ordered two-electron part can be written as

$$\hat{g} = \frac{1}{4}\sum_{pqrs}\langle pq||rs\rangle\,\{a_p^\dagger a_q^\dagger a_s a_r\} + \sum_{pri}\langle pi||ri\rangle\,\{a_p^\dagger a_r\} + \frac{1}{2}\sum_{ij}\langle ij||ij\rangle \tag{B.12}$$

Final form

If we sum up Eq.(B.3) and Eq.(B.12) we get

$$\hat{H} = \sum_{pq} h_{pq}\{a_p^\dagger a_q\} + \frac{1}{4}\sum_{pqrs}\langle pq||rs\rangle\,\{a_p^\dagger a_q^\dagger a_s a_r\} + \sum_{pri}\langle pi||ri\rangle\,\{a_p^\dagger a_r\} + \sum_i h_{ii} + \frac{1}{2}\sum_{ij}\langle ij||ij\rangle \tag{B.13}$$

where we may recognize the matrix element of the Fock matrix

$$f_{pq} = h_{pq} + \sum_i \langle pi||qi\rangle\,, \tag{B.14}$$

and the Hartree-Fock energy

$$E_{\mathrm{HF}} = \sum_i h_{ii} + \frac{1}{2}\sum_{ij}\langle ij||ij\rangle\,. \tag{B.15}$$

Therefore, we may write

$$\hat{H} = \sum_{pq} f_{pq}\{a_p^\dagger a_q\} + \frac{1}{4}\sum_{pqrs}\langle pq||rs\rangle\,\{a_p^\dagger a_q^\dagger a_s a_r\} + E_{\mathrm{HF}}. \tag{B.16}$$

We define the *normal-ordered Hamiltonian* as the following quantity

$$\hat{H}_N = \sum_{pq} f_{pq}\{a_p^\dagger a_q\} + \frac{1}{4}\sum_{pqrs}\langle pq||rs\rangle\,\{a_p^\dagger a_q^\dagger a_s a_r\} \tag{B.17}$$

which can be written more compactly as

$$\hat{H}_N = \hat{H} - E_{\mathrm{HF}}. \tag{B.18}$$

B.2 Proof of the BCH Expansion for the similarity-transformed Operator

Let A and B be (possibly non-commuting) operators. Consider

$$f(\lambda) = e^{-\lambda A} B e^{\lambda A}, \tag{B.19}$$

so that

$$f(0) = B, \qquad f(1) = e^{-A} B e^{A}. \tag{B.20}$$

The derivatives of $f(\lambda)$ can be written as

$$\begin{aligned}
\frac{d}{d\lambda} f(\lambda) &= \frac{d}{d\lambda}\left(e^{-\lambda A} B e^{\lambda A}\right) \\
&= -A e^{-\lambda A} B e^{\lambda A} + e^{-\lambda A} B A e^{\lambda A} \\
&= -[A, f(\lambda)], \\
\frac{d^2}{d\lambda^2} f(\lambda) &= \frac{d}{d\lambda}\left(-[A, f(\lambda)]\right) \\
&= -[A, \frac{d}{d\lambda} f(\lambda)] \\
&= [A, [A, f(\lambda)]], \\
\frac{d^n}{d\lambda^n} f(\lambda) &= \underbrace{[A, [A, \cdots [A,}_{n \text{ times}} f(\lambda)] \cdots]].
\end{aligned} \tag{B.21}$$

Expanding $f(\lambda)$ in a Taylor series about $\lambda = 0$ gives

$$\begin{aligned}
f(1) &= f(0) + f'(0) + \frac{1}{2!} f''(0) + \frac{1}{3!} f'''(0) + \cdots \\
&= B + [A, B] + \frac{1}{2!}[A, [A, B]] + \frac{1}{3!}[A, [A, [A, B]]] + \cdots ,
\end{aligned} \tag{B.22}$$

which is the BCH expansion for the similarity-transformed operator $e^{-A} B e^{A}$.

B.3 Why similarity transformations preserve the spectrum

The reasoning followed in these notes is largely inspired by the clear and insightful explanation provided in Strang's textbook.[433]

Let A and B be two $n \times n$ matrices, and let T be an invertible matrix. We say that B is similar to A if

$$B = T^{-1}AT. \tag{B.23}$$

Theorem

Similar matrices have the same spectrum, i.e., the same set of eigenvalues (with the same algebraic and geometric multiplicities).

Proof

The characteristic polynomial of A is

$$p_A(\lambda) = \det(A - \lambda I), \tag{B.24}$$

and for B we have

$$\begin{aligned} p_B(\lambda) &= \det(B - \lambda I) && \text{(B.25)}\\ &= \det(T^{-1}AT - \lambda I) && \text{(B.26)}\\ &= \det(T^{-1}AT - T^{-1}\lambda IT) && \text{(B.27)}\\ &= \det(T^{-1}(A - \lambda I)T) && \text{(B.28)}\\ &= \det(T^{-1})\det(A - \lambda I)\det(T) && \text{(B.29)}\\ &= \det(A - \lambda I), && \text{(B.30)} \end{aligned}$$

since $\det(T^{-1})\det(T) = 1$. Therefore,

$$p_B(\lambda) = p_A(\lambda), \tag{B.31}$$

i.e., A and B have the same characteristic polynomial and thus the same eigenvalues.

If x is an eigenvector of A with eigenvalue λ, i.e., $Ax = \lambda x$, then $y = T^{-1}x$ is an eigenvector of B with the same eigenvalue:

$$By = T^{-1}ATy = T^{-1}Ax = T^{-1}(\lambda x) = \lambda T^{-1}x = \lambda y. \tag{B.32}$$

Appendix C

Complements to Chapter 3

C.1 Second-order molecular properties

Unfortunately, due to time-constrains, I did not have time to implement these developments for high-order CC methods in either `tenpi` or `ExaCorr`. However, following Saue's advice that a doctoral thesis should also serve as a reference for future students, I instead report here some preliminary thoughts and formulas on the computation of second-order molecular properties, including polarizabilities, magnetizabilities, NMR parameters, and related quantities.

We aim to compute the second derivative of the CC Lagrangian with respect to two perturbations, ε_A and ε_B:

$$\frac{d^2 L_{\mathrm{CC}}}{d\varepsilon_A d\varepsilon_B} = \frac{d}{d\varepsilon_B}\left(\frac{\partial L_{\mathrm{CC}}}{\partial \varepsilon_A} + \sum_\mu \frac{\partial L_{\mathrm{CC}}}{\partial t_\mu}\frac{dt_\mu}{d\varepsilon_A} + \sum_\mu \frac{\partial L_{\mathrm{CC}}}{\partial \bar{t}_\mu}\frac{d\bar{t}_\mu}{d\varepsilon_A}\right). \tag{C.1}$$

One might ask why we do not simply use Eqn.(3.58) instead of the full expression given in Eqn. (C.1). Both approaches are, in principle, valid. However, applying Eqn.(3.58) leads to an expression that is generally non-symmetric and not straightforward to use in practice. For this reason, we adopt the approach outlined in Eqn. (C.1).

Applying the derivative term-by-term, we get

$$\frac{d^2 L_{\mathrm{CC}}}{d\varepsilon_A d\varepsilon_B} = \frac{d}{d\varepsilon_B}\left(\frac{\partial L_{\mathrm{CC}}}{\partial \varepsilon_A}\right) + \frac{d}{d\varepsilon_B}\left(\sum_\mu \frac{\partial L_{\mathrm{CC}}}{\partial t_\mu}\frac{dt_\mu}{d\varepsilon_A}\right) + \frac{d}{d\varepsilon_B}\left(\sum_\mu \frac{\partial L_{\mathrm{CC}}}{\partial \bar{t}_\mu}\frac{d\bar{t}_\mu}{d\varepsilon_A}\right). \tag{C.2}$$

Each term is expanded as follows:

First term:

$$\frac{d}{d\varepsilon_B}\left(\frac{\partial L_{\mathrm{CC}}}{\partial \varepsilon_A}\right) = \frac{\partial^2 L_{\mathrm{CC}}}{\partial \varepsilon_B \partial \varepsilon_A} + \sum_\mu \frac{\partial^2 L_{\mathrm{CC}}}{\partial t_\mu \partial \varepsilon_A}\frac{dt_\mu}{d\varepsilon_B} + \sum_\mu \frac{\partial^2 L_{\mathrm{CC}}}{\partial \bar{t}_\mu \partial \varepsilon_A}\frac{d\bar{t}_\mu}{d\varepsilon_B}. \tag{C.3}$$

Second term:

$$\frac{d}{d\varepsilon_B}\left(\sum_\mu \frac{\partial L_{\mathrm{CC}}}{\partial t_\mu}\frac{dt_\mu}{d\varepsilon_A}\right) = \sum_\mu \frac{d}{d\varepsilon_B}\left(\frac{\partial L_{\mathrm{CC}}}{\partial t_\mu}\right)\frac{dt_\mu}{d\varepsilon_A} + \sum_\mu \frac{\partial L_{\mathrm{CC}}}{\partial t_\mu}\frac{d^2 t_\mu}{d\varepsilon_A d\varepsilon_B} \tag{C.4}$$

$$= \sum_\mu \left(\frac{\partial^2 L_{\mathrm{CC}}}{\partial \varepsilon_B \partial t_\mu} + \sum_\nu \frac{\partial^2 L_{\mathrm{CC}}}{\partial t_\nu \partial t_\mu}\frac{dt_\nu}{d\varepsilon_B} + \sum_\nu \frac{\partial^2 L_{\mathrm{CC}}}{\partial \bar{t}_\nu \partial t_\mu}\frac{d\bar{t}_\nu}{d\varepsilon_B}\right)\frac{dt_\mu}{d\varepsilon_A} \tag{C.5}$$

$$+ \sum_\mu \frac{\partial L_{\mathrm{CC}}}{\partial t_\mu}\frac{d^2 t_\mu}{d\varepsilon_A d\varepsilon_B}. \tag{C.6}$$

Third term:

$$\frac{d}{d\varepsilon_B}\left(\sum_\mu \frac{\partial L_{\mathrm{CC}}}{\partial \bar{t}_\mu}\frac{d\bar{t}_\mu}{d\varepsilon_A}\right) = \sum_\mu \frac{d}{d\varepsilon_B}\left(\frac{\partial L_{\mathrm{CC}}}{\partial \bar{t}_\mu}\right)\frac{d\bar{t}_\mu}{d\varepsilon_A} + \sum_\mu \frac{\partial L_{\mathrm{CC}}}{\partial \bar{t}_\mu}\frac{d^2 \bar{t}_\mu}{d\varepsilon_A d\varepsilon_B} \tag{C.7}$$

$$= \sum_\mu \left(\frac{\partial^2 L_{\mathrm{CC}}}{\partial \varepsilon_B \partial \bar{t}_\mu} + \sum_\nu \frac{\partial^2 L_{\mathrm{CC}}}{\partial t_\nu \partial \bar{t}_\mu}\frac{dt_\nu}{d\varepsilon_B} + \sum_\nu \frac{\partial^2 L_{\mathrm{CC}}}{\partial \bar{t}_\nu \partial \bar{t}_\mu}\frac{d\bar{t}_\nu}{d\varepsilon_B}\right)\frac{d\bar{t}_\mu}{d\varepsilon_A} \tag{C.8}$$

$$+ \sum_\mu \frac{\partial L_{\mathrm{CC}}}{\partial \bar{t}_\mu}\frac{d^2 \bar{t}_\mu}{d\varepsilon_A d\varepsilon_B}. \tag{C.9}$$

From the stationarity of the Lagrangian, Eqns.(3.56)-(3.57), the last terms in the second and third expressions vanish:

$$\sum_\mu \frac{\partial L_{\mathrm{CC}}}{\partial t_\mu}\frac{d^2 t_\mu}{d\varepsilon_A d\varepsilon_B} = 0, \quad \sum_\mu \frac{\partial L_{\mathrm{CC}}}{\partial \bar{t}_\mu}\frac{d^2 \bar{t}_\mu}{d\varepsilon_A d\varepsilon_B} = 0. \tag{C.10}$$

Collecting all terms, the second derivative of the Lagrangian evaluates to

$$\frac{d^2 L_{\mathrm{CC}}}{d\varepsilon_A d\varepsilon_B} = \underbrace{\frac{\partial^2 L_{\mathrm{CC}}}{\partial\varepsilon_B \partial\varepsilon_A}}_{(1)} + \underbrace{\sum_\mu \frac{\partial^2 L_{\mathrm{CC}}}{\partial t_\mu \partial\varepsilon_A}\frac{dt_\mu}{d\varepsilon_B}}_{(2)} + \underbrace{\sum_\mu \frac{\partial^2 L_{\mathrm{CC}}}{\partial \bar{t}_\mu \partial\varepsilon_A}\frac{d\bar{t}_\mu}{d\varepsilon_B}}_{(3)} \tag{C.11}$$

$$+ \underbrace{\sum_\mu \frac{\partial^2 L_{\mathrm{CC}}}{\partial\varepsilon_B \partial t_\mu}\frac{dt_\mu}{d\varepsilon_A}}_{(4)} + \underbrace{\sum_{\mu,\nu} \frac{\partial^2 L_{\mathrm{CC}}}{\partial t_\nu \partial t_\mu}\frac{dt_\nu}{d\varepsilon_B}\frac{dt_\mu}{d\varepsilon_A}}_{(5)} + \underbrace{\sum_{\mu,\nu} \frac{\partial^2 L_{\mathrm{CC}}}{\partial \bar{t}_\nu \partial t_\mu}\frac{d\bar{t}_\nu}{d\varepsilon_B}\frac{dt_\mu}{d\varepsilon_A}}_{(6)} \tag{C.12}$$

$$+ \underbrace{\sum_\mu \frac{\partial^2 L_{\mathrm{CC}}}{\partial\varepsilon_B \partial \bar{t}_\mu}\frac{d\bar{t}_\mu}{d\varepsilon_A}}_{(7)} + \underbrace{\sum_{\mu,\nu} \frac{\partial^2 L_{\mathrm{CC}}}{\partial t_\nu \partial \bar{t}_\mu}\frac{dt_\nu}{d\varepsilon_B}\frac{d\bar{t}_\mu}{d\varepsilon_A}}_{(8)} + \underbrace{\sum_{\mu,\nu} \frac{\partial^2 L_{\mathrm{CC}}}{\partial \bar{t}_\nu \partial \bar{t}_\mu}\frac{d\bar{t}_\nu}{d\varepsilon_B}\frac{d\bar{t}_\mu}{d\varepsilon_A}}_{(9)}. \tag{C.13}$$

Furthermore, it is worth noting that the Lagrange multipliers in the CC Lagrangian enter linearly, and therefore (9) is zero.

It is interesting to note that, up to this point, computing the second derivatives of the CC Lagrangian requires both the first-order response of the amplitudes and that of the multipliers. Our goal now is to eliminate all terms involving the response of the multipliers. Once again, variational perturbation theory comes to our aid. Let us proceed to compute

$$\frac{d}{d\varepsilon_A}\left(\frac{\partial L_{\mathrm{CC}}}{\partial \bar{t}_\mu}\right) = 0 \Rightarrow \frac{\partial^2 L_{\mathrm{CC}}}{\partial\varepsilon_A \partial \bar{t}_\mu} = -\frac{\partial L_{CC}}{\partial t_\nu \partial \bar{t}_\mu}\frac{dt_\nu}{d\varepsilon_A} \tag{C.14}$$

and inserting it in (3) we get

$$\frac{\partial^2 L_{\mathrm{CC}}}{\partial\varepsilon_A \partial \bar{t}_\mu}\frac{d\bar{t}_\mu}{d\varepsilon_B} = -\frac{\partial^2 L_{\mathrm{CC}}}{\partial t_\nu \partial \bar{t}_\mu}\frac{dt_\nu}{d\varepsilon_A}\frac{d\bar{t}_\mu}{d\varepsilon_B} \tag{C.15}$$

which corresponds exactly to (6)[1], but with the opposite sign, and therefore they cancel each other out. For the same reasons, (7) can be written as

$$\frac{\partial^2 L_{\mathrm{CC}}}{\partial \bar{t}_\nu \partial\varepsilon_B}\frac{d\bar{t}_\nu}{d\varepsilon_A} = -\frac{\partial^2 L_{\mathrm{CC}}}{\partial t_\mu \partial \bar{t}_\nu}\frac{dt_\mu}{d\varepsilon_B}\frac{d\bar{t}_\nu}{d\varepsilon_A} \tag{C.16}$$

[1]Since both μ and ν are summed over, their labels can be freely renamed.

which is exactly (8) but with opposite sign. The final expression is therefore

$$\frac{d^2 L_{\mathrm{CC}}}{d\varepsilon_A d\varepsilon_B} = \frac{\partial^2 L_{\mathrm{CC}}}{\partial\varepsilon_B \partial\varepsilon_A} + \sum_\mu \frac{\partial^2 L_{\mathrm{CC}}}{\partial t_\mu \partial\varepsilon_A}\frac{dt_\mu}{d\varepsilon_B} \tag{C.17}$$

$$+ \sum_\mu \frac{\partial^2 L_{\mathrm{CC}}}{\partial\varepsilon_B \partial t_\mu}\frac{dt_\mu}{d\varepsilon_A} + \sum_{\mu,\nu} \frac{\partial^2 L_{\mathrm{CC}}}{\partial t_\nu \partial t_\mu}\frac{dt_\nu}{d\varepsilon_B}\frac{dt_\mu}{d\varepsilon_A}. \tag{C.18}$$

This expression contains only quantities involving t_μ and their derivatives, and no longer includes any derivative of $\bar{t}_\mu$. This is a clear manifestation of the $(2n+2)$ rule: to compute the second derivative of the Lagrangian, only the zeroth-order multipliers $\bar{t}_\eta$ are required, whereas the amplitudes t_μ must be known up to first order in the perturbation. By using this symmetric expression, there is a trade-off: we need to know the response of the amplitudes with respect to *both* ε_A and ε_B.

C.1.1 Response equations

The terms involving $dt_\mu/d\varepsilon$ represent the response of the wavefunction parameters to the external perturbations. These are obtained by differentiating the amplitude equations $\Omega_\mu = 0$ with respect to ε, where

$$\Omega_\mu := \frac{\partial \mathcal{L}}{\partial \bar{t}_\mu} = J_{\mu 0} = 0, \quad J_{\mu 0} = \langle \Phi_\mu | \hat{\overline{H}} | \Phi_0 \rangle \,.$$

Differentiating with respect to ε gives:

$$\frac{d\Omega_\mu}{d\varepsilon} = \frac{\partial J_{\mu 0}}{\partial \varepsilon} + \sum_\nu \frac{\partial J_{\mu 0}}{\partial t_\nu}\frac{dt_\nu}{d\varepsilon} = 0, \tag{C.19}$$

which defines a system of linear equations for the unknowns $\frac{dt_\nu}{d\varepsilon}$. The matrix of this system is the Jacobian of the amplitude equations, and is often denoted as

$$A_{\mu\nu} := \frac{\partial J_{\mu 0}}{\partial t_\nu} = \langle \Phi_\mu | [\hat{\overline{H}}, \hat{\tau}_\nu] | \Phi_0 \rangle \,,$$

so that Eq. (C.19) becomes

$$\sum_\nu A_{\mu\nu}\frac{dt_\nu}{d\varepsilon} = -\frac{\partial J_{\mu 0}}{\partial \varepsilon},$$

or, in matrix notation

$$\mathbf{A}\,\mathbf{t}_\varepsilon^{[1]} = -\mathbf{g}_\varepsilon \Rightarrow \mathbf{t}_\varepsilon^{[1]} = -\mathbf{A}^{-1}\mathbf{g}_\varepsilon \tag{C.20}$$

where $\mathbf{A}$ is the Jacobian matrix with elements $A_{\mu\nu} = \partial J_\mu / \partial t_\nu$, $\mathbf{t}_{\boldsymbol{\varepsilon}}^{[1]}$ is the first-order response of the cluster amplitudes with respect to the perturbation $\boldsymbol{\varepsilon}$, and $\mathbf{g}_{\boldsymbol{\varepsilon}}$ is the perturbation-dependent source term with components $\partial J_{\mu 0} / \partial \varepsilon$. Eqn.(C.20) defines a linear system of equations for the first-order amplitude corrections. Although the formal solution involves the inverse of $\mathbf{A}$, in practice the system is solved iteratively, typically using methods such as preconditioned conjugate gradients or Davidson-type algorithms, since $\mathbf{A}$ is large, sparse, and not explicitly inverted.

Appendix D

Complements to Chapter 4

D.1 Derivatives of the electrostatic potential

The electrostatic potential at a point $\mathbf{r}$ generated by a charge distribution $\rho(\mathbf{r}')$ is

$$\varphi(\mathbf{r}) = \frac{1}{4\pi\varepsilon_0}\int \frac{\rho(\mathbf{r}')}{|\mathbf{r}-\mathbf{r}'|}\, d^3r'. \tag{D.1}$$

First Derivative

The first partial derivative of Eqn. (D.1) with respect to a Cartesian coordinate r_α reads

$$\frac{\partial\varphi(\mathbf{r})}{\partial r_\alpha} = \frac{1}{4\pi\varepsilon_0}\int \rho(\mathbf{r}')\frac{\partial}{\partial r_\alpha}\frac{1}{|\mathbf{r}-\mathbf{r}'|}\, d^3r'. \tag{D.2}$$

Defining $s = |\mathbf{r}-\mathbf{r}'| = \sqrt{\sum_\mu (r_\mu - r'_\mu)^2}$, we have

$$\frac{\partial s}{\partial r_\alpha} = \frac{r_\alpha - r'_\alpha}{s}. \tag{D.3}$$

By the chain rule,

$$\frac{\partial}{\partial r_\alpha}\frac{1}{s} = -\frac{1}{s^2}\frac{\partial s}{\partial r_\alpha} = -\frac{r_\alpha - r'_\alpha}{|\mathbf{r}-\mathbf{r}'|^3}. \tag{D.4}$$

Hence, the first derivative of the potential is

$$\frac{\partial\varphi(\mathbf{r})}{\partial r_\alpha} = -\frac{1}{4\pi\varepsilon_0}\int \rho(\mathbf{r}')\frac{r_\alpha - r'_\alpha}{|\mathbf{r}-\mathbf{r}'|^3}\, d^3r'. \tag{D.5}$$

Second Derivative

For the second derivative, we differentiate again:

$$\frac{\partial^2\varphi(\mathbf{r})}{\partial r_\alpha \partial r_\beta} = -\frac{1}{4\pi\varepsilon_0}\int \rho(\mathbf{r}')\frac{\partial}{\partial r_\beta}\frac{r_\alpha - r'_\alpha}{|\mathbf{r}-\mathbf{r}'|^3}\,d^3r'. \tag{D.6}$$

Applying the product rule:

$$\frac{\partial}{\partial r_\beta}\frac{r_\alpha - r'_\alpha}{s^3} = \frac{\partial(r_\alpha - r'_\alpha)}{\partial r_\beta}\cdot\frac{1}{s^3} + (r_\alpha - r'_\alpha)\frac{\partial}{\partial r_\beta}\frac{1}{s^3} \tag{D.7}$$

$$= \frac{\delta_{\alpha\beta}}{s^3} + (r_\alpha - r'_\alpha)(-3s^{-4})\frac{\partial s}{\partial r_\beta} \tag{D.8}$$

$$= \frac{\delta_{\alpha\beta}}{s^3} - 3\frac{(r_\alpha - r'_\alpha)(r_\beta - r'_\beta)}{s^5}. \tag{D.9}$$

Therefore, the second derivative of the electrostatic potential is

$$\frac{\partial^2\varphi(\mathbf{r})}{\partial r_\alpha \partial r_\beta} = \frac{1}{4\pi\varepsilon_0}\int \rho(\mathbf{r}')\frac{3(r_\alpha - r'_\alpha)(r_\beta - r'_\beta) - \delta_{\alpha\beta}|\mathbf{r}-\mathbf{r}'|^2}{|\mathbf{r}-\mathbf{r}'|^5}\,d^3r'. \tag{D.10}$$

This expression is valid only for points $\mathbf{r} \neq \mathbf{r}'$, because the integrand diverges when $\mathbf{r}' \to \mathbf{r}$. To treat this singularity rigorously, we interpret the derivatives in the *distributional* sense, which introduces a local, δ-function contribution. Starting from the pointwise identity for $\mathbf{r} \neq \mathbf{r}'$,

$$\partial_\alpha\partial_\beta\left(\frac{1}{|\mathbf{r}-\mathbf{r}'|}\right) = \frac{3(r_\alpha - r'_\alpha)(r_\beta - r'_\beta) - \delta_{\alpha\beta}|\mathbf{r}-\mathbf{r}'|^2}{|\mathbf{r}-\mathbf{r}'|^5}, \tag{D.11}$$

we note that as $\mathbf{r}' \to \mathbf{r}$, the kernel becomes singular. To account for this singularity, we make the ansatz

$$\partial_\alpha\partial_\beta\frac{1}{|\mathbf{r}-\mathbf{r}'|} = \mathrm{PV}\left[\frac{3(r_\alpha - r'_\alpha)(r_\beta - r'_\beta) - \delta_{\alpha\beta}|\mathbf{r}-\mathbf{r}'|^2}{|\mathbf{r}-\mathbf{r}'|^5}\right] + C\,\delta_{\alpha\beta}\,\delta(\mathbf{r}-\mathbf{r}'), \tag{D.12}$$

where the "PV" denotes the *principal value*, defined as

$$\mathrm{PV}\int f(\mathbf{r}')d^3r' \equiv \lim_{\epsilon\to 0}\int_{|\mathbf{r}-\mathbf{r}'|>\epsilon} f(\mathbf{r}')\,d^3r'. \tag{D.13}$$

This limit prescription removes an infinitesimal sphere around the singularity, integrates the remainder, and then takes the radius to zero, ensuring the integral is well-defined.

To determine the constant C, we take the trace ($\alpha = \beta$). On the left-hand side (see, for instance, Ref. [75]),

$$\partial_\alpha \partial_\alpha \frac{1}{|\mathbf{r}-\mathbf{r}'|} = \nabla^2 \frac{1}{|\mathbf{r}-\mathbf{r}'|} = -4\pi\delta(\mathbf{r}-\mathbf{r}'). \tag{D.14}$$

On the right-hand side, the principal value term vanishes due to symmetry, leaving

$$C\,\delta_{\alpha\alpha}\,\delta(\mathbf{r}-\mathbf{r}') = 3C\,\delta(\mathbf{r}-\mathbf{r}') \quad \Rightarrow \quad C = -\frac{4\pi}{3}. \tag{D.15}$$

Thus, the exact distributional identity reads

$$\partial_\alpha \partial_\beta \frac{1}{|\mathbf{r}-\mathbf{r}'|} = \mathrm{PV}\left[\frac{3(r_\alpha - r'_\alpha)(r_\beta - r'_\beta) - \delta_{\alpha\beta}|\mathbf{r}-\mathbf{r}'|^2}{|\mathbf{r}-\mathbf{r}'|^5}\right] - \frac{4\pi}{3}\,\delta_{\alpha\beta}\,\delta(\mathbf{r}-\mathbf{r}'). \tag{D.16}$$

Applying this to the electrostatic potential, we have

$$\partial_\alpha \partial_\beta \varphi(\mathbf{r}) = \frac{1}{4\pi\varepsilon_0}\mathrm{PV}\int \rho(\mathbf{r}')\frac{3(r_\alpha - r'_\alpha)(r_\beta - r'_\beta) - \delta_{\alpha\beta}|\mathbf{r}-\mathbf{r}'|^2}{|\mathbf{r}-\mathbf{r}'|^5}\,d^3r' - \frac{1}{3\varepsilon_0}\delta_{\alpha\beta}\rho(\mathbf{r}). \tag{D.17}$$

Defining the traceless tensor

$$\chi^{[1]}_{\alpha\beta}(\mathbf{r}) = \frac{1}{4\pi\varepsilon_0}\mathrm{PV}\int \rho(\mathbf{r}')\frac{3(r_\alpha - r'_\alpha)(r_\beta - r'_\beta) - \delta_{\alpha\beta}|\mathbf{r}-\mathbf{r}'|^2}{|\mathbf{r}-\mathbf{r}'|^5}\,d^3r', \quad \chi^{[1]}_{\alpha\alpha} = 0, \tag{D.18}$$

we can write

$$\partial_\alpha \partial_\beta \varphi(\mathbf{r}) = \chi^{[1]}_{\alpha\beta}(\mathbf{r}) - \frac{1}{3\varepsilon_0}\delta_{\alpha\beta}\rho(\mathbf{r}). \tag{D.19}$$

Finally, since $\mathcal{E}_\alpha = -\partial_\alpha \varphi$, the gradient of the electric field is

$$\partial_\beta \mathcal{E}_\alpha(\mathbf{r}) = -\partial_\beta \partial_\alpha \varphi(\mathbf{r}) = -\chi^{[1]}_{\alpha\beta}(\mathbf{r}) + \frac{1}{3\varepsilon_0}\delta_{\alpha\beta}\rho(\mathbf{r}), \tag{D.20}$$

which separates the traceless, non-local part from the local contribution proportional to the charge density.

D.2 Sternheimer shielding

In a 1950 letter to the editor, Sternheimer writes [213]

> It was pointed out by Rabi that the hyperfine splitting due to the nuclear quadrupole moment includes the effect of an electric quadrupole moment induced in the electron shells.

He then proceeds, using the Thomas-Fermi model, to provide "as crude estimate of the moment induced in a core of closed shells". In a 1951 follow-up paper Sternheimer extends his analysis to the Hartree-Fock level [434]. It is clear that the calculations reported in the present paper does not feature the variational inclusion of a nuclear quadrupole moment, and so one may worry if some effect is missing. This is analyzed in the following.

The general electrostatic interaction of two charge densities A and B is expressed as

$$E_{AB} = \frac{1}{4\pi\varepsilon_0} \int d^3\mathbf{r}_1 \int d^3\mathbf{r}_2 \frac{\rho_A(\mathbf{r}_1)\,\rho_B(\mathbf{r}_2)}{|\mathbf{r}_1 - \mathbf{r}_2|}$$

Using a Laplace expansion, we obtain

$$E_{AB} = \frac{1}{4\pi\varepsilon_0} \sum_{\ell=0}^{\infty} \sum_{m=-\ell}^{+\ell} \frac{4\pi}{2\ell+1} \int d^3\mathbf{r}_1 \int d^3\mathbf{r}_2 \frac{r_<^\ell}{r_>^{\ell+1}} Y_{\ell m}(\boldsymbol{n}_1)\, Y^*_{\ell m}(\boldsymbol{n}_2)\, \rho_A(\mathbf{r}_1)\, \rho_B(\mathbf{r}_2)\,. \tag{D.21}$$

When $r_2 > r_1$, a spherical electric multipole expansion is obtained

$$E = \sum_{\ell=0}^{\infty} \sum_{m=-\ell}^{+\ell} q^*_{\ell m} \mathcal{E}_{\ell m}; \qquad \begin{array}{rcl} q_{\ell m} & = & \sqrt{\frac{4\pi}{2\ell+1}} \int r_2^\ell Y_{\ell m}(\boldsymbol{n}_1)\, \rho_A(\mathbf{r}_1)\, d^3\mathbf{r}_1 \\ \mathcal{E}_{\ell m} & = & \frac{1}{4\pi\varepsilon_0} \sqrt{\frac{4\pi}{2\ell+1}} \int \frac{1}{r_1^{\ell+1}} Y_{\ell m}(\boldsymbol{n}_2)\, \rho_B(\mathbf{r}_1)\, d^3\mathbf{r}_2 \end{array} ; \quad r_2 > r_1. \tag{D.22}$$

Focusing on the electric quadrupole component $\ell = 2$ and $m = 0$ we get

$$E_{20} = q^*_{20}\mathcal{E}_{20}; \qquad \begin{array}{rcl} q_{20} & = & \int \frac{1}{2}\left(3z_1^2 - r_1^2\right) \rho_A(\mathbf{r}_1)\, d^3\mathbf{r}_1 \\ \mathcal{E}_{20} & = & \dfrac{1}{4\pi\varepsilon_0} \displaystyle\int \frac{\left(3z_2^2 - r_2^2\right)}{2r_2^5} \rho_B(\mathbf{r}_2)\, d^3\mathbf{r}_2 \end{array} ; \quad r_2 > r_1, \tag{D.23}$$

where we used that

$$Y_{20}(\theta,\phi) = \sqrt{\frac{5}{4\pi}} \frac{1}{2} \left(3\cos^2\theta - 1\right). \tag{D.24}$$

Let us now investigate the Sternheimer shielding effect. We consider an atom A, placed at the origin, with a nuclear quadrupole moment Q, associated with the operator

$$\hat{h}_Q = -\frac{e^2 Q}{4\pi\varepsilon_0} \frac{\left(3\cos^2\theta - 1\right)}{4r^3}; \quad eQ = 2q_{20}. \tag{D.25}$$

	coupled	uncoupled
δQ	-0.082	-1.027
$1s$	0.058	0.056
$2s$	0.161	0.144
$3s$	0.631	0.429
$2p$	-2.166	-1.656
$2p \rightarrow p$	-1.288	-1.083
$2p \rightarrow f$	-0.682	-0.573

TABLE D.1: Induced quadrupole moment (in units of Q) of the aluminium atom, calculated at the non-relativistic HF level using the Lévy-Leblond Hamiltonian, a dyall.ae3z basis and the DIRAC code.

The induced quadrupole moment can be calculated as a linear response function

$$e\delta Q = 2\delta q_{20} = 2\left\langle\left\langle -\frac{e}{2}\left(3z^2 - r^2\right); \hat{h}_Q\right\rangle\right\rangle. \tag{D.26}$$

We have investigated this for the [Mg] core of the aluminum atom. We first did an average-of-configuration (AOC) HF calculation [435] of the aluminium atom at the non-relativistic level using the Lévy-Leblond Hamiltonian,[280, 436] a dyall.ae3z basis [437, 438] and the DIRAC code [275]. We next calculated the above linear response function Eqn. (D.26), but not allowing the Al $3p$ orbitals to respond. We find that the total induced quadrupole moment is $e\delta Q$=-0.820E-01Q, which increases significantly to -1.027Q at the uncoupled HF-level. The uncoupled linear response function can be exactly decomposed into individual orbital contributions, as seen in Table D.1. At the coupled HF-level, reponse can be restricted to selected occupied orbitals, but the contributions no longer sum up to the total value. In both cases, it is seen that the response from s and p orbitals is shielding (+) and anti-shielding (-), respectively. Finally, it is possible to separate the contribution from $2p$ into excitations to virtual p and f orbitals, as also shown in Table D.1.

We have seen that the quadrupole moment induced in the electronic cloud may be of the same order as the nuclear one. We now investigate its effect on energies. In his first two papers, Sternheimer investigated open-shell atoms. It is clear that the expectation value of the spherically symmetric closed core shells with respect to the operator, Eqn. (D.25), is zero; any non-zero contribution comes from the open-shell valence, which now may also interact with the polarized core. The operator form Eqn. (D.25) assumes a point-like

nuclear quadrupole moment. The induced quadrupole moment

$$e\delta Q = 2q_{20} = -e\int \left(3z_2^2 - r_2^2\right)\delta_Q n\left(\mathbf{r}_2\right) d^3\mathbf{r}_2$$

is certainly not point-like and so we should use the general interaction expression, Eqn. (D.21), picking out the contribution from $\ell = 2$ and $m = 0$. It may be written as

$$E_{A\delta Q} = -\frac{e}{4\pi\varepsilon_0}\int d^3\mathbf{r}_1 \rho_A\left(\mathbf{r}_1\right)\frac{\left(3z_1^2 - r_1^2\right)}{4r_1^5}\gamma\left(r_1\right)Q \tag{D.27}$$

where appears the Sternheimer *screening* factor [439]

$$\gamma\left(r_1\right) = (1/Q)\left[\int_{r_2<r_1} d^3\mathbf{r}_2\left(3z_2^2 - r_2^2\right)\delta_Q n\left(\mathbf{r}_2\right) + r_1^5\int_{r_2>r_1} d^3\mathbf{r}_2\frac{\left(3z_2^2 - r_2^2\right)}{r_2^5}\delta_Q n\left(\mathbf{r}_2\right)\right].$$

We note that the total induced quadrupole moment can be expressed as

$$\delta Q = \gamma_\infty Q; \quad \gamma_\infty = \lim_{r\to\infty}\gamma\left(r\right).$$

In Eqn. (D.27) ρ_A refers to whatever non-symmetric charge distribution is in interaction with the induced quadrupole moment, for instance the open-shell valence in an atom.

In subsequent papers [439, 440], Sternheimer and co-workers moved on to the consideration of diatomic molecules. In the first paper, devoted to the Li_2 molecule, we find the statement

> In order to obtain the shielding effect without ambiguity, it is best to study this effect as a result of the distortion of the $1s$ shell by the asymmetric potential caused by the other charges. The correction to q is the due to the part of the distortion which behaves as $\left(3\cos^2\theta - 1\right)$. This picture is equivalent to the consideration of the induced moment, as will now be shown.

The demonstration is somewhat convoluted and we therefore give a simplified version here. We follow the second paper, considering the highly polar NaCl molecule. We investigate the effect of a nuclear quadrupole moment of the chlorine nucleus at the origin and represent the Na^+ moiety as a point charge $+e$ at the position $\mathbf{r}_{Na} = (0, 0, R)$ well outside the electron cloud of the Cl^- moiety, as reported in Figure D.1. The interaction

energy Eqn. (D.27) can then be written as

$$E_{\mathrm{Na},\delta Q_{Cl}} = -\frac{e^2}{4\pi\varepsilon_0}\frac{\gamma_\infty Q}{2R^3} = -\frac{e^2}{4\pi\varepsilon_0}\frac{1}{2R^3}\int d^3\mathbf{r}\left(3z^2 - r^2\right)\delta_Q n\left(\mathbf{r}\right). \tag{D.28}$$

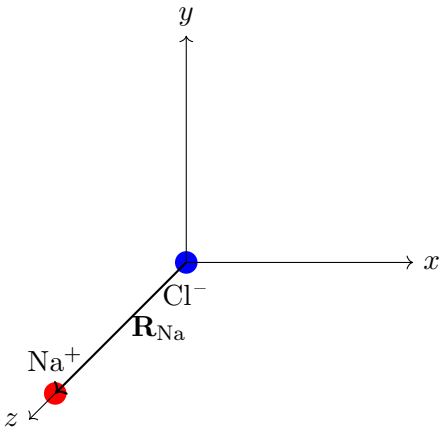

FIGURE D.1: Schematic representation of the NaCl molecule, with the Cl^- nucleus at the origin and the Na^+ ion positioned along the z-axis at $\mathbf{R}_{\mathrm{Na}} = (0, 0, R)$.

The induced charge distribution can itself be expressed as a linear response function

$$\delta n_Q\left(\mathbf{r}\right) = \left\langle\left\langle \delta\left(\mathbf{r}\right); \hat{h}_Q \right\rangle\right\rangle.$$

For the present purposes, it suffices to look at the linear response function at the uncoupled HF-level. Starting from a perturbation operator on the form

$$V = \sum_X \varepsilon_X \hat{h}_X,$$

the linear response function is then given by

$$\left\langle\left\langle \hat{h}_A; \hat{h}_B \right\rangle\right\rangle = \left[\frac{d^2E}{d\varepsilon_A d\varepsilon_B}\right]_{\boldsymbol{\varepsilon}=\mathbf{0}} = \sum_{ai}\left[\frac{\langle\Phi_0|\hat{h}_A|\Phi_i^a\rangle\langle\Phi_i^a|\hat{h}_B|\Phi_0\rangle}{\varepsilon_i - \varepsilon_a} + \text{c.c.}\right] = \left\langle\left\langle \hat{h}_B; \hat{h}_A \right\rangle\right\rangle. \tag{D.29}$$

In the present case we obtain

$$\delta n_Q\left(\mathbf{r}\right) = \sum_{ai}\frac{1}{\varepsilon_i - \varepsilon_a}\left[\varphi_i^*\left(\mathbf{r}\right)\varphi_a\left(\mathbf{r}\right)\langle\Phi_i^a|\hat{h}_Q|\Phi_0\rangle + \text{c.c.}\right]$$

The interaction energy therefore reads

$$E_{\mathrm{Na},\delta Q_{Cl}} = -\frac{e^2}{4\pi\varepsilon_0}\frac{1}{2R^3}\sum_{ai}\frac{1}{\varepsilon_i-\varepsilon_a}\int d^3\mathbf{r}_2\left(3z_2^2-r_2^2\right)\left[\varphi_i^*\left(\mathbf{r}_2\right)\varphi_a\left(\mathbf{r}_2\right)\langle\Phi_i^a|\hat{h}_Q|\Phi_0\rangle+\mathrm{c.c.}\right]. \tag{D.30}$$

Let us now consider the distortion of the Cl^- moiety by the sodium charge. The associated interaction operator is

$$\hat{h}_{\mathrm{Na}} = -e\phi_{\mathrm{Na}} = \frac{-e^2}{4\pi\varepsilon_0}\frac{1}{|\mathbf{r}-\mathbf{r}_{\mathrm{Na}}|}$$

However, we shall be interested only in the component associated with $\ell = 2$ and $m = 0$, which is

$$\hat{h}_{\mathrm{Na},E2} = \frac{-e^2}{4\pi\varepsilon_0}\frac{1}{2}\left(3z^2-r^2\right)R^{-3}$$

Returning to the above interaction energy, Eqn. (D.30), we find that it can be expressed as a linear response function

$$E_{\mathrm{Na},\delta Q_{Cl}} = \left\langle\left\langle\hat{h}_{\mathrm{Na},E2};\hat{h}_Q\right\rangle\right\rangle.$$

Such a response function gives the modification of expectation value of $\hat{h}_{P,E2}$ under the influence of $\hat{h}_Q$, but equally well the opposite, as clearly seen from Eqn. (D.29). The statement by Sternheimer and co-workers has therefore been shown to hold true. Our SCF calculations do not include the operator Eqn. (D.25) associated with a nuclear quadrupole moment, but do generate a fully relaxed electron cloud, which enters the perturbative calculation of their interaction. The Sternheimer shielding is therefore fully accounted for.

D.3 Time reversal symmetry and Kramers partners

An operator $\hat{\mathcal{K}}$ is antiunitary if it satisfies:

1. $\hat{\mathcal{K}}(a\psi+b\phi) = a^*\hat{\mathcal{K}}\psi + b^*\hat{\mathcal{K}}\phi$ (antilinearity),
2. $\langle\hat{\mathcal{K}}\psi|\hat{\mathcal{K}}\phi\rangle = \langle\phi|\psi\rangle$ (antiunitarity).

Antiunitary operators can always be written in the form $\hat{\mathcal{K}} = U\hat{\mathcal{K}}_0$, where U is unitary and $\hat{\mathcal{K}}_0$ denotes complex conjugation in a fixed basis. Systems are time-reversal symmetric if the Hamiltonian commutes with the time-reversal operator. This is generally true in absence of an external magnetic field.

It is easy to verify that the momentum operator $\hat{\mathbf{p}}$ is *odd* under time reversal, which implies

$$\hat{\mathcal{K}}\,\hat{\mathbf{p}}\,\hat{\mathcal{K}}^{-1} = -\hat{\mathbf{p}}. \tag{D.31}$$

Therefore, in order to preserve the time-reversal symmetry of the Dirac Hamiltonian, we require that

$$\hat{\mathcal{K}}\,\boldsymbol{\alpha}\,\hat{\mathcal{K}}^{-1} = -\boldsymbol{\alpha}, \tag{D.32}$$

which is satisfied if and only if the time-reversal operator takes the form

$$\hat{\mathcal{K}} = -i\,(\mathbf{I}_2 \otimes \sigma_y)\,\hat{\mathcal{K}}_0. \tag{D.33}$$

When dealing with fermionic wavefunctions φ, it is convenient to define the time-reversal operator $\hat{\mathcal{K}}$ by its action on a scalar multiple of the wavefunction:

$$\hat{\mathcal{K}}\,a\varphi = a^*\hat{\mathcal{K}}\varphi, \qquad \hat{\mathcal{K}}^2\phi = -\varphi, \tag{D.34}$$

where a is a complex scalar and the star denotes complex conjugation. The first relation shows that $\hat{\mathcal{K}}$ is an *antiunitary* operator: it is antilinear with respect to complex scalars, i.e., it conjugates complex coefficients. The second relation, $\hat{\mathcal{K}}^2 = -1$ on fermion wavefunctions, reflects the fundamental *Kramers degeneracy* theorem [441]: time reversal squares to -1 when acting on half-integer spin systems, ensuring that all energy eigenstates come in degenerate pairs known as *Kramers partners*. We adopt the convention

$$\hat{\mathcal{K}}\varphi = \bar{\varphi}, \tag{D.35}$$

where φ and $\bar{\varphi}$ form a pair of Kramers partners related by time reversal. Using the alternative definition (D.34), one can classify Hermitian operators $\hat{\Omega}^t$ according to their behavior under time reversal:

$$\hat{\mathcal{K}}\hat{\Omega}^t\hat{\mathcal{K}}^{-1} = t\hat{\Omega}^t, \quad t = \pm 1. \tag{D.36}$$

Here, $t = +1$ corresponds to operators $\hat{\Omega}^+$ that are *symmetric* under time reversal (time-reversal even operators), while $t = -1$ corresponds to operators $\hat{\Omega}^-$ that are *antisymmetric* under time reversal (time-reversal odd operators).Let us investigate the matrix structure of these operators. Let $\{\varphi_p\}$ be an orthonormal set of single-particle fermionic spinors. Acting with the antiunitary time-reversal operator $\hat{\mathcal{K}}$ on this set, we generate the corresponding Kramers partners, according to Eqn(D.35).

The Kramers-restricted basis is then defined as the union of the two sets:

$$\{\varphi_p, \bar{\varphi}_p\}_{p=1}^n \equiv \{\varphi_p\}_{p=1}^n \cup \{\bar{\varphi}_p\}_{p=1}^n \tag{D.37}$$

We consider a Hermitian operator $\hat{\Omega}^t$ that is either symmetric ($t = +1$) or antisymmetric ($t = -1$) under time-reversal, according to Eqn.(D.36). To derive the matrix structure of such operators, we analyze their matrix elements in the Kramers basis:

$\boxed{pq}$:

$$\Omega_{pq} := \langle\varphi_p|\hat{\Omega}^t|\varphi_q\rangle = A_{pq}. \tag{D.38}$$

$\boxed{p\bar{q}}$:

$$\Omega_{p\bar{q}} := \langle\varphi_p|\hat{\Omega}^t|\bar{\varphi}_q\rangle = B_{p\bar{q}}. \tag{D.39}$$

$\boxed{\bar{p}q}$:

$$\Omega_{\bar{p}q} := \langle\bar{\varphi}_p|\hat{\Omega}^t|\varphi_q\rangle = \langle\varphi_p|\hat{\mathcal{K}}^{-1}\hat{\Omega}^t|\varphi_q\rangle^* = \langle\varphi_p|\underbrace{\hat{\mathcal{K}}^{-1}\hat{\Omega}^t\hat{\mathcal{K}}}_{=t\hat{\Omega}^t}\hat{\mathcal{K}}^{-1}|\varphi_q\rangle^* = -tB_{p\bar{q}} \tag{D.40}$$

$\boxed{\bar{p}\bar{q}}$:

$$\Omega_{\bar{p}\bar{q}} := \langle\bar{\varphi}_p|\hat{\Omega}^t|\bar{\varphi}_q\rangle = \langle\hat{\mathcal{K}}\varphi_p|\hat{\Omega}^t|\hat{\mathcal{K}}\varphi_q\rangle = \langle\varphi_p|\hat{\mathcal{K}}^{-1}\hat{\Omega}^t\hat{\mathcal{K}}|\varphi_q\rangle^* = tA_{pq}^* \tag{D.41}$$

From that, we see that the matrix elements of $\hat{\Omega}^t$ in the Kramers basis satisfy the following structure:

$$\Omega = \begin{pmatrix} \mathbf{A} & \mathbf{B} \\ -t\mathbf{B}^* & t\mathbf{A}^* \end{pmatrix}, \tag{D.42}$$

The matrix structure shown in Eqn.(D.42) is fully determined by the two unique blocks $\mathbf{A}$ and $\mathbf{B}$, since the lower half is related to the upper half by time-reversal symmetry. As a result, only $\mathbf{A}$ and $\mathbf{B}$ need to be explicitly stored and manipulated during the SCF

procedure, which significantly reduces the computational cost. To retain this symmetry throughout the SCF iterations, it is essential to ensure that the matrix structure is preserved at each step. Different approaches have been proposed to exploit time-reversal symmetry in relativistic electronic structure theory. The first to exploit time-reversal symmetry in molecular calculations using quaternion algebra was Nötker [442]. Aucar *et al.* [443] introduced a Kramers-adapted basis, defining $X_{pq}^{\pm}$ operators that replace the spin-adapted basis of non-relativistic theory and enable symmetry blocking for efficient relativistic calculations. Later, Saue and Jensen [363] developed a more general symmetry scheme based on the irreducible corepresentations of the full molecular symmetry group. Their approach reformulates the Dirac–Hartree–Fock equations in terms of quaternion algebra and combines time-reversal with molecular point group symmetry to maximize computational reduction.

We now study the eigenvalue problem:

$$\Omega \begin{pmatrix} \mathbf{c}_1 \\ \mathbf{c}_2 \end{pmatrix} = \varepsilon \begin{pmatrix} \mathbf{c}_1 \\ \mathbf{c}_2 \end{pmatrix} \Rightarrow \begin{cases} \mathbf{A}\mathbf{c}_1 + \mathbf{B}\mathbf{c}_2 = \varepsilon \mathbf{c}_1, \\ -t\mathbf{B}^*\mathbf{c}_1 + t\mathbf{A}^*\mathbf{c}_2 = \varepsilon \mathbf{c}_2. \end{cases} \tag{D.43}$$

Now, we take the complex conjugate of both equations:

$$\mathbf{A}^*\mathbf{c}_1^* + \mathbf{B}^*\mathbf{c}_2^* = \varepsilon^*\mathbf{c}_1^*, \tag{D.44}$$

$$-t\mathbf{B}\mathbf{c}_1^* + t\mathbf{A}\mathbf{c}_2^* = \varepsilon^*\mathbf{c}_2^*. \tag{D.45}$$

We multiply the first equation by t and the second by $-t$:

$$t\mathbf{A}^*\mathbf{c}_1^* + t\mathbf{B}^*\mathbf{c}_2^* = t\varepsilon^*\mathbf{c}_1^*, \tag{D.46}$$

$$\mathbf{B}\mathbf{c}_1^* - \mathbf{A}\mathbf{c}_2^* = -t\varepsilon^*\mathbf{c}_2^*. \tag{D.47}$$

These two equations can be rearranged as

$$\Omega \begin{pmatrix} -\mathbf{c}_2^* \\ \mathbf{c}_1^* \end{pmatrix} = t\varepsilon^* \begin{pmatrix} -\mathbf{c}_2^* \\ \mathbf{c}_1^* \end{pmatrix}. \tag{D.48}$$

We conclude that if $\begin{pmatrix} \mathbf{c}_1 \\ \mathbf{c}_2 \end{pmatrix}$ is an eigenvector of Ω with eigenvalue ε, then its Kramers

conjugate $\begin{pmatrix} -\mathbf{c}_2^* \\ \mathbf{c}_1^* \end{pmatrix}$ is also an eigenvector with eigenvalue $t\varepsilon^*$. Since Ω is Hermitian, the eigenvalues are real. This leads to the following important consequences:

- If $\hat{\Omega}^t$ is symmetric under time reversal ($t = +1$), the two eigenvectors form a Kramers pair with the *same* eigenvalue:

$$\begin{pmatrix} \mathbf{c}_1 \\ \mathbf{c}_2 \end{pmatrix} \quad \leftrightarrow \quad \begin{pmatrix} -\mathbf{c}_2^* \\ \mathbf{c}_1^* \end{pmatrix}.$$

- If $\hat{\Omega}^t$ is antisymmetric under time reversal ($t = -1$), the two eigenvectors form a pair with eigenvalues of *opposite sign* but equal magnitude:

$$\begin{pmatrix} \mathbf{c}_1 \\ \mathbf{c}_2 \end{pmatrix} \quad \leftrightarrow \quad \begin{pmatrix} -\mathbf{c}_2^* \\ \mathbf{c}_1^* \end{pmatrix}.$$

Therefore, time-reversal symmetry imposes strong structural constraints on the matrix form of Hermitian operators in a relativistic context, producing pairs of eigenvectors that either share the same eigenvalue or have opposite signs depending on the symmetry type.

Appendix E

Complements to Chapter 5

E.1 Localization and core orbitals

Orbital localization in the DIRAC code is based on the Pipek–Mezey criterion [284]. A first implementation was based on the steepest ascent method [221]. Building upon the work of Jørgensen and co-workers [444, 445], we have next implemented localization of orbitals using the trust-region algorithm of Fletcher [446], in particular as outlined in Ref.[141] (Section 12.3). Our algorithm takes into account Kramers pairing due to time-reversal symmetry.

The Pipek–Mezey localization criterion minimizes the number of centers spanned by the individual MOs. However, in practice, we see that our localization procedure touches core orbitals, which are maximally localized. In the following we first specify the exponential parametrization of our algortim, allowing unconstrained optimization as well as the straightforward identification and elimination of redundancies. We then derive expression for the gradient and Hessian, and finally address the question as to whether the Pipek–Mezey algorithm may modify core orbitals.

E.1.1 Basic theory

We use the localization criterion of Pipek and Mezey [284], where the localized orbitals are obtained by maximization of the functional (inverse mean delocalization)

$$G\left[\{\varphi_i\}\right] = \frac{1}{N}\sum_{i=1}^{N}\sum_{A}\left(Q_i^A\right)^2; \quad Q_i^A = \langle\varphi_i|P_A|\varphi_i\rangle. \tag{E.1}$$

The quantity Q_i^A is the contribution from MO with index i to the Mulliken charge of atom A and is a diagonal element of the Hermitian matrix

$$Q_{ij}^A = \boldsymbol{c}_i^{A\dagger} S^{AA} \boldsymbol{c}_j^A + \frac{1}{2}\sum_{B\neq A}\left(\boldsymbol{c}_i^{A\dagger} S^{AB} \boldsymbol{c}_j^B + \boldsymbol{c}_i^{B\dagger} S^{BA} \boldsymbol{c}_j^A\right), \tag{E.2}$$

The expression assumes that the overlap matrix S in the atomic basis is sorted on atomic centers, so that S^{AB} is an off-diagonal block associated with centers A and B. The vector $\boldsymbol{c}_i^A$ collects expansion coefficients from center A for orbital of index i. Obviously,

$$\sum_A Q_{ij}^A = \delta_{ij}. \tag{E.3}$$

To set up our second-order algorithm, we introduce an exponential parametrization

$$\tilde{\varphi}_p = \sum_q \varphi_q U_{qp}; \quad U = \exp\left[-\kappa\right]; \quad \kappa_{pq}^* = -\kappa_{qp}. \tag{E.4}$$

Let us first investigate redundancies. In the ensuing manipulations, it will be helpful to expand the Pipek–Mezey functional in orders of the orbital rotation parameters $\{\kappa_{pq}\}$. For e.g. the Hartree–Fock method in second quantization, this is achieved using the Baker–Campbell–Haussdorf expansion [141]. We obtain a suitable expansion in the present case starting from

$$G\left(\lambda\right) = \sum_i \sum_A \sum_{pqrs} \langle\varphi_p \left\{\exp\left[-\lambda\kappa\right]\right\}_{pi} |P_A| \varphi_q \left\{\exp\left[-\lambda\kappa\right]\right\}_{qi}\rangle \langle\varphi_r \left\{\exp\left[-\lambda\kappa\right]\right\}_{ri} |P_A| \varphi_s \left\{\exp\left[-\lambda\kappa\right]\right\}_{si}\rangle. \tag{E.5}$$

Next we consider the first derivative of $G\left(\lambda\right)$ at $\lambda = 0$

$$G'\left(0\right) = -2\sum_A \sum_i \sum_j \left(\kappa_{ji}^* Q_{ji}^A + \kappa_{ji} Q_{ij}^A\right) Q_i^A \tag{E.6}$$

We first note that for the contribution $i = j$, we get

$$Q_i^A \left(\kappa_{ii}^* + \kappa_{ii}\right) = 0. \tag{E.7}$$

since non-zero diagonal elements of an anti-Hermitian matrix can only be purely imaginary. We therefore conclude that diagonal elements of the κ matrix are redundant. From the matrix symmetry, it is clear that we only need one triangle, and we choose the lower one, that is $\left\{\kappa_{ij}, \kappa_{ij}^*, i > j\right\}$.

The parameter space is navigated starting from a quadratic expansion of the Pipek–Mezey function

$$\tilde{G}(\{\kappa\}) = G[0] + G^{[1]\dagger}\kappa + \frac{1}{2}\kappa^\dagger G^{[2]}\kappa \tag{E.8}$$

Elements of the gradient $G^{[1]}$ are:

$$\left[\frac{\partial G}{\partial \kappa_{ij}^*}\right]_{\boldsymbol{\kappa}=\mathbf{0}} = 2\sum_A Q_{ij}^A \left(Q_i^A - Q_j^A\right); \quad i > j. \tag{E.9}$$

Elements of the Hessian $G^{[2]}$ are ($i > j$, $k > l$):

$$\begin{aligned}
\left[\frac{\partial^2 G}{\partial \kappa_{ij}^* \partial \kappa_{kl}}\right]_{\boldsymbol{\kappa}=\mathbf{0}} &= 2\sum_A Q_{ij}^A \left(\delta_{ik} Q_{li}^A - \delta_{il} Q_{ik}^A + \delta_{jl} Q_{jk}^A - \delta_{jk} Q_{lj}^A\right) && \text{(E.10)}\\
&+ \sum_A \left(\delta_{ik} Q_{lj}^A \left(2Q_i^A - Q_j^A - Q_l^A\right) + \delta_{jl} Q_{ik}^A \left(2Q_j^A - Q_i^A - Q_k^A\right)\right) && \text{(E.11)}\\
\left[\frac{\partial^2 G}{\partial \kappa_{ij}^* \delta \kappa_{kl}^*}\right]_{\boldsymbol{\kappa}=\mathbf{0}} &= 2\sum_A Q_{ij}^A \left(\delta_{ik} Q_{il}^A - \delta_{il} Q_{ki}^A + \delta_{jl} Q_{kj}^A - \delta_{jk} Q_{jl}^A\right) && \text{(E.12)}\\
&- \sum_A \left(\delta_{jk} Q_{il}^A \left(2Q_j^A - Q_l^A - Q_i^A\right) + \delta_{il} Q_{kj}^A \left(2Q_i^A - Q_j^A - Q_k^A\right)\right) && \text{(E.13)}
\end{aligned}$$

The remaining combinations are obtained by complex conjugation. Within the validity of the quadratic model Eqn. (E.8), the stationary point is found by taking the Newton step

$$G^{[2]}\kappa = -G^{[1]}; \tag{E.14}$$

beyond a level-shifted Newton step is determined to find the optimal step on the boundary of the trust region [141].

E.1.2 Will the Pipek–Mezey algorithm modify core orbitals ?

For simplicity let us limit attention to single orbital rotation parameter κ_{ij} and two centers A and B. Matrix elements, Eqn. (E.2), reduce to

$$Q_{ij}^{A} = \frac{1}{2}\left(\boldsymbol{c}_i^{A\dagger} S^{AB} \boldsymbol{c}_j^{B} + 2\boldsymbol{c}_i^{A\dagger} S^{AA} \boldsymbol{c}_j^{A} + \boldsymbol{c}_i^{B\dagger} S^{BA} \boldsymbol{c}_j^{A}\right) \tag{E.15}$$

and the sum rule, Eqn. (E.3), is now

$$Q_{ij}^{A} + Q_{ij}^{B} = 0; \quad Q_{i}^{A} + Q_{i}^{B} = 1. \tag{E.16}$$

The Newton step, Eqn. (E.14), can thereby be expressed as

$$\begin{bmatrix} 8\left|Q_{ij}^{A}\right|^2 - 4\left(Q_i^A - Q_j^A\right)^2 & 8Q_{ij}^{A}Q_{ij}^{A} \\ 8Q_{ij}^{A*}Q_{ij}^{A*} & 8\left|Q_{ij}^{A}\right|^2 - 4\left(Q_i^A - Q_j^A\right)^2 \end{bmatrix} \begin{bmatrix} \kappa_{ij} \\ \kappa_{ij}^{*} \end{bmatrix} = - \begin{bmatrix} 4Q_{ij}^{A}\left(Q_i^A - Q_j^A\right) \\ 4Q_{ij}^{A*}\left(Q_i^A - Q_j^A\right) \end{bmatrix}; \quad i \neq j \tag{E.17}$$

We clearly see that the gradient is zero if $Q_i^A = Q_j^A$ or $Q_{ij}^A = 0$. Let us consider what happens when $\boldsymbol{c}_i^B = \boldsymbol{0}$ such that $Q_i^A = 1$ for some specific nucleus A. The solution to the above Newton equation is then

$$\begin{bmatrix} \kappa_{ij} \\ \kappa_{ij}^{*} \end{bmatrix} = -\frac{1}{\det G^{[2]}} \begin{bmatrix} 8\left|Q_{ij}^{A}\right|^2 - 4\left(1 - Q_j^A\right)^2 & -8Q_{ij}^{A*}Q_{ij}^{A*} \\ -8Q_{ij}^{A}Q_{ij}^{A} & 8\left|Q_{ij}^{A}\right|^2 - 4\left(1 - Q_j^A\right)^2 \end{bmatrix} \begin{bmatrix} 4Q_{ij}^{A}\left(1 - Q_j^A\right) \\ 4Q_{ij}^{A}\left(1 - Q_j^A\right) \end{bmatrix}, \tag{E.18}$$

where

$$\det G^{[2]} = 16\left(1 - Q_j^A\right)^2 \left(\left(1 - Q_j^A\right)^2 - 2\left|Q_{ij}^{A}\right|^2\right) \tag{E.19}$$

These manipulations are not valid if the gradient is zero, but the result clearly suggests that the Pipek–Mezey algorithm may touch fully localized orbitals.

Appendix F

Complements to Chapter 6

F.1 Rovibrationally-averaged properties

The starting point is the Born–Oppenheimer approximation (also known as the clamped-nuclei approximation) [91], in which the electronic motion is separated from that of the nuclei. Consequently, the rovibrational structure of a diatomic molecule can be determined by solving the Schrödinger equation for an effective Hamiltonian:

$$\left(-\frac{\hbar^2}{2\mu}\frac{d^2}{dr^2} + V(r) + \frac{\hbar^2 J(J+1)}{2\mu r^2}\right)\psi(\mathbf{r}) = E\psi(\mathbf{r}), \tag{F.1}$$

where $\hbar$ is the reduced Planck constant, μ is the reduced mass of the system, r is the internuclear distance, $V(r)$ is the potential energy as a function of r, J is the rotational quantum number ($J = 0, 1, 2, \ldots$), $\psi(\mathbf{r})$ is the rovibrational wavefunction, and E is the total energy of the system.

We rewrite Eq. (F.1) as

$$\left(H_{\text{vib}} + H_{\text{rot}}\right)\psi(\mathbf{r}) = E\psi(\mathbf{r}), \tag{F.2}$$

by identifying

$$H_{\text{vib}} = -\frac{\hbar^2}{2\mu}\frac{d^2}{dr^2} + V(r), \tag{F.3}$$

$$H_{\text{rot}} = \frac{\hbar^2 J(J+1)}{2\mu r^2}. \tag{F.4}$$

For the vibrational part, we expand the potential $V(r)$ in a Taylor series about the equilibrium distance r_e. Defining the displacement as

$$x = r - r_e, \tag{F.5}$$

we have

$$V(r) = V^{[0]}(r_e) + V^{[1]}\,x + \frac{1}{2}V^{[2]}\,x^2 + \cdots, \quad \text{with} \quad V^{[k]} = \left.\frac{d^k V(r)}{dx^k}\right|_{x=0}. \tag{F.6}$$

Since r_e is the minimum of the potential, the first derivative vanishes:

$$V^{[1]} = 0. \tag{F.7}$$

Thus, we define the zero-order vibrational Hamiltonian as

$$H_{\text{vib}}^{(0)} = -\frac{\hbar^2}{2\mu}\frac{d^2}{dx^2} + V^{[0]} + \frac{1}{2}V^{[2]}\,x^2. \tag{F.8}$$

The constant term $V^{[0]}$ simply shifts the energy and may be absorbed into E, so that the essential zero-order vibrational Hamiltonian is that of a harmonic oscillator:

$$H_{\text{vib}}^{(0)} = -\frac{\hbar^2}{2\mu}\frac{d^2}{dx^2} + \frac{1}{2}V^{[2]}\,x^2. \tag{F.9}$$

All higher-order terms (cubic, quartic, etc.) are collected as

$$\sum_{k=1}^{n} H_{\text{vib}}^{(k)} = \sum_{k=1}^{n} \frac{1}{(k+2)!}\,V^{[k+2]}\,x^{k+2}, \quad k \geq 1. \tag{F.10}$$

For the rotational part, we start from the expression

$$H_{\text{rot}} = \frac{\hbar^2 J(J+1)}{2\mu r^2} = \frac{\hbar^2 J(J+1)}{2\mu\,(r_e + x)^2}, \tag{F.11}$$

Expanding the factor $\frac{1}{(r_e+x)^2}$ in powers of x, assuming $|x| \ll r_e$, gives

$$\frac{1}{(r_e+x)^2} = \frac{1}{r_e^2}\left(1 - 2\frac{x}{r_e} + 3\left(\frac{x}{r_e}\right)^2 - 4\left(\frac{x}{r_e}\right)^3 + \cdots\right). \tag{F.12}$$

Thus, the rotational Hamiltonian becomes

$$H_{\text{rot}} = \frac{\hbar^2 J(J+1)}{2\mu\, r_e^2}\left(1 - 2\frac{x}{r_e} + 3\left(\frac{x}{r_e}\right)^2 - 4\left(\frac{x}{r_e}\right)^3 + \cdots\right). \tag{F.13}$$

The zero-order term, corresponding to the rigid rotor approximation, is

$$H_{\text{rot}}^{(0)} = \frac{\hbar^2 J(J+1)}{2\mu\, r_e^2}, \tag{F.14}$$

while the higher-order corrections can be grouped as

$$\sum_{k=1}^{n} H_{\text{rot}}^{(k)} = \frac{\hbar^2 J(J+1)}{2\mu\, r_e^2}\sum_{k=1}^{n}(-1)^k(k+1)\left(\frac{x}{r_e}\right)^k, \quad k \geq 1. \tag{F.15}$$

Again, the rigid-rotor term will be incorporated in the total energy term. In compact form, the full Hamiltonian is expressed as

$$H = \left[H_{\text{vib}}^{(0)} + H_{\text{rot}}^{(0)}\right] + \left[\sum_{k=1}^{n} H_{\text{vib}}^{(k)} + \sum_{k=1}^{n} H_{\text{rot}}^{(k)}\right], \tag{F.16}$$

where the zero-order terms correspond to the harmonic oscillator (vibrational) and rigid rotor (rotational) contributions, and the remaining terms represent the perturbative corrections arising from the Taylor expansions.

Now, assume that the property P depends on the displacement x and can be expanded in a Taylor series about the equilibrium configuration ($x = 0$):

$$P(x) = P_\nu^{[0]} + x\, P^{[1]} + \frac{1}{2}\, x^2\, P^{[2]} + \frac{1}{6}\, x^3\, P^{[3]} + \cdots, \tag{F.17}$$

where

$$P^{[k]} = \left.\frac{d^k P}{dx^k}\right|_{x=0}.$$

The expectation value of P in a given rovibrational state $|v, J\rangle$ is

$$\langle P\rangle_{v,J} = \langle\psi_{v,J}|P(x)|\psi_{v,J}\rangle. \tag{F.18}$$

Assuming that the rovibrational wavefunction separates into a vibrational part (which, in the harmonic approximation, has definite parity) and a rotational part, we can write

$$\langle P\rangle_{v,J} = P_\nu^{[0]} + P^{[1]}\langle x\rangle_{v,J} + \frac{1}{2}P^{[2]}\langle x^2\rangle_{v,J} + \frac{1}{6}P^{[3]}\langle x^3\rangle_{v,J} + \cdots . \tag{F.19}$$

There are several methods to compute expectation values for a given vibrational level ν. A particularly clear method is presented in Griffiths [447]. In that framework the coordinate x is expressed in terms of the creation $a^\dagger$ and annihilation a operators:

$$x = \eta\,(a + a^\dagger), \tag{F.20}$$

with

$$\eta = \sqrt{\frac{\hbar}{2\mu\omega_e}}, \tag{F.21}$$

where ω_e is the vibrational frequency. These operators act as follows:

$$a^\dagger\,|\nu\rangle = \sqrt{\nu+1}\;|\nu+1\rangle\,, \quad a\,|\nu\rangle = \sqrt{\nu}\;|\nu-1\rangle\,. \tag{F.22}$$

where $|\nu\rangle$ are the eigenstates of the harmonic Hamiltonian. Let us now examine the vibrational contributions in the purely harmonic approximation.

For any eigenstate $|\nu\rangle$ of a symmetric potential—such as that of the harmonic oscillator—the expectation value of the position operator vanishes:

$$\langle x\rangle = \int_{-\infty}^{\infty} \psi_\nu^*(x)\, x\, \psi_\nu(x)\, dx = 0. \tag{F.23}$$

This follows from the parity properties of the harmonic oscillator wavefunctions, which are either even or odd:

- If $\psi_\nu(x)$ is even, then $\psi_\nu(-x) = \psi_\nu(x)$,
- If $\psi_\nu(x)$ is odd, then $\psi_\nu(-x) = -\psi_\nu(x)$.

Since the coordinate x is an odd function, the integrand $x\,|\psi_\nu(x)|^2$ is odd for both cases, and thus its integral over symmetric limits vanishes. More generally, any expectation

value involving an odd power of x also vanishes:

$$\langle x^k \rangle_{\nu,J} = 0, \quad \forall\, k = 2n+1, \quad n \in \mathbb{N}. \tag{F.24}$$

The subsequent term to evaluate is the quadratic one:

$$\langle \nu | x^2 | \nu \rangle = \eta^2 \langle \nu | (a + a^\dagger)^2 | \nu \rangle. \tag{F.25}$$

Using the properties of the ladder operators (and noting that only the cross terms contribute because $a^2 \, |\nu\rangle$ and $(a^\dagger)^2 \, |\nu\rangle$ yield states orthogonal to $|\nu\rangle$), one obtains

$$\langle \nu | (a + a^\dagger)^2 | \nu \rangle = 2\nu + 1. \tag{F.26}$$

Thus,

$$\langle \nu | x^2 | \nu \rangle = \eta^2 \, (2\nu + 1) = \frac{\hbar}{\mu \omega_e} \, (\nu + 1/2). \tag{F.27}$$

For the rotational part, we treat it as a small perturbation of the harmonic oscillator. The first-order rotational Hamiltonian correction is

$$H^{(1)}_{\text{rot}} = -\frac{\hbar^2 J(J+1)}{2\mu r_e^3} \, x. \tag{F.28}$$

It is convenient to define

$$\lambda \equiv \frac{\hbar^2 J(J+1)}{\mu r_e^3}, \tag{F.29}$$

so that

$$H^{(1)}_{\text{rot}} = -\lambda \, x. \tag{F.30}$$

Using perturbation theory, the first-order correction to the property P is given by

$$P^{(1)}_\nu = -2 \, \Re \left[\sum_{m \neq \nu} \frac{\langle \nu | x | m \rangle \, \langle m | H^{(1)}_{\text{rot}} | \nu \rangle}{E_\nu - E_m} \right]. \tag{F.31}$$

Since $H^{(1)}_{\text{rot}} = -\lambda \, x$, we have

$$\langle m | H^{(1)}_{\text{rot}} | \nu \rangle = -\lambda \, \langle m | x | \nu \rangle, \tag{F.32}$$

so that

$$P_\nu^{(1)} = -2\lambda \sum_{m\neq\nu} \frac{\langle\nu|x|m\rangle \langle m|x|\nu\rangle}{E_\nu - E_m}. \tag{F.33}$$

For the harmonic oscillator the operator x connects only states that differ by one quantum; thus, the only nonzero matrix elements are

$$\langle\nu|x|\nu+1\rangle = \eta\sqrt{\nu+1} \quad \text{and} \quad \langle\nu|x|\nu-1\rangle = \eta\sqrt{\nu}.$$

Contribution from $m = \nu + 1$:

$$\frac{\langle\nu|x|\nu+1\rangle \langle\nu+1|x|\nu\rangle}{E_\nu - E_{\nu+1}} = -\frac{\eta^2(\nu+1)}{\hbar\omega_e}.$$

Contribution from $m = \nu - 1$:

$$\frac{\langle\nu|x|\nu-1\rangle \langle\nu-1|x|\nu\rangle}{E_\nu - E_{\nu-1}} = \frac{\eta^2\,\nu}{\hbar\omega_e}.$$

Summing these contributions,

$$\sum_{m\neq\nu} \frac{\langle\nu|x|m\rangle \langle m|x|\nu\rangle}{E_m - E_\nu} = -\frac{\eta^2(\nu+1)}{\hbar\omega_e} + \frac{\eta^2\,\nu}{\hbar\omega_e} = -\frac{\eta^2}{\hbar\omega_e}.$$

Thus, the first-order correction is

$$P_\nu^{(1)} = -2\lambda\left(-\frac{\eta^2}{\hbar\omega_e}\right) = \frac{2\lambda\,\eta^2}{\hbar\omega_e} = \frac{\hbar^2 J(J+1)}{\omega_e^2\mu^2 r_e^3}. \tag{F.34}$$

Anharmonicity can be introduced through a cubic force field

$$H^{\text{anh}} = \frac{1}{3}V^{[3]}x^3, \quad V^{[3]} = \frac{d^3E}{dx^3}, \tag{F.35}$$

and treated invoking the perturbation theory machinery.

In the harmonic approximation, rovibrationally averaged properties can be computed as

$$P_{\nu J} = P^{[0]} + P^{[2]}\left(\frac{\hbar}{\mu\omega_e}\right)(\nu+1/2) + P^{[1]}\frac{\hbar^2 J(J+1)}{\mu^2\omega_e^2 r_e^3} - \frac{1}{2}P^{[1]}V^{[3]}\left(\frac{\hbar}{\mu\omega_e}\right)^2\left(\frac{\nu+1/2}{\hbar\omega_e}\right), \tag{F.36}$$

This expression corresponds to that originally derived by Buckingham in the context of temperature-dependent chemical shifts in NMR spectra [448], and now is in the utility program VIBCAL, which is part of the DIRAC code [29]. For a more extensive discussion on the evaluation of rovibrationally averaged properties, we refer the reader to Ref. [449].

Appendix G

Résumé en Français

Introduction

Au milieu des années 1920, les physiciens avaient développé un cadre fondamentalement nouveau pour décrire les atomes : la mécanique quantique, qui traite les électrons comme des entités ondulatoires plutôt que comme des particules classiques. Cette théorie a révolutionné la chimie en fournissant une explication rigoureuse des niveaux d'énergie atomiques, des configurations électroniques et de la nature des liaisons chimiques. Dans ce cadre, la chimie quantique est apparue comme une discipline dédiée à la résolution du problème de la structure électronique avec une précision croissante. L'un de ses objectifs centraux est d'atteindre la plus grande précision possible dans la prédiction théorique des énergies et des propriétés moléculaires. Cette ambition est motivée à la fois par la nécessité de soutenir et d'interpréter les résultats expérimentaux, et par la capacité à fournir des données fiables dans les cas où les expériences sont difficiles, coûteuses ou impossibles à réaliser.

Pour les systèmes contenant des éléments lourds (typiquement au-delà de $Z \approx 40$), cependant, la mécanique quantique non relativiste devient fondamentalement inadéquate. Dans ces atomes, les électrons des couches internes se déplacent à des vitesses proches d'une fraction significative de la vitesse de la lumière, et leur description correcte nécessite l'incorporation des effets relativistes. Si l'on cherche un accord quantitatif avec l'expérience

dans ces systèmes, notamment pour les propriétés spectroscopiques, les longueurs de liaison ou l'énergie, les corrections relativistes ne sont pas optionnelles — elles sont essentielles. La chimie quantique relativiste, basée sur l'équation de Dirac pour les électrons, fournit le cadre théorique approprié pour tenir compte de ces phénomènes. Les contributions relativistes, tant scalaires que spin-orbite, influencent profondément le comportement chimique des composés à éléments lourds, façonnant leur structure, leur liaison, leur réactivité et leurs signatures spectroscopiques. Ignorer ces effets en chimie des éléments lourds conduit à des écarts significatifs par rapport aux résultats expérimentaux et compromet le pouvoir prédictif des calculs quantiques.

Un second pilier essentiel de la chimie quantique de haute précision est le traitement approprié de la corrélation électronique. Dans les systèmes à plusieurs électrons, les électrons se repoussent et ont tendance à s'éviter dynamiquement. La méthode Hartree–Fock (HF) n'incorpore qu'une approximation moyenne de cette répulsion, négligeant les interactions instantanées qui abaissent l'énergie totale lorsque les électrons s'évitent mutuellement. La contribution manquante est connue sous le nom d'*énergie de corrélation*. Pour la récupérer, on utilise des méthodes post-HF. Parmi elles, la théorie Coupled Cluster (CC) est devenue la référence pour atteindre une précision chimique dans les systèmes de petite et moyenne taille. La théorie CC se base sur la fonction d'onde de référence HF en introduisant un opérateur de cluster exponentiel qui inclut systématiquement la corrélation électronique à travers des déterminants excités. Le tronquage de l'expansion au niveau des excitations simples et doubles (CCSD), ou l'inclusion de termes d'ordre supérieur tels que les triples (CCSDT) et quadruples (CCSDTQ), permet une amélioration systématique de la précision. Bien que la théorie CC soit conceptuellement puissante, la mise en œuvre des CC de haut ordre est notoirement difficile. Les équations CC pour CCSDT ou CCSDTQ comprennent des centaines de termes tensoriaux, chacun correspondant à des diagrammes ou des contributions algébriques. Les dériver à la main — algébriquement ou via des diagrammes de Goldstone — est extrêmement fastidieux et sujet à erreurs. Beaucoup de travail a été réalisé pour la construction de générateurs d'équations CC d'ordre général. Récemment, Brandejs et ses collaborateurs ont introduit le Tensor Programming Interface (`tenpi`), un cadre open-source générant systématiquement des équations CC de rang d'excitation arbitraire. `tenpi` utilise l'algèbre symbolique et diagrammatique pour produire un code optimisé pour différents backends tensoriaux (bibliothèques GPU, MPI, etc.). Cette approche a rendu accessibles les CCSDT et CCSDTQ relativistes dans le

programme `DIRAC`.

Il est souvent avancé que les éléments lourds, en raison de leur grand nombre d'électrons, présentent des effets de corrélation électronique prononcés. On pourrait envisager de traiter séparément relativité et corrélation — par exemple en effectuant d'abord un calcul relativiste non corrélé puis en tenant compte de la corrélation. Cependant, de nombreuses études ont montré que ce traitement séquentiel est généralement inadéquat, car relativité et corrélation interagissent de manière fortement couplée et non additive. Ainsi, une théorie appropriée pour les atomes lourds doit traiter simultanément relativité et corrélation, ce qui signifie utiliser un Hamiltonien totalement relativiste (Dirac–Coulomb ou Dirac–Coulomb–Gaunt, etc.) et résoudre le problème des électrons corrélés.

L'équation de Dirac suffit-elle à fournir une description complète de la structure atomique ? Une observation clé, démontrée par Lamb et Retherford dans leur expérience historique, a révélé que les états hydrogéniques $2s_{1/2}$ et $2p_{1/2}$ ne sont pas dégénérés, contrairement aux prédictions de l'équation de Dirac. Cette différence d'énergie, connue sous le nom de décalage de Lamb, ne peut être expliquée par la mécanique quantique relativiste seule. Sa compréhension correcte nécessite la théorie plus complète de l'électrodynamique quantique (QED), qui prend en compte l'interaction entre l'électron et le vide quantique fluctuant ainsi que le champ électromagnétique quantifié. Ces corrections radiatives lèvent la dégénérescence, produisant un petit écart énergétique mesurable expérimentalement et démontrant la nécessité d'aller au-delà de la formalisation de Dirac pour les calculs atomiques de haute précision. Parmi les corrections radiatives introduites par la QED, deux effets principaux se distinguent : la *polarisation du vide* et l'*auto-énergie*. La polarisation du vide modifie le comportement à courte distance du potentiel coulombien via la création virtuelle de paires électron–positron, modifiant ainsi la charge perçue. L'auto-énergie provient de l'interaction de l'électron avec son propre champ électromagnétique quantifié, entraînant des décalages de sa masse et de ses niveaux d'énergie. Ces corrections deviennent de plus en plus significatives pour les atomes lourds. D'un point de vue chimique, les effets QED sont observables : par exemple, pour l'or, les corrections QED sur les potentiels d'ionisation et les affinités électroniques sont comparables en magnitude aux effets de corrélation électronique d'ordre élevé. De plus, les contributions QED réduisent généralement les effets relativistes d'environ 1%. Dans les systèmes moléculaires, des effets QED subtils peuvent aussi être détectés, comme l'écart persistant entre les longueurs

de liaison calculées et expérimentales dans AuCN , attribué à l'absence de contributions QED, hypothèse récemment confirmée par des calculs QED relativistes de pointe.

Beaucoup de chimie repose sur des éléments légers tels que C, H, O, N et quelques autres. On pourrait alors se demander si l'inclusion de corrections élaborées est vraiment nécessaire. Cependant, même pour les atomes légers, atteindre une grande précision exige l'incorporation systématique de plusieurs effets — corrections relativistes, QED, corrélation électronique de haut ordre et contributions du mouvement nucléaire. Cette nécessité est clairement démontrée dans des études récentes de haute précision, comme le travail d'Usov et collaborateurs sur la courbe d'énergie potentielle et le moment dipolaire de CO, où relativité, QED, effets adiabatiques et non-adiabatiques sont tous pris en compte à un niveau élevé de théorie. Comme souligné récemment dans une mini-revue par Saue, *la chimie a besoin de plus de physique.*

Au-delà des énergies totales, l'intérêt se porte sur les propriétés moléculaires — constantes spectroscopiques, polarisabilités, couplages hyperfins, etc. — qui relient théorie et expérience. Une raison principale est que les propriétés calculées peuvent être comparées directement aux mesures, offrant des tests rigoureux de la théorie et des informations prédictives. Cependant, les propriétés dans la théorie CC ne sont pas triviales à calculer. Contrairement aux méthodes variationnelles, l'énergie CC n'est pas un minimum variationnel vrai pour tous les paramètres de la fonction d'onde, donc le théorème de Hellmann–Feynman ne s'applique pas directement. Une approche simple consiste à utiliser des techniques numériques comme les différences finies, évaluant l'énergie à des géométries légèrement perturbées et approximant la dérivée par différences appropriées. Bien que simple à mettre en œuvre, cette méthode est moins précise et coûteuse en calcul. Pour calculer les dérivées analytiques CC, nous utilisons donc le formalisme de Lagrange, qui permet d'obtenir des dérivées précises en résolvant un ensemble linéaire indépendant perturbé pour les multiplicateurs.

L'objectif principal de cette thèse a été la formulation et l'implémentation des premières dérivées analytiques de l'énergie à des niveaux d'excitation arbitraires dans la théorie Coupled Cluster, en utilisant la chaîne d'outils `tenpi`.

Une des propriétés centrales étudiées est le tenseur du gradient de champ électrique

(EFG) aux positions nucléaires. L'EFG est défini comme la dérivée seconde de la potential électrostatique au noyau, ou comme le gradient du champ électrique local. Il quantifie la variation du champ électrique près d'un noyau due aux distributions de charges électroniques et nucléaires. Les noyaux avec un spin nucléaire $I > 1/2$ peuvent posséder un moment quadrupolaire nucléaire (NQM) Q, décrivant l'asymétrie intrinsèque de la distribution de charge nucléaire. Physiquement, le moment quadrupolaire reflète la distribution de charge selon différents axes spatiaux, généralement oblate ou prolate. Ce moment interagit avec l'EFG via un *couplage quadrupolaire*, produisant des décalages et des fractionnements de niveaux nucléaires, mesurables par des techniques expérimentales telles que la résonance quadrupolaire nucléaire (NQR), la spectroscopie Mössbauer, ou la spectroscopie de corrélation angulaire perturbée. Une synthèse complète est fournie par Stone.

L'étude de l'EFG est particulièrement intéressante dans le cadre de cette thèse. L'EFG est extrêmement sensible à la distribution électronique locale, proportionnelle à $\langle r^{-3} \rangle$, et donc très affectée par les effets relativistes. De plus, les couches sphériquement symétriques n'apportent pas de contribution à l'EFG ; selon le théorème d'Unsöld, les couches totalement occupées se comportent comme sphériques et ne contribuent pas. L'EFG est donc très sensible à la structure électronique de valence et à la corrélation électronique, ce qui rend sa description théorique précise particulièrement exigeante.

Pourquoi l'EFG est-il si intéressant ? Deux types d'information peuvent être extraits :

- **Information chimique :** L'EFG d'un noyau est intimement lié à la distribution électronique autour de l'atome, fournissant des informations sur son environnement chimique. Le modèle classique de Dailey et Townes suggère que l'EFG est principalement déterminé par les orbitales p partiellement occupées. Dans les composés halogénés, la contribution dominante provient de l'occupation asymétrique des orbitales p. Cependant, que se passe-t-il pour les éléments lourds où les effets relativistes sont importants et où la couche de valence peut inclure des orbitales au-delà de p ?

- **Information physique :** L'interaction entre le moment quadrupolaire nucléaire (NQM) et l'EFG produit la constante de couplage quadrupolaire (NQCC), mesurable expérimentalement avec précision. Si l'EFG est calculé avec exactitude, la NQCC

mesurée peut être utilisée pour extraire le NQM, propriété nucléaire fondamentale souvent difficile à mesurer directement. Quels effets physiques et chimiques doivent être inclus pour que cette extraction soit fiable ?

Les réponses à ces questions constituent le cœur des résultats présentés dans cette thèse doctorale.

Chapitre 1 : Chimie Quantique Relativiste

Ce chapitre expose les raisons pour lesquelles les effets relativistes doivent être intégrés en chimie quantique et la manière dont ils transforment notre compréhension des systèmes atomiques et moléculaires. Pour les éléments légers, l'approximation non relativiste fournit généralement une description satisfaisante de la structure électronique et des propriétés chimiques. En revanche, pour les atomes lourds, les électrons internes atteignent des vitesses proches de celle de la lumière ; dans ce régime, les modèles classiques deviennent insuffisants et des corrections relativistes s'imposent pour décrire fidèlement la structure électronique, la liaison et la réactivité.

La première partie du chapitre présente les principaux effets observés dans ce contexte. Les *effets scalaires* se traduisent par une contraction prononcée des orbitales s et p, accompagnée d'une expansion relative des orbitales d et f. Ces phénomènes expliquent plusieurs propriétés chimiques remarquables : la couleur jaune de l'or, due à la réduction de l'écart énergétique entre les bandes $5d$ et $6s$; la liquidité du mercure à température ambiante, liée à l'affaiblissement relativiste des liaisons métal–métal ; ou encore la valeur correcte du potentiel électrochimique de la batterie au plomb, qui ne peut être reproduite qu'en incluant les corrections relativistes. Un second effet majeur est le *couplage spin-orbite*, qui couple le moment cinétique orbital et le spin électronique. Ce mécanisme modifie la classification des orbitales atomiques, entraîne un fort mélange des états électroniques et joue un rôle déterminant dans de nombreuses propriétés spectroscopiques et chimiques. Ainsi, il rend compte des décalages RMN observés à proximité des atomes lourds et conduit à une réinterprétation de l'ordre de liaison dans la molécule U_2 lorsque le SOC est pris en compte de façon variationnelle. Ces différents exemples illustrent que, sans la prise en compte explicite des effets relativistes, la description théorique de la chimie des éléments lourds demeure fondamentalement incomplète.

La deuxième section présente la transition de la mécanique newtonienne, basée sur le concept de temps et d'espace absolus et valable dans tous les référentiels inertiels via les transformations galiléennes, vers la relativité restreinte. Les équations de Maxwell révèlent que la vitesse de la lumière c est constante, indépendamment du mouvement de la source ou de l'observateur, ce qui contredit les transformations galiléennes et nécessite un nouveau cadre théorique. En 1905, Einstein propose les principes fondamentaux de la relativité restreinte : les lois de la physique sont identiques dans tous les référentiels inertiels et la vitesse de la lumière c reste la même dans tous les référentiels. Ces principes conduisent aux transformations de Lorentz, qui unissent l'espace et le temps entre référentiels et se réduisent aux transformations galiléennes dans la limite non relativiste $v \ll c$. Elles introduisent des effets tels que la dilatation du temps et la contraction des longueurs, ainsi que des grandeurs relativistes comme la quadrivitesse et la quadrimpulsion, permettant de dériver la célèbre relation énergie-momentum $E^2 = c^2|\mathbf{p}|^2 + m^2c^4$ et de retrouver les expressions classiques pour de faibles vitesses.

La troisième section présente la description relativiste des systèmes microscopiques. De nos jours, la description des atomes et des molécules relève de la mécanique quantique, régie par l'équation de Schrödinger dépendant du temps :

$$i\hbar\frac{\partial}{\partial t}\psi(\mathbf{r},t) = \left(-\frac{\hbar^2}{2m}\nabla^2 + V(\mathbf{r})\right)\psi(\mathbf{r},t),$$

où $\psi(\mathbf{r},t)$ est la fonction d'onde, m la masse de la particule, et $V(\mathbf{r})$ le potentiel. Cette équation n'est pas invariante de Lorentz, car le dérivé temporel est d'ordre un tandis que le Laplacien spatial est d'ordre deux. Pour inclure la relativité, on part de la relation relativiste pour l'énergie et on effectue les substitutions $\mathbf{p} \to -i\hbar\nabla$, $E \to i\hbar\partial/\partial t$, ce qui conduit à l'équation de Klein-Gordon :

$$\left(\Box - \frac{m^2c^2}{\hbar^2}\right)\psi(\mathbf{r},t) = 0, \quad \Box = \frac{1}{c^2}\frac{\partial^2}{\partial t^2} - \nabla^2.$$

Elle est covariante sous transformation de Lorentz et décrit des particules sans spin, avec une densité de courant conservée :

$$j^\mu = \frac{i\hbar}{2m}\left(\psi^*\partial^\mu\psi - \psi\partial^\mu\psi^*\right), \quad \partial_\mu j^\mu = 0.$$

Cependant, les solutions d'énergie négative posent un problème physique, car elles donnent

une densité de probabilité négative. Dirac a proposé de linéariser l'équation relativiste pour obtenir une équation du premier ordre en temps :

$$i\hbar\frac{\partial\psi}{\partial t} = \hat{h}_D\psi, \quad \hat{h}_D = c\,(\boldsymbol{\alpha}\cdot\mathbf{p}) + \beta mc^2,$$

avec des matrices 4×4 α_i et β satisfaisant $\{\alpha_i,\alpha_j\} = 2\delta_{ij}$, $\{\alpha_i,\beta\} = 0$, $\beta^2 = 1$. La fonction d'onde devient un spineur à quatre composantes :

$$\psi(\mathbf{r},t) = \begin{pmatrix} \psi_\alpha^L \\ \psi_\beta^L \\ \psi_\alpha^S \\ \psi_\beta^S \end{pmatrix},$$

où L et S désignent les grandes et petites composantes. La version covariante de l'équation de Dirac s'écrit avec les matrices γ^μ :

$$\left(-i\gamma^\mu\partial_\mu + \frac{mc}{\hbar}\right)\psi = 0, \quad \{\gamma^\mu,\gamma^\nu\} = 2g^{\mu\nu}\mathbb{I}_4.$$

La densité et le courant de Dirac sont :

$$j^0 = c\psi^\dagger\psi, \quad \mathbf{j} = c\psi^\dagger\boldsymbol{\alpha}\psi, \quad \partial_\mu j^\mu = 0.$$

Pour les états stationnaires, la séparation temporelle $\psi(\mathbf{r},t) = e^{-iEt/\hbar}\psi(\mathbf{r})$ conduit à l'équation indépendante du temps :

$$\hat{h}_D\psi(\mathbf{r}) = E\psi(\mathbf{r}), \quad \hat{h}_D = \begin{pmatrix} mc^2 & c\,\boldsymbol{\sigma}\cdot\mathbf{p} \\ c\,\boldsymbol{\sigma}\cdot\mathbf{p} & -mc^2 \end{pmatrix}.$$

Dirac a interprété les états d'énergie négative comme un 'océan' rempli d'électrons : le *Dirac Sea*. Les trous dans ce vide correspondent à des positrons. Cette interprétation prédit l'existence d'antiparticules et permet de conserver la densité de probabilité positive. L'électron et le positon (l'antiparticule de l'électron) peuvent être liés par conjugaison de charge.

Dans la dernière section, nous introduisons le calcul de la structure électronique moléculaire à l'aide de méthodes relativistes. L'approximation de Born–Oppenheimer constitue un point de départ pratique : les noyaux sont considérés comme des sources statiques du

champ électromagnétique, ce qui permet de négliger les effets magnétiques liés au mouvement nucléaire et de poser le potentiel vectoriel $\mathbf{A}(\mathbf{r}) = 0$. Cependant, cette simplification rompt explicitement la covariance de Lorentz, puisque les noyaux sont fixés dans un référentiel privilégié. Des corrections relativistes supplémentaires à l'interaction noyau-noyau peuvent être ajoutées pour affiner cette approximation.

Dans le régime relativiste, l'interaction monoélectronique est décrite par l'hamiltonien de Dirac, qui inclut l'énergie cinétique relativiste et l'interaction électrostatique électron-noyau. L'interaction biélectronique devient plus complexe : au-delà du potentiel de Coulomb instantané, il faut inclure des corrections dépendant de la vitesse et du spin des électrons. L'approximation de Darwin introduit un terme de contact lié à la *Zitterbewegung* de l'électron, tandis que l'opérateur de Breit ajoute les contributions magnétiques et les effets de retard. Ces corrections sont essentielles pour décrire correctement les interactions dans les atomes lourds, bien que l'opérateur résultant ne soit pas entièrement invariant de Lorentz.

La résolution variationnelle de l'équation de Dirac pour plusieurs électrons rencontre un obstacle fondamental : l'hamiltonien n'est pas borné inférieurement en raison des solutions à énergie négative, ce qui peut conduire à un *effondrement variationnel*. Pour contourner ce problème, on applique le principe du minimax et l'approximation *no-pair*, qui projette les états d'énergie négative hors de l'espace de Hilbert, permettant ainsi une optimisation variationnelle sûre des solutions électroniques.

L'expansion en base linéaire de fonctions atomiques ($LCAO$) reste un outil central, mais doit être adaptée pour respecter la *condition d'équilibre cinétique* (*kinetic balance*). Celle-ci relie les fonctions petites et grandes composantes de l'onde électronique, garantissant que l'énergie cinétique relativiste converge correctement vers la limite non-relativiste lorsque $c \to \infty$. Si cette condition n'est pas respectée, l'énergie cinétique peut être sous-estimée, conduisant à des résultats incorrects.

Les méthodes Hartree–Fock et DFT peuvent être généralisées au cadre relativiste. Dans ce contexte, l'opérateur de Fock inclut l'hamiltonien de Dirac et les interactions biélectroniques moyenne-champ. Les orbitales sont représentées par des spinors à quatre composantes, et la solution des équations HF ou DFT se fait de manière auto-cohérente, tout en respectant les contraintes de *kinetic balance* et, si nécessaire, en excluant les couples électron-positron via l'approximation *no-pair*.

Pour réduire la complexité et faciliter les calculs, des méthodes à deux composantes ont été développées, parmi lesquelles la transformation exacte à deux composantes (*X2C*) est particulièrement notable. Cette approche permet de projeter rigoureusement les quatre composantes de Dirac sur un espace à deux composantes électroniques, tout en préservant les effets relativistes principaux, comme le couplage spin-orbite et les corrections de masse cinétique. X2C offre ainsi un compromis optimal entre précision et coût computationnel, permettant l'application de méthodes de chimie quantique avancées à des systèmes contenant des atomes lourds.

Chapitre 2 : Théorie Coupled Cluster

Ce chapitre présente la méthode Coupled Cluster (CC) à référence unique, ses équations fondamentales et les techniques diagrammatiques pour les méthodes de haut ordre.

Un défi central en chimie quantique est la description correcte de la corrélation électronique. Les électrons interagissent via la force de Coulomb, ce qui les pousse à s'éviter spatialement. La théorie Hartree–Fock (HF) approxime la fonction d'onde par un seul déterminant de Slater, chaque électron se déplaçant indépendamment dans un champ moyen V_{eff} généré par les autres. Cette approche capture partiellement l'effet du principe d'exclusion de Pauli (corrélation d'échange) mais néglige la corrélation dynamique, menant à l'énergie de corrélation :

$$E_{\text{corr}} = E_{\text{exact}} - E_{\text{HF}}.$$

La corrélation électronique se divise en :

1. *Corrélation statique* : importante lorsque plusieurs configurations électroniques contribuent significativement à l'état fondamental (ex. dégénérescence, dissociation de liaisons), nécessitant des méthodes multi-références.

2. *Corrélation dynamique* : ajustements rapides et de courte portée dus à la répulsion coulombienne instantanée, même pour des systèmes bien décrits par un seul déterminant.

Une des premières méthodes pour traiter la corrélation au-delà de HF est l'*Interaction de Configurations* (CI), où la fonction d'onde est une combinaison linéaire de déterminants

excités :

$$|\Psi_{\mathrm{CI}}\rangle = c_0|\Phi_0\rangle + \sum_{i,a} c_i^a|\Phi_i^a\rangle + \sum_{i<j,a<b} c_{ij}^{ab}|\Phi_{ij}^{ab}\rangle + \cdots$$

Le *Full CI* inclut toutes les excitations possibles et constitue la référence exacte pour un ensemble de base donné. Cependant, le nombre de déterminants croît combinatoirement, limitant son applicabilité. Les méthodes CI tronquées (ex. CISD) ne sont pas extensives ni consistantes en taille, car elles manquent de factorisation multiplicative correcte pour des systèmes non-interactifs. La théorie *Coupled Cluster* (CC) résout ce problème via une ansatz exponentielle :

$$|\Psi_{\mathrm{CC}}\rangle = e^{\hat{T}}|\Phi_0\rangle, \quad \hat{T} = \hat{T}_1 + \hat{T}_2 + \hat{T}_3 + \cdots,$$

où $\hat{T}_n$ génère les excitations de rang n. Pour deux sous-systèmes non-interactifs A et B, on a

$$|\Psi_{\mathrm{CC}}^{AB}\rangle = |\Psi_{\mathrm{CC}}^{A}\rangle \wedge |\Psi_{\mathrm{CC}}^{B}\rangle,$$

démontrant que CC est extensif et consistant en taille, même lorsqu'on tronque $\hat{T}$ (ex. CCSD).

Dans la troisième section, la méthode CC et les équations CC sont dérivées et discutées de manière critique. On présente les concepts d'excitations *connectées* et *déconnectées* et on discute l'approche variationnelle, en soulignant ses limites. Pour surmonter les limites de l'approche variationnelle, les équations CC sont dérivées par projection. On introduit l'Hamiltonien *similaire* :

$$\bar{H} = e^{-\hat{T}}\hat{H}e^{\hat{T}},$$

et l'énergie et les amplitudes sont déterminées en résolvant

$$\langle\Phi_\mu|\bar{H}|\Phi_0\rangle = E\delta_{\mu 0}.$$

L'expansion de Baker-Campbell-Hausdorff (BCH) :

$$\bar{H} = \hat{H} + [\hat{H},\hat{T}] + \frac{1}{2}[[\hat{H},\hat{T}],\hat{T}] + \frac{1}{3!}[[[\hat{H},\hat{T}],\hat{T}],\hat{T}] + \frac{1}{4!}[[[[\hat{H},\hat{T}],\hat{T}],\hat{T}],\hat{T}],$$

permet de garantir une forme close des équations CC. L'utilisation de l'ordre normal et du théorème de Wick simplifie considérablement la dérivation des équations, mais pour

les méthodes CC à haut ordre, le nombre de contractions et de diagrammes devient rapidement très important, rendant la dérivation manuelle extrêmement complexe.

Les équations CC peuvent être formulées dans le cadre diagrammatique. Dans cette thèse, nous utilisons le formalisme diagrammatique de Goldstone antisymétrisé, tel que développé et popularisé par Kucharski et Bartlett. Dans cette quatrième section, l'approche diagrammatique en théorie CC est introduite, avec discussion de son utilité et de ses règles de construction. Les diagrammes permettent de représenter visuellement les contributions des excitations connectées et déconnectées, et facilitent la dérivation systématique des équations CC.

La cinquième section est consacrée à la définition des intermédiaires dans la théorie CC. Ces intermédiaires sont des combinaisons de tenseurs et de contributions aux amplitudes qui apparaissent fréquemment dans les équations CC. Grâce à leur définition, il est possible de factoriser certaines sommes et produits de tenseurs, ce qui permet de réduire de manière significative le coût de calcul, en évitant la répétition de sous-expressions complexes. Cette approche optimise l'évaluation des amplitudes et de l'énergie CC, en particulier pour les méthodes d'ordre élevé telles que CCSDT ou CCSDTQ. L'utilisation systématique des intermédiaires est essentielle pour rendre la théorie CC applicable à des systèmes de taille réaliste, tout en conservant l'exactitude des calculs.

Enfin, le chapitre aborde les excitations d'ordre élevé et présente *tenpi*, l'interface de programmation tensorielle utilisée pour implémenter et tester des méthodes Coupled Cluster avancées dans des codes modernes.

Chapitre 3 : Propriétés Moléculaires

Dans le troisième chapitre, les propriétés moléculaires statiques sont introduites, telles que moments dipolaires et polarisabilités, en lien avec les observables expérimentales. L'évaluation à partir de fonctions d'onde variationnelles est d'abord présentée, puis le cas des fonctions d'onde non-variationnelles, comme en théorie Coupled Cluster (CC), est abordé via les équations Λ et le formalisme lagrangien. Les techniques diagrammatiques CC sont soulignées pour leur efficacité dans le calcul systématique des propriétés moléculaires.

La première section est consacrée à la définition des propriétés moléculaires statiques à travers la perturbation d'un système. Ces propriétés peuvent être exprimées comme des dérivées de l'énergie par rapport à la perturbation, c'est-à-dire via un développement de Taylor de l'énergie. Un examen critique des méthodes numériques et analytiques pour le calcul de ces dérivées est présenté, en passant par le théorème de Hellmann-Feynman. L'approche analytique est retenue, mais elle soulève le problème que le théorème de Hellmann-Feynman n'est strictement valable que pour des fonctions d'onde exactes. La *variational perturbation theory* est alors introduite, permettant, pour des fonctions d'onde variationnelles, de calculer les dérivées premières de l'énergie directement via le théorème de Hellmann-Feynman.

La deuxième section traite du calcul des dérivées de l'énergie pour des méthodes non variationnelles, telles que la théorie Coupled Cluster (CC). Une différentiation directe de l'énergie nécessiterait de connaître la réponse des amplitudes à la perturbation, ce qui est très coûteux en termes de calcul. L'approche lagrangienne est alors introduite : en imposant la stationnarité de la lagrangienne par rapport aux amplitudes et aux multiplicateurs de Lagrange, il devient possible de calculer les dérivées premières de l'énergie CC via le théorème de Hellmann-Feynman. Cette approche nécessite toutefois la résolution d'un ensemble supplémentaire d'équations, les λ-équations,

$$\frac{\partial L_{\mathrm{CC}}}{\partial t_\mu} = 0 \quad \Rightarrow \quad \text{équations } \Lambda.$$

Ces dernières sont dérivées avec une attention particulière portée à l'utilisation de la formalisation diagrammatique. Le chapitre se conclut par une discussion sur le calcul des valeurs d'attente CC et l'introduction des matrices densité CC à un corps, qui, pour les méthodes CC tronquées, sont en général non hermitiennes.

Chapitre 4 : Interaction quadrupolaire électrique nucléaire

Le quatrième chapitre aborde l'interaction entre le moment quadrupolaire électrique des noyaux et le champ électrique créé par les électrons et les autres noyaux dans une molécule. Cette interaction est essentielle pour comprendre certains aspects de la spectroscopie nucléaire, en particulier la résonance magnétique nucléaire (RMN) des noyaux ayant un spin $I \geq 1$.

Dans la première section, on introduit l'interaction d'une distribution de charge électrique avec un potentiel électrostatique généré par une autre source. Le développement en multipôles est utilisé pour décomposer l'énergie d'interaction électrostatique en une somme d'interactions individuelles, dans laquelle, en poursuivant le développement, les contributions diminuent de plus en plus. On met ici en évidence l'interaction de second ordre, c'est-à-dire celle entre le moment quadrupolaire électrique et le gradient du champ électrique, dont la forme usuelle est

$$E_{E_2} = -\frac{1}{2}\sum_{\alpha\beta} Q_{\alpha\beta}\mathcal{E}^{[1]}_{\alpha;\beta}(\mathbf{0}).$$

La section suivante est consacrée au cas spécifique de l'interaction entre le moment quadrupolaire électrique nucléaire (généré par une distribution de charge localisée sur un certain noyau K) et le potentiel électrostatique généré par les charges autour du noyau considéré (électrons et autres noyaux). Pour les systèmes atomiques ou linéaires, cette énergie d'interaction prend une forme simple :

$$E_{E2}\left(I, m_I\right) = \frac{e^2 qQ}{4I\left(2I-1\right)}\left[3m_I^2 - I\left(I+1\right)\right]$$

où I est le nombre quantique de moment angulaire nucléaire, m_I est la projection du moment angulaire nucléaire sur un axe choisi, eQ est le moment quadrupolaire électrique nucléaire, eq est le gradient du champ électrique créé par les charges environnantes au niveau du noyau, e est la charge élémentaire. Une extension est également fournie pour les systèmes à symétrie non linéaire, où il est nécessaire d'introduire le paramètre d'asymétrie qui quantifie l'écart par rapport à la linéarité.

La dernière section s'attache à introduire et à décrire de manière critique le modèle de Dailey-Townes, un modèle proposé pour extraire des informations chimiques à partir de la connaissance du gradient de champ électrique évalué aux positions nucléaires. Ce modèle repose sur l'hypothèse principale selon laquelle les couches de symétrie sphérique ne contribuent pas au gradient de champ électrique. Ainsi, les orbitales s, de même que les orbitales de cœur occupées (théorème d'Unsöld), ne peuvent pas contribuer au gradient de champ électrique. Par conséquent, leur hypothèse est que la majorité de la contribution au gradient de champ électrique provient des orbitales p non occupées.

Ce modèle a donc été ré-analysé dans cette thèse en utilisant l'analyse par projection, qui exprime les orbitales moléculaires comme une combinaison linéaire d'orbitales atomiques (LCAO),

$$|\psi_i^{MO}\rangle = \sum_A \sum_{p\in A} c_{p,i}^A |\psi_p^A\rangle + |\psi_i^{\text{pol}}\rangle$$

en utilisant un ensemble d'orbitales atomiques occupées pré-calculées. Comme nous n'utilisons que les orbitales occupées, tout ce qui n'est pas inclus dans cet ensemble correspond au complément orthogonal de la base, appelé contribution de polarisation.

Dans ce formalisme, une valeur d'espérance peut être décomposée en contributions intra-atomiques (provenant du même atome), inter-atomiques (provenant de plusieurs centres) et en contributions de polarisation

$$\langle\hat{\Omega}\rangle = \sum_A \langle\hat{\Omega}\rangle_{\text{intra}}^{(A)} + \sum_A \sum_{B\neq A} \langle\hat{\Omega}\rangle_{\text{inter}}^{(A,B)} + \langle\hat{\Omega}\rangle_{\text{pol}}.$$

La contribution intra-atomique peut elle-même être décomposée en contributions principales (diagonales) et de hybridation (non-diagonales).

Cette approche a ainsi été utilisée pour analyser le gradient de champ électrique aux positions nucléaires, montrant que le modèle de Dailey-Townes n'est rien d'autre qu'un cas spécifique (approximatif) de notre analyse par projection plus générale

$$\langle e\hat{q}_K\rangle \approx \langle e\hat{q}_K^e\rangle_{\text{intra}}^{(K)} \approx \frac{2e}{4\pi\varepsilon_0}\langle r^{-3}\rangle_{np} \times \frac{2}{5}\left(n_x + n_y - 2n_z\right); \quad n_\alpha = D_{np_\alpha;np_\alpha}^{KK},$$

Nous présentons ensuite une discussion critique sur l'extension relativiste, dans laquelle, en présence de l'accouplement spin-orbite, le gradient de champ électrique n'est plus diagonal.

Chapitre 5 : Au-delà du modèle de Dailey-Townes : informations chimiques à partir du gradient de champ électrique

L'objectif principal de ce travail est l'analyse critique et la réévaluation du modèle de Dailey-Townes pour l'interprétation du gradient du champ électrique (EFG) évalué aux positions nucléaires. En effet, les noyaux possédant un nombre quantique de spin nucléaire I supérieur à 1/2 possèdent un moment de quadrupôle électrique nucléaire qui s'accole

avec le gradient du champ électrique généré par les particules voisines (électrons et noyaux). Dailey et Townes ont démontré comment l'EFG peut être utilisé pour extraire des informations de nature chimique, telles que la nature d'une liaison chimique. L'EFG est en effet hautement sensible à la déformation orbitale, comme lors de la formation de liaisons chimiques, car les couches avec une symétrie sphérique ne contribuent pas à l'EFG. Cela s'applique aux orbitales s (qui sont sphériquement symétriques) ainsi qu'aux orbitales de cœur occupées qui, conformément au théorème d'Unsöld, deviennent également sphériquement symétriques. De ce fait, Dailey et Townes arrivent à la conclusion, basée sur les systèmes légers analysés dans leur travail (principalement des halogènes), que la contribution prédominante à l'EFG est donnée par les orbitales p non entièrement occupées, tandis que toutes les autres orbitales, ainsi que les atomes autour du noyau étudié, ne contribuent pas à l'EFG.

Cependant, leur modèle ne tient pas compte de plusieurs aspects. Premièrement, il suppose que les orbitales de valence sont de type p. Or, les métaux de transition et les éléments du bloc f ont une structure électronique de valence plus complexe, qui inclut également des orbitales de type d et f. De plus, ils négligent complètement les effets relativistes, qui doivent être inclus pour une description plus réaliste, notamment en présence d'éléments lourds. Enfin, ils négligent totalement les effets liés à la polarisation. Par conséquent, dans ce travail, nous avons étudié et analysé de manière critique le modèle de Dailey-Townes en utilisant la méthode DFT relativiste combinée à l'analyse par projection. Pour commencer, nous nous sommes concentrés sur les systèmes étudiés par Dailey-Townes dans leur travail original, en analysant l'EFG évalué à la position de ^{35}Cl dans divers systèmes moléculaires.

Nous avons analysé l'information chimique que l'on peut extraire du gradient de champ électrique (EFG) dans une série de composés du chlore (Cl_2, ICl, ClCN, CH_3Cl, NaCl), dont plusieurs figuraient déjà dans l'article original de Dailey et Townes. L'étude de l'atome de chlore isolé confirme le théorème d'Unsöld : la somme des contributions intra-coquille s'annule, tandis que les valeurs des éléments de matrice sont cohérentes avec les valeurs attendues de $\langle r^{-3} \rangle$ pour les orbitales 2p et 3p. Pour les molécules ClX, classées par différence d'électronégativité $\Delta\chi_{Cl-X}$, les calculs montrent que l'EFG décroît avec l'augmentation du transfert de charge vers le chlore, tendant vers zéro dans le cas limite de l'anion Cl^-. Ce comportement est correctement reproduit par les valeurs totales eq_{Cl}, mais le modèle de Dailey–Townes (eq_{Cl}^{DT}) échoue souvent à prédire la tendance et présente

des écarts significatifs. Une analyse détaillée de la molécule ICl révèle que, contrairement à l'interprétation de Dailey et Townes basée sur une forte hybridation s, l'orbitale de liaison σ est presque exclusivement constituée des orbitales p_z de l'iode et du chlore. Le recours aux populations brutes (au lieu des populations nettes) améliore l'accord avec les valeurs calculées, ce qui rejoint partiellement les arguments de Gordy. La décomposition par analyse de projection met en évidence plusieurs contributions au-delà du modèle de Dailey–Townes :

- une contribution intra-atomique notable de l'iode, presque entièrement compensée par la contribution nucléaire correspondante;
- une contribution d'hybridation du chlore, due à un faible mélange avec l'orbitale $2\mathrm{p}_z$ mais amplifiée par de grands éléments de matrice ;
- une contribution de polarisation significative, interprétée comme une mesure de la déformation des densités atomiques lors de la formation de la molécule.

En outre, l'analyse relativiste montre que les corrections scalaires ne modifient pas qualitativement l'interprétation, tandis que l'accouplement spin-orbite rompt la diagonale de l'opérateur EFG dans la base du moment angulaire atomique. Dans ce contexte, le mélange entre orbitales $p_{1/2}$ et $p_{3/2}$ devient essentiel : bien que les orbitales $p_{1/2}$ aient une densité sphérique et ne contribuent pas directement à l'EFG, elles interviennent de manière indirecte par hybridation. Ce mécanisme conduit à une inversion des contributions principale et d'hybridation observées dans l'analyse par projection, phénomène absent du modèle de Dailey–Townes mais crucial pour les systèmes contenant des atomes lourds comme l'iode.

L'étude de l'ion uranyle $\mathrm{UO_2}^{2+}$ a permis d'aller au-delà du modèle de Dailey–Townes grâce à une analyse détaillée de sa structure électronique et de son gradient de champ électrique (EFG). Nos calculs montrent la présence d'une lacune marquée dans les orbitales U($6p$), confirmant l'hypothèse de Larsson et Pyykkö, et soulignent une hybridation significative avec les orbitales O($2s$) et O($2p$). Par ailleurs, les orbitales U($5f$) et U($6d$) présentent des occupations partielles, indiquant une participation directe de ces orbitales à la liaison. L'inclusion du couplage spin-orbite localise l'essentiel de la lacune sur l'orbitale U($6p_{3/2}$), tout en réduisant son implication dans les orbitales de liaison. L'analyse en termes d'orbitales localisées (critère de Pipek–Mezey) suggère la présence

de liaisons triples entre l'uranium et chacun des oxygènes, principalement portées par les orbitales U($5f$)/U($6d$) et O($2p$), mais avec une contribution non négligeable de U($6p$). Cette contribution diminue cependant de façon marquée lorsque l'on prend en compte les effets de spin-orbite, soulignant l'importance de ce dernier pour décrire correctement les systèmes lourds. En ce qui concerne l'EFG au noyau de l'uranium, la décomposition présentée dans la Table G.1 révèle plusieurs aspects importants. La contribution intra-atomique est relativement faible et résulte d'une compensation entre les termes principaux et d'hybridation. On remarque que ces contributions changent de signe avec l'activation du couplage spin-orbite (SO), inversant ainsi leur rôle relatif dans la valeur totale de l'EFG. Les contributions inter-atomiques, telles que celles entre l'uranium et les oxygènes (O_1-U et O_2-U) ou entre O_1-O_2, restent limitées, tandis que la polarisation électronique domine largement l'EFG total.

			sans SO	avec SO
intra-atomique	U	Principal	2.093	-3.501
		Hybridation	-2.673	2.365
	O_1	Principal	-0.457	-0.454
		Hybridation	0.021	0.018
	O_2	Principal	-0.457	-0.454
		Hybridation	0.021	0.018
inter-atomique	O_1-U		0.296	0.299
	O_2-U		0.296	0.299
	O_1-O_2		-0.002	-0.002
	Total		0.590	0.596
Polarisation			-6.400	-6.813
Total électronique			-7.262	-8.226
Total nucléaire			0.958	
EFG total			-6.304	-7.269

TABLE G.1: Décomposition de l'EFG au niveau du noyau d'uranium dans $UO_2{}^{2+}$, avec et sans couplage spin-orbite (SO). Toutes les valeurs sont exprimées en E_h/ea_0^2.

Chapitre 6 : Valeurs d'espérance hautement précises grâce à la théorie des couplages en cluster relativistes d'ordre élevé

L'objectif principal de ce travail est la génération automatique des dérivées premières analytiques de l'énergie pour des modèles de clusters couplés à l'aide de la chaîne d'outils tenpi. L'article se concentre sur l'implémentation des valeurs attendues pour les méthodes CCSDT et CCSDTQ dans le progiciel DIRAC pour les calculs moléculaires relativistes.

L'objectif principal de cette recherche est l'extraction des moments quadripolaires électriques nucléaires (MQEN), une propriété fondamentale décrivant la déviation de la distribution de charge nucléaire par rapport à une symétrie sphérique parfaite. L'étude se concentre sur le gradient de champ électrique (GCE), une quantité cruciale pour déterminer les MQEN, qui est très sensible aux effets relativistes et de corrélation électronique. Les contributions des excitations au-delà des doubles (triples et quadruples) peuvent être nécessaires pour obtenir une description précise de la propriété cible. Le besoin d'un programme d'ordre général est né de la complexité de la programmation explicite des divers éléments de matrice associés aux excitations supérieures. Ce travail vise à développer et à mettre en œuvre des valeurs attendues de clusters couplés relativistes d'ordre supérieur, en se concentrant sur les méthodes CCSDT et CCSDTQ, à l'aide de la chaîne d'outils tenpi pour la génération d'équations.

Les équations et les codes optimisés ont été générés via la chaîne d'outils `tenpi`. Les équations de Λ sont générées directement à partir des éléments de matrice contenant l'Hamiltonien transformé par similarité et l'opérateur $\hat{\Lambda}$. Les diagrammes Λ sont obtenus en ajoutant simplement $\hat{\Lambda}$ aux diagrammes d'amplitude, ce qui préserve la structure originale et simplifie la génération. Pour les matrices densité, l'opérateur un électron est remplacé par un opérateur factice $\hat{F}$ lors de la génération des diagrammes, puis retiré après traitement. Pour les excitations triples et quadruples, la règle des lignes équivalentes est étendue : un groupe de n lignes équivalentes contribue avec un facteur $1/n!$ à la représentation algébrique, garantissant des préfacteurs corrects pour les contractions complexes. Lors de l'optimisation des intermédiaires, des préfacteurs non entiers peuvent provoquer des instabilités. La solution consiste à mettre à l'échelle toutes les contractions par le plus petit commun multiple des dénominateurs, puis à revenir à l'échelle originale après optimisation.

Tous les calculs ont été réalisés avec des versions de développement de DIRAC et de la bibliothèque TAL-SH. Nous avons utilisé principalement l'Hamiltonien exact à deux composantes (X2C) avec correction du champ moyen moléculaire et un modèle gaussien des noyaux. Les intégrales Gaunt et la classe $\langle$SS|SS$\rangle$ ont été incluses au niveau SCF.

La validation du code pour les valeurs d'attente CC a été effectuée en comparant CCSD généré automatiquement avec l'implémentation manuelle, puis CCSDT et CCSDTQ ont été comparés avec MRCC non relativiste. L'espace actif est défini par AS(k,n), k étant

le nombre d'électrons et n le nombre de paires de Kramers actives, ordonnées par énergie orbitale.

Pour LiX (X = H, F, Cl), tous les électrons ont été corrélés au niveau CCSD avec la base dyall.ae4z augmentée par un p et un d tight. Pour AlY (Y = H, F, Cl, Br), des bases plus larges ont été utilisées pour CCSD, puis des bases plus petites (dyall.v3z) pour estimer les corrections triples et quadruples. Les EFGs sont optimisés en ajustant les exposants de manière even-tempered, en omettant les fonctions s car leur contribution est négligeable et quasi annulée par la symétrie et les contributions nucléaires.

Les corrections triples (T) et quadruples (Q) sont estimées via des calculs sur bases réduites et ajoutées aux valeurs CCSD obtenues avec une grande base :

$$\langle\Omega\rangle_{\mathrm{Q(T(CCSD))}} = \langle\Omega\rangle_{\mathrm{CCSD}}^{\text{opt-basis}} + T + Q.$$

Pour les systèmes LiX, tous les électrons sont corrélés, tandis que pour AlY, un seuil d'énergie limite la sélection des orbitaux virtuels pour éviter des oscillations importantes des EFGs dues aux orbitales de type p polarisées. Les espaces actifs utilisés pour chaque méthode et molécule sont résumés dans le tableau correspondant, indiquant le nombre d'électrons corrélés et de paires de Kramers. Les moments quadrupolaires nucléaires sont extraits par régression linéaire en intégrant les incertitudes expérimentales et théoriques.

Pour vérifier la validité de notre code tenpi pour le calcul des valeurs d'attente couplées en cluster à haut ordre, nous avons comparé le moment dipolaire de l'état fondamental de LiH avec les résultats du package MRCC et l'implémentation manuelle de DIRAC. Au niveau SCF, tous les codes donnent des valeurs pratiquement identiques, établissant une base solide pour les méthodes corrélées. Pour le CCSD, le code tenpi et l'implémentation manuelle de DIRAC produisent exactement le même résultat, tandis que MRCC montre une différence négligeable ($\sim 10^{-8}$). Les niveaux de théorie plus élevés, CCSDT et CCSDTQ, confirment un excellent accord entre tenpi et MRCC, démontrant la cohérence et la fiabilité de notre approche.

Nous avons ensuite étudié le moment quadrupolaire de ^{7}Li. L'inclusion de la corrélation électronique via CCSD modifie légèrement les valeurs HF de l'EFG pour LiH, LiF et LiCl. L'ajout des excitations triples (CCSDT) affine davantage les résultats, tandis que les quadruples ont un effet négligeable, indiquant que les corrélations d'ordre supérieur aux

triples sont minimes. Les effets vibrationnels, bien que modestes, entraînent des ajustements significatifs : par exemple, pour LiH, la valeur moyenne vibrationnelle de l'EFG réduit la magnitude d'environ 2,5%, ce qui augmente le moment quadrupolaire absolu de 2,6%. Une régression linéaire des constantes de couplage quadrupolaire expérimentales par rapport aux EFG calculés fournit un moment quadrupolaire $Q(^7\mathrm{Li}) = -0.0386$ b, en parfait accord avec les mesures récentes de Guan et coll., mais légèrement inférieur à la valeur acceptée précédemment (-0.0406 b). Les différences avec les travaux antérieurs proviennent principalement d'une meilleure description de la base et d'un traitement complet des excitations triples. Enfin, nous avons déterminé le moment quadrupolaire de ^{27}Al. Pour ^{27}Al, l'inclusion de la corrélation CCSD améliore significativement les valeurs HF de l'EFG et du moment quadrupolaire. Les excitations triples apportent des corrections non négligeables (environ 1 mb), tandis que les quadruples ont un effet plus faible mais encore pertinent pour les systèmes légers. L'inclusion des effets vibrationnels est également essentielle pour obtenir des valeurs précises. Une régression linéaire des constantes de couplage quadrupolaire expérimentales sur les EFG calculés donne $Q(^{27}\mathrm{Al}) = 0.1466$ b, en excellent accord avec les références précédentes, confirmant la fiabilité de notre approche qui inclut à la fois les effets relativistes et la convergence de la base.

Chapitre 7 : Le moment quadrupolaire électrique nucléaire de ^{87}Sr à partir de calculs moléculaires relativistes de très haute précision

Le moment quadrupolaire nucléaire (NQM) constitue une sonde sensible de la distribution de charge à l'intérieur du noyau et renseigne sur les déviations par rapport à la symétrie sphérique. Contrairement au moment dipolaire, il ne peut être déterminé directement par des mesures expérimentales simples, mais peut être extrait à partir de l'interaction entre le moment quadrupolaire nucléaire et le gradient de champ électrique (EFG) généré par la distribution électronique et les noyaux environnants. Cette interaction est mesurée expérimentalement par la constante de couplage quadrupolaire nucléaire (NQCC). La combinaison de NQCC expérimentales avec des EFG calculés de manière fiable constitue une approche indirecte robuste pour la détermination du NQM, généralement moins sujette aux erreurs systématiques que les méthodes purement atomiques.

Pour le strontium ($Z = 38$), seul l'isotope ^{87}Sr possède un moment quadrupolaire nucléaire non nul, ce qui en fait un noyau d'intérêt particulier pour les horloges optiques et les expériences de métrologie de haute précision. Les valeurs précédemment proposées pour $Q(^{87}\mathrm{Sr})$ incluent celle de Sahoo *et al.* (0.305(2) b), ainsi que la révision plus récente de Lu *et al.* (0.328(4) b), obtenue à partir de calculs atomiques multiconfigurationnels relativistes. Toutefois, aucune détermination reposant sur des constantes de couplage quadrupolaire moléculaires récentes et combinée à des calculs moléculaires relativistes de très haute précision n'avait été réalisée jusqu'à présent.

Dans ce travail, le moment quadrupolaire nucléaire de ^{87}Sr est déterminé à partir de deux systèmes moléculaires distincts, SrO et SrS, en combinant des NQCC expérimentales avec des gradients de champ électrique calculés à différents niveaux de corrélation électronique. Les calculs ont été réalisés avec le programme DIRAC, en utilisant un Hamiltonien relativiste exact à deux composantes de type X2Cmmf. Les effets relativistes scalaires, le couplage spin-orbite ainsi que l'interaction à deux électrons de Gaunt ont été explicitement inclus. Des corrections vibrationnelles ont également été prises en compte.

La corrélation électronique a été traitée de manière systématique à l'aide de méthodes de type coupled-cluster, incluant CCSD, CCSD(T), CCSD-T et CCSD$\tilde{\mathrm{T}}$. L'impact des excitations triples a été soigneusement analysé, tant sous forme perturbative qu'itérative. Grâce au développement récent d'une infrastructure parallèle multi-nœuds pour le calcul d'énergies et de valeurs d'espérance à haut ordre, reposant sur l'interface TAPP reliant la bibliothèque Cyclops Tensor Framework (CTF) au programme DIRAC, il a été possible d'élargir significativement les espaces actifs accessibles. Les résultats montrent que l'inclusion des excitations triples est indispensable pour une description fiable des EFG dans SrO et SrS.

Afin d'évaluer la cohérence interne des différentes approximations des triples, une analyse basée sur la déviation absolue moyenne (MAD) a été menée. Cette analyse indique que la méthode CCSD(T) fournit la description la plus stable et la plus cohérente des EFG pour les systèmes étudiés. Cette performance est attribuée au fait que les espaces actifs employés sont suffisamment larges pour assurer la convergence des EFG, tandis que les calculs CCSD$\tilde{\mathrm{T}}$ restent limités par l'absence actuelle de la symétrie de groupe ponctuel dans le module ExaCorr.

La valeur finale recommandée issue de ce travail est $Q(^{87}\mathrm{Sr}) = 0.33666 \pm 0.00258$ b. Cette estimation est légèrement supérieure à celle proposée par Lu *et al.*, mais elle est en excellent accord avec la valeur récemment obtenue par Tang (0.336(4) b) à partir d'une approche atomique hybride CI+CC. Le fait que des méthodes atomiques et moléculaires fondamentalement différentes convergent vers une valeur quasi identique renforce la robustesse et la fiabilité de la détermination actuelle du moment quadrupolaire nucléaire de ^{87}Sr. Ce travail met ainsi en évidence le rôle clé des calculs moléculaires relativistes de haute précision pour l'extraction de paramètres nucléaires fondamentaux.

Chapitre 8 : Résumé, conclusions et perspectives

Cette thèse de doctorat est consacrée à l'implémentation des valeurs d'espérance à ordres élevés de la théorie des Coupled Cluster, avec un accent particulier sur la détermination précise du gradient de champ électrique (EFG). Le travail est structuré en deux parties: la Partie I (*Théorie*) présente les concepts fondamentaux et les développements méthodologiques, tandis que la Partie II (*Applications*) fournit les résultats computationnels et les mises en œuvre pratiques. Un aspect central de cette thèse est la gestion efficace de la complexité des équations CC d'ordre élevé. L'approche diagrammatique permet d'identifier les termes équivalents, mais l'automatisation symbolique est essentielle pour l'optimisation des intermédiaires et la mise en œuvre de variantes de méthodes. Le cadre `tenpi` est introduit comme une plateforme modulaire et extensible unifiant dérivation symbolique, optimisation d'intermédiaires et contractions de tenseurs indépendantes du backend.

Les conclusions principales du premier article reposent sur l'analyse de l'EFG aux positions nucléaires. Le modèle de Dailey-Townes y a été réexaminé et confronté à notre analyse par projection plus générale, révélant que les effets d'hybridation et de polarisation du cœur sont souvent significatifs et ne peuvent être négligés, en particulier pour les atomes lourds et le complexe uranyle. De plus, les effets relativistes, et notamment l'accouplement spin-orbite, rompent la diagonale de l'opérateur EFG, rendant indispensable la prise en compte des contributions indirectes des orbitales $p_{1/2}$.

Le deuxième article présente en détail l'implémentation des valeurs d'espérance CCSDT et CCSDTQ dans le programme `DIRAC`, rendue possible grâce au cadre `tenpi`. Les

équations Λ ainsi que les matrices de densité correspondantes ont été dérivées pour des niveaux d'excitation arbitraires, et la validité de l'implémentation a été confirmée par le calcul du moment dipolaire de LiH. L'application centrale de ce travail est la détermination précise des moments quadrupolaires nucléaires de ^{7}Li et ^{27}Al, avec une prise en compte systématique de la convergence des bases, des corrections relativistes, ainsi que des effets vibrationnels et rotationnels. Cette approche conduit aux valeurs affinées $Q(^{7}\mathrm{Li}) = -0.0387\,\mathrm{b}$ et $Q(^{27}\mathrm{Al}) = 0.1466\,\mathrm{b}$.

Enfin, dans le dernier article, nous avons déterminé le moment quadrupolaire nucléaire de ^{87}Sr en combinant des constantes de couplage quadrupolaire expérimentales pour SrO et SrS avec des gradients de champ électrique calculés par des méthodes de corrélation électronique de haute précision, incluant les excitations triples (CCSD(T), CCSD-T, CCSD$\tilde{\mathrm{T}}$) dans un cadre relativiste exact à deux composantes (X2Cmmf). L'utilisation d'une infrastructure multi-nœuds via TAPP et la bibliothèque CTF a permis d'élargir les espaces actifs et d'obtenir des valeurs d'espérance fiables. Notre meilleure estimation, $Q(^{87}\mathrm{Sr}) = 0.33666 \pm 0.00258$ b, est en excellent accord avec les approches atomiques récentes et illustre la robustesse de la méthode moléculaire relativiste. Ces résultats ouvrent la voie à des améliorations computationnelles, à l'extension à d'autres noyaux et à l'implémentation de symétries ponctuelles pour des calculs encore plus précis.

Les perspectives futures incluent: l'exploitation des symétries de point-groupe et de permutation pour réduire le coût de calcul, l'élargissement du cadre `tenpi` aux propriétés de réponse et aux méthodes EOM-CC, la relaxation orbitale pour les propriétés magnétiques relativistes, ainsi que le développement de corrections perturbatives au-delà de CCSDT (CCSD(T) et CCSDT(Q)) pour traiter des systèmes plus lourds avec une grande précision.

Bibliography

[1] P. Pyykkö. Relativistic effects in chemistry: more common than you thought. *Annual Review of Physical Chemistry*, 63:45–64, 2012. doi:10.1146/annurev-physchem-032511-143755. Epub 2012 Jan 30, PMID: 22404585.

[2] P. A. M. Dirac. The Quantum Theory of the Electron. *Proceedings of the Royal Society of London. Series A, Containing Papers of a Mathematical and Physical Character*, 117(778):610–624, 1928. doi:10.1098/rspa.1928.0023.

[3] P. A. M. Dirac. A Theory of Electrons and Protons. *Proceedings of the Royal Society A*, 126(801):360–365, 1930. doi:10.1098/rspa.1930.0013.

[4] P. Pyykkö and J. P. Desclaux. Relativity and the periodic system of elements. *Accounts of Chemical Research*, 12(8):276–281, 1979. doi:10.1021/ar50140a002.

[5] P. Pyykkö. Relativistic Effects in Structural Chemistry. *Chemical Reviews*, 88: 563–594, 05 1988. doi:10.1021/cr00085a006.

[6] C. Gourlaouen, J.-P. Piquemal, T. Saue, and O. Parisel. Relativistic Effects on the Metal-Water Bonding in Mono-Hydrated Gold(I) and Silver(I) Cations: A Theoretical Study. *Journal of Computational Chemistry*, 27(1):142–153, 2006. doi:10.1002/jcc.20317.

[7] F. Calvo, E. Pahl, M. Wormit, and P. Schwerdtfeger. Relativity and the liquid nature of mercury. *Angewandte Chemie International Edition*, 52(29):7583–7586, 2013. doi:10.1002/anie.201301438.

[8] R. Ahuja, A. Blomqvist, P. Pyykkö, and P. Zaleski-Ejgierd. Relativity and the lead–acid battery. *Physical Review Letters*, 106(1):018301, 2011. doi:10.1103/PhysRevLett.106.018301.

[9] J. Vícha, J. Novotný, S. Komorovsky, M. Straka, M. Kaupp, and R. Marek. Relativistic Heavy-Neighbor-Atom Effects on NMR Shifts: Concepts and Trends Across the Periodic Table. *Chemical Reviews*, 120(15):7065–7103, 2020. doi:10.1021/acs.chemrev.9b00785.

[10] J. Vícha, P. Švec, Z. Růžičková, M. A. Samsonov, K. Bártová, A. Růžička, M. Straka, and M. Dračínský. Experimental and Theoretical Evidence of Spin-Orbit Heavy Atom on the Light Atom 1H NMR Chemical Shifts Induced through H$\cdots$ I^- Hydrogen Bond. *Chemistry–A European Journal*, 26(40):8698–8702, 2020. doi:10.1002/chem.202001532.

[11] L. Gagliardi and B. O. Roos. Quantum chemical calculations show that the uranium molecule U2 has a quintuple bond. *Nature*, 433:848–851, 2005. doi:10.1038/nature03249.

[12] D. R. Hartree. The Wave Mechanics of an Atom with a Non-Coulomb Central Field. Part I. Theory and Methods. *Mathematical Proceedings of the Cambridge Philosophical Society*, 24:89–110, 1928. doi:10.1017/S0305004100011919.

[13] V. Fock. Näherungsmethode zur Lösung des quantenmechanischen Mehrkörperproblems. *Zeitschrift für Physik*, 61:126–148, 1930. doi:10.1007/BF01340294.

[14] P.-O. Löwdin. *Correlation Problem in Many-Electron Quantum Mechanics I. Review of Different Approaches and Discussion of Some Current Ideas*, pages 207–322. John Wiley & Sons, Ltd, 1958. doi:10.1002/9780470143483.ch7.

[15] R. J. Bartlett and M. Musiał. Coupled-cluster theory in quantum chemistry. *Rev. Mod. Phys.*, 79:291–352, Feb 2007. doi:10.1103/RevModPhys.79.291.

[16] R. A. Kendall, E. Aprà, D. E. Bernholdt, E. J. Bylaska, M. Dupuis, G. I. Fann, R. J. Harrison, J. Ju, J. A. Nichols, J. Nieplocha, and et al. High performance computational chemistry: An overview of NWChem a distributed parallel application. *Computer Physics Communications*, 128(1):260–283, 2000. doi:10.1016/S0010-4655(00)00065-5.

[17] M. Kállay and P. R. Surján. Higher excitations in coupled-cluster theory. *The Journal of Chemical Physics*, 115(7):2945–2954, 08 2001. doi:10.1063/1.1383290.

[18] S. Hirata. Tensor Contraction Engine: Abstraction and Automated Parallel Implementation of Configuration-Interaction, Coupled-Cluster, and Many-Body Perturbation Theories. *The Journal of Physical Chemistry A*, 107(46):9887–9897, 2003. doi:10.1021/jp034596z.

[19] A. D. Bochevarov, E. F. Valeev, and C. D. Sherrill. The electron and nuclear orbitals model: current challenges and future prospects. *Molecular Physics*, 102(1):111–123, 2004. doi:10.1080/00268970410001668525.

[20] A. Köhn, G. W. Richings, and D. P. Tew. Implementation of the full explicitly correlated coupled-cluster singles and doubles model CCSD-F12 with optimally reduced auxiliary basis dependence. *The Journal of Chemical Physics*, 129(20):201103, 2008. doi:10.1063/1.3028546.

[21] E. Neuscamman, T. Yanai, and G. K.-L. Chan. Quadratic canonical transformation theory and higher order density matrices. *The Journal of Chemical Physics*, 130 (12):124102, 2009. doi:10.1063/1.3086932.

[22] M. Saitow, Y. Kurashige, and T. Yanai. Multireference configuration interaction theory using cumulant reconstruction with internal contraction of density matrix renormalization group wave function. *The Journal of Chemical Physics*, 139(4): 044118, 2013. doi:10.1063/1.4816627.

[23] T. Shiozaki. BAGEL: Brilliantly Advanced General Electronic-structure Library. *WIREs Computational Molecular Science*, 8(1):e1331, 2018. doi:10.1002/wcms.1331.

[24] R. Song, T. M. Henderson, and G. E. Scuseria. A power series approximation in symmetry projected coupled cluster theory. *The Journal of Chemical Physics*, 156 (10):104–105, 2022. doi:10.1063/5.0080165.

[25] R. Quintero-Monsebaiz and P.-F. Loos. Equation generator for equation-of-motion coupled cluster assisted by computer algebra system. *AIP Advances*, 13(8):085035, 2023. doi:10.1063/5.0163846.

[26] M. H. Lechner, A. Papadopoulos, K. Sivalingam, A. A. Auer, A. Koslowski, U. Becker, F. Wennmohs, and F. Neese. Code generation in ORCA: progress, efficiency and tight integration. *Phys. Chem. Chem. Phys.*, 26:15205–15220, 2024. doi:10.1039/D4CP00444B.

[27] M. D. Liebenthal, S. H. Yuwono, L. N. Koulias, R. R. Li, N. C. Rubin, and A. E. DePrince III. Automated Quantum Chemistry Code Generation with the p†q Package. *The Journal of Physical Chemistry A*, 129(29):6679–6693, 2025. doi:10.1021/acs.jpca.5c00329.

[28] J. Brandejs, J. Pototschnig, and T. Saue. Generating Coupled Cluster Code for Modern Distributed-Memory Tensor Software. *Journal of Chemical Theory and Computation*, 21(15):7320–7334, 2025. doi:10.1021/acs.jctc.5c00219.

[29] T. Saue, R. Bast, A. S. P. Gomes, H. J. Aa. Jensen, L. Visscher, I. A. Aucar, R. Di Remigio, K. G. Dyall, E. Eliav, and E. Fasshauer et al. The DIRAC code for relativistic molecular calculations. *The Journal of Chemical Physics*, 152(20): 204104, 05 2020. doi:10.1063/5.0004844.

[30] L. Visscher and K. G. Dyall. Relativistic and correlation effects on molecular properties. I. The dihalogens F_2, Cl_2, Br_2, I_2, and At_2. *J. Chem. Phys.*, 104(22):9040–9046, 06 1996. doi:10.1063/1.471636.

[31] V. Arcisauskaite, S. Knecht, S. P. A. Sauer, and L. Hemmingsen. Fully relativistic coupled cluster and DFT study of electric field gradients at Hg in ^{199}Hg compounds. *Phys. Chem. Chem. Phys.*, 14(8):2651–2657, 2012. doi:10.1039/C2CP23080A.

[32] A. Shee, L. Visscher, and T. Saue. Analytic one-electron properties at the 4-component relativistic coupled cluster level with inclusion of spin-orbit coupling. *The Journal of Chemical Physics*, 145(18):184107, Nov 2016. doi:10.1063/1.4966643.

[33] W. E. Lamb and R. C. Retherford. Fine Structure of the Hydrogen Atom by a Microwave Method. *Physical Review*, 72:241–243, 1947. doi:10.1103/PhysRev.72.241.

[34] W. Greiner and J. Reinhardt. *Quantum Electrodynamics*. Springer, Berlin, 2009. ISBN 978-3-540-87560-4. doi:10.1007/978-3-540-87561-1.

[35] V. A. Yerokhin and V. M. Shabaev. Lamb Shift of $n = 1$ and $n = 2$ States of Hydrogen-like Atoms, $1 \leq Z \leq 110$. *Journal of Physical and Chemical Reference Data*, 44(3):033103, 08 2015. doi:10.1063/1.4927487.

[36] L. Pašteka, E. Eliav, A. Borschevsky, U. Kaldor, and P. Schwerdtfeger. Relativistic Coupled Cluster Calculations with Variational Quantum Electrodynamics Resolve the Discrepancy between Experiment and Theory Concerning the Electron Affinity

and Ionization Potential of Gold. *Physical Review Letters*, 118:023002, 01 2017. doi:10.1103/PhysRevLett.118.023002.

[37] P. Pyykkö, M. Tokman, and L. N. Labzowsky. Estimated valence-level Lamb shifts for group 1 and group 11 metal atoms. *Physical Review A*, 57:R689–R692, 1998. doi:10.1103/PhysRevA.57.R689.

[38] P. Zaleski-Ejgierd, M. Patzschke, and P. Pyykkö. Structure and bonding of the MCN molecules, M = Cu, Ag, Au, Rg. *The Journal of Chemical Physics*, 128: 224303, 2008. doi:10.1063/1.2936779.

[39] J. Grant Hill, A. O. Mitrushchenkov, and K. A. Peterson. Ab initio ro-vibrational spectroscopy of the group 11 cyanides: CuCN, AgCN, and AuCN. *The Journal of Chemical Physics*, 138:134314, 2013. doi:10.1063/1.4804834.

[40] T. Okabayashi, E. Y. Okabayashi, F. Koto, T. Ishida, and M. Tanimoto. Detection of free monomeric silver (I) and gold (I) cyanides, AgCN and AuCN: microwave spectra and molecular structure. *Journal of the American Chemical Society*, 131: 11712–11718, 2009. doi:10.1021/ja905507t.

[41] A. Sunaga, M. Salman, and T. Saue. 4-component relativistic Hamiltonian with effective QED potentials for molecular calculations. *The Journal of Chemical Physics*, 157:164101, 2022. doi:10.1063/5.0107644.

[42] D. P. Usov, Y. S. Kozhedub, V. V. Meshkov, A. V. Stolyarov, N. K. Dulaev, A. M. Ryzhkov, I. M. Savelyev, V. M. Shabaev, and I. I. Tupitsyn. Ground-state potential and dipole moment of carbon monoxide: Contributions from electronic correlation, relativistic effects, QED, adiabatic correction, and nonadiabatic correction. *Physical Review A*, 109:042822, 2024. doi:10.1103/PhysRevA.109.042822.

[43] T. Saue. Does chemistry need more physics? *Pure and Applied Chemistry*, 2025. doi:10.1515/pac-2025-0497.

[44] J. Gauss. Molecular Properties. In J. Grotendorst, editor, *Modern Methods and Algorithms of Quantum Chemistry*, volume 3 of *NIC Series*, pages 541–592. John von Neumann Institute for Computing, Jülich, 2000. ISBN 3-00-005834-6. URL https://juser.fz-juelich.de/record/152462/files/FZJ-2014-02064.pdf. Proceedings, Second Edition. © 2000 by John von Neumann Institute for Computing.

[45] H. Hellmann. *Einführung in die Quantenchemie*. F. Deuticke, 1937. URL https://books.google.fr/books?id=AggwAAAAIAAJ.

[46] R. P. Feynman. Forces in Molecules. *Phys. Rev.*, 56(4):340–343, Aug 1939. doi:10.1103/PhysRev.56.340.

[47] T. Helgaker and P. Jørgensen. Configuration-interaction energy derivatives in a fully variational formulation. *Theor. Chem. Acc.*, 75:111–127, 03 1989. doi:10.1007/BF00527713.

[48] H. Koch, H. J. Aa. Jensen, P. Jørgensen, T. Helgaker, G. E. Scuseria, and H. F. Schaefer. Coupled cluster energy derivatives. Analytic Hessian for the closed-shell coupled cluster singles and doubles wave function: Theory and applications. *The Journal of Chemical Physics*, 92(8):4924–4940, 04 1990. doi:10.1063/1.457710.

[49] P. Pyykkö. Spectroscopic nuclear quadrupole moments. *Molecular Physics*, 99(19): 1617–1629, 2001. doi:10.1080/00268970110069010.

[50] A. Weiss, L. Guibé, W. Zeil, and E. A. C. Lucken. Nuclear quadrupole resonance. *Springer-Verlag*, 1972. doi:10.1007/BFb0051350.

[51] N. N. Greenwood and T. C. Gibb. *Hyperfine Interactions*, pages 46–79. Springer Netherlands, Dordrecht, 1971. ISBN 978-94-009-5697-1. doi:10.1007/978-94-009-5697-1_3.

[52] R. Neugart and G. Neyens. *Nuclear Moments*, pages 135–189. Springer Berlin Heidelberg, Berlin, Heidelberg, 2006. doi:10.1007/3-540-33787-3_4.

[53] N. J. Stone. Table of recommended nuclear electric quadrupole moments. Technical Report INDC(NDS)-0833, IAEA, 2021. URL https://www-nds.iaea.org/publications/indc/indc-nds-0833.pdf.

[54] G. A. Canella, R. T. Santiago, and R. L. A. Haiduke. Accurate determination of the nuclear quadrupole moment of xenon from the molecular method. *Chemical Physics Letters*, 660:228–232, 2016. ISSN 0009-2614. doi:https://doi.org/10.1016/j.cplett.2016.08.031.

[55] R. Bast and P. Schwerdtfeger. The accuracy of density functionals for electric field gradients. Test calculations for ScX, CuX and GaX (X=F, Cl, Br, I, H and Li). *The Journal of Chemical Physics*, 119:5988–5994, 09 2003. doi:10.1063/1.1597674.

[56] P. Dufek, P. Blaha, and K. Schwarz. Determination of the Nuclear Quadrupole Moment of ^{57}Fe. *Phys. Rev. Lett.*, 75:3545–3548, Nov 1995. doi:10.1103/PhysRevLett.75.3545. URL https://link.aps.org/doi/10.1103/PhysRevLett.75.3545.

[57] L. Belpassi, F. Tarantelli, A. Sgamellotti, H. M. Quiney, J. N. P. van Stralen, and L. Visscher. Nuclear electric quadrupole moment of gold. *J. Chem. Phys.*, 126:064314, 2007. doi:10.1063/1.2436881.

[58] V. Kellö and A. J. Sadlej. Relativistic contributions to molecular electric-field gradients in hydrogen halides. *Chemical Physics Letters*, 174(6):641–648, 1990. doi:10.1016/0009-2614(90)85501-3.

[59] P. Pyykkö and M. Seth. Relativistic effects in nuclear quadrupole coupling. *Theoretical Chemistry Accounts*, 96(2):92–104, 1997. doi:10.1007/s002140050209.

[60] A. Unsöld. Beiträge zur Quantenmechanik der Atome. *Annalen der Physik*, 387(3): 355–393, 1949. doi:10.1002/andp.19273870304.

[61] C. H. Townes and B. P. Dailey. Determination of electronic structure of molecules from nuclear quadrupole effects. *J. Chem. Phys.*, 17:782–796, 1949. doi:10.1063/1.1747400.

[62] H. Minkowski. Raum und Zeit. *Jahresbericht der Deutschen Mathematiker-Vereinigung*, 18:75–88, 1908. Presented at the 80th Meeting of the German Mathematical Society, Cologne, 21 September 1908. English translation often cited.

[63] K. G. Dyall and K. Faegri. *Introduction to Relativistic Quantum Chemistry*. Oxford University Press, New York, online edition, 2007. doi:10.1093/oso/9780195140866.001.0001.

[64] M. Reiher and A. Wolf. *Relativistic Quantum Chemistry: The Fundamental Theory of Molecular Science*. WILEY-VCH Verlag GmbH, Weinheim, Germany, 2014. ISBN 9783527334155. doi:10.1002/9783527667550. First published: 12 November 2014, Online ISBN: 9783527667550.

[65] CODATA Task Group on Fundamental Constants. CODATA Recommended Values of the Fundamental Physical Constants: 2018. https://physics.nist.gov/cuu/Constants/, 2018. Accessed: 2025-07-14.

[66] S. Knecht, H. J. Aa. Jensen, and T. Saue. Relativistic quantum chemical calculations show that the uranium molecule U_2 has a quadruple bond. *Nature Chemistry*, 11, Jan 2019. doi:10.1038/s41557-018-0158-9.

[67] I. Newton. *Philosophiae Naturalis Principia Mathematica. Auctore Js. Newton ...* Jussu Societatis Regiae ac Typis Josephi Streater, Londini [i.e. London], 1687. doi:10.3931/e-rara-440.

[68] J. Kepler. *Astronomia Nova*. E. Rhambau, Prague, 1609.

[69] J. Kepler. *Harmonices Mundi*. J. Planck, Linz, 1619.

[70] G. Galilei. *Dialogues Concerning Two New Sciences*. Macmillan, New York, 1638. Translated by Henry Crew and Alfonso de Salvio.

[71] G. Galilei. *Discorsi e Dimostrazioni Matematiche Intorno a Due Nuove Scienze*. Elsevier, Leiden, 1638.

[72] G. Galilei. *Dialogo sopra i due massimi sistemi del mondo*. Giunti, Firenze, 1632.

[73] J. C. Maxwell. A Dynamical Theory of the Electromagnetic Field. *Philosophical Transactions of the Royal Society of London*, 155:459–512, 1864. doi:10.1098/rstl.1865.0008.

[74] J. D. Jackson. *Classical Electrodynamics*. Wiley, New York, 3rd edition, 1999. ISBN 978-0471309321.

[75] D. J. Griffiths. *Introduction to Electrodynamics*. Pearson, Boston, 4th edition, 2017. ISBN 978-0138053260.

[76] A. A. Michelson and E. W. Morley. On the Relative Motion of the Earth and the Luminiferous Ether. *American Journal of Science*, s3-34(203):333–345, 1887. doi:10.2475/ajs.s3-34.203.333.

[77] A. Einstein. Zur Elektrodynamik bewegter Körper. *Annalen der Physik*, 17:891–921, 1905. doi:10.1002/andp.19053221004.

[78] A. Einstein. Ist die Trägheit eines Körpers von seinem Energieinhalt abhängig? *Annalen der Physik*, 18:639–641, 1905. doi:10.1002/andp.19053231314.

[79] H. A. Lorentz. Electromagnetic Phenomena in a System Moving with Any Velocity Less than That of Light. *Proceedings of the Royal Netherlands Academy of Arts and Sciences*, 6:809–831, 1904. Original in Dutch: "Electromagnetische Verschijnselen in een Systeem dat Zich met Eenige Snelheid Minder dan Die van het Licht Beweegt".

[80] E. Schrödinger. Quantisierung als Eigenwertproblem. *Annalen der Physik*, 79(4): 361–376, 1926. doi:10.1002/andp.19263840404.

[81] O. Klein. Quantentheorie und fünfdimensionale Relativitätstheorie. *Zeitschrift für Physik*, 37:895–906, 1926.

[82] W. Gordon. Der comptoneffekt nach der schrödingerschen theorie. *Zeitschrift für Physik*, 40(1–2):117–133, 1926. doi:10.1007/BF01390840.

[83] V. Fock. Zur Theorie der Quantenelektrodynamik. *Zeitschrift für Physik*, 39:226–232, 1926.

[84] H. Kragh. Equation with the many fathers. The Klein-Gordon equation in 1926. *American Journal of Physics*, 52:1024–1033, 1984. doi:10.1119/1.13782.

[85] W. Greiner. *Relativistic quantum mechanics.* Springer, Berlin/Heidelberg/New York, 3rd edition, 2000.

[86] R. H. Landau. *Quantum mechanics II. A second course in quantum theory.* John Wiley, New York, 1996.

[87] H. Weyl. Electron and gravitation. *Zeitschrift für Physik*, 56(5-6):330–352, 1929.

[88] C. D. Anderson. The Positive Electron. *Physical Review*, 43(6):491–494, 1933. doi:10.1103/PhysRev.43.491.

[89] M. Gell-Mann. The interpretation of the new particles as displaced charge multiplets. *Il Nuovo Cimento (1955-1965)*, 4(2):848–866, 1956. doi:10.1007/BF02748000.

[90] H. A. Kramers. The use of charge-conjugated wave-functions in the hole-theory of the electron. *Proceedings of the Royal Academy of Amsterdam*, 40:814–823, 1937. URL `https://www.dwc.knaw.nl/DL/publications/PU00017118.pdf`.

[91] M. Born and J. R. Oppenheimer. Zur Quantentheorie der Molekeln. *Annalen der Physik*, 389(20):457–484, 1927. doi:10.1002/andp.19273892002.

[92] H. H. Grelland. Einstein relativistic correction to the nucleus-nucleus interaction in molecules in the Born-Oppenheimer approximation. *Journal of Physics B: Atomic and Molecular Physics*, 13(12):L389, 1980. doi:10.1088/0022-3700/13/12/007.

[93] C. G. Darwin. The dynamical motion of charged particles. *Philosophical Magazine*, 39(233):537–551, 1920. doi:10.1080/14786440508636066.

[94] T. Saue. *Principles and Applications of Relativistic Molecular Calculations*. PhD thesis, University of Oslo, Department of Chemistry, Faculty of Mathematics and Natural Sciences, Oslo, N, 1996. pdf, 3.9 MB.

[95] R. E. Stanton and S. Havriliak. Kinetic balance: A partial solution to the problem of variational safety in dirac calculations. *Journal of Chemical Physics*, 81(4):1910–1918, 1984. doi:10.1063/1.447865.

[96] K. G. Dyall, I. P. Grant, and S. Wilson. Matrix representation of operator products. *Journal of Physics B: Atomic and Molecular Physics*, 17:498, 1984. doi:10.1088/0022-3700/17/3/013.

[97] F. Mark and F. Rosicky. Analytical relativistic Hartree-Fock equations within scalar basis sets. *Chemical Physics Letters*, 74(3):562–567, 1980. doi:10.1016/0009-2614(80)85274-2.

[98] F. Mark, B. Lischka, and F. Rosicky. Variational solution of the Dirac equation within a multicentre basis set of Gaussian functions. *Chemical Physics Letters*, 71 (3):507–512, 1980. doi:10.1016/0009-2614(80)80214-4.

[99] R. S. Mulliken. Electronic Structures of Polyatomic Molecules and Valence. II. General Considerations. *Phys. Rev.*, 41:49–71, Jul 1932. doi:10.1103/PhysRev.41.49.

[100] R. S. Mulliken. Spectroscopy, molecular orbitals, and chemical bonding. *Science*, 157(3784):13–24, 1967. doi:10.1126/science.157.3784.13.

[101] J. C. Slater. The Theory of Complex Spectra. *Physical Review*, 34:1293–1322, 1929. doi:10.1103/PhysRev.34.1293.

[102] G. E. Brown and D. G. Ravenhall. On the interaction of two electrons. *Proc. R. Soc. Lond. A*, 208:348–362, 1951. doi:10.1098/rspa.1951.0181.

[103] J. D. Talman. Minimax Principle for the Dirac Equation. *Phys. Rev. Lett.*, 57: 1091–1094, Sep 1986. doi:10.1103/PhysRevLett.57.1091.

[104] J. Sucher. Foundations of the relativistic theory of many-electron atoms. *Phys. Rev. A*, 22:348–362, Aug 1980. doi:10.1103/PhysRevA.22.348.

[105] B. Swirles and D. R. Hartree. The relativistic self-consistent field. *Proceedings of the Royal Society of London. Series A - Mathematical and Physical Sciences*, 152 (877):625–649, 1935. doi:10.1098/rspa.1935.0211.

[106] C. C. J. Roothaan. New Developments in Molecular Orbital Theory. *Reviews of Modern Physics*, 23:69–89, 1951. doi:10.1103/RevModPhys.23.69.

[107] P.-O. Löwdin. Quantum Theory of Many-Particle Systems. III. Extension of the Hartree–Fock Scheme to Include Degenerate Systems and Correlation Effects. *Physical Review*, 97:1509–1520, 1955. doi:10.1103/PhysRev.97.1509.

[108] P. Hohenberg and W. Kohn. Inhomogeneous Electron Gas. *Phys. Rev. 136*, 136, 1964. doi:10.1103/PhysRev.136.B864.

[109] W. Kohn and L. J. Sham. Self-Consistent Equations Including Exchange and Correlation Effects. *Physical Review*, 140:1133–1138, 1965. doi:10.1103/PhysRev.140.A1133.

[110] J. P. Perdew and K. Schmidt. Jacob's Ladder of Density Functional Approximations for the Exchange-Correlation Energy. In *AIP Conference Proceedings*, volume 577, pages 1–20, 2001. doi:10.1063/1.1390175.

[111] E. Engel. Chapter 10 - Relativistic Density Functional Theory: Foundations and Basic Formalism. In P. Schwerdtfeger, editor, *Relativistic Electronic Structure Theory*, volume 11 of *Theoretical and Computational Chemistry*, pages 523–621. Elsevier, 2002. doi:10.1016/S1380-7323(02)80036-X.

[112] A. K. Rajagopal and J. Callaway. Inhomogeneous Electron Gas. *Phys. Rev. B*, 7: 1912–1919, 1973. doi:10.1103/PhysRevB.7.1912.

[113] L. L. Foldy and S. A. Wouthuysen. On the Dirac theory of spin 1/2 particles and its nonrelativistic limit. *Phys. Rev.*, 78:29–36, 1950. doi:10.1103/PhysRev.78.29.

[114] M. Barysz and A. J. Sadlej. Two-component methods of relativistic quantum chemistry: from the Douglas–Kroll approximation to the exact two-component formalism. *J. Mol. Struct. THEOCHEM*, 573(1):181–200, 2001. doi:10.1016/S0166-1280(01)00542-5.

[115] M. Douglas and N. M. Kroll. Quantum electrodynamical corrections to the fine structure of helium. *Ann. Phys. (N.Y.)*, 82:89–155, 1974. doi:10.1016/0003-4916(74)90333-9.

[116] B. A. Hess. Applicability of the no-pair equation with free-particle projection operators to atomic and molecular structure calculations. *Phys. Rev. A*, 32:756–763, 1985. doi:10.1103/PhysRevA.32.756.

[117] B. A. Hess. Relativistic electronic-structure calculations employing a two-component no-pair formalism with external-field projection operators. *Phys. Rev. A*, 33:3742–3748, Jun 1986. doi:10.1103/PhysRevA.33.3742.

[118] K. G. Dyall. Interfacing relativistic and nonrelativistic methods. I. Normalized elimination of the small component in the modified Dirac equation. *J. Chem. Phys.*, 106(22):9618–9626, 1997. doi:10.1063/1.473860.

[119] M. Filatov and D. Cremer. Connection between the regular approximation and the normalized elimination of the small component method. *J. Chem. Phys.*, 122: 064104, 2005. doi:10.1063/1.1844298.

[120] M. Filatov. Comment on "Quasirelativistic theory equivalent to fully relativistic theory" [J. Chem. Phys. 123, 241102 (2005)]. *J. Chem. Phys.*, 125(10):107101, 2006. doi:10.1063/1.2338033.

[121] M. Filatov and K. G. Dyall. On convergence of the normalized elimination of the small component (NESC) method. *Theor. Chem. Acc.*, 117:333–338, 2007. doi:10.1007/s00214-006-0161-x.

[122] C. Chang, M. Pelissier, and P. Durand. Regular two-component pauli-like effective hamiltonians in dirac theory. *Physica Scripta*, 34(5):394, nov 1986. doi:10.1088/0031-8949/34/5/007.

[123] E. van Lenthe, E. J. Baerends, and J. G. Snijders. Relativistic regular two-component Hamiltonians. *J. Chem. Phys.*, 99:4597–4610, 1993. doi:10.1063/1.466059.

[124] E. van Lenthe, J. G. Snijders, and E. J. Baerends. The zero-order regular approximation for relativistic effects: The effect of spin–orbit coupling in closed-shell molecules. *J. Chem. Phys.*, 105:6505–6516, 1996. doi:10.1063/1.472460.

[125] H. J. Aa. Jensen, 2005. *Douglas–Kroll the Easy Way*, Talk at Conference on Relativistic Effects in Heavy Elements - REHE, Mülheim, Germany, April, 2005. Available at `https://doi.org/10.6084/m9.figshare.12046158`.

[126] M. Iliaš, H. J. Aa. Jensen, V. Kellö, B. O. Roos, and M. Urban. Implementation of an exact two-component relativistic hamiltonian in molecular electronic structure calculations. *Chemical Physics Letters*, 408(3-4):210–214, 2005. doi:10.1016/j.cplett.2005.03.048.

[127] W. Kutzelnigg and W. Liu. Quasirelativistic theory equivalent to fully relativistic theory. *J. Chem. Phys.*, 123:241102, 2005. doi:10.1063/1.2137315.

[128] W. Kutzelnigg and W. Liu. Quasirelativistic theory. i. theory in terms of a quasi-relativistic operator. *Molecular Physics*, 104(13-14):2225–2240, 2006. doi:10.1080/00268970600662481.

[129] W. Liu and W. Kutzelnigg. Quasirelativistic theory. ii. theory at matrix level. *The Journal of Chemical Physics*, 126(11):114107, 2007. doi:10.1063/1.2710258.

[130] W. Liu and D. Peng. Infinite-order quasirelativistic density functional method based on the exact matrix quasirelativistic theory. *The Journal of Chemical Physics*, 125 (4):044102, 2006. doi:10.1063/1.2222365.

[131] M. Iliaš and T. Saue. An infinite-order two-component relativistic Hamiltonian by a simple one-step transformation. *The Journal of Chemical Physics*, 126(6):064102, 02 2007. doi:10.1063/1.2436882.

[132] D. Peng, W. Liu, Y. Xiao, and L. Cheng. Making four- and two-component relativistic density functional theory practical: Exact two-component Hamiltonians revisited. *The Journal of Chemical Physics*, 127(10):104106, 2007. doi:10.1063/1.2772856.

[133] W. Liu and D. Peng. Exact two-component hamiltonians revisited. *J. Chem. Phys.*, 131:031104, 2009. doi:10.1063/1.3159445.

[134] T. Saue. Relativistic hamiltonians for chemistry: A primer. *ChemPhysChem*, 12 (17):3077–3094, 2011. doi:10.1002/cphc.201100682.

[135] E. J. Baerends, W. H. E. Schwarz, P. Schwerdtfeger, and J. G. Snijders. Relativistic atomic orbital contractions and expansions: magnitudes and explanations. *Journal of Physics B: Atomic, Molecular and Optical Physics*, 23(19):3225, 1990. doi:10.1088/0953-4075/23/19/010.

[136] V. Kellö and J. Sadlej. Picture change and calculations of expectation values in approximate relativistic theories. *International Journal of Quantum Chemistry*, 68(3):159–174, 1998. doi:10.1002/(SICI)1097-461X(1998)68:3<159::AID-QUA3>3.0.CO;2-U.

[137] V. Kellö and A. J. Sadlej. The change of picture of the hellmann–feynman force operator in approximate relativistic methods. *Journal of Molecular Structure: THEOCHEM*, 547(1–3):35–53, 2001. doi:10.1016/S0166-1280(01)00458-4.

[138] J. Liu and L. Cheng. An atomic mean-field spin–orbit approach within exact two-component theory for a non-perturbative treatment of spin–orbit coupling. *J. Chem. Phys.*, 148:144108, 2018. doi:10.1063/1.5023750.

[139] J. Sikkema, L. Visscher, T. Saue, and M. Iliaš. The molecular mean-field approach for correlated relativistic calculations. *J. Chem. Phys.*, 131:124116, 2009. doi:10.1063/1.3239505.

[140] T. D. Crawford and H. F. Schaefer. An introduction to coupled cluster theory for computational chemists. In K. B. Lipkowitz and D. B. Boyd, editors, *Reviews in Computational Chemistry*. John Wiley & Sons, Inc, 2000. doi:10.1002/9780470125915.ch2.

[141] T. Helgaker, P. Jørgensen, and J. Olsen. *Molecular Electronic Structure Theory*. John Wiley & Sons, Ltd, Chichester, 2000.

[142] I. Shavitt and R. J. Bartlett. *Calculation of properties in coupled-cluster theory*, page 347–405. Cambridge Molecular Science. Cambridge University Press, 2009. URL https://doi.org/10.1017/CBO9780511596834.

[143] R. J. Bartlett and M. Musiał. Coupled-cluster theory in quantum chemistry. *Rev. Mod. Phys.*, 79:291–352, 2007. doi:10.1103/RevModPhys.79.291.

[144] C. D. Sherrill. An Introduction to Configuration Interaction Theory, 1995. URL `https://vergil.chemistry.gatech.edu/static/content/ci.pdf`. Section 3.3: Why are Coupled-Cluster and MBPT Energies not Variational?, p. 18.

[145] I. Shavitt. The history and evolution of configuration interaction. *Molecular Physics*, 94(1):3–17, 1998. doi:10.1080/00268979809483118.

[146] S. R. Langhoff and E. R. Davidson. Configuration interaction calculations on the nitrogen molecule. *International Journal of Quantum Chemistry*, 8(1):61–72, 1974. doi:10.1002/qua.56008010.

[147] A. Szabo and N. S. Ostlund. *Modern Quantum Chemistry: Introduction to Advanced Electronic Structure Theory*. Dover Publications, New York, 1996. Chapter 4: Configuration Interaction.

[148] F. Coester. Bound states of a many-particle system. *Nucl. Phys.*, 7:421–424, 1958. doi:10.1016/0029-5582(58)90061-5.

[149] P. Jørgensen and J. Simons. *Second Quantization-Based Methods in Quantum Chemistry*. Academic Press, New York, 1981. ISBN 978-0123918508.

[150] G. C. Wick. The Evaluation of the Collision Matrix. *Phys. Rev.*, 80(2):268–272, Oct 1950. doi:10.1103/PhysRev.80.268.

[151] J. B. Robinson and P. J. Knowles. Approximate variational coupled cluster theory. *J. Chem. Phys.*, 135(4):044113, 07 2011. doi:10.1063/1.3615060.

[152] G. Harsha, T. Shiozaki, and G. E. Scuseria. On the difference between variational and unitary coupled cluster theories. *J. Chem. Phys.*, 148(4):044107, 2018. doi:10.1063/1.5011033.

[153] A. Marie, F. Kossoski, and P.-F. Loos. Variational coupled cluster for ground and excited states. *The Journal of Chemical Physics*, 155(10):104105, 09 2021. doi:10.1063/5.0060698.

[154] H. J. Monkhorst. Calculation of properties with the coupled-cluster method. *Int. J. Quantum Chem.*, 12(S11):421–432, 1977. doi:10.1002/qua.560120850.

[155] J. E. Campbell. On a Law of Combination of Operators Bearing on the Theory of Continuous Transformation Groups. *Proc. Lond. Math. Soc.*, s1-29(1):381–390, 1897. doi:10.1112/plms/s1-29.1.381.

[156] H. F. Baker. Alternants and Continuous Groups. *Proc. Lond. Math. Soc.*, s1-34(1): 347–360, 1902. doi:10.1112/plms/s1-34.1.347.

[157] F. Hausdorff. Die symbolische Exponentialformel in der Gruppentheorie. *Berichte über die Verhandlungen der Königlich Sächsischen Gesellschaft der Wissenschaften zu Leipzig, Mathematisch-Physische Klasse*, 58:19–48, 1906.

[158] J. Goldstone. Derivation of the Brueckner many-body theory. *Proc. R. Soc. Lond. A*, 239(1217):267–279, 1957. doi:10.1098/rspa.1957.0037.

[159] J. Čížek. On the use of the cluster expansion and the technique of diagrams in calculations of correlation effects in atoms and molecules. *Adv. Chem. Phys.*, 14: 35–89, 1969. doi:10.1002/9780470143599.ch2.

[160] F. M. Faulstich and M. Oster. Coupled Cluster Theory: Toward an Algebraic Geometry Formulation. *SIAM J. Appl. Algebra Geom.*, 8(1):138–188, 2024. doi:10.1137/22M1491113.

[161] F. M. Faulstich. Recent mathematical advances in coupled cluster theory. *Int. J. Quantum Chem.*, 124(13):e27437, 2024. doi:10.1002/qua.27437.

[162] H. Koch and P. Jørgensen. Coupled cluster response functions. *The Journal of Chemical Physics*, 93:3333–3344, 1990. doi:10.1063/1.458814.

[163] G. D. Purvis III and R. J. Bartlett. A full coupled-cluster singles and doubles model: The inclusion of disconnected triples. *J. Chem. Phys.*, 76(4):1910–1918, 02 1982. doi:10.1063/1.443164.

[164] Y. S. Lee, S. A. Kucharski, and R. J. Bartlett. A coupled cluster approach with triple excitations. *J. Chem. Phys.*, 81(12):5906–5912, 12 1984. doi:10.1063/1.447591.

[165] M. Urban, J. Noga, S. J. Cole, and R. J. Bartlett. Towards a full CCSDT model for electron correlation. *J. Chem. Phys.*, 83(8):4041–4046, 10 1985. doi:10.1063/1.449067.

[166] J. Noga and R. J. Bartlett. The full CCSDT model for molecular electronic structure. *J. Chem. Phys.*, 86(12):7041–7050, 06 1987. doi:10.1063/1.452353.

[167] S. A. Kucharski and R. J. Bartlett. Coupled-cluster theory for high-spin, open-shell reference wave functions. *J. Chem. Phys.*, 97(6):4282–4288, 1992. doi:10.1063/1.463949.

[168] M. Musiał, S. A. Kucharski, and R. J. Bartlett. Formulation and implementation of the full coupled-cluster method through pentuple excitations. *J. Chem. Phys.*, 116 (11):4382–4388, 03 2002. doi:10.1063/1.1445744.

[169] J. Noga, R. J. Bartlett, and M. Urban. Towards a full CCSDT model for electron correlation. CCSDT-n models. *Chem. Phys. Lett.*, 134(2):126–132, 1987. doi:10.1016/0009-2614(87)87107-5.

[170] K. Raghavachari, G. W. Trucks, J. A. Pople, and M. Head-Gordon. A fifth-order perturbation comparison of electron correlation theories. *Chem. Phys. Lett.*, 157(6): 479–483, 1989. doi:10.1016/S0009-2614(89)87395-6.

[171] R. J. Bartlett, J. D. Watts, S. A. Kucharski, and J. Noga. Non-iterative fifth-order triple and quadruple excitation energy corrections in correlated methods. *Chem. Phys. Lett.*, 165(6):513–522, 1990. doi:10.1016/0009-2614(90)87031-L.

[172] J. F. Stanton. Why CCSD(T) works: a different perspective. *Chem. Phys. Lett.*, 281(1):130–134, 1997. doi:10.1016/S0009-2614(97)01144-5.

[173] A. Taube and R. J. Bartlett. Improving upon CCSD(T): ΛCCSD (T). I. Potential energy surfaces. *J. Chem. Phys.*, 128:044110, 01 2008. doi:10.1063/1.2830236.

[174] S. A. Kucharski and R. J. Bartlett. Coupled-cluster methods correct through sixth order. *Chem. Phys. Lett.*, 206(5):574–583, 1993. doi:10.1016/0009-2614(93)80186-S.

[175] S. A. Kucharski and R. J. Bartlett. Sixth-order energy corrections with converged coupled cluster singles and doubles amplitudes. *The Journal of Chemical Physics*, 108(13):5255–5264, 04 1998. doi:10.1063/1.475962.

[176] Y. J. Bomble, J. F. Stanton, M. Kállay, and J. Gauss. Coupled-cluster methods including noniterative corrections for quadruple excitations. *J. Chem. Phys.*, 123 (5):054101, 08 2005. doi:10.1063/1.1950567.

[177] T. D. Crawford. Coupled cluster theory. In S. Reine and T. Saue, editors, *European Summerschool in Quantum Chemistry 2024, Book II*, page 97. ESQC Committee-2024, 2024.

[178] R. P. Feynman. Space–time approach to quantum electrodynamics. *Phys. Rev.*, 76: 769–789, 1949. doi:10.1103/PhysRev.76.769.

[179] F. J. Dyson. The S matrix in quantum electrodynamics. *Phys. Rev.*, 75:1736–1755, 1949. doi:10.1103/PhysRev.75.1736.

[180] K. A. Brueckner. Many-body problem for strongly interacting particles. II. linked-cluster expansion. *Phys. Rev.*, 100:36–45, 1955. doi:10.1103/PhysRev.100.36.

[181] J. Goldstone. Derivation of the Brueckner Many-Body Theory. *Proc. Roy. Soc. Lond. A*, 239:267–279, 1957. doi:10.1098/rspa.1957.0088.

[182] N. M. Hugenholtz. Diagram technique for the many-body problem. *Physica*, 23: 533–540, 1957. doi:10.1016/S0031-8914(57)80107-4.

[183] D. A. Matthews and J. F. Stanton. Chapter 10 - Diagrams in coupled-cluster theory: Algebraic derivation of a new diagrammatic method for closed shells. In S. M. Blinder and J. E. House, editors, *Mathematical Physics in Theoretical Chemistry*, Developments in Physical & Theoretical Chemistry, pages 327–375. Elsevier, 2019. doi:10.1016/B978-0-12-813651-5.00010-3.

[184] D. Kats. ccdiag: Coupled cluster diagram package. `https://github.com/dkats/ccdiag`. Accessed: 2025-07-17.

[185] A. Karton and J. M. L. Martin. Accurate Coupled Cluster Calculations of the Reaction Barrier Heights of Two $CH_3^{\cdot}$ + CH_4 Reactions. *J. Phys. Chem. A*, 113 (43):11679–11684, 2009. doi:10.1021/jp902753s.

[186] P. Hobza and J. Šponer. Non-covalent interactions: A challenge for experiment and theory. *Chem. Rev.*, 108(11):4917–4934, 2008. doi:10.1021/cr9900331.

[187] J. Gauss. Coupled-cluster calculations of nuclear magnetic resonance chemical shifts. *J. Chem. Phys.*, 109(13):5251–5256, 1998. doi:10.1063/1.470240.

[188] R. J. Bartlett and M. Musiał. Multireference coupled-cluster methods. In I. Shavitt and R. J. Bartlett, editors, *Many-Body Methods in Chemistry and Physics: MBPT*

and Coupled-Cluster Theory, chapter 14, pages 462–495. Cambridge University Press, 2009. doi:10.1017/CBO9780511596834.015.

[189] D. Lyakh, M. Musial, V. Lotrich, and R. Bartlett. Multireference Nature of Chemistry: The Coupled-Cluster View. *Chemical Reviews*, 112:182–243, 01 2012. doi:10.1021/cr2001417.

[190] T. Shiozaki, M. Kamiya, S. Hirata, and E. F. Valeev. Equations of explicitly-correlated coupled-cluster methods. *Phys. Chem. Chem. Phys.*, 10(23):3358–3370, 2008. doi:10.1039/B803704N.

[191] M. Kállay, P. R. Nagy, D. Mester, Z. Rolik, G. Samu, J. Csontos, J. Csóka, P. B. Szabó, L. Gyevi-Nagy, B. Hégely, and et al. The MRCC program system: Accurate quantum chemistry from water to proteins. *Journal of Chemical Physics*, 152: 074107, 2020. doi:10.1063/1.5142048.

[192] J. Brandejs and T. Saue. tenpi: Tensor Programming Interface. `https://gitlab.com/janbrandejs/tenpi`, 2025. Accessed: 2025-06-02.

[193] J. V. Pototschnig, A. Papadopoulos, D. I. Lyakh, M. Repisky, L. Halbert, A. S. P. Gomes, H. J. Aa. Jensen, and L. Visscher. Implementation of Relativistic Coupled Cluster Theory for Massively Parallel GPU-Accelerated Computing Architectures. *Journal of Chemical Theory and Computation*, 17(9):5509–5529, 2021. doi:10.1021/acs.jctc.1c00260.

[194] D. I. Lyakh. Domain-specific virtual processors as a portable programming and execution model for parallel computational workloads on modern heterogeneous high-performance computing architectures. *International Journal of Quantum Chemistry*, 119(12):e25926, 2019. doi:10.1002/qua.25926. Accessed: 2025-06-02.

[195] P.-W. Lai, H. Zhang, S. Rajbhandari, E. Valeev, K. Kowalski, and P. Sadayappan. Effective Utilization of Tensor Symmetry in Operation Optimization of Tensor Contraction Expressions. *Procedia Computer Science*, 9:412–421, 2012. doi:10.1016/j.procs.2012.04.044. Proceedings of the International Conference on Computational Science, ICCS 2012.

[196] P. A. M. Dirac. The Evolution of the Physicist's Picture of Nature. *Scientific American*, May 1963. URL `https://physics.gu.se/~tfkhj/F3/FYP380.1.pdf`.

[197] P. Norman, K. E. Ruud, and T. Saue. *Principles and Practices of Molecular Properties: Theory, Modelling and Simulations*. John Wiley & Sons, Hoboken, NJ, first edition edition, 2018. doi:10.1002/9781118794821.

[198] S. P. A. Sauer. *Molecular Electromagnetism: A Computational Chemistry Approach*. Oxford University Press, 08 2011. ISBN 9780199575398. doi:10.1093/acprof:oso/9780199575398.001.0001.

[199] E. A. Hylleraas. *Z. Phys.*, 65:348–362, 1930. doi:10.1007/BF01397032.

[200] E. Wigner. On a modification of the Rayleigh-Schrödinger perturbation theory. *Math. Natur. Anz. (Budapest)*, 53:1–46, 1935.

[201] D. J. Thouless. Stability conditions and nuclear rotations in the Hartree-Fock theory. *Nuclear Physics*, 21:225–232, 1960. doi:10.1016/0029-5582(60)90048-1.

[202] E. A. Salter, G. W. Trucks, and R. J. Bartlett. Analytic energy derivatives in many-body methods. I. First derivatives. *The Journal of Chemical Physics*, 90(3): 1752–1766, 02 1989. doi:10.1063/1.456069.

[203] T. Helgaker. Simple derivation of the potential energy gradient for an arbitrary electronic wave function. *International Journal of Quantum Chemistry*, 21(5):939–940, 1982. doi:https://doi.org/10.1002/qua.560210520.

[204] E. A. Salter, H. Sekino, and R. J. Bartlett. Property evaluation and orbital relaxation in coupled cluster methods. *J. Chem. Phys.*, 87(1):502–509, 07 1987. doi:10.1063/1.453596.

[205] L. Adamowicz, W. D. Laidig, and R. J. Bartlett. Analytical gradients for the coupled-cluster method. *Int. J. Quantum Chem.*, 26(S18):245–254, 1984. doi:10.1002/qua.560260825.

[206] T. Helgaker, P. Jørgensen, and J. Olsen. *Coupled-Cluster Theory*, chapter 13, pages 648–723. John Wiley & Sons, Ltd, 2000. ISBN 9781119019572. doi:https://doi.org/10.1002/9781119019572.ch13.

[207] M. Kállay, J. Gauss, and P. G. Szalay. Analytic first derivatives for general coupled-cluster and configuration interaction models. *The Journal of Chemical Physics*, 119 (6):2991–3004, 08 2003. doi:10.1063/1.1589003.

[208] K. E. Weflen, M. R. Bentley, J. H. Thorpe, P. R. Franke, J. M. L. Martin, D. A. Matthews, and J. F. Stanton. Exploiting a Shortcoming of Coupled-Cluster Theory: The Extent of Non-Hermiticity as a Diagnostic Indicator of Computational Accuracy. *The Journal of Physical Chemistry Letters*, 16(20):5121–5127, 2025. doi:10.1021/acs.jpclett.5c00885.

[209] G. Fabbro, J. Pototschnig, and T. Saue. Beyond the Dailey–Townes Model: Chemical Information from the Electric Field Gradient. *The Journal of Physical Chemistry A*, 129:1006–1025, 2025. doi:10.1021/acs.jpca.4c06884.

[210] A. D. Buckingham. Molecular quadrupole moments. *Q. Rev. Chem. Soc.*, 13:183–214, 1959. doi:10.1039/QR9591300183.

[211] J. Thyssen, P. Schwerdtfeger, M. Bender, W. Nazarewicz, and P. B. Semmes. Quadrupole and hexadecapole couplings for ^{127}I in Li^{127}I. *Phys. Rev. A*, 63:022505, Jan 2001. doi:10.1103/PhysRevA.63.022505.

[212] K. Koch, K. Koepernik, D. Van Neck, H. Rosner, and S. Cottenier. Electron penetration into the nucleus and its effect on the quadrupole interaction. *Phys. Rev. A*, 81:032507, Mar 2010. doi:10.1103/PhysRevA.81.032507.

[213] R. Sternheimer. On nuclear quadrupole moments. *Phys. Rev.*, 80:102–103, Oct 1950. doi:10.1103/PhysRev.80.102.2.

[214] C. H. Townes and B. P. Dailey. Nuclear quadrupole effects and electronic structure of molecules in the solid state. *J. Chem. Phys.*, 20(1):35–40, 01 1952. doi:10.1063/1.1700192.

[215] R. V. Pound. Nuclear electric quadrupole interactions in crystals. *Phys. Rev.*, 79 (4):685–702, Aug 1950. doi:10.1103/PhysRev.79.685.

[216] P. Gütlich, E. Bill, and A. X. Trautwein. *Hyperfine Interactions*, pages 73–135. Springer Berlin Heidelberg, Berlin, Heidelberg, 2011. doi:10.1007/978-3-540-88428-6_4.

[217] S. L. Ruby and P. A. Flinn. Determination of the sign of the electric field gradient in randomly oriented samples. *Rev. Mod. Phys.*, 36(1):351–352, 1964. doi:10.1103/RevModPhys.36.351.

[218] R. L. Collins. Mössbauer Studies of Iron Organometallic Complexes. IV. Sign of the Electric-Field Gradient in Ferrocene. *J. Chem. Phys.*, 42(3):1072–1080, 02 1965. doi:10.1063/1.1696044.

[219] J. R. Gabriel and S. L. Ruby. Computation of Mössbauer spectra. *Nuclear Instruments and Methods*, 36:23–28, 1965. doi:10.1016/0029-554X(65)90401-5.

[220] H. R. Brooker and R. B. Creel. Zeeman nuclear quadrupole resonance line shapes in powders (I = 3/2). *J. Chem. Phys.*, 61(9):3658–3664, 11 1974. doi:10.1063/1.1682549.

[221] S. Dubillard, J. B. Rota, T. Saue, and K. Faegri. Bonding analysis using localized relativistic orbitals: Water, the ultrarelativistic case and the heavy homologues H_2X (X=Te, Po, eka-Po). *J. Chem. Phys.*, 124(15), 2006. doi:10.1063/1.2187001.

[222] R. Bast, A. Koers, A. S. P. Gomes, M. Ilias, L. Visscher, P. Schwerdtfeger, and T. Saue. Analysis of parity violation in chiral molecules. *Phys. Chem. Chem. Phys.*, 13:864–876, 2011. doi:10.1039/C0CP01483D.

[223] E. A. C. Lucken. *Nuclear Quadrupole Resonance. Theoretical Interpretation*, pages 155–171. Springer-Verlag, Berlin, 1972.

[224] W. Zeil. *Bestimmung der Kernquadrupolkopplungskonstanten aus Mikrowellenspektren*, pages 103–153. Springer-Verlag, Berlin, 1972.

[225] E. A. C. Lucken. *Vibrational Dependencies and Isotope Effects on Nuclear Quadrupole Coupling Constants*, pages 83–124. John Wiley & Sons, Chichester, 1983.

[226] T. Saue, K. Faegri, and O. Gropen. Relativistic effects on the bonding of heavy and superheavy hydrogen halides. *Chemical Physics Letters*, 263:360, 1996. doi:10.1016/S0009-2614(96)01250-X.

[227] J. E. Lennard-Jones. The electronic structure of some diatomic molecules. *Trans. Faraday Soc.*, 25:668–686, 1929. doi:10.1039/TF9292500668.

[228] L. Pauling. The Application of the Quantum Mechanics to the Structure of the Hydrogen Molecule and Hydrogen Molecule-Ion and to Related Problems. *Chemical Reviews*, 5(2):173–213, 1928. doi:10.1021/cr60018a003.

[229] G. Knizia. Intrinsic Atomic Orbitals: An Unbiased Bridge between Quantum Theory and Chemical Concepts. *J. Chem. Theory Comp.*, 9(11):4834–4843, 2013. doi:10.1021/ct400687b.

[230] R. Mulliken. Electronic Population Analysis on LCAO-MO Molecular Wave Functions. I. *J. Chem. Phys.*, 23:1833, 1955. doi:10.1063/1.1740588.

[231] R. McWeeny. *Coulson's Valence*. Oxford University Press, Oxford, 1979.

[232] H. B. G. Casimir. *On the Interaction between Atomic Nuclei and Electrons*. Springer, Dordrecht, 1936. doi:10.1007/978-94-017-6067-6.

[233] G. Racah. Theory of Complex Spectra. II. *Phys. Rev.*, 62:438–462, Nov 1942. doi:10.1103/PhysRev.62.438.

[234] L. Belpassi, F. Tarantelli, A. Sgamellotti, H. M. Quiney, J. N. P. van Stralen, and L. Visscher. Nuclear electric quadrupole moment of gold. *The Journal of Chemical Physics*, 126(6):064314, 02 2007. doi:10.1063/1.2436881.

[235] C. Thierfelder, P. Schwerdtfeger, and T. Saue. ^{63}Cu and ^{197}Au nuclear quadrupole moments from four-component relativistic density-functional calculations using correct long-range exchange. *Phys. Rev. A*, 76:034502, Sep 2007. doi:10.1103/PhysRevA.76.034502.

[236] J. Bieroń and P. Pyykkö. Nuclear quadrupole moments of bismuth. *Phys. Rev. Lett.*, 87:133003, Sep 2001. doi:10.1103/PhysRevLett.87.133003.

[237] T. Q. Teodoro and R. L. A. Haiduke. Nuclear electric quadrupole moment of bismuth from the molecular method. *Phys. Rev. A*, 88:052504, Nov 2013. doi:10.1103/PhysRevA.88.052504.

[238] P. Pyykkö. Year-2017 nuclear quadrupole moments. *Molecular Physics*, 116:1–11, 02 2018. doi:10.1080/00268976.2018.1426131.

[239] L. V. Skripnikov, A. V. Oleynichenko, A. V. Zaitsevskii, D. E. Maison, and A. E. Barzakh. Relativistic Fock space coupled-cluster study of bismuth electronic structure to extract the Bi nuclear quadrupole moment. *Phys. Rev. C*, 104:034316, Sep 2021. doi:10.1103/PhysRevC.104.034316.

[240] J.-P. Dognon and P. Pyykkö. Determining nuclear quadrupole moments of Bi and Sb from molecular data. *Phys. Chem. Chem. Phys.*, 25:2758–2761, 2023. doi:10.1039/D2CP04747K.

[241] M. Joosten, M. Repisky, M. Kadek, P. Pyykkö, and K. Ruud. Electric field gradients at the nuclei from all-electron four-component relativistic density functional theory using gaussian-type orbitals. *Phys. Rev. B*, 110:045141, Jul 2024. doi:10.1103/PhysRevB.110.045141.

[242] L. V. Skripnikov and A. E. Barzakh. Reexamination of nuclear magnetic dipole and electric quadrupole moments of polonium isotopes. *Phys. Rev. C*, 109:024315, Feb 2024. doi:10.1103/PhysRevC.109.024315.

[243] I. Lindgren and J. Morrison. *Atomic Many-Body Theory*. Berlin, 1986.

[244] I. P. Grant. *Relativistic Quantum Theory of Atoms and Molecules*. Springer Series on Atomic, Optical, and Plasma Physics. Springer, 2007. doi:10.1007/978-0-387-35069-1.

[245] R. Szmytkowski. Recurrence and differential relations for spherical spinors. *Journal of Mathematical Chemistry*, 42(3):397–413, 2007. ISSN 1572-8897. doi:10.1007/s10910-006-9110-0.

[246] H. Schüler and T. Schmidt. Über abweichungen des atomkerns von der kugelsymmetrie. *Z. Phys.*, 94:457–468, 1935. doi:10.1007/BF01330611.

[247] P. Brix. Fifty years of nuclear quadrupole moments. *Zeitschrift für Naturforschung A*, 41(1-2):2–14, 1986. doi:10.1515/zna-1986-1-203.

[248] H. Schüler and Th. Schmidt. Über die Abweichung des Cassiopeiumatomkerns von der Kugelsymmetrie. *Zeitschrift für Physik*, 95(5):265–273, May 1935. ISSN 0044-3328. doi:10.1007/BF01338636.

[249] J. A. S. Smith. Nuclear quadrupole interactions in solids. *Chem. Soc. Rev.*, 15: 225–260, 1986. doi:10.1039/CS9861500225.

[250] H. Casimir. Über die hyperfeinstruktur des europiums. *Physica*, 2(1):719–723, 1935. doi:10.1016/S0031-8914(35)90148-3.

[251] C. H. Townes, H. M. Foley, and W. Low. Nuclear quadrupole moments and nuclear shell structure. *Phys. Rev.*, 76:1415–1416, Nov 1949. doi:10.1103/PhysRev.76.1415.

[252] M. G. Mayer. On closed shells in nuclei. ii. *Phys. Rev.*, 75:1969–1970, Jun 1949. doi:10.1103/PhysRev.75.1969.

[253] O. Haxel, J. H. D. Jensen, and H. E. Suess. On the "magic numbers" in nuclear structure. *Phys. Rev.*, 75:1766–1766, Jun 1949. doi:10.1103/PhysRev.75.1766.2.

[254] J. Rainwater. Background for the spheroidal nuclear model proposal. *Rev. Mod. Phys.*, 48:385–391, Jul 1976. doi:10.1103/RevModPhys.48.385.

[255] A. Bohr. Rotational motion in nuclei. *Rev. Mod. Phys.*, 48:365–374, Jul 1976. doi:10.1103/RevModPhys.48.365.

[256] B. Mottelson. Elementary modes of excitation in the nucleus. *Rev. Mod. Phys.*, 48: 375–383, Jul 1976. doi:10.1103/RevModPhys.48.375.

[257] S. A. Moszkowski. *Models of Nuclear Structure*, pages 411–550. Springer, Berlin, Heidelberg, 1957. doi:10.1007/978-3-642-45872-9_5.

[258] P. Ring and P. Schuck. *The Nuclear Many-Body Problem*. Springer-Verlag, New York, 1980.

[259] P. Pyykkö. Year-2008 nuclear quadrupole moments. *Molecular Physics*, 106(16-18): 1965–1974, aug 2008. doi:10.1080/00268970802018367.

[260] N. J. Stone. Table of nuclear magnetic dipole and electric quadrupole moments. *Atomic Data and Nuclear Data Tables*, 90(1):75–176, 2005. ISSN 0092-640X. doi:10.1016/j.adt.2005.04.001.

[261] N. J. Stone. Table of nuclear electric quadrupole moments. *Atomic Data and Nuclear Data Tables*, 111-112:1–28, 2016. doi:10.1016/j.adt.2015.12.002.

[262] Á. Koszorús, R. P. de Groote, B. Cheal, P. Campbell, and I. D. Moore. Nuclear structure studies by collinear laser spectroscopy. *The European Physical Journal A*, 60(1):20, Jan 2024. doi:10.1140/epja/s10050-024-01230-9.

[263] S. L. Kaufman. High-resolution laser spectroscopy in fast beams. *Optics Communications*, 17(3):309–312, 1976. doi:10.1016/0030-4018(76)90267-4.

[264] D. C. Kean. Measurement of quadrupole moments through coulomb excitation. In B. A. Robson, editor, *Nuclear Interactions*, pages 80–94, Berlin, Heidelberg, 1976. Springer Berlin Heidelberg. doi:10.1007/3-540-09102-5_583.

[265] A. Antognini, N. Berger, T. E. Cocolios, R. Dressler, R. Eichler, A. Eggenberger, P. Indelicato, K. Jungmann, C. H. Keitel, K. Kirch, and et al. Measurement of the quadrupole moment of ^{185}Re and ^{187}Re from the hyperfine structure of muonic x rays. *Phys. Rev. C*, 101:054313, May 2020. doi:10.1103/PhysRevC.101.054313.

[266] F. Wang, T. C. Steimle, A. G. Adam, L. Cheng, and J. F. Stanton. The pure rotational spectrum of ruthenium monocarbide, RuC, and relativistic ab initio predictions. *The Journal of Chemical Physics*, 139(17):174318, Nov 2013. doi:10.1063/1.4828458.

[267] B. P. Dailey and C. H. Townes. The ionic character of diatomic molecules. *The Journal of Chemical Physics*, 23(1):118–123, Jan 1955. doi:10.1063/1.1740508.

[268] F. A. Cotton and C. B. Harris. Correlation of nuclear quadrupole coupling constants with molecular electronic structure using molecular orbital theory. *Proc. Natl. Acad. Sci. U.S.A.*, 56(1):12–, 1966. ISSN 0027-8424. doi:10.1073/pnas.56.1.12.

[269] M. Y. Balakina, O. D. Fominykh, I. Morozova, and D. Y. Osokin. The Townes and Dailey approach to the interpretation of NQR parameters in the light of non-empirical calculations. Three-membered rings. *Magnetic Resonance in Chemistry*, 33:761–766, 1995. doi:10.1002/mrc.1260331002.

[270] P. A. Nikitin, L. M. Lazarev, and G. V. Dolgushin. Mndo refinement of the townes-dailey theory. calculation of nqr frequencies of chloro-containing compounds. *Russ. Chem. Bull.*, 44(1):38–42, 1995. doi:10.1007/BF00696953.

[271] S. E. Novick. Extended Townes–Dailey analysis of the nuclear quadrupole coupling tensor. *Journal of Molecular Spectroscopy*, 267(1):13–18, 2011. doi:10.1016/j.jms.2011.01.004.

[272] A. Rinaldi and G. Wu. A Modified Townes-Dailey Model for Interpretation and Visualization of Nuclear Quadrupole Coupling Tensors in Molecules. *J. Phys. Chem. A*, 124:1176–1186, 2020. doi:10.1021/acs.jpca.0c00439.

[273] J. Autschbach, S. Zheng, and R. W. Schurko. Analysis of electric field gradient tensors at quadrupolar nuclei in common structural motifs. *Concepts in Magnetic Resonance Part A*, 36A(2):84–126, 2010. doi:10.1002/cmr.a.20155.

[274] T. Saue, R. Bast, A. S. P. Gomes, H. J. Aa. Jensen, L. Visscher, I. A. Aucar, R. Di Remigio, K. G. Dyall, E. Eliav, E. Fasshauer, and et al. The DIRAC code for relativistic molecular calculations. *The Journal of Chemical Physics*, 152(20): 204104, 2020. doi:10.1063/5.0004844.

[275] DIRAC, a relativistic ab initio electronic structure program, Release DIRAC24 (2024), written by L. Visscher, H. J. Aa. Jensen, R. Bast, A. S. P. Gomes and T. Saue, with contributions from I. A. Aucar, V. Bakken, J. Brandejs, C. Chibueze, J. Creutzberg et al. (available at `https://doi.org/110.5281/zenodo.10680560`, see also `https://www.diracprogram.org`).

[276] L. Visscher and K. G. Dyall. Dirac-Fock atomic electronic structure calculations using different nuclear charge distributions. *Atomic Data and Nuclear Data Tables*, 67(207):207–224, 1997. doi:10.1006/adnd.1997.0751.

[277] T. Saue and T. Helgaker. Four-component relativistic kohn-sham theory. *J. Comput. Chem.*, 23(8):814–823, 2002. doi:10.1002/jcc.10066.

[278] O. Fossgaard, O. Gropen, M. Corral Valero, and T. Saue. On the performance of four-component relativistic density functional theory: Spectroscopic constants and dipole moments of the diatomics HX and XY (X,Y=F, Cl, Br, and I). *J. Chem. Phys.*, 118(23):10418–10430, 2003. doi:10.1063/1.1574317.

[279] J. P. Perdew, K. Burke, and M. Ernzerhof. Generalized Gradient Approximation Made Simple. *Phys. Rev. Lett.*, 77:3865–3868, 1996. doi:10.1103/PhysRevLett.77.3865.

[280] L. Visscher and T. Saue. Approximate relativistic electronic structure methods based on the quaternion modified Dirac equation. *J. Chem. Phys.*, 113:3996, 2000. doi:10.1063/1.1288371.

[281] K. G. Dyall. Relativistic double-zeta, triple-zeta, and quadruple-zeta basis sets for the 4d elements Y–Cd. *Theoretical Chemistry Accounts*, 117:483–489, 2007. doi:10.5281/zenodo.7574628.

[282] K. G. Dyall. Relativistic quadruple-zeta and revised triple-zeta and double-zeta basis sets for the 4p, 5p, and 6p elements. *Theoretical Chemistry Accounts*, 115: 441–447, 2006. doi:10.1007/s00214-006-0126-0.

[283] K. G. Dyall. Relativistic double-zeta, triple-zeta, and quadruple-zeta basis sets for the light elements h–ar. *Theoretical Chemistry Accounts*, 135:441–447, 2016. doi:10.1007/s00214-016-1884-y.

[284] J. Pipek and P. G. Mezey. A fast intrinsic localization procedure applicable for ab initio and semiempirical linear combination of atomic orbital wave functions. *The Journal of Chemical Physics*, 90(9):4916–4926, 05 1989. doi:10.1063/1.456588.

[285] C. South, A. Shee, D. Mukherjee, A. K. Wilson, and T. Saue. 4-Component relativistic calculations of L3 ionization and excitations for the isoelectronic species UO_2^{2+}, OUN^+ and UN_2. *Phys. Chem. Chem. Phys.*, 18:21010–21023, 2016. doi:10.1039/C6CP00262E.

[286] S. Shaik, D. Danovich, and P. C. Hiberty. Valence bond theory—its birth, struggles with molecular orbital theory, its present state and future prospects. *Molecules*, 26 (6), 2021. ISSN 1420-3049. doi:10.3390/molecules26061624.

[287] W. Gordy. Relation of nuclear quadrupole couplings to the chemical bond. *The Journal of Chemical Physics*, 22(8):1470–1471, Aug 1954. doi:10.1063/1.1740436.

[288] W. Gordy. Microwave spectroscopy. introductory paper: quadrupole couplings, dipole moments and the chemical bond. *Discuss. Faraday Soc.*, 19:14–29, 1955. doi:10.1039/DF9551900014.

[289] R. S. Mulliken. Quelques aspects de la théorie des orbitales moléculaires. *J. Chim. Phys.*, 46:497–542, 1949. doi:10.1051/jcp/1949460497.

[290] R. S. Mulliken. Quelques aspects de la théorie des orbitales moléculaires (suite et fin). *J. Chim. Phys.*, 46:675–713, 1949. doi:10.1051/jcp/1949460675.

[291] J. J. Aucar, F. A. Maldonado, and J. I. Melo. Relativistic corrections of the electric field gradient in dihalogen molecules XY (X, Y = F, Cl, Br, I, At) within the linear response elimination of the small component formalism. *International Journal of Quantum Chemistry*, 121(20), 2021. doi:10.1002/qua.26769.

[292] M. Pepper and B. E. Bursten. The electronic structure of actinide-containing molecules: A challenge to applied quantum chemistry. *Chem. Rev.*, 91:719–741, 1991. doi:10.1021/cr00005a005.

[293] R. G. Denning. *Electronic structure and bonding in actinyl ions*, pages 215–276. Springer Berlin Heidelberg, Berlin, Heidelberg, 1992. ISBN 978-3-540-46694-9. doi:10.1007/BFb0036502.

[294] R. G. Denning. Electronic structure and bonding in actinyl ions and their analogs. *The Journal of Physical Chemistry A*, 111(20):4125–4143, 2007. doi:10.1021/jp071061n.

[295] A. Kovács, R. J. M. Konings, J. K. Gibson, I. Infante, and L. Gagliardi. Quantum chemical calculations and experimental investigations of molecular actinide oxides. *Chemical Reviews*, 115(4):1725–1759, 2015. doi:10.1021/cr500426s.

[296] B. W. Veal, D. J. Lam, W. T. Carnall, and H. R. Hoekstra. X-ray photoemission spectroscopy study of hexavalent uranium compounds. *Phys. Rev. B*, 12:5651–5663, Dec 1975. doi:10.1103/PhysRevB.12.5651.

[297] P. F. Walch and D. E. Ellis. Effects of secondary ligands on the electronic structure of uranyls. *The Journal of Chemical Physics*, 65(6):2387–2392, Sep 1976. doi:10.1063/1.433354.

[298] C. Y. Yang, K. H. Johnson, and J. A. Horsley. Relativistic xα-scattered-wave calculations for the uranyl ion. *The Journal of Chemical Physics*, 68(3):1001–1005, 02 1978. doi:10.1063/1.435790.

[299] R. L. DeKock, E. J. Baerends, P. M. Boerrigter, and J. G. Snijders. On the nature of the first excited states of the uranyl ion. *Chemical Physics Letters*, 105(3):308–316, 1984. doi:10.1016/0009-2614(84)85036-8.

[300] K. Tatsumi and R. Hoffmann. Bent cis d^0 MoO_2^{2+} vs. linear trans d^0 f^0 UO_2^{2+}: a significant role for nonvalence 6p orbitals in uranyl. *Inorganic Chemistry*, 19: 2656–2658, 1980. doi:10.1021/ic50211a035.

[301] P. Pyykkö and L. L. Lohr Jr. Relativistically parameterized extended hückel calculations. 3. structure and bonding for some compounds of uranium and other heavy elements. *Inorganic Chemistry*, 20(7):1950–1959, 1981. doi:10.1021/ic50221a002.

[302] P. Pyykkö and L. Laaksonen. Relativistically parameterized extended hückel calculations. 8. double-ζ parameters for the actinoids thorium, protactinium, uranium, neptunium, plutonium, and americium and an application on uranyl. *The Journal of Physical Chemistry*, 88(21):4892–4895, 1984. doi:10.1021/j150665a017.

[303] S. Larsson and P. Pyykkö. Relativistically parameterized extended Hückel calculations. IX. An iterative version with applications to some xenon, thorium and uranium compounds. *Chemical Physics*, 101(3):355–369, 1986. doi:10.1016/0301-0104(86)85071-6.

[304] P. Pyykkö. Recent developments in the theory of f-element molecules. *Inorganica Chimica Acta*, 139(1):243–245, 1987. doi:10.1016/S0020-1693(00)84086-4.

[305] D. P. Grechukhin, V. I. Zhudov, A. G. Zelenkov, V. M. Kulakov, B. V. Odinov, A. A. Soldatov, and Yu. A. Teterin. Direct observation of strong-electron orbit hybridization in the internal-conversion electron spectra. *Pis'ma Zh. Eksp. Teor. Fiz.*, 31:627, 1980. URL `http://jetpletters.ru/ps/0/article_20495.shtml`.

[306] R. G. Denning, J. C. Green, T. E. Hutchings, C. Dallera, A. Tagliaferri, K. Giarda, N. B. Brookes, and L. Braicovich. Covalency in the uranyl ion: A polarized x-ray spectroscopic study. *The Journal of Chemical Physics*, 117(17):8008–8020, 11 2002. doi:10.1063/1.1510445.

[307] J. P. Desclaux. Relativistic Dirac-Fock expectation values for atoms with Z = 1 to Z = 120. *Atomic Data and Nuclear Data Tables*, 12(4):311–406, 1973. doi:10.1016/0092-640X(73)90020-X.

[308] E. M. van Wezenbeek, E. J. Baerends, and J. G. Snijders. Relativistic bond lengthening of UO_2^{2+} and UO_2. *Theoretica chimica acta*, 81(3):139–155, May 1991. ISSN 1432-2234. doi:10.1007/BF01126676.

[309] W. R. Wadt. Why uranyl ion(2+) is linear and isoelectronic thorium dioxide is bent. *Journal of the American Chemical Society*, 103(20):6053–6057, 1981. doi:10.1021/ja00410a011.

[310] J. A. Monard, P. G. Huray, and J. O. Thomson. Mössbauer studies of electric hyperfine interactions in ^{234}U, ^{236}U, ^{238}U. *Phys. Rev. B*, 9:2838–2845, Apr 1974. doi:10.1103/PhysRevB.9.2838.

[311] J. L. C. Ford, P. H. Stelson, C. E. Bemis, F. K. McGowan, R. L. Robinson, and W. T. Milner. Precise coulomb excitation $b(e2)$ values for first 2^+ states of the actinide nuclei. *Phys. Rev. Lett.*, 27:1232–1234, Nov 1971. doi:10.1103/PhysRevLett.27.1232.

[312] M. Schmorak, C. E. Bemis, M. J. Zender, N. B. Gove, and P. F. Dittner. Ground state rotational bands in doubly even actinide nuclei. *Nuclear Physics A*, 178(2): 410–416, 1972. ISSN 0375-9474. doi:10.1016/0375-9474(72)90468-X.

[313] B. Pritychenko, M. Birch, B. Singh, and M. Horoi. Tables of e2 transition probabilities from the first 2+ states in even–even nuclei. *Atomic Data and Nuclear Data Tables*, 107:1–139, 2016. ISSN 0092-640X. doi:10.1016/j.adt.2015.10.001.

[314] P. Gütlich, E. Bill, and A. X. Trautwein. *Mössbauer Spectroscopy and Transition Metal Chemistry. Fundamentals and Applications*. Springer, Heidelberg, 2011.

[315] G. K. Shenoy and B. D. Dunlap. Method for the analysis of pure quadrupole spectra in nuclear gamma-ray resonance. *Nuclear Instruments and Methods*, 71(3):285–291, 1969. doi:10.1016/0029-554X(69)90316-4.

[316] W. A. de Jong, L. Visscher, and W. C. Nieuwpoort. On the bonding and the electric field gradient of the uranyl ion. *Journal of Molecular Structure: THEOCHEM*, 458 (1):41–52, 1998. doi:10.1016/S0166-1280(98)00347-9.

[317] P. Belanzoni, E. J. Baerends, and E. Van Lenthe. The uranyl ion revisited: the electric field gradient at U as a probe of environmental effects. *Molecular Physics*, 103(6-8):775–787, 2005. doi:10.1080/00268970512331338153.

[318] F. Aquino, N. Govind, and J. Autschbach. Electric field gradients calculated from two-component hybrid density functional theory including spin-orbit coupling. *Journal of Chemical Theory and Computation*, 6(9):2669–2686, 2010. doi:10.1021/ct1002847.

[319] J. Autschbach, D. Peng, and M. Reiher. Two-component relativistic calculations of electric-field gradients using exact decoupling methods: Spin–orbit and picture-change effects. *Journal of Chemical Theory and Computation*, 8(11):4239–4248, 2012. doi:10.1021/ct300623j.

[320] A. E. Reed and F. Weinhold. Natural localized molecular orbitals. *The Journal of Chemical Physics*, 83(4):1736–1740, 08 1985. ISSN 0021-9606. doi:10.1063/1.449360.

[321] G. Cazzoli, C. Puzzarini, S. Stopkowicz, and J. Gauss. The hyperfine structure in the rotational spectra of bromofluoromethane: Lamb-dip technique and quantum-chemical calculations. *Molecular Physics*, 106(9–10):1181–1192, 2008. doi:10.1080/00268970802056052.

[322] Gabriele Cazzoli, Lino Cludi, Cristina Puzzarini, Paolo Stoppa, Andrea Pietropolli Charmet, Nicola Tasinato, Agostino Baldacci, Alessandro Baldan, Santi Giorgianni, René Wugt Larsen, Stella Stopkowicz, and Jürgen Gauss. Microwave, High-Resolution Infrared, and Quantum Chemical Investigations of $CHBrF_2$: Ground and v4 = 1 States. *J. Phys. Chem. A*, 115(4):453–459, 2011. doi:10.1021/jp110510v.

[323] Cristina Puzzarini, Gabriele Cazzoli, Juan Carlos López, José Luis Alonso, Agostino Baldacci, Alessandro Baldan, Stella Stopkowicz, Lan Cheng, and Jürgen Gauss. Spectroscopic investigation of fluoroiodomethane, CH_2FI: Fourier-transform microwave and millimeter-/submillimeter-wave spectroscopy and quantum-chemical calculations. *J. Chem. Phys.*, 134(17):174312, 2011. doi:10.1063/1.3583498. URL https://doi.org/10.1063/1.3583498.

[324] W. Gordy. Relation of nuclear quadrupole moment to nuclear shell structure. *Phys. Rev.*, 76(1):139–140, 1949. doi:10.1103/PhysRev.76.139. URL https://link.aps.org/doi/10.1103/PhysRev.76.139.

[325] C. H. Townes, H. M. Foley, and W. Low. Nuclear quadrupole moments and nuclear shell structure. *Phys. Rev.*, 76(9):1415–1416, 1949. doi:10.1103/PhysRev.76.1415. URL https://link.aps.org/doi/10.1103/PhysRev.76.1415.

[326] S. A. Moszkowski and C. H. Townes. The tendency for positive nuclear quadrupole moments. *Phys. Rev.*, 93(2):306–312, 1954. doi:10.1103/PhysRev.93.306. URL https://link.aps.org/doi/10.1103/PhysRev.93.306.

[327] E. Marshalek, L. W. Person, and R. K. Sheline. Systematics of deformations of atomic nuclei. *Rev. Mod. Phys.*, 35(1):108–116, 1963. doi:10.1103/RevModPhys.35.108. URL https://link.aps.org/doi/10.1103/RevModPhys.35.108.

[328] Y. Y. Sharon. On the signs of nuclear quadrupole moments. *Nuclear Physics A*, 99 (2):321–336, 1967. doi:10.1016/0375-9474(67)90344-2.

[329] J. N. P. van Stralen and L. Visscher. Molecular relativistic electric field gradient calculations suggest revision of the value of the nuclear electric quadrupole moment of ^{127}I. *Molecular Physics*, 101(13):2115–2124, 2003. doi:10.1080/0026897031000109428.

[330] R. J. Bartlett and C. E. Dykstra. *Coupled-Cluster Methods for Molecular Calculations*, pages 127–159. Springer Netherlands, 1984. doi:https://doi.org/10.1007/978-94-009-6451-8_8.

[331] T. Helgaker, T. A. Ruden, P. Jørgensen, J. Olsen, and W. Klopper. A priori calculation of molecular properties to chemical accuracy. *Journal of Physical Organic Chemistry*, 17(11):913–933, 2004. doi:https://doi.org/10.1002/poc.841.

[332] J. Paldus, J. Čížek, and I. Shavitt. Correlation Problems in Atomic and Molecular Systems. IV. Extended Coupled-Pair Many-Electron Theory and Its Application to the BH_3 Molecule. *Phys. Rev. A*, 5:50–67, Jan 1972. doi:10.1103/PhysRevA.5.50.

[333] J. A. Pople, R. Krishnan, H. B. Schlegel, and J. S. Binkley. Electron correlation theories and their application to the study of simple reaction potential surfaces. *International Journal of Quantum Chemistry*, 14(5):545–560, 1978. doi:https://doi.org/10.1002/qua.560140503.

[334] S. Pal, M. Durga Prasad, and D. Mukherjee. Development of a size-consistent energy functional for open shell states. *Theoretica chimica acta*, 66(5):311–332, 1984. doi:10.1007/BF00554787.

[335] M. Hanrath. On the concepts of connectivity, separability, and consistency: An illustration by partitioned diagrams and numerical probing. *Chemical Physics*, 356 (1):31–38, 2009. doi:https://doi.org/10.1016/j.chemphys.2008.10.039.

[336] J. Čížek. On the correlation problem in atomic and molecular systems. calculation of wavefunction components in ursell-type expansion using quantum-field theoretical methods. In I. Prigogine and S. A. Rice, editors, *Adv. Chem. Phys.*, volume 14, pages 35–89. 1969. doi:10.1002/9780470143551.ch2.

[337] G. Fitzgerald, R. J. Harrison, and R. J. Bartlett. Analytic energy gradients for general coupled-cluster methods and fourth-order many-body perturbation theory. *J. Chem. Phys.*, 85(9):5143–5150, 11 1986. doi:10.1063/1.451823.

[338] P. Jørgensen, H. J. Aa. Jensen, and J. Olsen. Linear response calculations for large scale multiconfiguration self-consistent field wave functions. *The Journal of Chemical Physics*, 89(6):3654–3661, September 1988. doi:10.1063/1.454885.

[339] J. Gauss, J. F. Stanton, and R. J. Bartlett. Coupled-cluster open-shell analytic gradients: Implementation of the direct product decomposition approach in energy gradient calculations. *J. Chem. Phys.*, 95(4):2623–2638, 1991. doi:10.1063/1.460915.

[340] J. Gauss and J. F. Stanton. Coupled-cluster calculations of nuclear magnetic resonance chemical shifts. *The Journal of Chemical Physics*, 103(9):3561–3577, 09 1995. doi:10.1063/1.470240.

[341] H. Koch, H. J. Aa. Jensen, P. Jørgensen, and T. Helgaker. Excitation energies from the coupled cluster singles and doubles linear response function (CCSDLR). Applications to Be, CH^+, CO, and H_2O. *The Journal of Chemical Physics*, 93(5): 3345–3350, 09 1990. doi:10.1063/1.458815.

[342] J. F. Stanton. Many-body methods for excited state potential energy surfaces. I. General theory of energy gradients for the equation-of-motion coupled-cluster method. *The Journal of Chemical Physics*, 99(11):8840–8847, 12 1993. doi:10.1063/1.465552.

[343] J. F. Stanton and R. J. Bartlett. The equation of motion coupled-cluster method. A systematic biorthogonal approach to molecular excitation energies, transition probabilities, and excited state properties. *J. Chem. Phys.*, 98(9):7029, 1993. doi:10.1063/1.464746.

[344] M. Kállay and J. Gauss. Analytic second derivatives for general coupled-cluster and configuration-interaction models. *The Journal of Chemical Physics*, 120(15): 6841–6848, Apr 2004. doi:10.1063/1.1668632.

[345] L. Visscher, T. Enevoldsen, T. Saue, and J. Oddershede. Molecular relativistic calculations of the electric field gradients at the nuclei in the hydrogen halides. *The Journal of Chemical Physics*, 109(22):9677–9684, 1998. doi:10.1063/1.477637.

[346] M. Pernpointner. Chapter 5 - accurate determination of electric field gradients for heavy atoms and molecules. In P. Schwerdtfeger, editor, *Theoretical and Computational Chemistry*, volume 14, pages 289–351. Elsevier, 2004. doi:10.1016/S1380-7323(04)80032-3.

[347] P. Pyykkö. The physics behind chemistry and the periodic table. *Chem Rev.*, 112: 371–84, 01 2012. doi:10.1021/cr200042e.

[348] P. Pyykkö. Relativistic Effects in Chemistry: More Common Than You Thought. *Annual Review of Physical Chemistry*, 63(Volume 63, 2012):45–64, 2012. ISSN 1545-1593. doi:https://doi.org/10.1146/annurev-physchem-032511-143755.

[349] J. Autschbach. Perspective: Relativistic effects. *The Journal of Chemical Physics*, 136(15):150902, 04 2012. doi:10.1063/1.3702628.

[350] L. Cheng and J. Gauss. Analytical evaluation of first-order electrical properties based on the spin-free Dirac-Coulomb Hamiltonian. *The Journal of Chemical Physics*, 134(24):244112, 06 2011. doi:10.1063/1.3601056.

[351] L. Cheng and J. Gauss. Analytic energy gradients for the spin-free exact two-component theory using an exact block diagonalization for the one-electron Dirac Hamiltonian. *The Journal of Chemical Physics*, 135(8):084114, 08 2011. doi:10.1063/1.3624397.

[352] L. Cheng and J. Gauss. Analytic second derivatives for the spin-free exact two-component theory. *The Journal of Chemical Physics*, 135(24):244104, 12 2011. doi:10.1063/1.3667202.

[353] A. Shee, L. Visscher, and T. Saue. Analytic one-electron properties at the 4-component relativistic coupled cluster level with inclusion of spin-orbit coupling. *The Journal of Chemical Physics*, 145(18):184107, 11 2016. doi:10.1063/1.4966643.

[354] L. Visscher, K. G. Dyall, and T. J. Lee. Kramers-restricted closed-shell CCSD theory. *International Journal of Quantum Chemistry*, 56(S29):411–419, 1995. doi:https://doi.org/10.1002/qua.560560844.

[355] L. Visscher, T. J. Lee, and K. G. Dyall. Formulation and implementation of a relativistic unrestricted coupled-cluster method including noniterative connected triples. *The Journal of Chemical Physics*, 105(19):8769–8776, 11 1996. doi:10.1063/1.472655.

[356] L. Visscher, E. Eliav, and U. Kaldor. Formulation and implementation of the relativistic Fock-space coupled cluster method for molecules. *The Journal of Chemical Physics*, 115(21):9720–9726, 12 2001. doi:10.1063/1.1415746.

[357] J. V. Pototschnig, A. Papadopoulos, L. Visscher, D. I. Lyakh, L. Halbert, and A. S. P. Gomes. Implementation of Relativistic Coupled Cluster Theory for Massively Parallel GPU-Accelerated Computing Architectures. *J. Chem. Theory Comput.*, 17:5509–5529, 09 2021. doi:10.1021/acs.jctc.1c00260.

[358] M. Pernpointner and L. Visscher. Nuclear quadrupole moments for ^{27}Al and ^{69}Ga derived from four-component molecular coupled cluster calculations. *The Journal of Chemical Physics*, 114(23):10389–10395, 06 2001. doi:10.1063/1.1374576.

[359] S. Stopkowicz and J. Gauss. Revised values for the nuclear quadrupole moments of ^{33}S and ^{35}S. *Phys. Rev. A*, 90(2):022507, Aug 2014. doi:10.1103/PhysRevA.90.022507.

[360] TAPP working group. Tensor Algebra Processing Primitives. https://github.com/TAPPorg/tensor-interfaces, 2024. Accessed: 2025-06-02.

[361] P. Pyykkö. Year-2008 Nuclear Quadrupole Moments. *Molecular Physics*, 106:1965–1974, 08 2008. doi:10.1080/00268970802018367.

[362] D. I. Lyakh. TAL-SH: Tensor Algebra Library for Shared Memory Computers: Nodes equipped with multicore CPU, NVIDIA GPU, AMD GPU, and Intel Xeon Phi. https://github.com/DmitryLyakh/TAL_SH, 2014–2022. The library implements basic tensor algebra operations with interfaces to C, C++11, and Fortran 90+. Copyright (C) 2014–2022 Dmitry I. Lyakh (Liakh) and Oak Ridge National Laboratory (UT-Battelle). Licensed under BSD 3-Clause. Accessed: 2025-06-02.

[363] T. Saue and H. J. Aa. Jensen. Quaternion symmetry in relativistic molecular calculations: The Dirac–Hartree–Fock method. *The Journal of Chemical Physics*, 111 (14):6211–6222, 1999. doi:10.1063/1.479958.

[364] Python Software Foundation. *math.gcd — Compute the greatest common divisor*, 2025. URL https://docs.python.org/3/library/math.html#math.gcd.

[365] G. Fabbro, J. Brandejs, and T. Saue. Highly Accurate Nuclear Quadrupole Moments Using High-Order Relativistic Coupled Cluster Theory. *ZENODO*, 2025. URL https://doi.org/10.5281/zenodo.15283150.

[366] R. Ditchfield, W. J. Hehre, and J. A. Pople. Self-Consistent Molecular-Orbital Methods. IX. An Extended Gaussian-Type Basis for Molecular-Orbital Studies of

Organic Molecules. *The Journal of Chemical Physics*, 54(2):724–728, 01 1971. doi:10.1063/1.1674902.

[367] J. D. Dill and J. A. Pople. Self-consistent molecular orbital methods. XV. Extended Gaussian-type basis sets for lithium, beryllium, and boron. *The Journal of Chemical Physics*, 62(7):2921–2923, 04 1975. doi:10.1063/1.430801.

[368] F. J. Lovas, E. Tiemann, J. S. Coursey, S. A. Kotochigova, J. Chang, K. Olsen, and R. A. Dragoset. Diatomic Spectral Database, NIST Standard Reference Database 114, 2005. URL https://dx.doi.org/10.18434/T4T59X. Last update to data content: November 2005.

[369] M. Urban and A. J. Sadlej. The nuclear quadrupole moment of Li: Refined calculations of electric field gradients in LiH, LiF, and LiCl. *Chemical Physics Letters*, 173(2):157–163, 1990. doi:10.1016/0009-2614(90)80070-T.

[370] E. Rothstein. Molecular constants of lithium hydrides by the molecular-beam electric resonance method. *The Journal of Chemical Physics*, 50(4):1899–1900, February 1969. doi:10.1063/1.1671294.

[371] D. T. Halfen and L. M. Ziurys. Precise rest frequencies for AlH and AlD ($X^1\Sigma^+$): A reassessment of the aluminum hyperfine structure. *Astrophysical Journal*, 607: 63–66, may 2004. doi:10.1086/421083.

[372] F. J. Lovas and E. Tiemann. Microwave Spectral Tables I. Diatomic Molecules. *Journal of Physical and Chemical Reference Data*, 3(3):609–770, 07 1974. doi:10.1063/1.3253146.

[373] M. P. Aliev and A. F. Krupnov. Microwave spectra of molecules, by walter gordy and robert l. cook. 3rd edition (wiley interscience, new york, 1984). *Optics and Spectroscopy*, 59(5):699, November 1985. Available from https://ui.adsabs.harvard.edu/abs/1985OptSp..59..699A/abstract.

[374] TOP500.org. Top500 list. https://www.top500.org, accessed: 2024-09-06; accessed: 2025-06-02.

[375] E. Solomonik, D. Matthews, J. R. Hammond, J. F. Stanton, and J. Demmel. A massively parallel tensor contraction framework for coupled-cluster computations. *Journal of Parallel and Distributed Computing*, 74(12):3176–3190, 2014. doi:10.1016/j.jpdc.2014.06.002.

[376] Paul T. Boggs and Janet E. Rogers. Orthogonal Distance Regression. Technical Report NISTIR 89-4197, NASA, 1990. available from https://nvlpubs.nist.gov/nistpubs/Legacy/Ir/nostir89-4197.pdf.

[377] M. Kállay, P. R. Nagy, D. Mester, L. Gyevi-Nagy, J. Csóka, P. B. Szabó, Z. Rolik, G. Samu, J. Csontos, B. Hégely, and et al. MRCC, a quantum chemical program suite, 2024. See *www.mrcc.hu*.

[378] S. L. Kahalas and R. K. Nesbet. Electronic Structure of LiH and Quadrupole Moment of ^{7}Li. *The Journal of Chemical Physics*, 39(3):529–544, August 1963. doi:10.1063/1.1734290.

[379] Paul E. Cade and Winifred M. Huo. Electronic Structure of Diatomic Molecules. VI.A. Hartree—Fock Wavefunctions and Energy Quantities for the Ground States of the First-Row Hydrides, AH. *The Journal of Chemical Physics*, 47(2):614–648, July 1967. doi:10.1063/1.1711938.

[380] J. C. Browne and F. A. Matsen. Quantum-mechanical calculations for the electric field gradients and other electronic properties of lithium hydride: The use of mixed orbital sets. *Phys. Rev.*, 135(5A):A1227–A1232, August 1964. doi:10.1103/PhysRev.135.A1227.

[381] C. F. Bender and E. R. Davidson. A natural orbital based energy calculation for helium hydride and lithium hydride. *The Journal of Physical Chemistry*, 70(8): 2675–2685, August 1966. doi:10.1021/j100880a036.

[382] Sheldon Green. Quadrupole Moment of Li. *Phys. Rev. A*, 4(1):251–253, July 1971. doi:10.1103/PhysRevA.4.251.

[383] D. Sundholm, P. Pyykkö, L. Laaksonen, and A. J. Sadlej. Nuclear quadrupole moment of lithium from combined fully numerical and discrete basis set calculations on LiH. *Chemical Physics Letters*, 112(1):1–6, 1984. doi:10.1016/0009-2614(84)87030-X.

[384] G. H. F. Diercksen, A. J. Sadlej, D. Sundholm, and P. Pyykkö. Towards an accurate determination of the nuclear quadrupole moment of Li from molecular data: LiF. *Chemical Physics Letters*, 143(2):1–6, 1988. doi:10.1016/0009-2614(88)87031-3.

[385] S. P. Karna and F. Grein. Ab initio SCF and CI studies of the electric field gradient in LiH. *Molecular Physics*, 69(4):661–670, 1990. doi:10.1080/00268979000100361. URL https://doi.org/10.1080/00268979000100361.

[386] P. Pyykkö. The nuclear quadrupole moments of the 20 first elements: High-precision calculations on atoms and small molecules. *Zeitschrift für Naturforschung A*, 47(1-2):189–196, 1992. doi:10.1515/zna-1992-1-233.

[387] H. Guan et al. Precision spectroscopy and nuclear structure parameters in ^{7}li^{+} ion. 3 2024. doi:10.48550/arXiv.2403.06384. arXiv preprint; submission history: v1 (2024-03-11); accessed 2025-06-02.

[388] V. Kellö, A. J. Sadlej, P. Pyykkö, D. Sundholm, and M. Tokman. Electric quadrupole moment of the ^{27}Al nucleus: Converging results from the AlF and AlCl molecules and the Al atom. *Chemical Physics Letters*, 304(5):414–422, 1999. doi:10.1016/S0009-2614(99)00340-1.

[389] A. Brown and R. E. Wasylishen. Hyperfine constants for aluminum hydride and aluminum deuteride. *Journal of Molecular Spectroscopy*, 292:8–14, 2013. ISSN 0022-2852. doi:10.1016/j.jms.2013.08.003.

[390] A. Aerts and A. Brown. A revised nuclear quadrupole moment for aluminum: Theoretical nuclear quadrupole coupling constants of aluminum compounds. *The Journal of Chemical Physics*, 150(22):224302, 06 2019. doi:10.1063/1.5097151.

[391] V. Kellö and A. J. Sadlej. Quadrupole moments of CuH, AgH, and AuH. A study of the electron correlation and relativistic effects. *The Journal of Chemical Physics*, 95(11):8248–8253, 12 1991. doi:10.1063/1.461303.

[392] T. Saue. HAMP-vQED. URL https://dirac.ups-tlse.fr/hamp-vqed/doku.php?id=public:overview.

[393] A. Sunaga, M. Salman, and T. Saue. 4-component relativistic hamiltonian with effective qed potentials for molecular calculations. *The Journal of Chemical Physics*, 157(16):164101, 2022. doi:10.1063/5.0116140.

[394] M. Salman and T. Saue. Calculating the many-potential vacuum polarization density of the dirac equation in the finite-basis approximation. *Phys. Rev. A*, 108(1): 012808, 2023. doi:10.1103/PhysRevA.108.012808.

[395] D. Ferenc, M. Salman, and T. Saue. Gaussian-basis-set approach to one-loop self-energy. *Physical Review A*, 111:L040802, 2025. doi:10.1103/PhysRevA.111.L040802.

[396] J. A. S. Smith. Nuclear quadrupole resonance spectroscopy. General principles. *Journal of Chemical Education*, 48(1):39, 1971. doi:10.1021/ed048p39.

[397] A. Jerschow. From nuclear structure to the quadrupolar NMR interaction and high-resolution spectroscopy. *Progress in Nuclear Magnetic Resonance Spectroscopy*, 46 (1):63–78, 2005. doi:10.1016/j.pnmrs.2004.12.001.

[398] P. Pyykkö. Year-2008 nuclear quadrupole moments. *Molecular Physics*, 106:1965–1974, 2008.

[399] C. Dean. Zeeman Splitting of Nuclear Quadrupole Resonances. *Phys. Rev.*, 96: 1053–1059, Nov 1954. doi:10.1103/PhysRev.96.1053.

[400] Roberto Luiz Andrade Haiduke. The nuclear quadrupole moment of barium from the molecular method. *Chemical Physics*, 603:113055, 2026. ISSN 0301-0104. doi:https://doi.org/10.1016/j.chemphys.2025.113055.

[401] Andrei Derevianko, U. C. Perera, Marek Krośnicki, Kamil Nalikowski, H. W. T. Morgan, and Valera Veryazov. Electric field gradient in accurate quantum chemical calculations, 2026. URL https://arxiv.org/abs/2601.07098.

[402] T. Q. Teodoro and R. L. A. Haiduke and L. Visscher. Nuclear electric quadrupole moment of potassium from the molecular method. *Phys. Rev. A*, 91:032516, Mar 2015. doi:10.1103/PhysRevA.91.032516. URL https://link.aps.org/doi/10.1103/PhysRevA.91.032516.

[403] G. Fabbro, J. Brandejs, and T. Saue. Highly Accurate Expectation Values Using High-Order Relativistic Coupled Cluster Theory. *The Journal of Physical Chemistry A*, 129(30):6942–6958, 2025. ISSN 1089-5639. doi:10.1021/acs.jpca.5c02844.

[404] G. P. Barwood and H. S. Margolis and G. Huang and P. Gill and H. A. Klein. Measurement of the Electric Quadrupole Moment of the 4d $^2D_{5/2}$ Level in $^{88}Sr^+$. *Physical Review Letters*, 93(13):133001, 2004. doi:10.1103/PhysRevLett.93.133001.

[405] M. M. Boyd. *High precision spectroscopy of strontium in an optical lattice: Towards a new standard for frequency and time*. PhD thesis, University of Colorado, Boulder, January 2007.

[406] T. Bothwell and J. M. Robinson and E. Oelker and W. R. Milner and C. J. Kennedy and A. Brusch and K. Peterson and D. Kedar and A. W. Young and R. B. Hutson and X. Zhang and C. Sanner and S. L. Bromley and J. Ye. Clock with 8×10^{-19} Systematic Uncertainty. *Physical Review Letters*, 133(2):023401, 2024. doi:10.1103/PhysRevLett.133.023401.

[407] N. J. Stone. Table of nuclear electric quadrupole moments. *Atomic Data and Nuclear Data Tables*, 90:75–176, 2005.

[408] B. K. Sahoo. Determination of the nuclear quadrupole moment of ^{87}Sr. *Phys. Rev. A*, 73(6):062501, June 2006. doi:10.1103/PhysRevA.73.062501.

[409] A.-M. Mårtensson-Pendrill. Hyperfine structure in the 4d states of Rb-like Sr. *J. Phys. B: At. Mol. Opt. Phys.*, 35(4):917–927, 2002. doi:10.1088/0953-4075/35/4/315.

[410] K.-Z. Yu and L.-J. Wu and B.-C. Gou and T.-Y. Shi. Calculation of the hyperfine structure constants in $^{43}Ca^{+}$ and $^{87}Sr^{+}$. *Phys. Rev. A*, 70:012506, Jul 2004. doi:10.1103/PhysRevA.70.012506.

[411] B. Lu and T. Zhang and H. Chang and J. Li and Y. Wu and J. Wang. Reevaluation of the nuclear electric quadrupole moment for ^{87}Sr by hyperfine structures and relativistic atomic theory. *Phys. Rev. A*, 100:012504, Jul 2019. doi:10.1103/PhysRevA.100.012504.

[412] Y.-B. Tang. Determination of nuclear quadrupole moments of ^{25}Mg,^{78} Sr, and ^{135,137}Ba via configuration-interaction combined with a coupled-cluster approach. *Phys. Rev. A*, 113:022812, Feb 2026. doi:10.1103/1jxh-c6hw.

[413] C. E. Blom, H. G. Hedderich, F. J. Lovas, R. D. Suenram, and A. G. Maki. Measurement of rotational spectra of sro and determination of electric quadrupole coupling constants. *Journal of Molecular Spectroscopy*, 152:109–119, 1992. doi:10.1016/0022-2852(92)90121-4.

[414] K. C. Etchison, C. T. Dewberry, and S. A. Cooke. Born–oppenheimer breakdown effects and hyperfine structure in the rotational spectrum of strontium monosulfide, srs. *Chemical Physics*, 342(1):71–77, 2007. doi:10.1016/j.chemphys.2007.09.029.

[415] Fabbro, G., Brandejs, J., and Saue, T. The nuclear electric quadrupole moment of ^{87}Sr from highly accurate molecular relativistic calculations [Data set]. Zenodo, 2026. URL https://doi.org/10.5281/zenodo.18271266.

[416] M. J. O. Deegan and P. J. Knowles. Perturbative corrections to account for triple excitations in closed and open shell coupled cluster theories. *Chemical Physics Letters*, 227(3):321–326, 1994. ISSN 0009-2614. doi:https://doi.org/10.1016/0009-2614(94)00815-9.

[417] Roberto L.A. Haiduke, Albérico B.F. da Silva, and Lucas Visscher. The nuclear electric quadrupole moment of lutetium from the molecular method. *Chemical Physics Letters*, 445(4):95–98, 2007. doi:https://doi.org/10.1016/j.cplett.2007.07.061.

[418] R. L. A. Haiduke and A. B. F. da Silva and L. Visscher. The nuclear electric quadrupole moment of antimony from the molecular method. *The Journal of Chemical Physics*, 125(6):064301, 08 2006. ISSN 0021-9606. doi:10.1063/1.2234369.

[419] J. Dognon and P. Pyykkö. Nuclear electric quadrupole moment of ^{45}sc: reconfirmation and extension to diatomic scn. *Phys. Chem. Chem. Phys.*, 27:2758–2761, 2025. doi:10.1039/D5CP01943E.

[420] Régis Tadeu Santiago and Roberto Luiz Andrade Haiduke. Nuclear electric quadrupole moment of gold from the molecular method. *Phys. Rev. A*, 91:042516, Apr 2015. doi:10.1103/PhysRevA.91.042516.

[421] E. F. Gusmão, R. T. Santiago, and R. L. A. Haiduke. Accurate nuclear quadrupole moment of ruthenium from the molecular method. *Journal of Chemical Physics*, 151(19):194306, 2019. doi:10.1063/1.5128655.

[422] M. Pernpointner, M. Seth, and P. Schwerdtfeger. A point-charge model for the nuclear quadrupole moment: Coupled-cluster, Dirac–Fock, Douglas–Kroll, and nonrelativistic Hartree–Fock calculations for the Cu and F electric field gradients in CuF. *J. Chem. Phys.*, 108:6722–6738, 1998. doi:10.1063/1.476088. URL https://doi.org/10.1063/1.476088.

[423] M. Pernpointner, P. Schwerdtfeger, and B. A. Hess. The nuclear quadrupole moment of ^{133}Cs: Accurate relativistic coupled cluster calculations for CsF within the point-charge model for nuclear quadrupole moments. *J. Chem. Phys.*, 108:6739–6747, 1998. doi:10.1063/1.476089. URL https://doi.org/10.1063/1.476089.

[424] J. Gauss and J. F. Stanton. Analytic gradients for the coupled-cluster singles, doubles, and triples (CCSDT) model. *The Journal of Chemical Physics*, 116(5): 1773–1782, 02 2002. doi:10.1063/1.1429244.

[425] Jan Brandejs, Niklas Hörnblad, Edward F. Valeev, Alexander Heinecke, Jeff Hammond, Devin Matthews, and Paolo Bientinesi. Tensor Algebra Processing Primitives (TAPP): Towards a Standard for Tensor Operations, 2026. URL https://arxiv.org/abs/2601.07827.

[426] Devin A. Matthews. High-Performance Tensor Contraction without Transposition. *SIAM Journal on Scientific Computing*, 40(1):C1–C24, January 2018. doi:10.1137/16m108968x. URL https://doi.org/10.1137/16m108968x.

[427] NVIDIA cuTENSOR: A High-Performance CUDA Library For Tensor Primitives. https://docs.nvidia.com/cuda/cutensor/latest/index.html, November 2019.

[428] Jan Brandejs. TAPP CTF branch. https://github.com/TAPPorg/reference-implementation/tree/jan-ctf-bindings, 2025.

[429] Michael L. Neidig, David L. Clark, and Richard L. Martin. Covalency in f-element complexes. *Coordination Chemistry Reviews*, 257(2):394–406, 2013. ISSN 0010-8545. doi:10.1016/j.ccr.2012.04.029. A Tribute to Edward I. Solomon on his 65th Birthday: Part 2.

[430] M. Pernpointner. The effect of the Gaunt interaction on the electric field gradient. *Journal of Physics B: Atomic, Molecular and Optical Physics*, 35(2):383, jan 2002. doi:10.1088/0953-4075/35/2/314.

[431] Ronald E. Walpole, Raymond H. Myers, Sharon L. Myers, and Keying E. Ye. *Probability and Statistics for Engineers and Scientists*. Pearson, Boston, 9th edition, 2012. ISBN 978-0-321-62911-1.

[432] J. Bieroń, P. Pyykkö, D. Sundholm, V. Kellö, and J. Sadlej. Nuclear quadrupole moments of bromine and iodine from combined atomic and molecular data. *Physical Review A*, 64:52507–, 11 2001. doi:10.1103/PhysRevA.64.052507.

[433] G. Strang. *Linear Algebra and Its Applications*. Brooks Cole, 4 edition, 2006. ISBN 9780030105678.

[434] R. Sternheimer. On nuclear quadrupole moments. *Phys. Rev.*, 84:244–253, Oct 1951. doi:10.1103/PhysRev.84.244.

[435] J. Thyssen. *Development and Applications of Methods for Correlated Relativistic Calculations of Molecular Properties*. PhD thesis, University of Southern Denmark, 2001. Available from http://www.diracprogram.org/lib/exe/fetch.php?media=dissertations:joern_thyssen.pdf.

[436] J.-M. Lévy-Leblond. Nonrelativistic particles and wave equations. *Commun. Math. Phys.*, 6:286, 1967. doi:10.1007/BF01646020.

[437] K. G. Dyall. Relativistic double-zeta, triple-zeta, and quadruple-zeta basis sets for the light elements H–Ar. *Theoretical Chemistry Accounts*, 135(5):128, Apr 2016. doi:10.1007/s00214-016-1884-y.

[438] K. G. Dyall. Dyall dz, tz, and qz basis sets for relativistic electronic structure calculations, jan 2023. URL https://doi.org/10.5281/zenodo.7574629.

[439] R. M. Sternheimer and H. M. Foley. Nuclear Quadrupole Coupling in the Li_2 Molecule. *Phys. Rev.*, 92:1460–1468, Dec 1953. doi:10.1103/PhysRev.92.1460.

[440] H. M. Foley, R. M. Sternheimer, and D. Tycko. Nuclear quadrupole coupling in polar molecules. *Phys. Rev.*, 93:734–742, Feb 1954. doi:10.1103/PhysRev.93.734.

[441] H. A. Kramers. Théorie générale de la rotation paramagnétique dans les cristaux. *Proc. Acad. Amst*, 33(6), 1930. URL https://dwc.knaw.nl/DL/publications/PU00015981.pdf.

[442] N. Rösch. Time-reversal symmetry, Kramers' degeneracy and the algebraic eigenvalue problem. *Chemical Physics*, 80(1):1–5, 1983. ISSN 0301-0104. doi:https://doi.org/10.1016/0301-0104(83)85163-5.

[443] G. A. Aucar, H. J. Aa. Jensen, and J. Oddershede. Operator representations in Kramers bases. *Chemical Physics Letters*, 232(1-2):47–53, 1995. doi:10.1016/0009-2614(94)01332-p.

[444] B. Jansík, S. Høst, K. Kristensen, and P. Jørgensen. Local orbitals by minimizing powers of the orbital variance. *The Journal of Chemical Physics*, 134(19):194104, 05 2011. ISSN 0021-9606. doi:10.1063/1.3590361.

[445] I.-M. Høyvik, B. Jansik, and P. Jørgensen. Trust region minimization of orbital localization functions. *Journal of Chemical Theory and Computation*, 8(9):3137–3146, 2012. doi:10.1021/ct300473g.

[446] R. Fletcher. *Practical Methods of Optimization*. Wiley, Chichester, 1990.

[447] D. J. Griffiths. *Introduction to Quantum Mechanics*. Pearson, 3rd edition, 2018. ISBN 978-1107189638.

[448] A. D. Buckingham. Temperature-Dependent Chemical Shifts in the NMR Spectra of Gases. *The Journal of Chemical Physics*, 35(4):1174–1178, 10 1961. doi:10.1063/1.1732019.

[449] C. J. Jameson. *Rovibrational Averaging of Molecular Electronic Properties*, pages 457–519. Springer Berlin Heidelberg, Berlin, Heidelberg, 1991. doi:10.1007/978-3-642-58179-3_12.